From strong to ultrastrong coupling in circuit QED architectures

Thomas Niemczyk

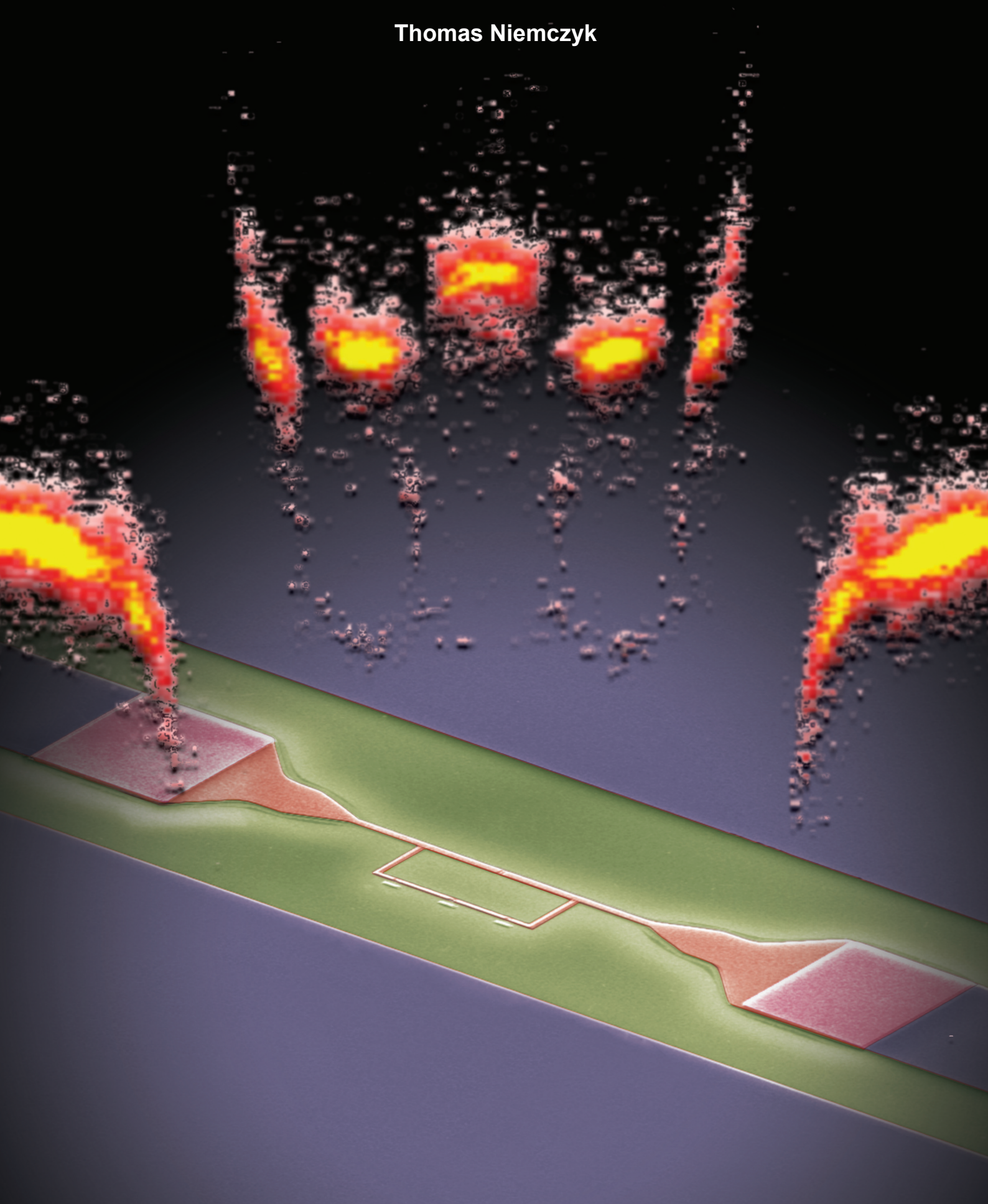

TECHNISCHE UNIVERSITÄT MÜNCHEN

Lehrstuhl E23 für Technische Physik

Walther-Meißner-Institut für Tieftemperaturforschung
der Bayerischen Akademie der Wissenschaften

From strong to ultrastrong coupling in circuit QED architectures

Thomas Niemczyk

Vollständiger Abdruck der von der Fakultät für Physik der Technischen Universität München zur Erlangung des akademischen Grades eines

Doktors der Naturwissenschaften

genehmigten Dissertation.

Vorsitzender:	Univ.-Prof. Dr. H. Friedrich
Prüfer der Dissertation:	1. Univ.-Prof. Dr. R. Gross
	2. Univ.-Prof. Dr. G. Abstreiter

Die Dissertation wurde am 30.06.2011 bei der Technischen Universität München eingereicht und durch die Fakultät für Physik am 10.08.2011 angenommen.

You know my steez

Method Man

Abstract

The field of cavity quantum electrodynamics (cavity QED) studies the interaction between light and matter on a fundamental level: a single atom interacts with a single photon. If the atom-photon coupling is larger than any dissipative effects, the system enters the strong-coupling limit. A peculiarity of this regime is the possibility to form coherent superpositions of light and matter excitations – a kind of 'molecule' consisting of an atomic *and* a photonic contribution. The novel research field of circuit QED extends cavity QED concepts to solid-state based system. Here, a superconducting quantum bit is coupled to an on-chip superconducting one-dimensional waveguide resonator. Owing to the small mode-volume of the resonant cavity, the large dipole moment of the 'artificial atom' and the enormous engineering potential inherent to superconducting quantum circuits, remarkable atom-photon coupling strengths can be realized.

This thesis describes the theoretical framework, the development of fabrication techniques and the implementation of experimental characterization techniques for superconducting quantum circuits for circuit QED applications. In particular, we study the interaction between superconducting flux quantum bits and high-quality coplanar waveguide resonators in the strong-coupling limit. Furthermore, we report on the first experimental realization of a circuit QED system operating in the *ultrastrong-coupling* regime, where the atom-photon coupling rate reaches a considerable fraction of the relevant system frequencies. In these experiments we could observe phenomena that can not be explained within the renowned Jaynes-Cummings model.

Kurzfassung

Das Forschungsgebiet der Hohlraum-Quantenelektrodynamik (cavity QED) untersucht die Wechselwirkung zwischen Licht und Materie auf fundamentaler Ebene: ein einzelnes Atom wechselwirkt mit einem einzelnen Photon. Falls die Atom-Photon Kopplung stärker ist als alle anderen dissipativen Effekte, befindet sich das System im sogenannten Regime starker Kopplung. Eine Besonderheit dieses Regimes besteht in der Möglichkeit der Formierung eines kohärenten Superpositionszustands aus Licht- und Materieanregungen – einer Art 'Molekül' bestehend aus einem atomaren und einem photonischen Anteil. Das neuartige Forschungsfeld der Schaltkreis QED weitet Hohlraum QED Konzepte auf festkörperbasierte Systeme aus. Hierbei wird ein supraleitendes Quantenbit mit einem supraleitenden, eindimensionalen Wellenleiterresonator gekoppelt. Aufgrund des kleinen Modenvolumens der resonanten Kavität, des großen Dipolmoments des 'künstlichen Atoms' und der den supraleitenden Schaltkreisen anhaftenden Flexibilität im Herstellungsprozess lassen sich beachtliche Atom-Photon Kopplungsstärken realisieren.
Diese Arbeit beschreibt das theoretische Fundament zur Beschreibung supraleitender Schaltkreise sowie die Entwicklung von Fabrikationstechniken und die Implementierung experimenteller Charakterisierungsmethoden in Schaltkreis QED Anwendungen. Von besonderem Interesse ist hierbei die Wechselwirkung zwischen supraleitenden Fluss-Quantenbits und koplanaren Wellenleitern hoher Güte im Regime starker Kopplung. Weiterhin berichten wir über die erste experimentelle Realisierung eines Schaltkreis QED Systems welches im Bereich *ultrastarker Kopplung* betrieben wird, in dem die Atom-Photon Kopplungsrate einen beachtlichen Anteil der relevanten Systemfrequenzen erreicht. In diesen Experimenten zeigen sich Strukturen, welche nicht innerhalb des renommierten Jaynes-Cummings Models erklärt werden können.

Contents

Chapter 1

Introduction

In July 1962, Brian D. Josephson published a theoretical article [1], predicting phenomena associated with the tunneling of Cooper pairs between two superconductors. Shortly after, these phenomena generally known as *Josephson effects* were verified experimentally [2] and led to the invention of the *Josephson junction*. Roughly half a year after Josephson's findings, an important paper in a completely different field of physics was published. In this work, Edwin T. Jaynes and Fred W. Cummings theoretically studied the interaction between an atom and a *quantized mode* of a radiation field [3]. Many phenomena observed in quantum optics can be described correctly by treating the electromagnetic fields semi-classically, e.g. the existence of coherent excitation transfer between atom and field, the so-called Rabi oscillations. However, within the fully quantized *Jaynes-Cummings model*, additional phenomena were predicted, e.g. the collapse and revival of the Rabi nutation [4]. It took experimentalists working in the field of quantum optics 24 years until they were able to observe these phenomena [5].

Without much doubt, neither Josephson nor Jaynes and Cummings could imagine in the early 1960's how their pioneering works would be united in a fascinating new area of research, namely *circuit quantum electrodynamics*. This term – first introduced in 2004 [6,7] for superconducting circuits – is adopted from cavity quantum electrodynamics (QED), an area of research in the field of quantum optics. In cavity QED, photons and atoms are interacting inside a high finesse cavity, thus enabling the study of fundamental light-matter interaction. Such experiments can be conducted at a level involving only a few or even single quanta of light and 'matter'. Circuit QED can be thought of as the solid-state implementation of cavity QED. In the circuit QED architecture, microwave photons stored in an on-chip resonator are coupled to superconducting 'artificial atoms'. Although there are many different realizations of these superconducting solid-state atoms, they are all composed of small electrical circuits sharing a fundamental building block: the Josephson junction. Though consisting of many billions of atoms, macroscopic circuits involving one or more Josephson junctions reveal their quantum mechanical nature at sufficiently low temperatures. Similar to natural atoms, they exhibit a discrete multi-level structure. Moreover, owing to the inherent non-linearity of Josephson junctions, it is possible to isolate the two lowest energy levels from higher ones, effectively realizing a quantum two-level system or *qubit*. In general, qubits play an important role as the computational building blocks of future quantum computers.

Both in cavity and circuit QED, the atom-photon dynamics is conveniently described by the Jaynes-Cummings model, which was validated in many fascinating and far reaching experiments. Essentially, this model describes the dipole coupling of a two-level system to the quantized mode of an electromagnetic field. If the interaction rate g between atom and photon is larger than the cavity decay rate κ and the atom decay rate γ, the system enters the so-called *strong-coupling regime*. A peculiarity of this regime is the possibility to form coherent superpositions of light and matter excitations – a kind of 'molecule' consisting of a 50% atomic and 50% photonic component.
In cavity QED, the interaction strength is typically very weak due to the small dipole moment of natural atoms. However, the strong-coupling limit can be reached by using high-finesse cavities and due to the exceptional coherence times of isolated atoms. In contrast, circuit QED the qubit coherence times suffer from the unavoidable coupling to dissipative degrees of freedom in the solid-state environment. Compared to cavity QED, however, the lower coherence times are more than compensated by the huge atom-photon coupling strengths that can be realized – and engineered – in circuit QED systems. Ultimately, the strong-coupling limit can be reached far more easily in circuit QED architectures.

This thesis describes the theoretical framework and realization of a circuit QED architecture for studying fundamental light-matter interaction. To this end, fabrication and characterization techniques for a specific type of artificial atom – the superconducting flux qubit – had to be developed and implemented. As central point of this work, we studied different qubit-resonator coupling schemes, thereby reaching the strong-coupling regime. Moreover, during this thesis we were able to push a circuit QED system into the *ultrastrong-coupling limit* [8]. In this yet unexplored regime, the atom-photon coupling rate g becomes comparable to the cavity and atom transition frequencies. A cornerstone of ultrastrong-coupling physics is the breakdown of the Jaynes-Cummings model which could be observed in our experiment for the first time.

1.1 Quantum information processing

One of the great breakthroughs in science and technology in the twentieth century was the invention of integrated circuits. Continuous progress in semiconductor device fabrication and miniaturization gave rise to the current information age. Off-the-shelf powerful digital computers and the world wide web allow to process and transfer digital information fast and over long distances. The idea of a *universal quantum computer* was born in the early 1980's, when Richard Feynman [9], among others [10–12], began to investigate the generalization of conventional information science concepts to quantum physical systems. The field of *quantum information processing* was born, attracting and inspiring scientists from many different disciplines. It was shown theoretically that certain mathematical problems [13–18] can be solved much faster using a quantum computer instead of a classical computer. The superposition principle allows a quantum computer to perform a large number of computations simultaneously, a phenomena sometimes called 'quantum parallelism'. Furthermore, quantum information systems allow the simulation of large quantum systems [9, 19] and provide the possibility for secure communication using quantum cryptography [20, 21].

Scientists started to work on different approaches and physical implementations of qubits – the fundamental building block for future quantum computers – both theoretically and experimentally. Since the mid 1990's, tremendous progress has been made with NMR based systems [22, 23] and in quantum optics with trapped ions [24–28], polarization entangled photons [29–32] and cavity QED systems [33–38]. However, any concept has to meet the DiVincenzo criteria [39], which state simple but necessary (hardware) conditions for viable quantum computation and communication. In the above mentioned systems, molecules, ions or circular Rydberg atoms play the role of *microscopic* qubits. On the one hand, these types of qubits can be isolated quite efficiently from the environment and therefore these setups profit from long coherence times. On the other hand, they lack a good scalability potential. In terms of large-scale applications with 100 or even more qubits, solid-state approaches including quantum dots [40–44], nitrogen vacancy centers in diamond [45, 46], and superconducting qubits [47–49] are much more promising candidates. An up-to-date and very thorough overview of different experimental approaches towards the realization of a quantum computer can be found in Ref. [50] while Ref. [51] summarizes basic quantum information concepts.

Quantum computation and communication is a relatively novel field in modern physics. It is difficult to foretell which approach will prove successful. Even though we are still far away from the ambitious goal of a large-scale quantum computer, groundbreaking progress has been made in understanding the complex interplay of quantum mechanical systems. In this sense, the investigation of fundamental light-matter interaction and basic laws of quantum physics in this thesis has to be attributed to basic research rather than applied quantum information science.

1.2 Superconducting qubits vs. natural atoms

Superconducting qubits are electrical circuits consisting of inductors, capacitors and, most importantly, one or more Josephson junctions [52, 53]. This crucial building block – a dissipationless source of non-linearity – is discussed in detail in section 2.1. Owing to the amazing properties of superconductors in general and of Josephson junctions in particular, these circuits behave like *macroscopic* quantum objects when cooled to sufficiently low temperatures. With their discrete level structure, superconducting qubits resemble natural atoms in many ways. In addition, their inherent *in situ* tunability and their enormous engineering potential make them extremely versatile. Moreover, superconducting quantum bits can be fabricated with well-established lithographic and thin-film fabrication techniques as they are found in modern semiconductor device fabrication.
Depending on the ratio of the qubit's characteristic energy scales and thus the relevant macroscopic quantum variable, one distinguishes between three major types of superconducting qubits:

- Charge qubit: quantum information is encoded in the number of excess Cooper pairs (and thus the charge) located on a small superconducting island [54–58]. The island is connected to a much larger reservoir via one or more Josephson junctions. This type of qubit is also known as 'Cooper Pair Box' (CPB). Applying a gate voltage

changes the number of Cooper pairs on the island while an additional flux bias controls the transition energy between the ground and excited state.
Modified versions of the CPB are the 'quantronium' [59–61] and the 'fluxonium' [62].

- Flux qubit: the macroscopic quantum variable governing the dynamics is the magnetic flux threading the qubit loop. In general, flux qubits consist of a superconducting ring interrupted by one or more Josephson junctions [63–67]. The information is encoded in the sign of a persistent current flowing in the qubit loop. This type of qubit is at the heart of this thesis work and will be discussed in section 2.2 more thoroughly. Recently, the transmon qubit [68–70] – a flux sensitive qubit based on the CPB – gained a lot of attention due to its superior coherence properties.

- Phase qubit: this type of qubit consists of a relatively large current-biased Josephson junction [71–75]. The dynamic quantum variable is the phase difference across the junction and the quantum information is encoded in oscillatory states with distinct tunneling probabilities through a adjustable potential barrier.

In general, the electric and magnetic dipole moments associated with an atomic transition are a measure of the size of the atom. Superconducting qubits resemble 'artificial atoms' with dimensions ranging from few hundreds of nanometers up to more than 100 µm, while typical separations in natural atoms are of the order of ångström. For example, the magnetic dipole moment μ associated with a flux qubit (persistent current $I_\mathrm{p} = 100 - 500\,\mathrm{nA}$; area $A = 10 - 100\,\mu\mathrm{m}^2$) is $\mu = 10^5 - 10^6\,\mu_\mathrm{B}$. This value is $10^2 - 10^3$ times larger than that of circular Rydberg-atoms [34] used in cavity QED setups. In contrast to natural atoms, the large dipole moments of superconducting qubits allow one to considerably tune the transition energy between the ground and excited state by applying moderate control fields. Moreover, the dipole moment determines how strongly an atom interacts with a given electromagnetic field.
On the other hand, however, a large dipole moment increases the qubit's sensitivity to electric and magnetic noise sources effectively reducing the coherence times. Understanding decoherence mechanisms and eliminating microscopic and macroscopic noise sources [69, 76–87] is still one of the biggest challenges for any type of superconducting qubit.

1.3 Circuit vs. cavity QED

Circuit and cavity QED both investigate the interaction of atoms representing single quanta of 'matter' to quantized electromagnetic field modes. Under certain conditions, quantum entanglement of radiation and matter is possible, a phenomena unique to the world of quantum mechanics. Illustrations of typical experimental cavity and circuit QED setups are shown in Figure 1.1 a and b, respectively. In both fields, the interaction strength between atoms and photons is increased by confining the photons to a small volume between two highly reflecting mirrors. In a very figurative picture, photons are reflected by the mirrors many times and thus collide frequently with the atom whose size is proportional to its dipole moment. Eventually the photon is lost owing to mirror imperfections which in turn defines a photon loss rate κ. In general, the atom-photon coupling energy $\hbar g$ is given by the product of the dipole moment and the zero-point electromagnetic field

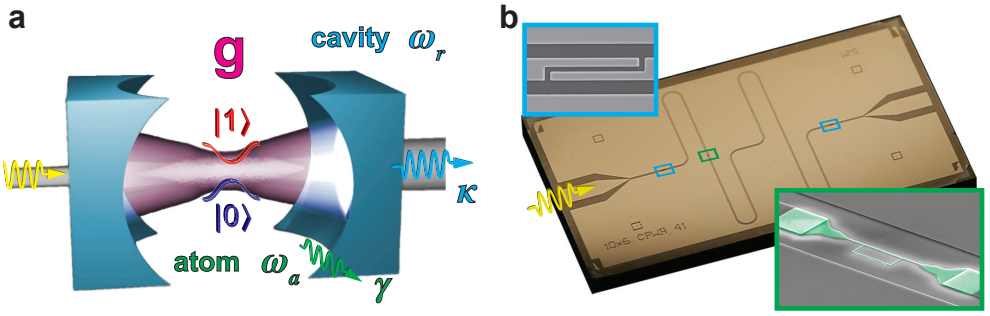

Figure 1.1: Analogies between cavity and circuit QED architectures. (a) Schematic of a cavity QED setup. The cavity (light blue) consists of two highly reflecting mirrors and supports the formation of a standing electromagnetic wave with fundamental resonance frequency ω_r. Mirror imperfections define a photon loss rate κ. An atom (green) with a transition frequency ω_a between the ground state $|0\rangle$ (blue) and the first excited state $|1\rangle$ (red) is placed inside the cavity. Spontaneous emission into modes other than the cavity mode is modeled by the atom decay rate γ. The atom-photon interaction rate g (magenta) depends on the atom's dipole moment and the electromagnetic field strength. (b) Photograph of a circuit QED setup as realized within this thesis. The cavity consists of a narrow, meandering strip of superconducting metal interrupted by small discontinuities (light blue box) acting analogue to the mirrors in the cavity QED setup. A superconducting flux qubit (green box) is fabricated at a suitable position and resembles an artificial atom. The decay rates κ and γ and the atom-photon interaction rate g are defined as in (a) but omitted in the picture for clarity.

strength $\mathcal{E}$ of the cavity mode. The latter can be enhanced by decreasing the available effective mode volume V_m since $\mathcal{E} \propto 1/\sqrt{V_\mathrm{m}}$.
The Fabry-Pérot cavities used in cavity QED setups are 3-dimensional (see Fig. 1.1a) with effective mode volumes of the order of $V_\mathrm{m}/\lambda^3 \approx 10^3 - 10^4$ and $V_\mathrm{m}/\lambda^3 \approx 1 - 10$ for optical [88, 89] and microwave [90, 91] wavelengths λ, respectively. With 2-dimensional photonic crystal nanocavities, effective mode volumes of $V_\mathrm{m}/\lambda^3 = 0.01 - 1$ have been reported [92–94].
On the other hand, the cavities used in circuit QED architectures (see Fig.1.1 b) are quasi-1-dimensional structures. While one dimension is of the order of the wavelength λ, the electromagnetic field is confined in the other two dimensions on length scales of $\sim 10\,\mu\mathrm{m}$. Therefore, the effective mode volume [6, 7] can be as small as $V_\mathrm{m}/\lambda^3 = 10^{-5} - 10^{-6}$. In combination with the huge dipole moment of superconducting artificial atoms, the tiny mode volume leads to greatly enhanced coupling rates $g \propto 1/\sqrt{V_\mathrm{m}}$. Another advantage of circuit QED setups is based on position-independent coupling strengths. The qubit can be fabricated by lithographic processes precisely at a desired position – usually at the nodes of the electromagnetic field – in order to maximize the coupling. In contrast, in cavity QED, beams of atoms effusing from vapor cells or ovens are sent through the cavity after velocity selection. Variations in the atoms trajectory with respect to the spatial mode and additional variations in the transit time through the cavity effectively lead to a position-dependent coupling.

A very interesting regime – the strong-coupling limit – is reached when the coupling rate g exceeds the atom (γ) and cavity (κ) decay rates, i.e. $g > \kappa, \gamma$. When the atomic transition from the excited state to the ground state is resonant with the cavity, a quantum of energy coherently oscillates with the vacuum Rabi frequency $\Omega = 2g$ between an atomic

excitation and a cavity photon. Quantum mechanically, atom and cavity are entangled, forming a kind of light-matter molecule. Using a very weak probe beam, the eigenenergies of the entangled atom-cavity system can be inferred, revealing two distinct split peaks in the cavity's transmission spectrum.
Reaching the strong-coupling limit[1] has been one of the major challenges in cavity QED for decades. In 1985, a one atom-maser operating in the strong-coupling limit was realized in Munich [96]. Later, in 1992, the vacuum Rabi splitting was observed at optical frequencies [97] with caesium atoms from a vapor cell passing through a high-finesse cavity. Solid-state systems have proven to be very promising for studying strong light-matter interaction: only a few years after the first realizations of superconducting qubits, the strong coupling limit could be reached experimentally [7] in a circuit QED architecture with a superconducting charge qubit embedded in a quasi-1-dimensional transmission line resonator. Shortly afterwards, this limit was reached with a single quantum dot in a photonic crystal nanocavity [98, 99].

1.4 Overview and state-of-the-art in circuit QED

Before concluding this brief introductory paragraph with an outline of this thesis, an overview of recent and current developments in the field of circuit QED is given. The term 'circuit QED' was first introduced in 2004 with the pioneering work involving the observation of the vacuum Rabi splitting using a charge qubit and a distributed resonator [7]. Simultaneously, the coherent dynamics of a flux qubit to a lumped element LC-circuit were observed [100]. Today, the term 'circuit QED' is used for systems investigating the interplay between superconducting qubits and quantum harmonic oscillators – which involves LC-circuits and microscopic defects but also nanomechanical resonators. However, in this overview we will restrict ourselves to research highlights mostly involving distributed transmission line cavities. Experiments comprising lumped element resonant circuits will be summarized at the end of Chapter 4.

After the development of basic techniques for the time-domain [101] and frequency-domain characterization [102] of qubits in a cavity, circuit QED entered the strong dispersive limit. In this regime, the quantum nature of the cavity field can be directly observed by means of photon number splitting [103, 104]. Quantum state tomography was performed with single and entangled phase qubits using a dc-SQUID readout [105, 106] and with a transmon qubit by mapping the qubit state onto the photon state [107]. This experiment realized for the first time an on-chip deterministic single-photon source in the microwave regime and showed the ability to utilize photons as 'flying qubits' for quantum communication. Shortly afterwards, quantum state transfer between two qubits using the cavity as a quantum bus was demonstrated [108, 109]. It was suggested that the cavity could function as a useful short-term quantum memory. The photon-storage capabilities of a high-quality-factor cavity were utilized in an experiment, demonstrating the controlled generation of multiphoton Fock states up to six [110] and shortly thereafter 15 photons [111]. Fock states were generated by an excitation of the qubit which was then transferred to the cavity by resonant interaction. The techniques developed in these experiments led to one of the

[1] The road towards the domain of strong-coupling in cavity QED is nicely reviewed in Ref. [95].

most beautiful experiments in circuit QED: the synthesization of arbitrary superpositions of Fock states in a superconducting resonator [112]. Here, complex superposition states of light were deterministically prepared and fully reconstructed by means of Wigner tomography. Further important experiments highlighting fundamental quantum physics included single artificial atom lasing [113], the confirmation of the non-linear scaling behavior inherent in the Jaynes-Cummings [114] and Tavis-Cummings models [115], the supersplitting of entangled light-matter states under resonant driving [116] and the violation of Bell's inequality [117]. Another important experimental contribution involving two-qubit entanglement was the first solid-state realization of a superconducting quantum processor and the implementation of two quantum algorithms [118]. Very recently, qubit energy relaxation and dephasing times of up to $T_1 \sim 60\,\mu s$ and $T_2 \sim 20\,\mu s$ were reported [119], thereby exceeding the coherence times of previous state-of-the-art superconducting qubits by more than one order of magnitude. Furthermore, a key ingredient for quantum error correction – multi-qubit entanglement – was demonstrated recently by different groups independently. First, tripartite entanglement between two qubits and a cavity was demonstrated [120] and shortly afterwards, three-qubit Greenberger-Horne-Zeilinger (GHZ) states as well as so-called W states were prepared deterministically and analyzed by quantum state tomography [121, 122] in different setups. Almost simultaneously, the novel and exciting regime of ultrastrong light-matter interaction could be accessed experimentally in a circuit QED setup for the first time [8]. In this regime, the qubit-cavity coupling rate becomes comparable to the atomic and photonic transition frequency and the renowned Jaynes-Cummings model is no longer valid. The experiments in this new limit – inaccessible yet in cavity QED setups – constitute one of the major results presented in this thesis.

1.5 Thesis outline

Prerequisites for experiments in the field of circuit QED are two fundamental devices: superconducting qubits and high finesse cavities. The first part of chapter 2 summarizes important theoretical aspects of the physics of Josephson junctions – the building block for all superconducting qubits. The physics of specific Josephson junction devices, the dc-SQUID and the flux qubit, are discussed in section 2.2.1 and 2.2.2 respectively. The second part of chapter 2 addresses important concepts of superconducting coplanar waveguide cavities. Chapter 3 deals with fabrication techniques and design considerations for our superconducting quantum circuits. Additional on-chip circuit elements enabling an improved flux qubit readout are presented. The characterization of superconducting resonators by means of transmission measurements is reported at the end of this chapter. Next, in chapter 4, flux qubits are characterized by a standard readout technique involving a dc-SQUID. The cryogenic setup and sample mounting techniques are introduced briefly. We then turn to the experimental results on flux qubits including current-voltage characteristics and switching current measurements (see section 4.2.1). In section 4.4, the qubit transition frequency from the ground to the first excited state is determined spectroscopically and evidence for multi-photon transitions is presented in section 4.4.1. In section 4.4.2 we demonstrate the excitation of red and blue qubit-SQUID sidebands by high-amplitude microwave irradiation. Chapter 5 is devoted to the realm of circuit QED. After the Jaynes-Cummings model and its implications are introduced theoretically, we analyze coupled qubit-cavity systems in the strong-coupling regime of circuit QED. Differ-

ent coupling schemes are realized, thereby enhancing the qubit-cavity coupling rate. This allows performing multi-photon spectroscopy (see section 5.5.2) and provides evidence for symmetry breaking in a circuit QED architecture. Furthermore, in section 5.6, we extend the matter-light coupling into the ultrastrong-coupling limit. A brief summary in chapter 6 is followed by an outlook on promising new research activities in the field of ultrastrong light-matter physics. Finally, the appendices summarize fabrication recipes, sample parameters and a short instruction manual for the electron beam evaporator.

Chapter 2

Superconducting Quantum Circuits

Superconducting circuits can be engineered to exhibit quantum mechanical properties on a macroscopic scale. Though these circuits consist of many billions of atoms they can have a discrete and anharmonic level structure making them resemble a single, natural atom. In analogy to classical circuits, quantum circuits can be constructed of capacitors and inductors.

However, there is one fundamental element unique to the world of superconductors without a classical counterpart: the Josephson junction. Without exaggeration, the Josephson junction is the most crucial element in the realization of macroscopic quantum two-level systems. It is the only electronic element that is both *non-linear* and *dissipationless* at sufficiently low temperatures [48]. In the case of a superconducting quantum bit, non-linearity is necessary to address distinctively the lowest two energy levels while low dissipation is accompanied by long coherence times.

A prerequisite for observing quantum phenomena in superconducting circuits are low temperatures. First of all, materials like aluminum and niobium have to be cooled below the respective superconducting transition temperature T_c. In the superconducting state, electrons are strongly bound in Cooper pairs which can be described by a single macroscopic wavefunction. Thus, macroscopic variables like voltages and currents can show quantum mechanical behavior. Second, the quasiparticle excitation spectrum is separated by an energy gap $2\Delta_\mathrm{s}(T) = 3.52\ k_\mathrm{B}T_\mathrm{c}\sqrt{1-T/T_\mathrm{c}}$ from the superconducting condensate. For $T \ll T_\mathrm{c}$, the density of quasiparticles as well as the intrinsic dissipation for frequencies below $2\Delta_\mathrm{s}(0)/h$ becomes exponentially small. For aluminum, $2\Delta_\mathrm{s}(0)/h \sim 80\,\mathrm{GHz}$ while typical transition frequencies of aluminum based quantum bits are between $\omega_\mathrm{q} \sim 2 - 20\,\mathrm{GHz}$. Most importantly, however, the temperature must be low enough to avoid thermal population of higher states. Therefore, superconducting quantum circuits have to be operated in dilution refrigerators at mK temperatures ($k_\mathrm{B}T \ll \hbar\omega_\mathrm{q} \ll \Delta_\mathrm{s}$).

The first sections of this chapter discuss the most important properties of Josephson junctions which are necessary to understand the physics of the two Josephson junction devices presented in this thesis – the dc-SQUID (see section 2.2.1) and the flux qubit (see section 2.2.2). Finally, in section 2.3, we shall address a special type of transmission line resonator. This device essentially behaves as a quantum harmonic oscillator and is a prerequisite for experiments in the field of circuit QED.

2.1 The Josephson junction

In general, a Josephson junction is established by a weak contact between two superconducting electrodes. A detailed introduction into the physics of Josephson junctions can be found in various textbooks, e.g. Ref. [52] and Ref. [53]. Throughout this work we are considering SIS-type Josephson junctions (see Fig. 2.1 a) consisting of two superconducting electrodes (S) separated by an insulating tunnel barrier (I) of appropriate thickness (typically $1-2\,\mathrm{nm}$). Figure 2.1 b shows a scanning electron microscope (SEM) image of an $Al/AlO_x/Al$ Josephson junction. Details on the fabrication process are given in Chapter 3.

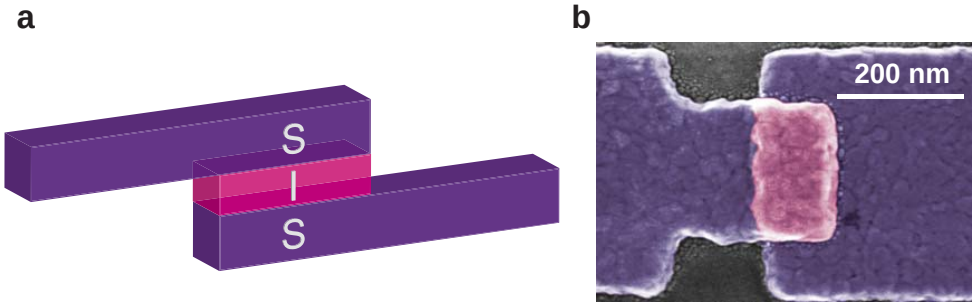

Figure 2.1: Josephson junction schematic and scanning electron microscope (SEM) image. (a) Sketch of a SIS-type Josephson junction. The superconducting electrodes (S) are separated by a thin insulating barrier (I). (b) False-color SEM image of a typical $Al/AlO_x/Al$ Josephson junction. The image resembles a top view of the junction sketched in (a). The area of the junction is roughly $100\,\mathrm{x}\,200\,\mathrm{nm}^2$.

2.1.1 Josephson effects and RCSJ model

In 1962, B. D. Josephson published a theoretical paper [1] predicting the existence of two fascinating phenomena supposed to occur in weakly linked superconductors. These so-called *Josephson effects* have their origin in the overlap (interference) of the macroscopic wavefunctions of each electrode and are a direct manifestation of a coherent macroscopic quantum effect. Semiclassically, the Josephson equations are given by

$$I_\mathrm{s} = I_\mathrm{c} \sin\varphi \qquad 1^\mathrm{st}\ \text{Josephson equation} \tag{2.1}$$

$$\frac{d\varphi}{dt} = \frac{2\pi}{\Phi_0} V \qquad 2^\mathrm{nd}\ \text{Josephson equation} \tag{2.2}$$

where I_s is the supercurrent flowing through the junction, I_c the critical current[1], φ the difference in phase of the macroscopic wavefunctions in each electrode, V the voltage across the junction and $\Phi_0 = h/2e$ the magnetic flux quantum.

Figure 2.2 a and b respectively show a sketch and the corresponding equivalent circuit of a Josephson junction biased by a current I. In this resistively and capacitively shunted junction (RCSJ) model, the Josephson junction is modeled by its self-capacitance C, a resistance R due to quasiparticle tunneling and an ideal Josephson branch carrying a

[1] The critical current is the maximum current that can be carried as supercurrent.

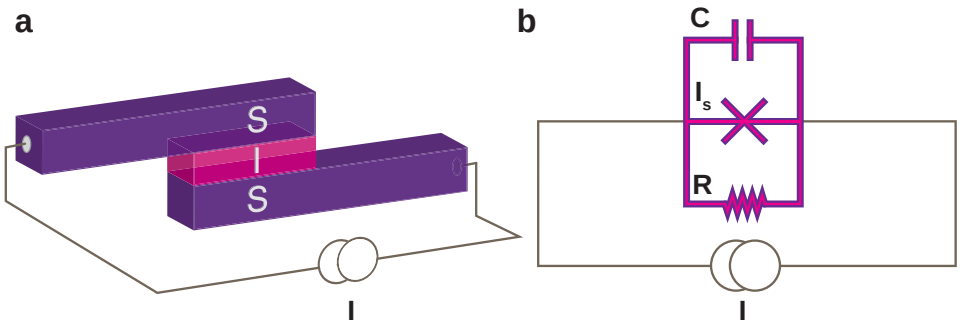

Figure 2.2: Schematic and equivalent circuit of a current driven Josephson junction. (a) Sketch of a SIS-type Josephson junction biased by a current I. (b) Equivalent circuit for the junction sketched in (a).

supercurrent I_s. For the circuit depicted in Fig. 2.2 b, current conservation leads to an equation of motion for the variable φ which can be interpreted as the motion of a 'phase particle' with mass M and damping η in a one-dimensional potential $U(\varphi)$, where

$$M = \left(\frac{\Phi_0}{2\pi}\right)^2 C \tag{2.3}$$

$$\eta = \left(\frac{\Phi_0}{2\pi}\right)^2 \frac{1}{R} \tag{2.4}$$

$$U(\varphi) = E_\mathrm{J}(1 - \cos\varphi - \frac{I}{I_\mathrm{c}}\varphi) \quad . \tag{2.5}$$

Here, $E_\mathrm{J} = \Phi_0 I_\mathrm{c}/2\pi$ is the Josephson coupling energy[2]. The potential $U(\varphi)$ is known as the *tilted washboard potential* and is visualized in Fig. 2.3 for different values of the bias current I. The RCSJ model gives an intuitive picture for understanding the dynamics of the Josephson junction devices discussed in section 2.2.

2.1.2 Non-linear inductance and characteristic energy scales

Using the Josephson equations, Eqs.(2.1) and (2.2), the ideal Josephson branch in the parallel circuit depicted in Fig. 2.2 b can be interpreted in terms of a non-linear inductance

$$L_\mathrm{J} = \frac{\Phi_0}{2\pi I_\mathrm{c}\cos(\varphi)} = \frac{L_\mathrm{J0}}{\cos(\varphi)} \quad . \tag{2.6}$$

It is this non-linearity which enables the design of superconducting circuits effectively mimicking quantum two-level systems. In terms of energy scales, the junction is conveniently described by the Josephson energy $E_\mathrm{J} = \Phi_0 I_\mathrm{c}/2\pi$ and the charging energy $E_\mathrm{C} = e^2/2C$. E_J and E_C are the energies required to store one flux quantum in the Josephson inductance L_J and to charge the junction's self-capacitance C with one elementary charge e, respectively.

Like position and momentum, charge and flux are conjugate variables in the framework of quantum mechanics and obey the commutation relation $[\hat{Q}, \hat{\Phi}] = i\hbar$. For the Josephson junction devices discussed in this work, $E_\mathrm{J}/E_\mathrm{C} \approx 20 - 80$ (*flux quantum circuits*). In this

[2] In general, the φ-dependent Josephson energy is given by $E_{\mathrm{J},\varphi} = E_\mathrm{J}(1 - \cos\varphi)$, where E_J is the maximum Josephson energy. In the remainder of this work, we will refer to E_J as the Josephson energy.

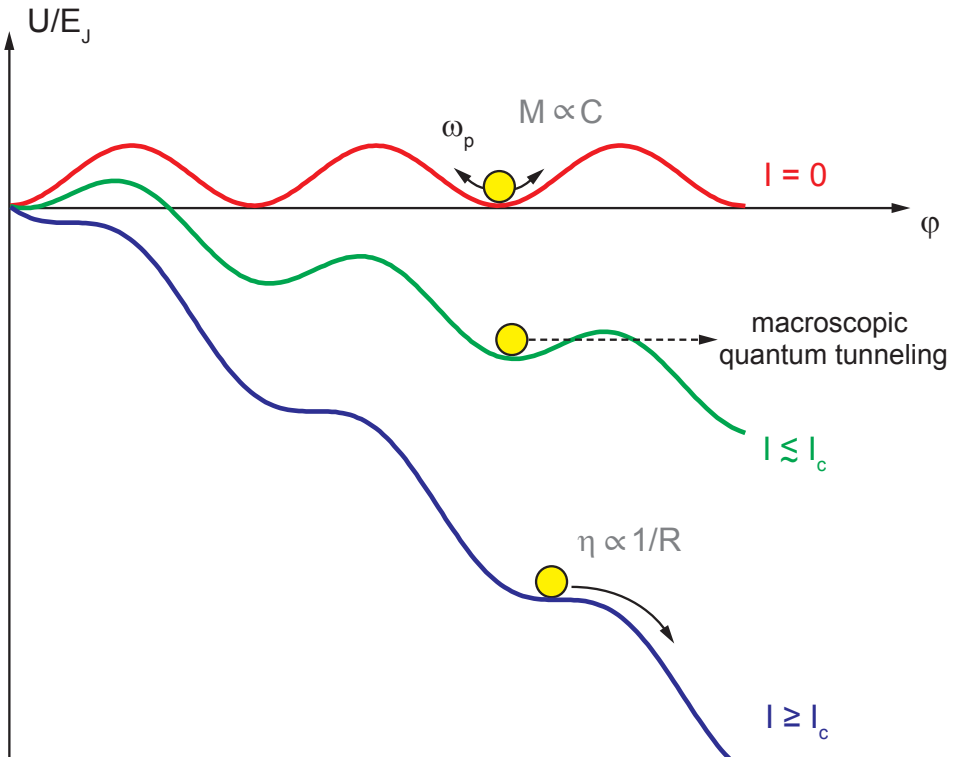

Figure 2.3: Sketch of the potential $U(\varphi)$ for various bias currents I. For $I > 0$ this potential is referred to as the tilted washboard potential. In general, three important cases can be distinguished. $I = 0$: the phase particle (yellow) with mass $M \propto C$ oscillates around the minimum with the plasma frequency $\omega_\mathrm{p} = \sqrt{\frac{2\pi I_\mathrm{c}}{\Phi_0 C}}$. $I \lesssim I_\mathrm{c}$: the phase particle can tunnel through the lowered potential barrier (macroscopic quantum tunneling [123]) if the potential is sufficiently tilted. The retrapping process depends on M and $\eta \propto 1/R$. For $T \to 0$, thermal activation over the potential barrier is suppressed exponentially. $I \geq I_\mathrm{c}$: independent on the damping, the phase particle can no longer be trapped due to the absence of potential minima. According to the 2$^{\mathrm{nd}}$ Josephson equation a change in φ results in a finite voltage drop across the junction. The retrapping process for decreasing bias current I follows similar dynamics.

case, the flux Φ (or equivalently the phase φ) is a well defined quantum variable whereas the charge Q (or equivalently the number N of charges) fluctuates strongly.

2.2 Josephson junction devices

In this section we review two devices based on the Josephson effects and fluxoid quantization [53,124,125]: the dc-SQUID and the flux qubit. While the dc-SQUID is widely used in many fields of application concerning everyday life (e.g. Magnetoencephalography (MEG), Magnetocardiography (MCG), SQUID microscopy for oil prospection), the flux qubit itself is living a dire existence in basic research. Since this section only covers the most important aspects of three-Josephson junction based flux qubits, we suggest Refs. [47,48,75] for a general overview and Refs. [59,65,68,73] for further reading covering different types of Josephson junction based qubits.

2.2.1 dc-SQUID

The direct-current superconducting quantum interference device (dc-SQUID) is a highly sensitive magnetometer. It consists of two Josephson junctions connected in parallel in a superconducting loop. A schematic and a false-color SEM image of a dc-SQUID are shown in Fig. 2.4 a and b, respectively. Effectively, a dc-SQUID is a flux-to-voltage converter and owing to its sensitivity, it can be used to read out the state of superconducting flux qubits. In this section we will only discuss the main features of the dc-SQUID that are necessary to understand the readout of flux qubits. For a more thorough investigation of the physics of dc-SQUIDs we refer the reader to Refs. [52, 53, 126, 127].
Figure 2.4 c shows a sketch of the current-voltage characteristic (IVC) of a current biased dc-SQUID for zero applied flux $\Phi_{sq} = 0$. In the following, we assume a dc-SQUID consisting of two identical junctions (each with a critical current $I_c/2$) and in absence of any noise. For increasing bias current I and as long as $I < I_c$, the current is flowing as supercurrent through the SQUID and no voltage drop is observed. We note that in our nomenclature I_c refers to the maximum critical current of the dc-SQUID, which is the sum of the critical currents of each junction. For $I = I_c$ the SQUID switches to the so-called *voltage state* and a finite voltage drop V_g is observed. In general, the SQUID behaves like an non-linear resistor $R_n(V)$ for $I > I_c$, however, in many cases it can be modeled as an ohmic resistor R_n. The three parameters I_c, V_g and R_n are related by the Ambegaokar-Baratoff

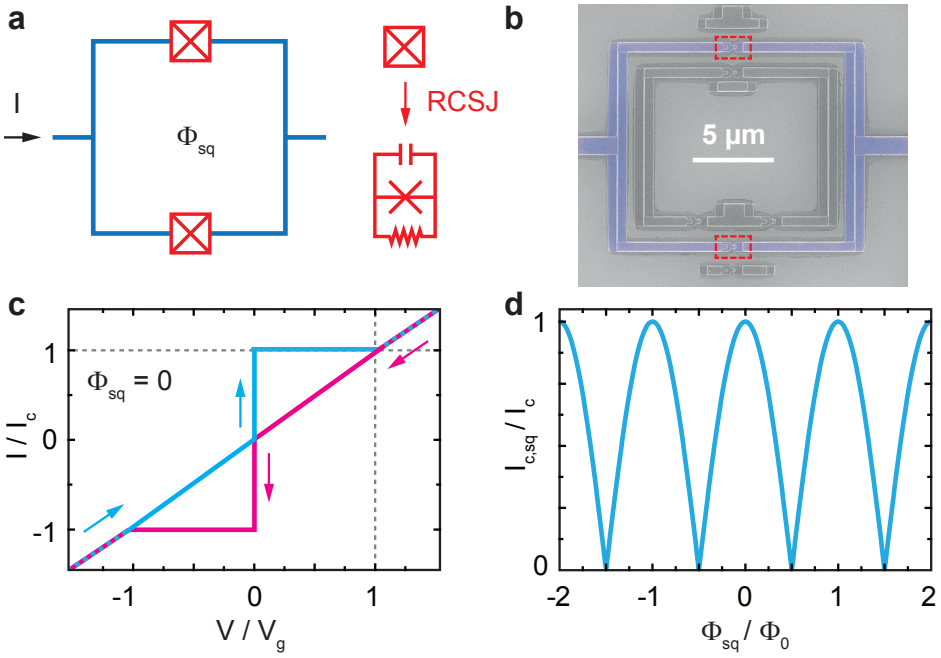

Figure 2.4: Direct-current superconducting quantum interference device (dc-SQUID). (a) Schematic of a current biased dc-SQUID. The Josephson junctions are visualized by a red box with a cross. The equivalent circuit of each junction is based on the RCSJ model. (b) False-color SEM image of a dc-SQUID (light blue) surrounding a flux qubit. The two Josephson junctions are highlighted by dashed red boxes. (c) Current-voltage characteristic (IVC) of an underdamped (large C and/or R_n) dc-SQUID. For increasing current I (light blue curve), a voltage drop of V_g is observed when $I = I_c$. For an underdamped SQUID, decreasing I (magenta curve) leads to a hysteresis in the IVC. (d) Maximum critical current $I_{c,sq}$ of the dc-SQUID as a function of the magnetic flux Φ_{sq} threading its loop. $I_{c,sq}$ is periodic in Φ_0 and oscillates with an amplitude of I_c.

relation [128]

$$I_c = \frac{\pi}{4}\frac{V_g}{R_n} \quad , \tag{2.7}$$

where $V_g = 2\Delta_s/e$. Here, $2\Delta_s$ denotes the superconducting energy gap. Originally, the Ambegaokar-Baratoff relation was stated for a single junction and is based on a microscopic description of the Josephson effects.
When decreasing I, the IVC of the SQUID depends strongly on C and R_n and can be described by the dimensionless Stewart-McCumber parameter[3] $\beta_C = \frac{\Phi_0}{2\pi} I_c R_n^2 C$ [129, 130]. The IVC depicted in Fig. 2.4 c shows a strong hysteresis which is characteristic for underdamped Josephson junctions. In the picture of a phase particle in a tilted (two-dimensional) washboard potential, this behavior corresponds to a high mass M (large C) and/or small damping η (large R) and consequently $\beta_C \gg 1$. Varying the external flux Φ_{sq} leads to an oscillatory behavior of $I_{c,sq}(\Phi_{sq})$ as shown in Fig. 2.4 d, where

$$I_{c,sq}(\Phi_{sq}) = I_c \left|\cos\left(\pi \frac{\Phi_{sq}}{\Phi_0}\right)\right| \quad . \tag{2.8}$$

In this sense, the dc-SQUID behaves like a single Josephson junction with tunable $I_{c,sq}$ [131, 132]. The Φ_0-periodicity is a direct consequence of the fluxoid quantization in superconducting loops [133, 134].

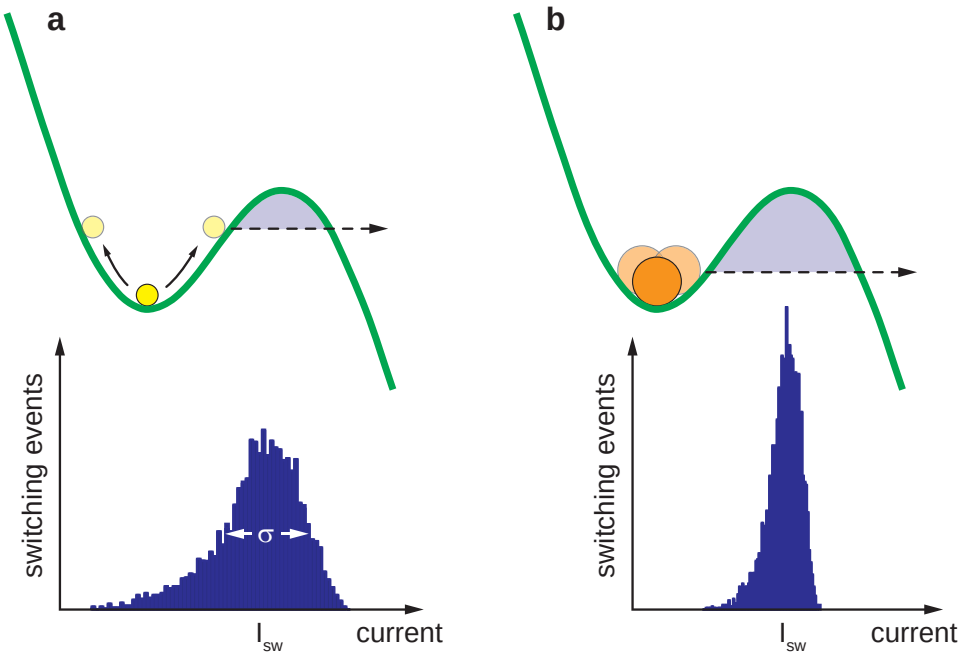

Figure 2.5: Switching current distributions. (a) Top panel: tilted washboard potential with phase particle of low mass and large plasma frequency ω_p. For temperatures below the so-called crossover temperature, the quantum tunneling rate exceeds the thermal activation rate [135]. In this regime, the escape rate $\Gamma \propto \sqrt{\omega_p U}\exp(-U/\omega_p)$, where U is proportional to the light blue colored area. Bottom panel: typical switching current histogram. The standard deviation σ is affected by thermal and quantum fluctuations. (b) same as in (a) but for a phase particle with large mass and therefore low ω_p.

[3] The Stewart-McCumber parameter β was originally defined for a single Josephson junction, however, its value remains unchanged when considering a dc-SQUID consisting of two identical Josephson junctions.

Switching current distribution

The switching of the dc-SQUID into the voltage state is a statistical process and occurs when the phase particle escapes from the metastable minimum in the tilted washboard potential. This escape is either governed by thermal activation ($k_\mathrm{B}T \gg \hbar\omega_\mathrm{p}$) or by quantum tunneling ($k_\mathrm{B}T \ll \hbar\omega_\mathrm{p}$) [136, 137]. Subsequent measurements of $I_\mathrm{c,sq}$ at a fixed flux bias will lead to a distribution of the switching current with a mean value I_sw and a standard deviation σ as shown in Fig. 2.5. The susceptibility to undesired switching events – and therefore σ – can be reduced by increasing the mass M of the phase particle. This is equivalent to lowering the plasma frequency $\omega_\mathrm{p} \propto \sqrt{1/C}$. Experimentally, this can be realized by an increase of the Josephson junction area or by shunting the dc-SQUID with large external or on-chip shunt capacitors [66, 138–140].

2.2.2 Superconducting flux qubit

The experiments presented in this thesis are based on a specific type of superconducting qubit: the three-Josephson-junction flux qubit [49,63,64]. This type of qubit, schematically shown in Fig. 2.6 a, comprises a superconducting loop interrupted by three Josephson junctions. Two of these junctions have an area A, while the third junction is smaller by a factor of α. Typically, $0.5 < \alpha < 0.8$ and $A \sim 0.02 - 0.04\,\mu\mathrm{m}^2$. Figure 2.6 b shows a false-color SEM image of a flux qubit surrounded by a readout dc-SQUID. An external magnetic field threading the superconducting qubit loop induces screening currents due to the fluxoid quantization. In turn, these clockwise or counter-clockwise circulating *persistent currents*

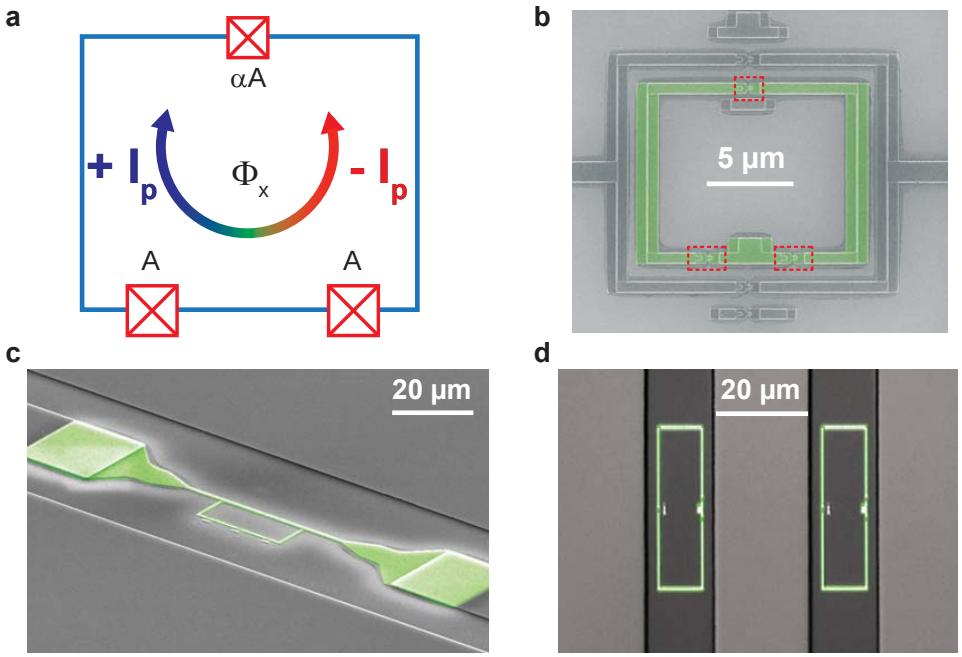

Figure 2.6: Schematic and SEM images of superconducting flux qubits. (a) Sketch of a superconducting three-Josephson-junction flux qubit. For an external flux bias $\Phi_\mathrm{x} \neq 0$, persistent screening currents $\pm I_\mathrm{p}$ are induced. (b) False-color SEM image of a flux qubit (green) surrounded by a dc-SQUID. The dashed red boxes mark the positions of the qubit's Josephson junctions. (c) and (d) False-color SEM images of flux qubits coupled (c) galvanically and (d) via the mutual inductance to resonant cavities.

$\pm I_\mathrm{p}$ generate a small magnetic flux, roughly $\sim 10^{-3}\,\Phi_0$ for realistic qubit parameters. It is exactly this small change in magnetic flux that can be detected by the dc-SQUID. Furthermore, fluxoid quantization demands that the total flux enclosed by the loop sums up to an integer multiple of a flux quantum Φ_0. Figure 2.6 c and d show images of flux qubits coupled to planar transmission lines. In this case, the readout of the qubit is based on dispersive interactions between qubit and cavity which will be explained in more detail in section 5.1.1.

Potential energy

The potential energy U_qu of the flux qubit sketched in Fig. 2.6 a is the sum of the potential energies of each individual junction in absence of any bias current. Following Ref. [63], U_qu can be written as

$$U_\mathrm{qu} = E_\mathrm{J}\left[(1-\cos\varphi_1)+(1-\cos\varphi_2)+\alpha(1-\cos\varphi_3)\right] \tag{2.9}$$

$$= E_\mathrm{J}\left[2+\alpha-\cos\varphi_1-\cos\varphi_2-\alpha\cos(2\pi f+\varphi_1-\varphi_2)\right] \quad , \tag{2.10}$$

where $f=\Phi_\mathrm{x}/\Phi_0$ is the so-called frustration and Φ_x represents the flux threading the qubit loop. In expression (2.9), one phase difference (in this case φ_3) can be eliminated utilizing fluxoid quantization[4]. In general, the qubit potential is 2π-periodic along each axis and exhibits a double-well structure if $\alpha > 0.5$. The two minima correspond to states with persistent currents $\pm I_\mathrm{p}$ of opposite direction. Furthermore, at the so-called *degeneracy points*, where $f = n + 1/2$ and $n \in \mathbb{Z}$, the potential U_qu is symmetric. Figure 2.7 a shows

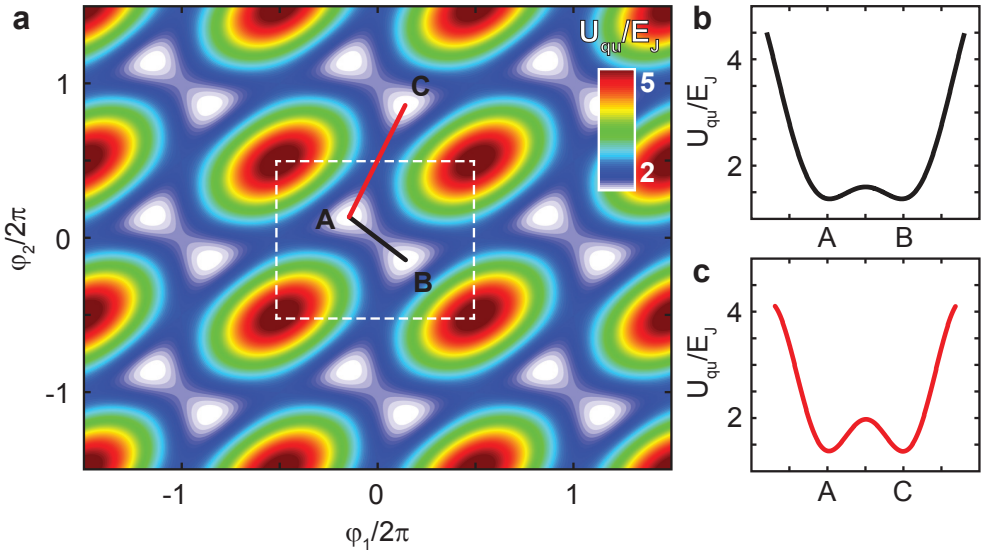

Figure 2.7: Potential energy landscape according to Eq. (2.10) for $f = 0.5$ and $\alpha = 0.8$. (a) Color-coded plot of the two-dimensional qubit potential U_qu. The two minima within a unit cell (dashed white box) correspond to states with opposite persistent current I_p. (b) Cut along $\varphi_1 = -\varphi_2$ connecting the nearest neighbor minima A and B within a unit cell. The cut is indicated by the solid black line in (a). (c) Cut along the direction connecting the minima A and C located in different unit cells. The cut is indicated by the solid red line in (a).

[4]Furthermore, for the derivation of Eq. (2.10) one has to assume that the geometric inductance of the qubit loop L is small compared to L_J. For all the junctions and qubit parameters presented in this work $L/L_\mathrm{J} \ll 1$.

a color-coded plot of U_{qu} as a function of the phase differences φ_1 and φ_2 for $f = 0.5$ and $\alpha = 0.8$. Figure 2.7 b shows a cut along the direction connecting the two minima within a unit cell, while Figure 2.7 c represents a cut along the direction to the next-nearest minimum. A comparison of Fig. 2.7 b and c suggests that the matrix element for intracell quantum tunneling will be much larger than for tunneling between minima of adjacent unit cells. Thus, for an appropriate choice of α and $E_{\mathrm{J}}/E_{\mathrm{C}}$ it is possible to engineer a well-defined quantum two-level system using macroscopic circuit elements.
Close to a degeneracy point the flux qubit can be described quantum mechanically by the Hamiltonian

$$\hat{H}_{\mathrm{q}} = \frac{\epsilon}{2}\,\hat{\sigma}_{\mathrm{z}} + \frac{\Delta}{2}\,\hat{\sigma}_{\mathrm{x}} = \frac{1}{2}\begin{pmatrix} \epsilon & \Delta \\ \Delta & -\epsilon \end{pmatrix} \quad , \tag{2.11}$$

where $\hat{\sigma}_{\mathrm{z}}$ and $\hat{\sigma}_{\mathrm{x}}$ are Pauli operators. This Hamiltonian has a very general form and describes a two-level system whose energy levels are coupled by a tunneling matrix element [141]. In our case, the two persistent current states $|+I_{\mathrm{p}}\rangle$ and $|-I_{\mathrm{p}}\rangle$, which are the eigenstates of $(\epsilon/2)\,\hat{\sigma}_{\mathrm{z}}$, are coupled by an off-diagonal energy term Δ which is proportional to the tunneling matrix element. The flux-dependent energy bias ϵ is given by

$$\epsilon \equiv \epsilon(\Phi_{\mathrm{x}}) = 2\frac{\partial U_{\mathrm{qu}}}{\partial \Phi_{\mathrm{x}}}\delta\Phi_{\mathrm{x}} = 2I_{\mathrm{p}}\delta\Phi_{\mathrm{x}} \quad , \tag{2.12}$$

where we introduced the relative flux bias $\delta\Phi_{\mathrm{x}} = \Phi_{\mathrm{x}} - f\Phi_0$. The derivative in Eq. (2.12) has to be evaluated in the minima of the double-well potential where

$$\varphi_1 = -\varphi_2 = \pm \arccos(1/2\alpha) \tag{2.13}$$

yielding the relation

$$I_{\mathrm{p}} = I_{\mathrm{c}}\sqrt{1-(1/2\alpha)^2} \quad . \tag{2.14}$$

The energy level spectrum of $\hat{H}_{\mathrm{q}}$ is plotted in the top panel of Fig. 2.8 a. At $\delta\Phi_{\mathrm{x}} = 0$, the degeneracy between the unperturbed eigenstates $|-I_{\mathrm{p}}\rangle$ and $|+I_{\mathrm{p}}\rangle$ is lifted by formation of an energy gap Δ. The qubit's ground state $|\mathrm{g}\rangle$ and excited state $|\mathrm{e}\rangle$ are symmetric and antisymmetric superpositions of $|+I_{\mathrm{p}}\rangle$ and $|-I_{\mathrm{p}}\rangle$. Sufficiently far away from $\delta\Phi_{\mathrm{x}} = 0$, where $\Delta \ll \epsilon$, the energy ground state $|\mathrm{g}\rangle$ and excited state $|\mathrm{e}\rangle$ of $\hat{H}_{\mathrm{q}}$ are in good approximation identical to $|-I_{\mathrm{p}}\rangle$ and $|+I_{\mathrm{p}}\rangle$. In general, the flux-dependent energy difference between the qubit levels is given by

$$E_{\mathrm{ge}} = \hbar\omega_{\mathrm{q}} = \sqrt{\Delta^2 + \epsilon(\Phi_{\mathrm{x}})^2} \quad . \tag{2.15}$$

At the qubit degeneracy points, $\epsilon = 0$ and therefore $\partial E_{\mathrm{ge}}/\partial\Phi_{\mathrm{x}} = 0$. This implies that E_{ge} is stationary with respect to small variations of $\delta\Phi_{\mathrm{x}}$ which in turn yields optimum qubit coherence properties [81]. The bottom panel of Fig. 2.8 a visualizes the flux dependence of the current $I_{\mathrm{q}} = I_{\mathrm{p}}\langle\hat{\sigma}_{\mathrm{z}}\rangle = \partial E_{\mathrm{ge}}/\partial\Phi_{\mathrm{x}}$ circulating in the qubit loop. Therefore, $I_{\mathrm{q}} \to 0$ when approaching a degeneracy point which complicates measurements that rely on the detection of a quantity $\propto I_{\mathrm{q}}$, e.g. the dc-SQUID readout presented in chapter 4. Figure 2.8 b shows schematically the shape of the qubit double-well potential (cf. Fig. 2.7 c). This shape can be adjusted by varying the relative flux bias $\delta\Phi_{\mathrm{x}}$. Only at the qubit degeneracy points the potential is symmetric and implies selection rules for specific photon-induced transitions (see section 5.5.2) [142].

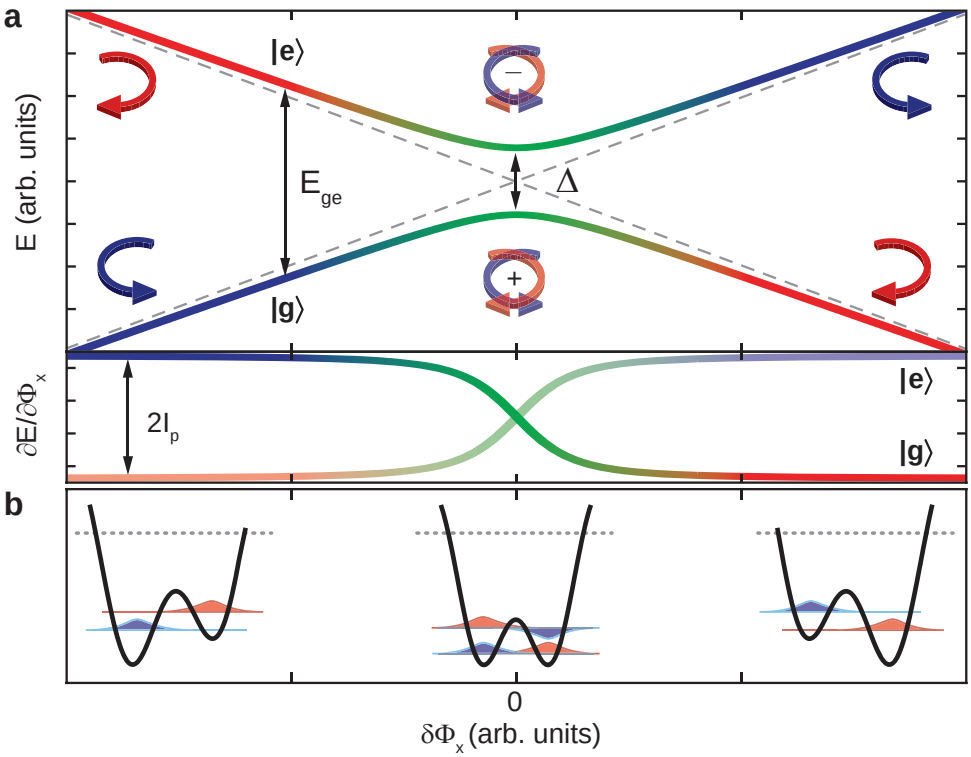

Figure 2.8: Qubit's energy level diagram, persistent current and double-well potential. (a) Top panel: eigenenergies of the qubit Hamiltonian $\hat{H}_\mathrm{q}$ as a function of the relative flux bias $\delta\Phi_\mathrm{x}$. The persistent current states $|-I_\mathrm{p}\rangle$ and $|+I_\mathrm{p}\rangle$ are indicated by blue and red arrows, respectively. For $\Delta = 0$, the eigenenergies are given by the dashed gray lines. In general, the energy difference E_ge between $|\mathrm{g}\rangle$ and $|\mathrm{e}\rangle$ has a hyperbolic flux dependence. Bottom panel: sketch of the circulating current $I_\mathrm{q} = I_\mathrm{p}\langle\hat{\sigma}_\mathrm{z}\rangle$. For clarity, I_q associated with $|\mathrm{e}\rangle$ is plotted with less opacity. (b) Sketch of the qubit's double-well potential along the black line in Fig. 2.7 a as a function of $\delta\Phi_\mathrm{x}$. Sketches of the wavefunctions are indicated. Furthermore, the energies of these states are well separated from higher energy states (gray dotted line).

Dependence of Δ on E_J and E_C

At the degeneracy point $\delta\Phi_\mathrm{x} = 0$, the qubit transition frequency from $|\mathrm{g}\rangle$ to $|\mathrm{e}\rangle$ is given by Δ/h. A prerequisite for a well-defined quantum two-level system is $\Delta \gg k_\mathrm{B}T$. Furthermore, it can be shown [63, 64, 138] that

$$\Delta \propto \hbar\omega_\mathrm{p} \exp(-a\sqrt{E_\mathrm{J}/E_\mathrm{C}}) \tag{2.16}$$

where the plasma frequency $\omega_\mathrm{p} = \sqrt{\frac{2\pi I_\mathrm{c}}{\Phi_0 C}}$ can be written as

$$\hbar\omega_\mathrm{p} \propto b\sqrt{E_\mathrm{J}E_\mathrm{C}} = b\,E_\mathrm{C}\sqrt{E_\mathrm{J}/E_\mathrm{C}} \quad . \tag{2.17}$$

In the above expressions, the parameters a and b are of the order of unity [64] and can be evaluated numerically. The expression for Δ in Eq. (2.16) can be interpreted in the picture of a phase particle performing oscillations with frequency ω_p in the one-dimensional qubit double-well potential (see Fig. 2.7 c and Fig. 2.8 b). $\omega_\mathrm{p} \propto E_\mathrm{C}$ can be interpreted as the attempt frequency for tunneling into the neighboring well. Furthermore, the tunneling probability is proportional to $\exp(-\sqrt{E_\mathrm{J}/E_\mathrm{C}})$. It is evident, that a large E_C is favorable since $E_\mathrm{C} \propto 1/C \propto 1/M$ (see Fig. 2.3 c). However, the ratio $E_\mathrm{J}/E_\mathrm{C}$ must be large enough

to ensure that flux is a well-defined quantum variable.
Summing up, large E_J/E_C ratios and simultaneously a large E_C is required, which implies Josephson junctions with a small area $A \propto C$. Because $E_J \propto I_c$, a small area in turn demands high critical current densities $j_c = I_c/A$. We give an estimate of typical flux qubit parameters: the frequency associated with a temperature of $T \sim 25\,\mathrm{mK}$ is roughly $0.5\,\mathrm{GHz}$. Thus, we require a moderate $E_C/h \sim 5\,\mathrm{GHz}$ which corresponds to a Josephson junction with area $A \sim 0.04\,\mu\mathrm{m}^2$ assuming a specific capacitance $c_s \sim 100\,\mathrm{fF}/\mu\mathrm{m}^2$ for aluminum based junctions [143, 144]. With $E_J/E_C \sim 50$, the critical current density of the junction has to be roughly $j_c \sim 1.3\,\mathrm{kA/cm}^2 = 13\,\mu\mathrm{A}/\mu\mathrm{m}^2$. We will see in chapter 3 that such small areas can be reproducibly realized by standard lithographic techniques. However, high critical current densities are technologically very challenging as j_c depends exponentially on the thickness of the insulating barrier. The reproducibility and the spread of j_c of our Josephson junctions is discussed in appendix A.10.

2.3 Coplanar waveguide resonators

One of the fundamental building blocks for experiments studying light-matter interaction is a device allowing for the storage of photons. In the field of optical cavity QED, such devices – commonly called cavities or resonators – are realized by two highly polished mirrors that enable the reflection of optical photons. In the microwave regime, cavities can be realized as superconducting on-chip transmission lines.
There are various transmission line geometries that can be used for engineering microwave cavities. We will focus on resonators in a coplanar waveguide (CPW) geometry. This specific geometry is the two-dimensional analog to a coaxial cable. Here, a center conductor is separated on both sides by gaps from lateral groundplanes. The most important advantages for using CPW resonators in the scope of this thesis were:

- In contrast to microstrip geometries, the characteristic impedance Z_0 is not significantly constrained by substrate properties. It is thus possible to fix Z_0 (usually to $50\,\Omega$) by keeping the aspect ratio of the relevant dimensions along the cross-section constant. However, the actual dimensions can vary by orders of magnitude making the CPW geometry extremely versatile in the context of microwave engineering.

- CPW resonators can be easily realized to operate between $1-10\,\mathrm{GHz}$ thus matching typical transition frequencies of quantum bits.

- Although their lengths are typically $l = 10-40\,\mathrm{mm}$, their lateral dimensions can be of the order of a few µm. This results in a small mode volume V_m which in turn enhances the electromagnetic field strength $\propto 1/\sqrt{V_\mathrm{m}}$ (cf. section 1.3).

Furthermore, by using superconducting materials like aluminum and niobium, quality factors up to several hundred thousands [145–149] can be realized, corresponding to photon storage times of the order of hundreds of µs.
In the following sections we will only emphasize the most important properties of CPW resonators relevant for understanding the results presented in this thesis. A more detailed theoretical overview, especially on mapping transmission line resonances to that of lumped element LCR-circuits, can be found in Refs. [148,150,151]. Furthermore, Ref. [148] constitutes a very thorough experimental analysis of aluminum based resonators and the transmission matrix model.

2.3.1 General properties of $\lambda/2$-resonators

Figure 2.9 a and b show schematic views of a $\lambda/2$-resonator and its cross-section geometry, respectively. The resonator is defined by a center conductor (length l and width w) coupled capacitively to in- and output ports. Furthermore, the center conductor is separated by a gap (width s) from the lateral groundplanes. Usually, the extent of the groundplanes is much larger than w and s. The conducting layers have a thickness t and are fabricated on a substrate with relative dielectric constant ϵ_r and height h.
Two general types of coupling capacitors are shown in Fig. 2.9 c and d. Owing to the large impedance mismatch, these coupling capacitors act similar to highly reflective dielectric mirrors and are the on-chip complement to the optical mirrors in cavity QED experiments. The resonator allows the formation of standing electromagnetic waves with wavelengths

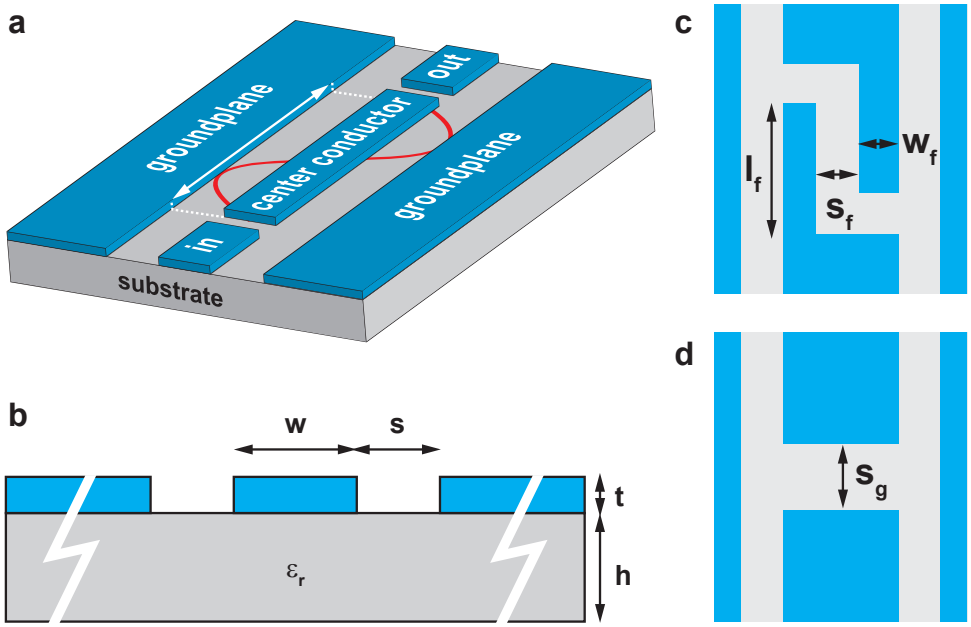

Figure 2.9: Schematic and cross-sectional view of a coplanar waveguide (CPW) $\lambda/2$-resonator. (a) The resonator is defined by a center conductor with length l (white arrow) coupled capacitively to in- and output ports. The red line indicates a standing wave ($\lambda = l$) corresponding to the position-dependent current amplitude. (b) Cross-section of a conventional CPW. For fixed substrate thickness h, the characteristic impedance Z_0 depends on the aspect ratio $w/(w+2s)$. For the devices studied in this work $l \gg h \gg w, s \gg t$. (c) Interdigital finger capacitor. Each finger has a length l_f and width w_f. The distance between each edge is s_f. (d) Gap capacitor with gap width s_g.

fulfilling the boundary conditions at the position of the coupling capacitors[5]. In a particle picture, these standing waves correspond to photons with specific *resonance frequencies* $\omega_n/2\pi$. The lifetime T of the photons inside the resonator depends predominately on the capacitance C_κ of the coupling capacitors ($T \propto C_\kappa^{-2}$). For the resonant cavity in Fig. 2.9 a, only standing waves with wavelengths

$$\lambda_n = \frac{2l}{n} \tag{2.18}$$

fulfill the boundary conditions. In the following, we present expressions for Z_0 and the resonance frequencies of a resonant cavity similar to the one in Fig. 2.9 a.

Characteristic impedance Z_0 and resonance frequencies ω_n

The impedance of a conventional CPW on a dielectric substrate of finite thickness is given by [152]

$$Z_0 = \frac{30\pi}{\sqrt{\epsilon_\mathrm{eff}}} \frac{K(k_0')}{K(k_0)} \tag{2.19}$$

with the effective dielectric constant

$$\epsilon_\mathrm{eff} = 1 + \frac{\epsilon_\mathrm{r} - 1}{2} \frac{K(k_1)}{K(k_1')} \frac{K(k_0')}{K(k_0)} \quad . \tag{2.20}$$

[5]The standing wave representing the position-dependent current amplitude has invariably a node at the position of the coupling capacitors (see red line in Fig. 2.9 a)

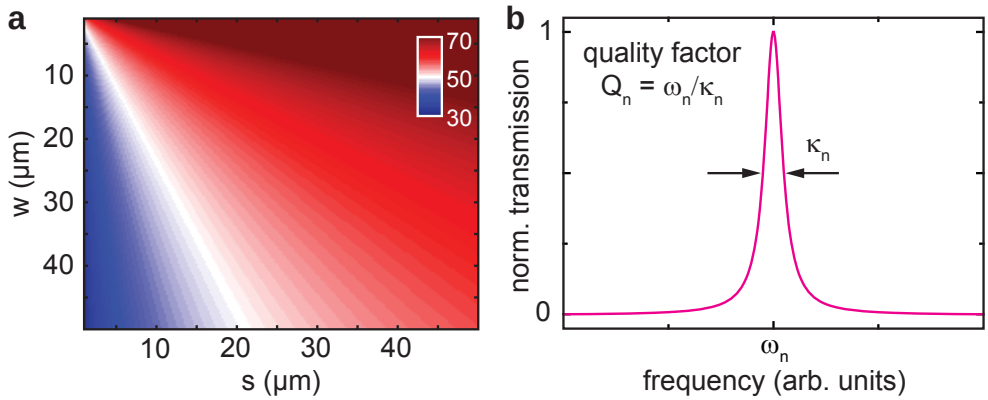

Figure 2.10: (a) Color-coded plot of Z_0 as a function of w and s. The plot was generated for $h = 525\,\mu$m and $\epsilon_r = 11.9$ (silicon) reflecting the substrate parameters of the resonators presented in this thesis. Impedances close to the optimum value of $Z_0 = 50\,\Omega$ (white regions) are realized when the aspect ratio $w/s \sim 5/3$. (b) Sketch of the normalized transmission spectrum of a capacitively coupled resonator as shown in Fig. 2.9 a. Close to a resonance ω_n the spectrum has a Lorentzian line shape (magenta) with a full width at half maximum of κ_n. The quality factor Q is a measure for the average storage time of photons inside the cavity.

Here, K denotes the complete elliptic integral of the first kind and

$$k_0 = \frac{w}{w + 2s} \tag{2.21}$$

$$k_1 = \frac{\sinh(\pi w/4h)}{\sinh[\pi(w + 2s)/4h]} \tag{2.22}$$

$$k_i' = \sqrt{1 - k_i^2} \qquad \text{with } i = 0, 1 \tag{2.23}$$

Figure 2.10 a shows a color-coded plot of Z_0 for a realistic range of w and s. For non-magnetic substrates, the phase velocity is given by $v_{\mathrm{ph}} = c/\sqrt{\epsilon_{\mathrm{eff}}}$. Therefore, the expression for the nth resonance frequency is

$$\omega_n/2\pi = \frac{v_{\mathrm{ph}}}{\lambda_{\mathrm{n}}} = n\,\frac{c}{2l\sqrt{\epsilon_{\mathrm{eff}}}} \quad . \tag{2.24}$$

A typical normalized transmission spectrum close to a resonance ω_n is shown schematically in Figure 2.10 b. The spectrum has a Lorentzian line shape with a full width at half maximum given by the *cavity decay rate* κ_n. The *quality factor* Q of the nth mode is given by

$$Q_n = \omega_n/\kappa_n \tag{2.25}$$

and is proportional to the energy stored in the circuit divided by the energy dissipation per cycle [150]. Thereby, a high quality factor corresponds to a long average photon lifetime inside the cavity. In Fig. 2.11, the resonance frequency ω_1 of the fundamental $\lambda/2$-mode is shown as a function of the resonator length l.

2.3.2 Capacitive coupling to an external load

In order to determine ω_n, κ_n and therefore Q_n, the resonator is inevitable coupled to a measurement device representing an external load R_{L}. In this section we review how the capacitive coupling to the outside world influences the properties of the resonant circuit.

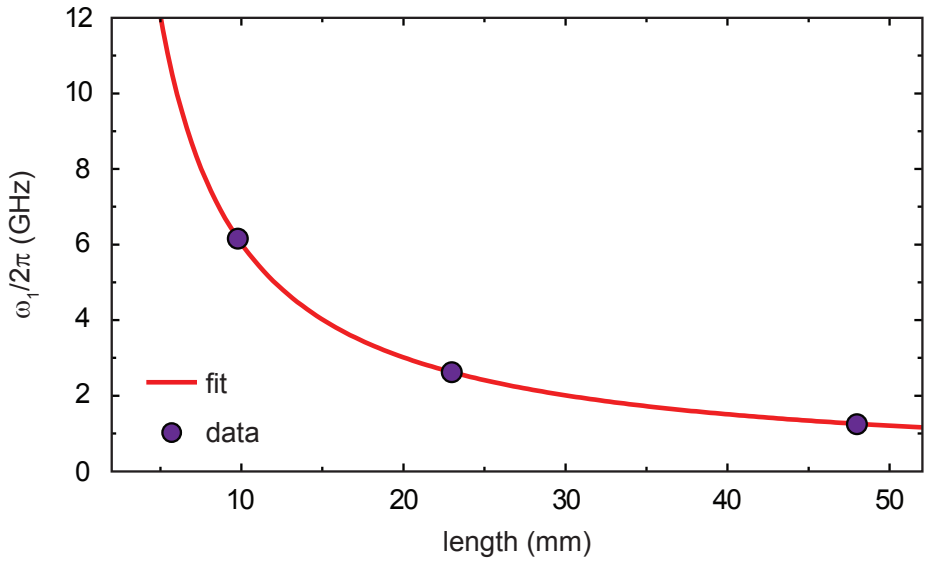

Figure 2.11: Measured fundamental resonance frequency $\omega_1/2\pi$ (violet data points) as a function of the length l of the resonator's center conductor. The red line is a fit to the data using Eq. (2.24) and ϵ_{eff} as fit parameter. The fit procedure yields $\epsilon_{\text{eff}} = 6.19$ which deviates by a maximum of 6% from the calculated values using Eq. (2.20).

The equivalent circuit of a distributed CPW resonator modeled as transmission line [150] is depicted in Fig. 2.12 a. Basically, the transmission line is modeled by many blocks consisting of lumped circuit elements, each block having the same characteristic impedance Z_0. Close to the resonance frequencies ω_n, the distributed resonator can be mapped [148, 151] onto a parallel lumped element LCR-circuit as shown in Fig. 2.12 b. The coupling through the capacitor C_κ in series to an external load R_{L} can be modeled by the effective circuit consisting of a parallel combination of R^* and C^* (see Fig. 2.12 c), where

$$R^* = \frac{1}{\omega_n^2 C_\kappa^2 R_{\text{L}}} + R_{\text{L}} \tag{2.26}$$

$$C^* = \frac{C_\kappa}{1 + \omega_n^2 C_\kappa^2 R_{\text{L}}^2} \quad . \tag{2.27}$$

With $\omega_n \sim 10^9 - 10^{10}\,\text{s}^{-1}$ and typically $C_\kappa \sim 10^{-15}\,\text{F}$, the small capacitors C_κ transform each resistive load $R_{\text{L}} = 50\,\Omega$ into a large impedance R^* equivalent to additional losses. The resonance frequency of the LCR-circuit is slightly shifted by $\delta\omega$ due to the capacitive loading (parallel combination of C and $C^* \approx C_\kappa$). This frequency shift is small and given by [148]

$$\delta\omega = -\omega_n \frac{C_\kappa}{C} \quad . \tag{2.28}$$

The overall losses can be expressed in terms of a loaded quality factor Q_{L} which is a parallel combination of internal and external quality factors

$$\frac{1}{Q_{\text{L}}} = \frac{1}{Q_{\text{int}}} + \frac{1}{Q_{\text{ext}}} \tag{2.29}$$

with

$$Q_{\text{int}} = \omega_n RC \quad \text{and} \quad Q_{\text{ext}} = \omega_n R^* C/2 \quad . \tag{2.30}$$

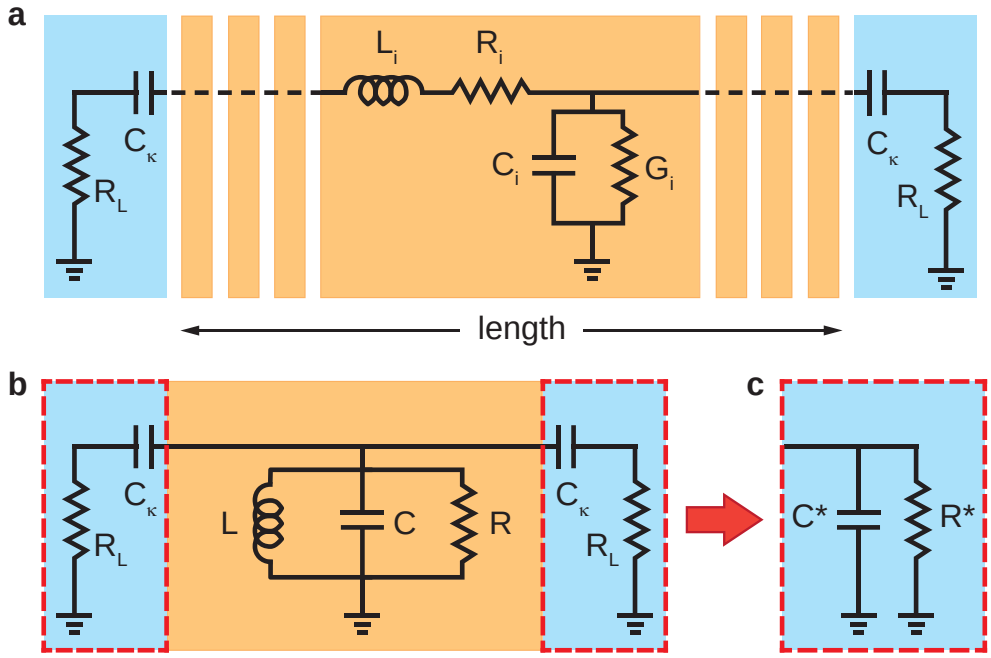

Figure 2.12: Equivalent circuit of a distributed CPW resonator. (a) The center conductor with length l (black arrow) is modeled by a series connection of small identical blocks (orange regions; ith block shown in detail). Each block consist of lumped circuit elements L_i, R_i, C_i and G_i which are defined per unit length. The resonator is symmetrically coupled to an external load R_L through the capacitors C_κ (blue regions). (b) Close to a resonance frequency ω_n, the circuit in (a) can be modeled as parallel lumped element LCR-circuit, with e.g. $L = l\,L_i$. (c) The series combination of R_L with C_κ can be transformed into an equivalent parallel circuit of C^* and R^* (dashed red boxes). The latter can act as an additional dissipative channel.

In essence, the capacitance C_κ determines whether Q_L is governed by Q_int or Q_ext. It is convenient to define the coupling coefficient $g_\mathrm{c} = Q_\mathrm{int}/Q_\mathrm{ext}$ and to distinguish two cases:

- $g_\mathrm{c} < 1$ (small C_κ, $Q_\mathrm{ext} > Q_\mathrm{int}$): the resonator is called *undercoupled*. In the extreme case of an uncoupled resonator ($C_\kappa = 0, Q_\mathrm{ext} \to \infty$), the loaded quality factor is governed only by intrinsic losses (e.g. dielectric or resistive losses).

- $g_\mathrm{c} > 1$ (large C_κ, $Q_\mathrm{ext} < Q_\mathrm{int}$): the resonator is called *overcoupled*. In this regime the loaded quality factor is governed by Q_ext and can be engineered by an appropriate choice of C_κ.

The internal losses can be minimized by using superconductors and low-loss substrates. In our case, $Q_\mathrm{int} \gg Q_\mathrm{ext}$ and the loaded quality factor can be well approximated by

$$Q_\mathrm{L} = Q_\mathrm{ext} = \frac{C}{2\omega_n C_\kappa^2 R_\mathrm{L}} \propto \frac{1}{C_\kappa^2} \tag{2.31}$$

and scales as $1/n$ for increasing mode index. The total capacitance $C = l\,C_i$ in Eq. (2.30) and Eq. (2.31) can be calculated using [152]

$$C_i = 4\epsilon_0 \epsilon_\mathrm{eff} \frac{K(k_0)}{K(k_0')} \quad , \tag{2.32}$$

where ϵ_0 is the vacuum permittivity.

2.3.3 Kinetic inductance

In general, the total inductance L_{tot} of a superconductor is the sum of a purely geometric contribution L and a kinetic contribution L_{kin}. The temperature independent part L resembles energy stored in magnetic fields. L_{kin} arises from kinetic energy stored in the motion of charge carriers. In the case of a CPW, the geometric contribution per unit length is given by

$$L_i = \frac{\mu_0}{4}\frac{K(k_0')}{K(k_0)} \quad , \tag{2.33}$$

where μ_0 is the vacuum permeability[6]. An explicit expression for L_{kin} can be found in Refs. [153, 154] and is omitted here[7]. However, the two most important and relevant aspects are:

- $L_{\mathrm{kin}} \propto \lambda_{\mathrm{L}}^2$ [53]. Here, the temperature-dependent London penetration depth [156] is given by $\lambda_{\mathrm{L}} \equiv \lambda_{\mathrm{L}}(T) = \lambda_0/\sqrt{1-Y_0(T)}$. In this expression, λ_0 is the zero-temperature London penetration depth and $Y_0(T) \propto \exp(-\Delta_{\mathrm{s}}/k_{\mathrm{B}}T)$ is the Yosida function [157]. Thus, for low temperatures $\lambda_{\mathrm{L}} \approx \lambda_0$. The London penetration depth is the characteristic decay length of magnetic fields in superconductors.

- $L_{\mathrm{kin}}/L \sim 10^{-2}$ for our niobium CPW resonators. The kinetic inductance has negligible influence on the value of the resonance frequencies and in good approximation $L_{\mathrm{tot}} \approx L$. However, a small temperature-dependent influence on the resonance frequencies remains since $\omega \propto 1/\sqrt{L_{\mathrm{tot}}}$.

2.3.4 Intrinsic resonator losses

In the overcoupled regime, the external losses can be 'engineered' and the capacitive coupling limits the quality factor. On the contrary, in the extremely undercoupled regime, intrinsic resonator losses are the dominant factor limiting Q_{int}. In this subsection we compare distinct internal loss mechanisms: resistive, dielectric and radiative losses.

Resistive Losses

Resistive losses in superconductors due to the presence of high-frequency alternating currents are well captured by the two-fluid model [53]. In this model, the superconductor is described by a resistive channel (quasiparticles or 'normal electrons') in parallel to an inductive channel (kinetic inductance of Cooper pairs). Thus, the presence of a finite resistance for any non-zero temperature and frequency involves dissipation.
It can be shown [53,151,154] that the resistive losses per surface area $R_{\mathrm{s}}(\omega)$ are frequency-dependent and scale as

$$R_{\mathrm{s}}(\omega) \propto \frac{n_{\mathrm{n}}}{n_{\mathrm{s}}} L_{\mathrm{kin}}\omega^2 \quad . \tag{2.34}$$

[6]This result can be obtained e.g. by using $v_{\mathrm{ph}} = c/\sqrt{\epsilon_{\mathrm{eff}}} = 1/\sqrt{L_iC_i}$ and $Z_0 = \sqrt{L_i/C_i}$ with the approximation $c \approx 3 \cdot 10^8$ m/s

[7]We note, that some text books and scientific publications cite Ref. [155] instead of Ref. [153] for the calculation of L_{kin}. The discrepancy between the calculated kinetic inductances from the formulas given in these two publications is significant (factor ~ 1.7 for our actual design parameters but a factor ~ 750 (!) for $w = 1\,\mu\mathrm{m}$ and $s = 20\,\mu\mathrm{m}$). Furthermore, the dependence of L_{kin} on the magnetic penetration depth is linear in Ref. [155] but quadratic in Ref. [153]. The calculations in this thesis are based on the formula given in Ref. [153] which is derived analytically by conformal mapping techniques. In contrast, the expression given in Ref. [155] is an analytical approximation to numerical results published elsewhere.

Here, n_i denotes the density of normal ($i = \mathrm{n}$) and superconducting ($i = \mathrm{s}$) electrons. For $T \to 0$ the BCS theory [156, 158] predicts $n_\mathrm{n}/n_\mathrm{s} \propto \exp(-T_\mathrm{c}/T)$ and therefore

$$Q_\mathrm{res} \propto 1/R_\mathrm{s} \propto \exp(T_\mathrm{c}/T) \quad . \tag{2.35}$$

The resistively limited Q_res scales exponentially with the reduced temperature T_c/T. At very low temperatures and input powers, however, the quality factor is limited by dielectric loss.

Dielectric losses

Dielectric loss is thought to be one of the primary sources of decoherence in superconducting quantum bits [83] and also a limiting factor for the maximum attainable quality factor for CPW resonators. When electric or magnetic fields pass a lossy substrate, energy is invariably lost. The dielectric loss can be expressed by an imaginary part ϵ_Im of the dielectric constant ϵ. It is then possible to define a quality factor Q_diel for an effective LCR-circuit with

$$Q_\mathrm{diel} = \frac{1}{\tan\delta} \quad . \tag{2.36}$$

The quantity $\tan\delta = \epsilon_\mathrm{Im}/\epsilon_\mathrm{Re}$ is the loss tangent. To minimize dielectric losses it is therefore essential to use substrate materials with a small $\tan\delta$ [147, 159]. Furthermore, it was observed that for very small input powers P_in the loss tangent scales $\propto 1/\sqrt{P_\mathrm{in}}$ and saturates at an intrinsic value [147]. This effect is attributed to two-level state (TLS) defects [160] in the dielectric which absorb energy at low powers but become saturated at higher powers and temperatures. It is beyond the scope of this thesis to give a detailed overview about dielectric losses and TLS defects. Thus, for further reading, the author suggests the following references, capturing properties of superconducting resonators including TLS dielectrics [159, 161, 162], the modeling of TLS defects [163] and resonator properties in the low power limit at mK temperatures [164, 165].

Radiative losses

Even at zero temperature and assuming no dielectric loss mechanisms, the internal quality factor of a CPW resonator would be limited by energy loss by radiation into free space. Assuming a straight CPW transmission line [166, 167] it can be shown that the radiation limited quality factor scales as

$$Q_\mathrm{rad} \propto 3 \left(\frac{l}{w+2s}\right)^2 \quad . \tag{2.37}$$

Here, w and s are defined as depicted in Fig. 2.9 b and l is the length of the CPW transmission line. The factor 3 in Eq. (2.37) was evaluated numerically and decreases for increasing mode index n. For GHz resonators with large aspect ratios $l/(w+2s) \approx (0.5-1)\cdot 10^3$ as they are presented in this thesis, radiation losses are not the limiting factor.

2.3.5 Quantization of the LC-resonant circuit

In section 2.3.2, the distributed CPW resonator was modeled as parallel lumped element circuit. Such an electronic harmonic oscillator can be described quantum mechanically,

with operators resembling electric circuit quantities.
The voltage across the inductance L and the capacitance C of a lossless LC-circuit is given by

$$V = Q/C = -L\frac{\partial I}{\partial t} \quad . \tag{2.38}$$

The classical Hamilton function representing the total energy can be written as

$$H = \frac{1}{2}LI^2 + \frac{1}{2}CV^2 = \frac{\Phi^2}{2L} + \frac{Q^2}{2C} \quad , \tag{2.39}$$

where we used $\Phi = LI$ representing the flux in the inductor and $Q = CV$ is the charge stored in the capacitor. We see that

$$\frac{\partial H}{\partial Q} = Q/C = V = -L\frac{\partial I}{\partial t} = -\dot{\Phi} \quad \text{and} \tag{2.40}$$

$$\frac{\partial H}{\partial \Phi} = \Phi/L = I = \dot{Q} \quad , \tag{2.41}$$

which implies that Q and Φ correspond to generalized canonical position and momentum variables, respectively. Therefore, we can map these classical variables directly to quantum mechanical operators $\hat{Q}$ and $\hat{\Phi}$ with the commutation relation

$$[\hat{Q}, \hat{\Phi}] = i\hbar \quad . \tag{2.42}$$

In analogy to a particle moving in a harmonic potential, the operators $\hat{Q}$ and $\hat{\Phi}$ can be expressed in terms of bosonic creation ($\hat{a}^\dagger$) and annihilation ($\hat{a}$) operators as [168]

$$\hat{Q} = \sqrt{\frac{\hbar}{2Z_\mathrm{c}}}(\hat{a}^\dagger + \hat{a}) \quad \text{and} \tag{2.43}$$

$$\hat{\Phi} = i\sqrt{\frac{\hbar Z_\mathrm{c}}{2}}(\hat{a}^\dagger - \hat{a}) \quad . \tag{2.44}$$

Here, $Z_\mathrm{c} = \sqrt{L/C}$ is the characteristic impedance of the LC-circuit and

$$\hat{a} = \frac{Z_\mathrm{c}\hat{Q} + i\hat{\Phi}}{\sqrt{2\hbar Z_\mathrm{c}}} \quad . \tag{2.45}$$

$\hat{a}^\dagger$ and $\hat{a}$ obey the renowned commutation relation $[\hat{a}, \hat{a}^\dagger] = 1$. Using Eqs. (2.43), (2.44), and (2.39), the Hamiltonian of a quantum mechanical oscillator with frequency $\omega = 1/\sqrt{LC}$ can be written as

$$\hat{H} = \hbar\omega\left(\hat{a}^\dagger\hat{a} + \frac{1}{2}\right) \quad . \tag{2.46}$$

Chapter 3

Design & Fabrication Technology

The primary goal of the author's efforts in the early stages of this thesis was the design and fabrication of superconducting quantum circuits. Unfortunately, former PhD and diploma students did not succeed in fabricating the main building block - the superconducting flux quantum bit. The last sentence is not to be misunderstood as derogating their commitment and efforts. Rather, it should point out that one of the most important contributions to a reproducible fabrication of flux qubits was the implementation of a new aluminum evaporation facility at the WMI by T. Brenninger [169]. In the framework of this thesis the fabrication processes for superconducting flux qubits were successfully established in the new evaporation system. Besides design considerations for resonators, Josephson junction devices and their electromagnetic on-chip environment, this chapter also covers different lithographic and deposition techniques. In general, our quantum circuits are fabricated using a mix and match process where high resolution electron beam lithography patterns are precisely aligned into existing patterns made by optical lithography. This process is illustrated in Fig. 3.1.
The fabrication processes described in this chapter involve many steps, each one important and some of them rather time-consuming. Process parameters may vary over time and consequently have to be adjusted. This requires a good knowledge of the interplay of these parameters and most importantly, constant monitoring. The detailed recipes and process parameters for each device in appendix A should serve as a good starting point.

3.1 Josephson junction devices

For flux quantum bits we require Josephson junctions with areas $A \sim 0.02 - 0.04\,\mu\text{m}^2$ to ensure a large charging energy E_C (see section 2.2.2). In addition, high critical current densities are needed to ensure a sufficently large E_J/E_C ratio. In a conventional readout scheme, the qubit is surrounded by a dc-SQUID, which detects the flux generated by the persistent currents in the qubit loop. Both devices are fabricated simultaneously using electron beam lithography and shadow evaporation [170] of aluminum. While the flux qubit is not connected galvanically to any device, the dc-SQUID has to be connected to a readout circuitry. Such devices are studied experimentally in chapter 4. For the circuit QED experiments discussed in chapter 5, a flux qubit is coupled to a distributed CPW resonator and the state of the qubit can be inferred from the shift of the transmission

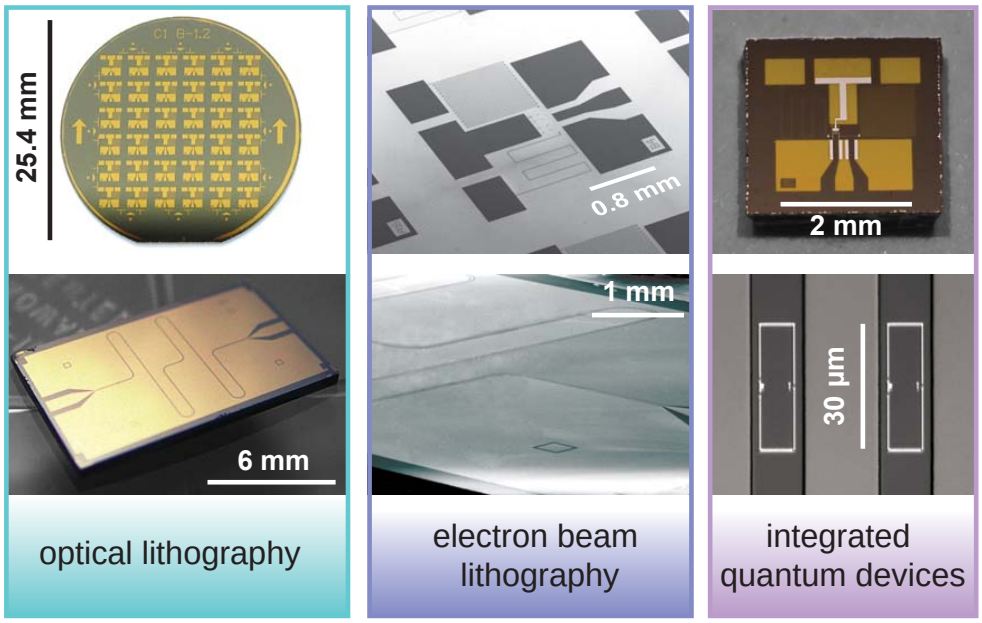

Figure 3.1: Roadmap towards integrated quantum circuits. The mix and match process used at the WMI combines optical and electron beam lithography. Each lithography step is followed by either a deposition or a removal of a thin metal film. The images in the top panel belong to qubit-SQUID devices while the images in the bottom panel depict flux quantum bits coupled to distributed coplanar waveguide resonators.

spectrum.
In both cases, prior to the fabrication of flux qubits, comparatively large patterns (e.g bias lines or CPW resonators) with dimensions of several mm have to be realized. This is done by optical lithography which allows the patterning of large areas within a single exposure step. The spatial resolution of optical lithography (at least with standard equipment) is limited by the wavelength of the ultraviolet (UV) light used and is typically $\geq 1\,\mu m$. Thus, small area Josephson junctions have to be realized using electron beam lithography (EBL). However, EBL is a serial lithography technique and is not suited for large area applications due to its limited throughput.

3.1.1 On-chip bias lines

The bias lines and contact pads necessary for a four-point readout of the dc-SQUID are fabricated in a lift-off process using optical lithography and sputter deposition of gold. The application of gold has several advantages, e.g. good thermal and electrical conductivity. In addition, as a noble metal gold barely oxidizes which is favorable for wire bonding. We used two different substrate materials for qubit-SQUID systems, silicon with native oxide and thermally oxidized silicon with an oxide thickness of 50 nm. Although flux qubits could be successfully fabricated and characterized on both substrate materials, the production process is now optimized for silicon wafers with a thermally grown oxide layer since the CPW resonators are fabricated on that material, too. The specific material characteristics can be found in appendix A. Figure 3.2 shows the two designs for bias lines and contact pads used for the majority of experimental results presented in this thesis. The layouts differ in complexity and in the available space for additional circuit elements.

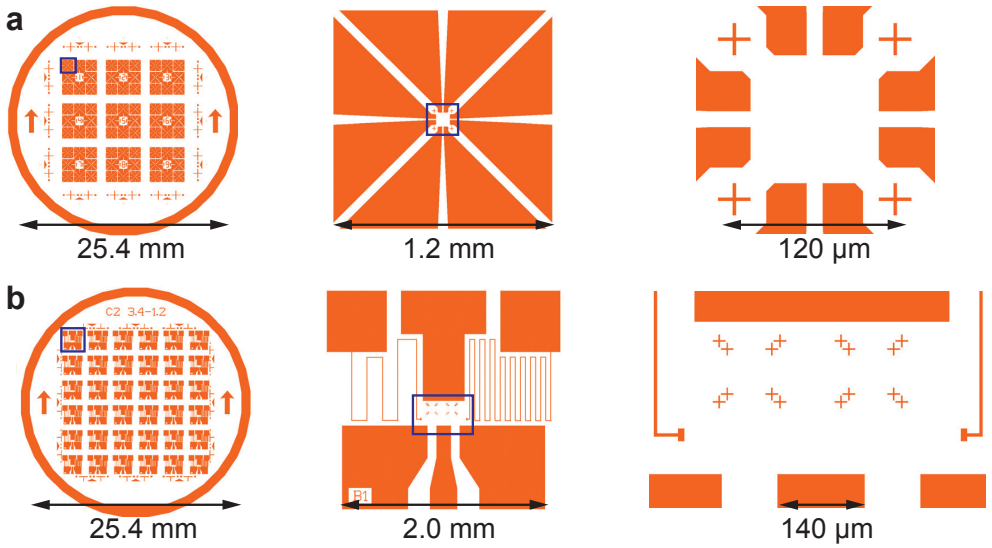

Figure 3.2: Layouts of optical masks. (a) Layout of an optical mask for lithography of dc-SQUID contact pads. Magnified views of the area indicated by the blue square are shown from left to right. Filled orange polygons correspond to subsequently metalized areas. In the right panel, an $120\,\mathrm{x}\,120\,\mu\mathrm{m}^2$ EBL writefield can be defined by the four crosses. (b) Sophisticated sample layout. The high resistance bias and readout leads attenuate external noise. The additional EBL writefields allow the patterning of circuit elements prior to flux qubit and dc-SQUID fabrication.

The simpler design (see Fig. 3.2 a) was used mainly in the early stages of flux qubit production. It contains 72 writefields for subsequent high-resolution EBL and therefore allows to vary design and/or exposure parameters over a wide range during a single EBL run. In addition, its simple geometry makes it especially easy to fabricate. The more complex design (see Fig. 3.2 b) comprises 36 chips, each with an $50\,\Omega$ impedance matched CPW transmission line that can be used as on-chip microwave antenna for time-domain measurements and qubit spectroscopy. Moreover, this layout provides enough space for the implementation of an on-chip controlled electromagnetic qubit environment e.g. dc-SQUID shunt capacitors [139]. The bias and readout lines consist of narrow, meandering strips representing ohmic on-chip resistors. These resistors reduce parasitic resonances and together with the shunt capacitors they form effective RC-low pass filters [87,132] with cut-off frequencies in the MHz regime. Although time-domain measurements were not carried out within the scope of this thesis, the majority of the qubit-SQUID measurements in chapter 4 were performed using this chip layout. Details on each layout can be found in Ref. [171].

Optical lithography for lift-off processes

Optical lithography is used to define a geometric pattern in a chemical resist layer using UV-light and a chromium photo mask. It is the most widely used process in microfabrication and shares fundamental principles with photography. For the on-chip bias lines we decided to use a lift-off process, where the pattern is defined prior to the deposition of the metal. This was done primarily to ensure smooth edge profiles of the sputtered gold films and therefore ensuring good galvanic contact of the aluminum layers evaporated

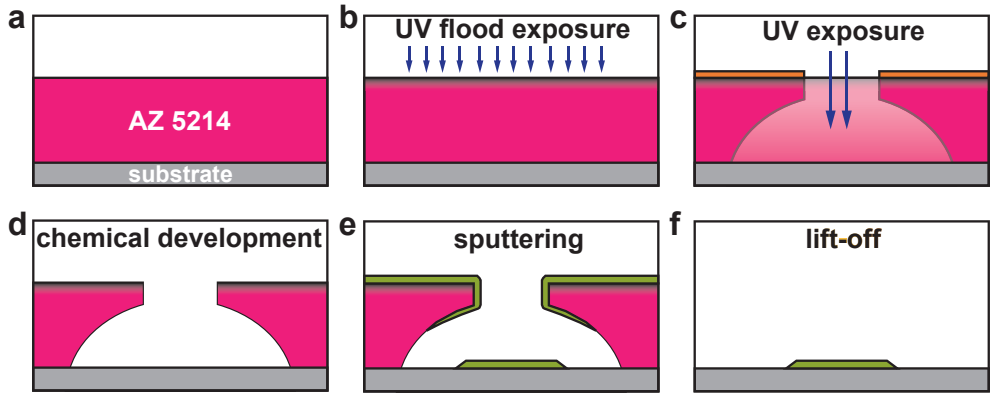

Figure 3.3: Schematic of optical lithography for lift-off processes. (a) A thin layer of AZ 5214 image-reversal resist is spun on the substrate and the wafer is heated on a hotplate to reduce the solvent content. (b) A flood exposure and an additional reversal bake procedure allow the definition of an undercut. The cross-linked resist region is slightly darkened. (c) The desired pattern is defined by UV-light and an optical mask using a mask aligner. (d) After the chemical development, the pronounced undercut profile allows the sputtering of thin-films which is shown in (e). (f) During the lift-off procedure, the resist with the excess metal is removed.

later on. The process steps for the fabrication of sputtered thin-films are visualized in Fig. 3.3 and summarized point-by-point in appendix A. We use a single-layer resist system (image-reversal resist AZ 5214E; *Microchemicals GmbH*) that is spun onto the cleaned wafer resulting in a resist thickness of roughly $\sim 1.4\,\mu m$ (see Fig. 3.3 a). After a baking process which reduces the remaining solvent content in the resist, the whole wafer is exposed shortly to UV-light without any photomask (flood exposure; see Fig. 3.3 b). This has the effect of exposing surface-near regions with a higher dose than substrate-near regions. In the following reversal bake, the stronger exposed surface-near resist areas are converted, which later on results in a pronounced undercut. Since sputtering is an isotropic process, the presence of an undercut is of utmost importance. Without the undercut, the metal would cover the resist edges completely, therefore making a subsequent lift-off in a solvent complicated if not unfeasible. Even if the lift-off worked, there is a high probability of an almost vertical, residual metallization at the edges, making a good galvanic contact virtually impossible. The desired pattern is defined using a chrome mask and a MJB3 Photomask Aligner from *Süss MicroTec* (see Fig. 3.3 c). After that, the exposed resist areas are removed using a chemical developer (see Fig. 3.3 d). We note, that the undercut profile strongly depends on the flood exposure time and the reversal bake parameters. Usually, the undercut is visible under an optical microscope as a 'corona' around the actual structures. The wafer is now ready to be transferred to the sputtering chamber.
Sputtering is a technique used to deposit thin films of a material onto a substrate by first creating a plasma and then accelerating the ions from this plasma onto a target material (see Fig. 3.3 e). The table-top sputtering chamber at the WMI allows the deposition of three different metal layers without breaking the vacuum. This feature is very useful as we use 5 nm chromium as an adhesive layer prior to the deposition of 25 nm gold. For the lift-off procedure (see Fig. 3.3 f), the wafer is ultrasonically cleaned in a warm acetone bath.

3.1.2 Submicron Josephson junctions

In this section we present fabrication details and layout considerations for realizing devices embedding submicron Josephson junctions. In particular, the flux qubit design discussed here is suitable for a conventional dc-SQUID readout scheme and also for circuit QED applications. Fortunately, several resist systems were already implemented at the WMI Nano-Facilities. Owing to the effort of former PhD and diploma students, the author of this thesis was already equipped with good initial process parameters [172, 173]. The layouts for flux qubits, SQUID loops and shunting capacitors can be designed with a CAD program[1]. Figure 3.4 a and b show an actual layout and a false-color SEM image of the fabricated device. For our designs we explicitly make use of the so-called *proximity effect*. In short, the proximity effect is the exposure of areas in close vicinity by backscattered electrons during EBL. In Fig. 3.4 a, the red polygons – the so-called proximity bars – have two functions. First, the presence of the two proximity bars to the left and right of the dc-SQUID results in a symmetrically exposed environment for the SQUID junctions. Second, from the geometry of our design, the flux qubit α-junction is not exposed as much as the other two junctions by the unavoidable proximity effect due to the dc-SQUID loop.

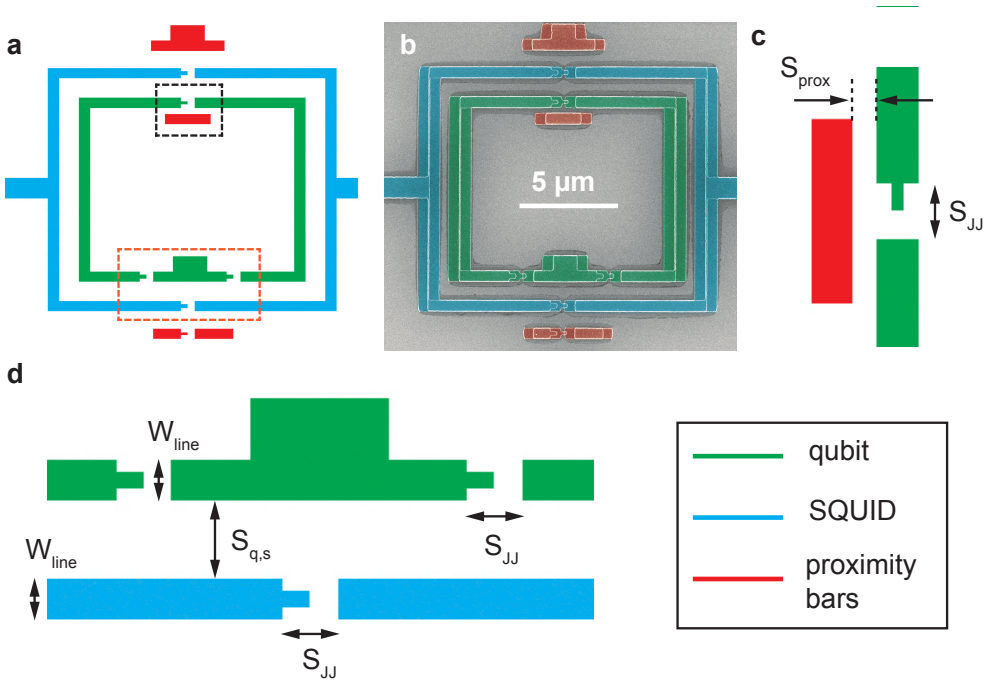

Figure 3.4: CAD layouts and fabricated structure. (a) CAD layout of a flux qubit (green) coupled inductively to a readout dc-SQUID (blue). The red polygons depict proximity bars. (b) False-color SEM image of the fabricated CAD layout shown in (a). The color code is the same in all panels. (c) Magnified view of the rotated area highlighted by the black dashed box in (a). S_{prox} is the distance between the inner proximity bar and the α-junction. In this particular layout $S_{\mathrm{prox}} \sim 300\,\mathrm{nm}$. The best results – with respect to the deviation between designed and fabricated area of the α-junction – were obtained for $S_{\mathrm{prox}} \sim 700\,\mathrm{nm}$. (d) Magnified view of the area highlighted by the orange dashed box in (a). The qubit and SQUID have the same width $W_{\mathrm{line}} \sim 500\,\mathrm{nm}$ and are separated by a distance $S_{\mathrm{q,s}} \sim 1\,\mu\mathrm{m}$. The spacing $S_{\mathrm{JJ}} \sim 600\,\mathrm{nm}$ is kept fixed in all designs presented in this thesis.

[1] We used Xic, LayoutEditor and the built-in editor of the EBL software. These programs are capable of writing GDS or GDSII files used by the EBL software.

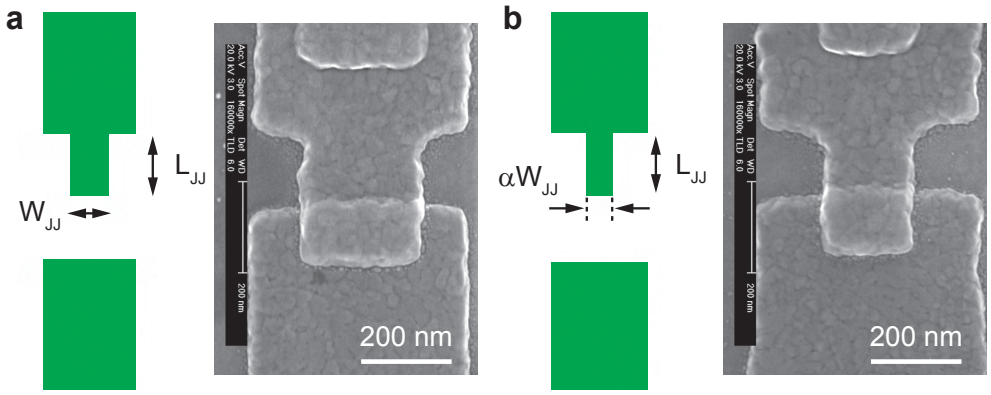

Figure 3.5: Layout and SEM images of flux qubit Josephson junctions. (a) Josephson junction with width $W_{JJ} \sim 200\,\text{nm}$ and length $L_{JJ} \sim 300\,\text{nm}$. (b) α-junction incorporated in the qubit loop ($\alpha \sim 0.63$). In all designs, $\alpha \sim 0.54 - 0.72$ is adjusted by the width of the finger-like structure while the length is kept constant.

One could increase the exposure time of the α-junction itself, however, we found that the additional proximity bar (see Fig. 3.4 c) resulted in a much better reproducibility of the α-junction area. In Fig. 3.4 d, designs for the other two junctions and one of the SQUID junctions is shown. Typical lateral dimensions are given in the caption of Fig. 3.4. A magnified view of the actual Josephson junction designs and SEM images of fabricated tunnel junctions are shown in Fig. 3.5.
The flux qubit designs for circuit QED applications are similar. Since the dc-SQUID is missing, proximity bars in vicinity to all Josephson junctions were introduced. Figure 3.6 shows the qubit layout and a false-color SEM image of a flux qubit galvanically coupled to the center strip of a CPW resonator.

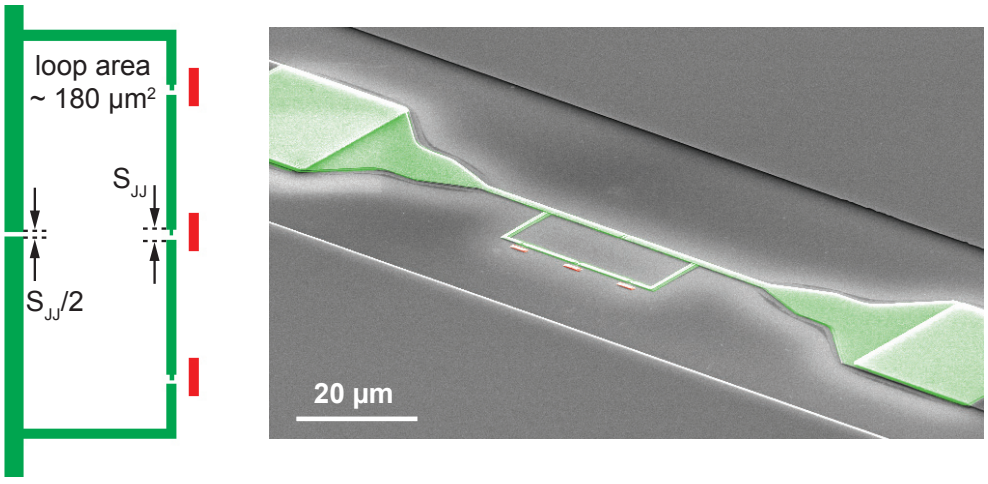

Figure 3.6: Specific circuit QED layout of a flux qubit (green) galvanically coupled to a CPW resonator. The qubit loop area is roughly $180\,\mu\text{m}^2$. An additional Josephson junction located in the narrow strip enhances the qubit-resonator coupling significantly. In comparison to qubit-SQUID systems, additional proximity bars (red) compensate the proximity effect due to the missing SQUID. In this design, $S_{JJ} \sim 600\,\text{nm}$.

Electron beam lithography and shadow evaporation

Electron beam lithography is an ideal technique for realizing structures with minimum feature sizes of about 20 nm. In contrast to optical lithography, a focused electron beam draws the circuit patterns in a serial manner into the resist. Owing to the small de-Broglie wavelength of the high energy electrons, EBL is one way to overcome the resolution limit given by the diffraction limit of UV-light. Although the throughput of EBL is limited compared to parallel lithography techniques, it is very versatile as layout modifications can be implemented easily. At the WMI Nano-Facilities we use a XL30-SFEG Scanning Electron Microscope from *FEI* that is equipped with a *Raith* laser-stage and a *Raith Elphy Plus* pattern generator for lithography applications. Figure 3.7 summarizes the most important lithographic steps in junction fabrication. For EBL we use a double-layer PMMA[2] electron beam resist system. The bottom layer consist of a 680 nm thick PMMA/MA copolymer layer. This resist has a significant higher sensitivity to high energy electrons than the top PMMA/950k layer, which is only 70 nm thin (see Fig. 3.7 a). The solvent content of each layer is reduced using a hotplate. During EBL, the double-layer resist system is exposed with 30 keV electrons (see Fig. 3.7 b). The bottom layer is 3 - 4 times more sensitive than the top layer which leads to a distinct undercut. It is

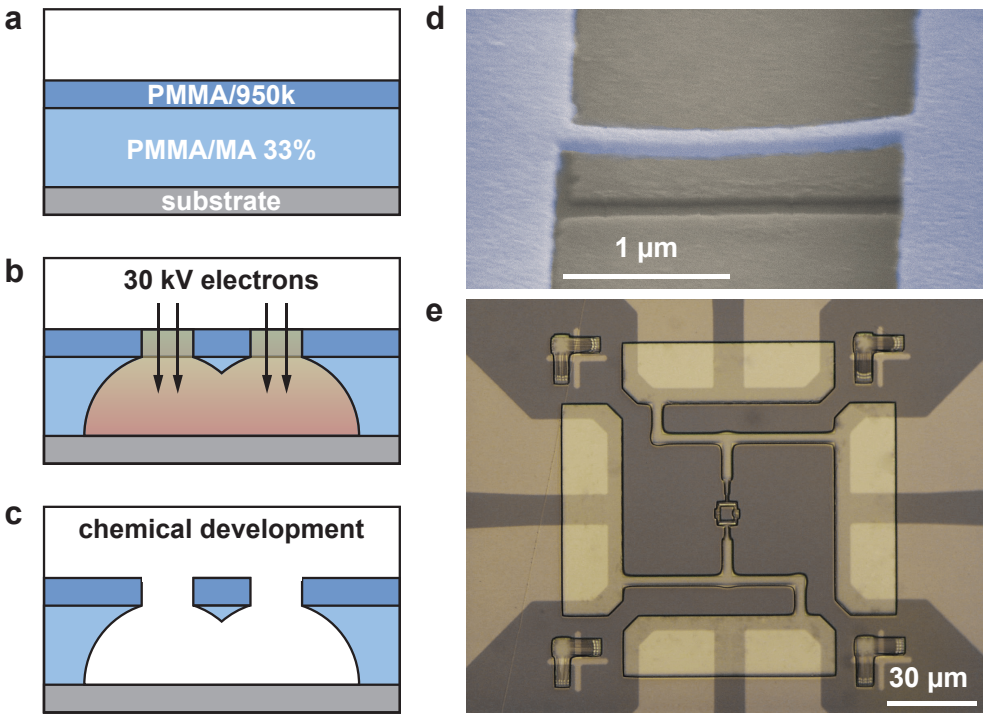

Figure 3.7: Schematic of essential steps in electron beam lithography. (a) For EBL a bi-layer resist system is used. (b) After mounting and aligning the wafer, the circuit pattern is directly drawn into the resist system by a focused electron beam. (c) The exposed resist is dissolved during development. If the structures are narrow enough, free standing resist bridges are formed due to the pronounced undercut. (d) False-color SEM image of a suspended resist bridge. The image was taken after the deposition of a thin metal layer. (e) Qubit-SQUID pattern after EBL and development. The rectangles close to the four crosses are remnants of the EBL automatic write field alignment.

[2] **P**oly**M**ethyl**M**eth**A**crylate is liquid Plexiglas®

thus possible to form free-standing resist bridges after development (see Fig. 3.7 c and d). We note, that in contrast to sputtering, the electron beam evaporation of metal is a very directional deposition technique which enables good lift-off properties with less pronounced undercuts. The smoothness of the edges of the circuit pattern is determined by the top layer which serves as mask during the following evaporation process. Figure 3.7 e shows a qubit-SQUID pattern after EBL and chemical development. The wafer is now mounted on a sample holder and installed in an electron beam evaporator tailored to the needs of Josephson junction fabrication. A very detailed description of this device is given in Ref. [169] while appendix A.9 captures the most important aspects. In order to form overlapping metal junctions, the sample holder can be tilted by a step motor. The bottom aluminum layer of the Josephson junction is evaporated under a fixed angle $-\theta = -16°$ (see Fig. 3.8 a). The sample is then brought into a horizontal position ($\theta = 0°$) and one of

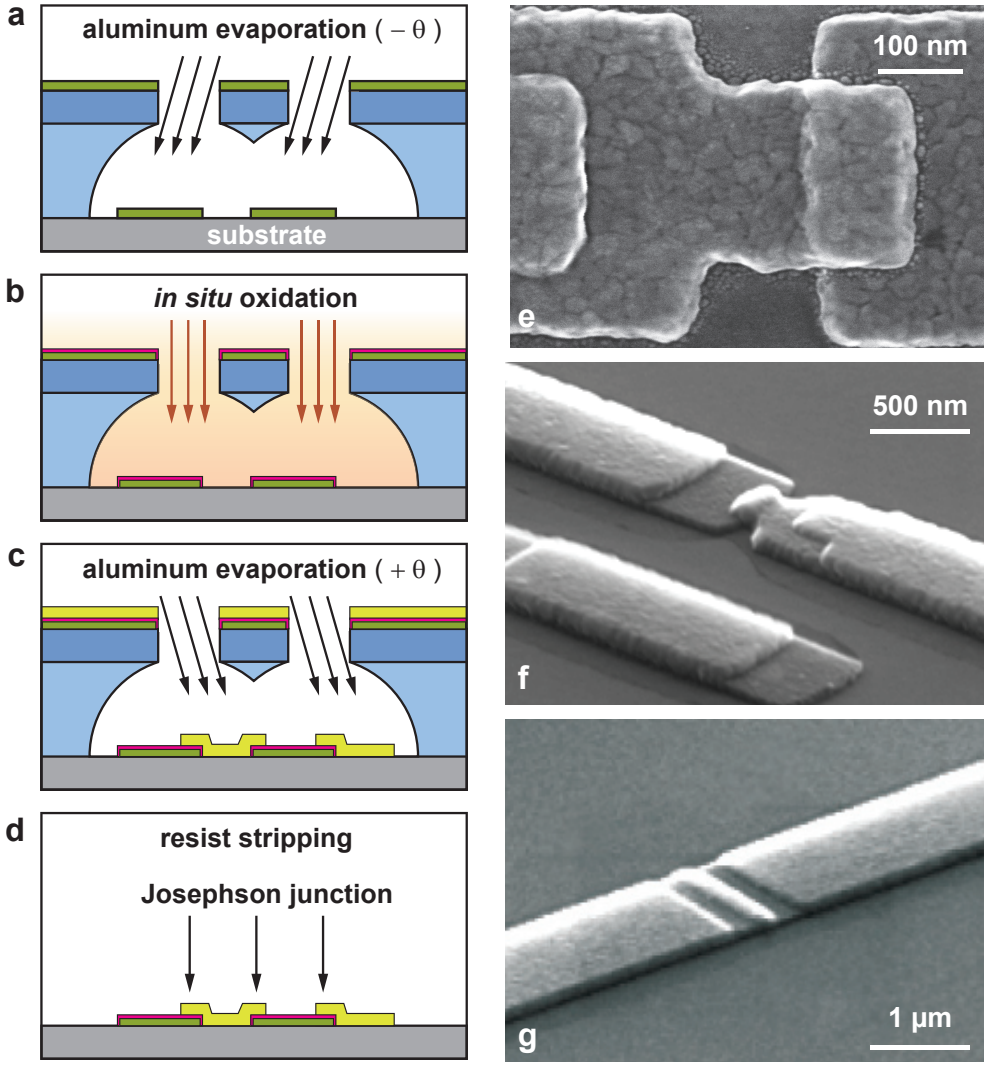

Figure 3.8: Schematic of double-angle electron beam evaporation. (a) Evaporation of the junction bottom layer under an angle $-\theta = -16°$. The angle is controlled reproducibly by a step motor. (b) In situ oxidation of the bottom layer. The oxidation can be stopped within a fraction of a second. (c) Evaporation of the top aluminum layer under an angle $+\theta = +16°$ defines the Josephson junction. (d) Resist stripping. (e)-(g) Different views of typical Josephson junctions. In (f), a proximity bar is located in vicinity of the junction.

the most crucial steps in Josephson junction fabrication – the *in situ* oxidation process – is initiated (see Fig. 3.8 b). At the WMI, we use pure oxygen to form tunnel barriers with an AlO_x thickness of $1-2\,\mathrm{nm}$, depending on the oxidation time and pressure. With a pressure of $p_{O_2} \approx 2\cdot 10^{-4}\,\mathrm{mbar}$ and oxidation times between $22-23$ minutes, we are able to produce Josephson junctions with critical current densities $j_c \sim 1.0-2.5\,\mathrm{kA/cm^2}$. The oxidation process is stopped by evacuating the process chamber and the top layer is evaporated under an angle $+\theta = +16°$ (see Fig. 3.8 c). To ensure a smooth coating of the bottom layer, the thickness of the top layer is larger by at least 10 nm. Finally, the wafer is sonicated in a warm acetone bath (see Fig. 3.8 d) for resist stripping. In Figure 3.8 e-g, SEM images of submicron Josephson junctions after resist stripping are shown. The detailed evaporation parameters are summarized in appendix A. Different techniques on how to form oxide barriers with a thickness of a few nanometers can be found in the literature. Some groups use an argon/oxygen mixture (90%/10% or 99%/1%) and usually they oxidize at a higher pressure for a shorter time [174,175]. The oxidation technique we use at the WMI was adapted from junction fabrication with the 'old' evaporation facility. This oxidation is not time-critical owing to a very low partial oxygen pressure. The oxidation pressure is established by a control valve in front of the turbo molecular pump while a mass flow controller induces a constant gas flow. We operate the control valve in the so-called position mode[3]. Here, the valve remains in a stable, half-open position and with an oxygen flow of 3 sccm we are able to adjust the pressure to $(2\pm 0.1)\cdot 10^{-4}\,\mathrm{mbar}$.

3.1.3 Shunting capacitors & on-chip microwave antenna

The dc-SQUID susceptibility to thermal and quantum fluctuations can be reduced by shunting it with a large capacitance. We use parallel plate shunt capacitors [87,140] owing to their much larger specific capacitance compared to interdigitated finger capacitors [139]. The fabrication steps for the top and bottom electrode as well as an optical microscope image of the entire circuit are shown in Fig. 3.9 a-c. While the top electrode of the shunt capacitor C_{sh} is fabricated in the same run as the qubit and the SQUID, the bottom electrode has to be fabricated beforehand. For this purpose we utilize the inner EBL writefield (see Fig. 3.2 b) and evaporate a 30 nm aluminum film at an angle $\theta = 0°$. We then oxidize the bottom electrode at ambient pressure on a hotplate for several hours yielding typical specific capacitances of $c_{sh} \approx 10-20\,\mathrm{fF/\mu m^2}$ [176]. The self-inductance of the aluminum leads and the shunt capacitors form an effective lumped element LC-circuit. The resonance frequency $\omega = 1/\sqrt{LC_{sh}}$ can be easily adjusted to the GHz regime enabling experiments in the realm of circuit QED. In contrast to distributed transmission line resonators as discussed in section 2.3, such LC-circuits usually suffer from large photon decay rates κ and support only a single resonant mode [132].
The characterization of flux qubits requires the irradiation with microwaves in order to induce transitions from the ground to the excited state. For this purpose, an on-chip microwave antenna is realized in close vicinity to the qubit. It consists of a 1 µm wide aluminum strip short-circuiting an impedance-matched coplanar waveguide transmission

[3] In the beginning of junction fabrication with the new evaporation facility, the valve was operated in a pressure mode, i.e. the valve was regulating the pressure to a preset value. For this technique to work properly, a correct calibration of the capacitive pressure gauge is of utmost importance. Moreover, during the first seconds of the oxidation process, the valves feedback mechanism is to slow, resulting in a large pressure spike.

line (see Fig. 3.9 d and inset therein). The large-area aluminum strips at the edges of the CPW minimize the contact resistance at the aluminum-gold interface.

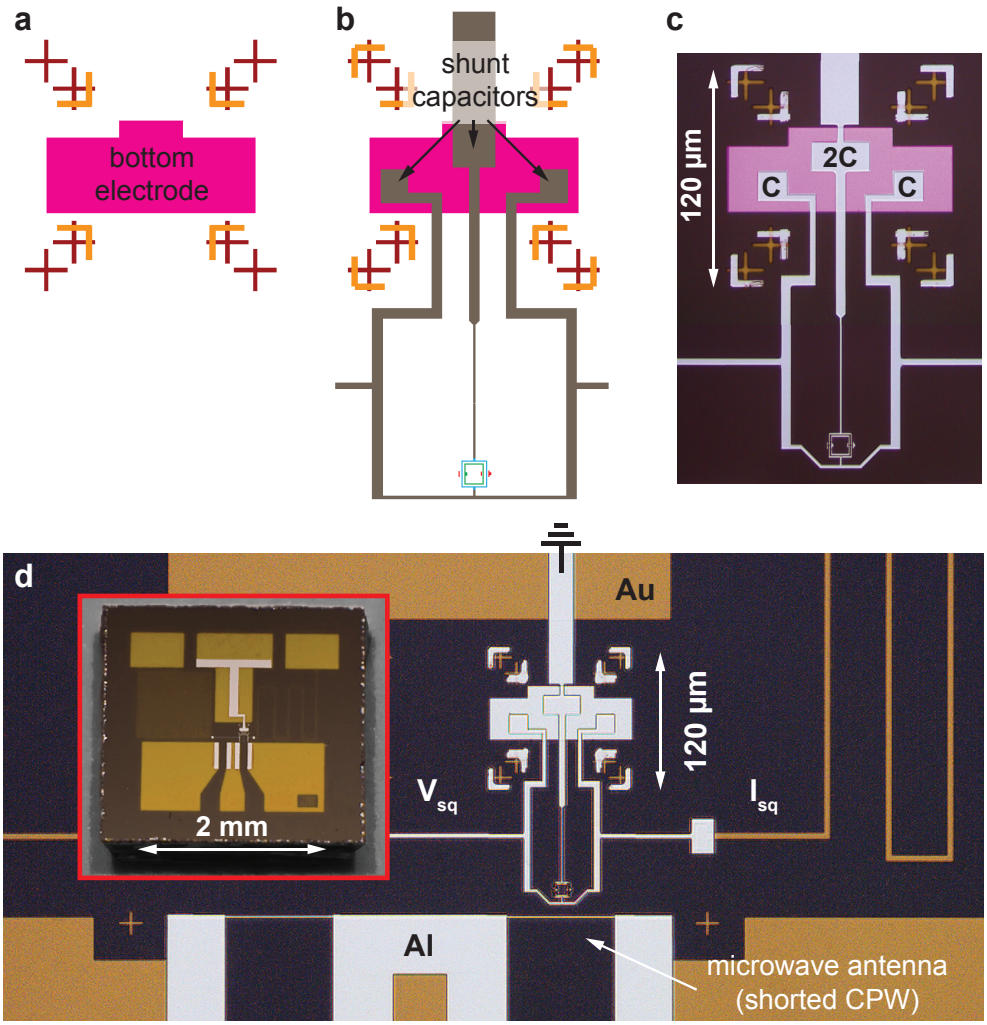

Figure 3.9: Shunt capacitor layout and optical image of a fabricated sample. (a) Schematic of the dc-SQUID shunt capacitor bottom electrode. The bottom electrode is fabricated in a separate EBL and evaporation step prior to the flux quantum circuits. The red crosses and orange bars represent EBL alignment marks. (b) The top electrode of the three shunt capacitors are evaporated together with the flux quantum circuits. The dc-SQUID and qubit loop are depicted in the lower part of the schematic. (c) Optical microscope image of a fabricated device. For better visibility, the bottom electrode is colored pink. (d) Optical microscope image showing the qubit in its electromagnetic on-chip environment. The microwave antenna is coupled inductively to the qubit and consists of a short-circuited coplanar waveguide (CPW) transmission line. The CPW structure is fabricated using optical lithography and can be identified more clearly in the inset image (red box), where a whole sample is shown.

3.2 Coplanar waveguide resonators

This section comprises the fabrication processes and characterization of coplanar waveguide (CPW) resonators which have been discussed theoretically in section 2.3. While the resonance frequency ω_r can be adjusted by changing the length l of the center conductor, the quality factor Q_n is predominantly determined by the value of the coupling capacitors C_κ. In order to be able to produce resonators with specific characteristics on-demand, many different designs have been realized on varying substrate materials, finally converging to CPW resonators similar to the one shown in Fig. 3.10 a. The resonator is defined by a meandering center strip with length $l = 23\,\text{mm}$ which is terminated by coupling capacitors (see Fig. 3.10 b and c). The center strip has a width of $w = 20\,\mu\text{m}$ and is separated from the lateral groundplanes by a gap of width $s = 12\,\mu\text{m}$. In order to connect the resonator to a readout circuitry, the dimensions of the CPW in- and output ports are much larger ($w = 500\,\mu\text{m}$ and $s = 245\,\mu\text{m}$). Both, w and s are smoothly and gradually tapered towards the dimensions of the center conductor, maintaining a characteristic impedance $Z_0 \approx 50\,\Omega$. As substrate material, we use high-resistivity silicon ($\rho > 3000\,\Omega\text{cm}$) wafers with a 50 nm thick, thermally grown SiO_2 layer. We chose niobium as superconducting material owing to its high $T_c \approx 9.2\,\text{K}$ which enables a characterization of our resonators at liquid helium temperatures ($T \sim 4.2\,\text{K}$). In addition, quasiparticle excitations can be safely neglected at these temperatures since the normal fluid density $n_n \propto \exp(-T_c/T)$ (see section 2.3.4).

3.2.1 Optical lithography and reactive ion etching

In contrast to the optical lithography for lift-off processes described earlier in section 3.1.1, the CPW resonators are fabricated using dry etching technology. A schematic overview of our fabrication process is illustrated in Fig. 3.11. After cleaning the substrate, a niobium layer is deposited by dc-magnetron sputtering (see Fig. 3.11 a). The quality of our Nb thin films is determined from a four-point transport measurement (residual resistance

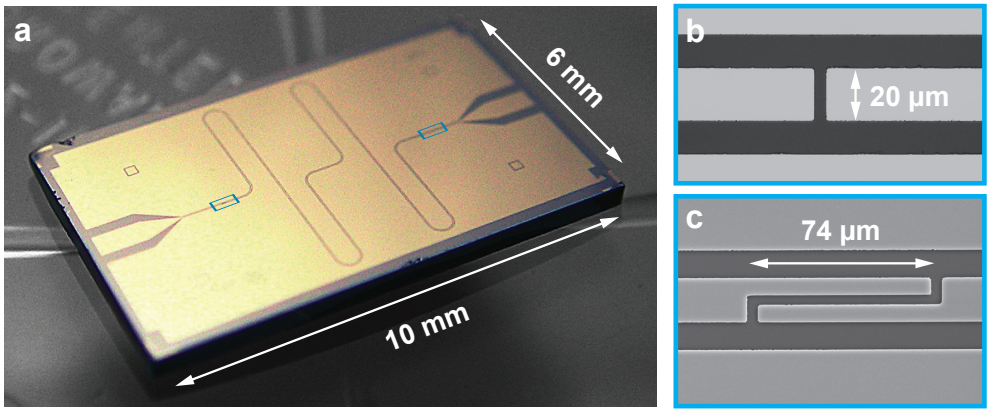

Figure 3.10: Images of a niobium CPW resonator and different coupling capacitors. (a) Our resonators have a length $l = 23\,\text{mm}$ and are fabricated on substrates with an area of $10\,\text{x}\,6\,\text{mm}^2$. The resonator is coupled to the readout circuitry by identical capacitors (light blue box). (b) SEM image of a gap capacitor with a gap width of $s_g = 4\,\mu\text{m}$ resulting in a capacitance $C_\kappa \approx 2\,\text{fF}$. (c) SEM image of a interdigitated finger capacitor. The two fingers with length $l_f = 74\,\mu\text{m}$ and width $w_f = 8\,\mu\text{m}$ are separated by $s_f = 4\,\mu\text{m}$. For this type of capacitor we calculated a capacitance of $C_\kappa \approx 7\,\text{fF}$. For a definition of coupling capacitor dimensions see Fig. 2.9 c and d.

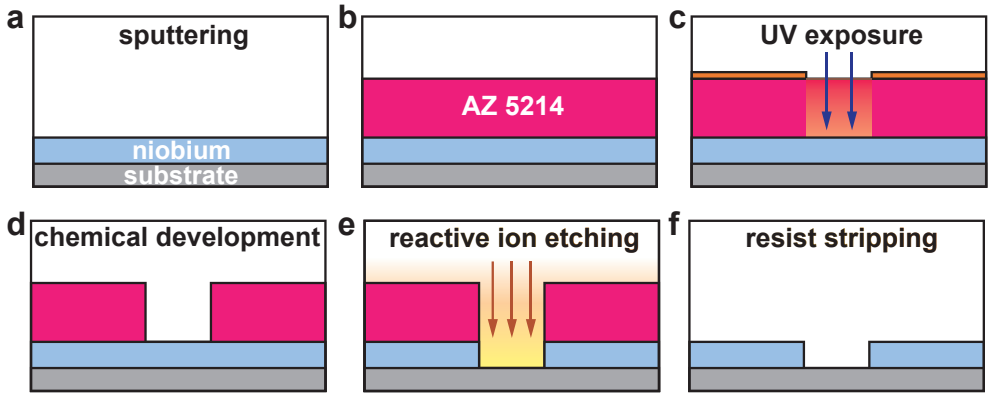

Figure 3.11: Fabrication schematic for CPW resonators. (a) Deposition of a thin niobium film by dc-magnetron sputtering. (b) Using a resist spinner, the wafer is covered by a roughly 1 µm thick AZ 5214 resist layer. (c) The wafer is exposed to UV-light using an optical mask and a mask aligner. (d) During a chemical development, the previously exposed resist is removed. (e) Using a more physical etching process, the niobium is removed in the reactive ion etcher. (f) A bath in sonicated, warm acetone is used for resist stripping.

ratio $\rho_{\mathrm{RRR}} \approx 5.1$ for a 200 nm-thick film; critical temperature $T_{\mathrm{c}} \approx 9.1\,\mathrm{K}$). For optical lithography we use the same resist (AZ 5214) as for the lift-off process of thin gold films. However, by omitting the flood exposure and the reversal bake, this resist is now used as positive resist (see Fig. 3.11 b). The CPW pattern is transferred into the resist using an optical mask and UV-light (see Fig. 3.11 c). The chemical development (see Fig. 3.11 d) dissolves the exposed resist and the wafer is transferred into a reactive ion etching (RIE) system. During the RIE process, the niobium can be etched both, chemically using a reactive fluoride plasma or physically using argon ions. It is furthermore possible to mix physical and chemical etching by an appropriate choice of process parameters, such as gas flow, pressure, radio frequency (RF) power and inductively coupled plasma (ICP) power. During the etching process (see Fig. 3.11 e), the resist acts as a sacrificial layer, protecting the niobium where it shall remain. We note that the physical RIE process is a highly anisotropic process and allows for a very steep edge profiles. Resist stripping in a sonicated, warm acetone bath removes the remaining resist and finalizes the production of superconducting CPW resonators.

3.2.2 Device mounting and experimental setup

Before we can characterize our CPW resonators in a transmission measurement, the wafer has to be mounted in a box and connected to a readout circuitry. Our sample holder consists of a gold-plated copper box into which a recess is milled so that our wafer fits in neatly. As shown in Fig. 3.12 a, the box contains two drillings for SMA connectors (Rosenberger, 32K724-600S5). Galvanic contact between the center pin of these connectors and the in- and output ports of our resonator is established using conductive silver glue (see Fig. 3.12 b) under a microscope. It is very important to cover the resonator ground planes extensively with silver glue and connect them to the sidewalls of the gold-plated box as shown in Fig. 3.12 c. A well-defined ground and small chip dimensions[4] are a prerequisite for suppressing parasitic groundplane modes. For transmission measurements, the box

[4] As a rule of thumb, the length of the center conductor should be at least twice the length of the largest wafer dimension.

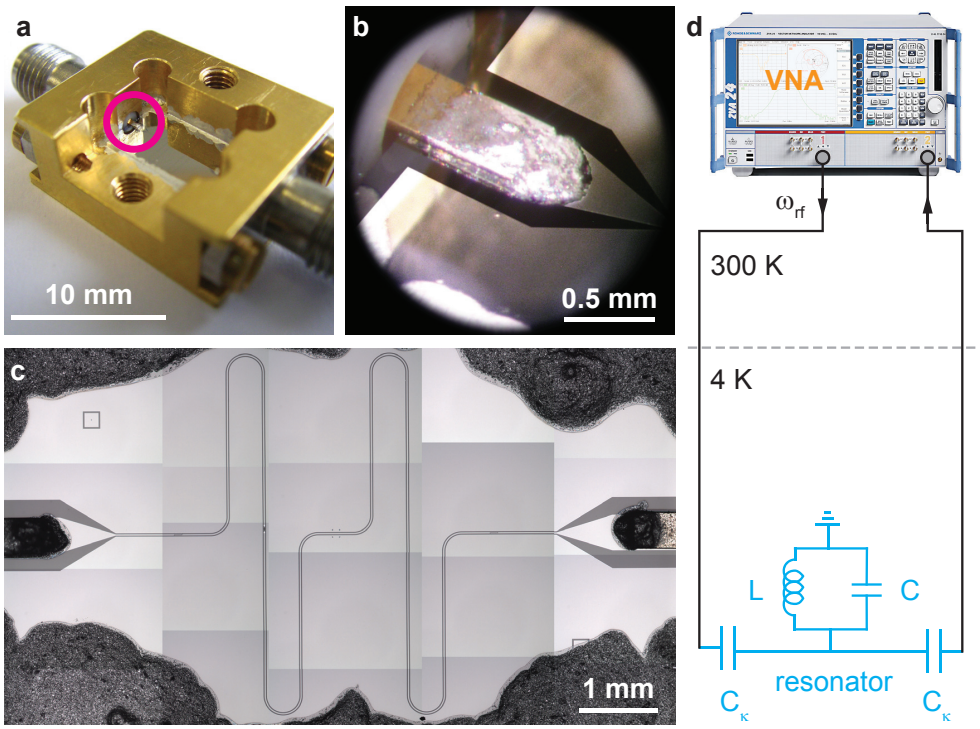

Figure 3.12: Device mounting and measurement setup. (a) Gold-plated copper box with a coplanar waveguide (CPW) resonator similar to the one shown in Fig. 3.10 a. (b) Magnified view of the area highlighted by the magenta circle in (a). The center pin of the microwave connector is connected galvanically to the input port of the CPW using conductive silver glue. For better visibility, the image was post processed to increase the contrast of the niobium. (c) Stitched image showing a top view of a mounted CPW resonator. To provide a good ground, all edges of the chip are excessively covered with silver glue and connected to the side walls of the box. (d) Schematic measurement setup for characterizing CPW resonators at liquid helium temperatures. The transmission through the resonator at a frequency ω_{rf} can be probed using a vector network analyzer (VNA).

is connected to a vector network analyzer (VNA) via stainless steel coaxial cables and mounted in a liquid helium dewar. A schematic of the measurement setup is shown in Fig. 3.12 d. This setup allows an easy and fast characterization, especially of overcoupled CPW resonators as they are used in our circuit QED experiments. By evaporative cooling, the temperature can be further reduced to roughly 1.5 K. However, this temperature limitation and the lack of a cryogenic amplifier prevent measurements at very low input powers and photon numbers.

3.2.3 Transmission measurements

The transmission power spectrum of a driven harmonic oscillator exhibits a Lorentzian line shape

$$P(\omega) = A\frac{(\kappa/2)}{(\omega-\omega_{\mathrm{r}})^2+(\kappa/2)^2} \quad , \tag{3.1}$$

where κ is the full width at half maximum, ω_{r} the bare resonance frequency and $A = P_0\kappa/2$ is related to the maximally transmitted power P_0. Figure 3.13 shows the transmission spectra of the first three modes of an overcoupled CPW resonator with length $l = 23\,\mathrm{mm}$. This choice of length is very convenient as our cryogenic amplifiers in the circuit QED

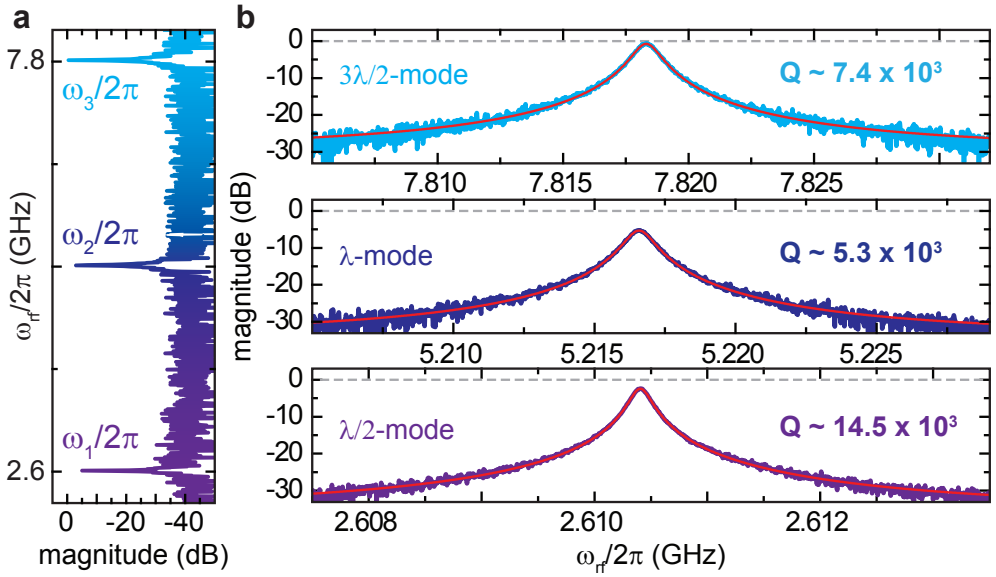

Figure 3.13: Transmission spectra of a $\lambda/2$-resonator. (a) Measured power transmission spectrum (dB-scale) of an overcoupled ($l_\mathrm{f} = 90\,\mu\mathrm{m}, C_\kappa \approx 9\,\mathrm{fF}$) CPW resonator at $T = 1.5\,\mathrm{K}$. The resonator acts as a frequency filter, strongly suppressing transmission at $\omega_\mathrm{rf} \neq \omega_n$. (b) Transmission spectra of the first three resonator modes close to their resonance frequencies. Bottom panel: fundamental $\lambda/2$-mode ($\omega_1/2\pi = 2.610\,\mathrm{GHz}$). Middle panel: λ-mode ($\omega_2/2\pi = 5.216\,\mathrm{GHz}$). Top panel: $3\lambda/2$-mode ($\omega_2/2\pi = 7.818\,\mathrm{GHz}$). The solid red line in each panel shows a Lorentzian fit to the transmission power spectrum. On resonance, the transmission is close to unity (0 dB; dashed gray lines), which is a characteristic of overcoupled resonators. The data was recorded with $P_\mathrm{out} = -40\,\mathrm{dBm}$.

setup operate between $2 - 8\,\mathrm{GHz}$. The power transmission is measured in a logarithmic scale, $10\log(P_\mathrm{in}/P_\mathrm{out})\,\mathrm{dB}$, where P_in and P_out are the powers at the in- and output ports of the VNA, respectively. According to Eq. (2.26) and Eq. (2.30), the quality factor of the nth resonator mode should scale as $Q_\mathrm{n}/Q_1 = 1/n$, where Q_1 refers to the fundamental $\lambda/2$-mode. Though we observe a decrease in Q_n/Q_1 with increasing n, our data lacks quantitative agreement. In particular, we observed that independent of the coupling capacitor geometry, the quality factor of the λ-mode (see Fig. 3.13 b, middle panel) is smallest. This behavior is most probably related to the specific geometry (and symmetry) of the meandering center conductor. However, for each resonator mode, the quality factor $Q_\mathrm{L} \approx Q_\mathrm{ext} = \omega_\mathrm{r}/\kappa$ is determined to be well above $5 \cdot 10^3$. This value relates to a maximum photon decay rate κ of roughly 1 MHz which is more than sufficient for many circuit QED applications. Figure 3.14 shows the measured quality factor Q_L as a function of the coupling capacitance C_κ. In the overcoupled regime, C_κ was increased by extending the length l_f of each finger ($l_\mathrm{f} = 74\,\mu\mathrm{m}$, $90\,\mu\mathrm{m}$ and $110\,\mu\mathrm{m}$ in Fig. 3.14). For some applications, however, it might be necessary to design CPW resonators with relatively low quality factors $Q_\mathrm{L} < 10^3$, e.g. for a fast cavity readout. Such strongly overcoupled resonators are most conveniently realized by increasing the number[5] of fingers [148, 175] instead of their length l_f.

In contrast, highly undercoupled resonators can be designed using gap capacitors as shown in Fig. 3.10 b. By increasing the gap width s_g it is possible to realize resonator modes with decay rates dominated by intrinsic losses. Figure 3.15 shows the transmission spectra

[5] Q_L scales inversely with the square of the number of fingers N assuming that $C_\kappa \propto N$

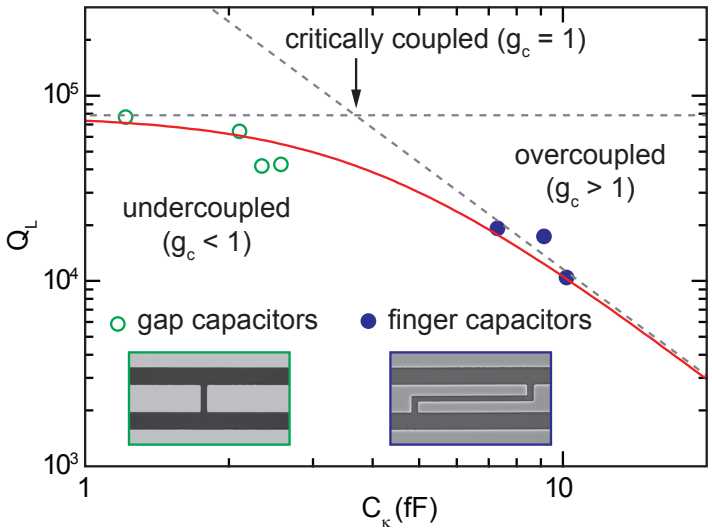

Figure 3.14: Measured loaded quality factor Q_L of the fundamental $\lambda/2$-mode as a function of C_κ. The data was recorded for a CPW resonator with $l = 23\,\mathrm{mm}$ at $T = 1.5\,\mathrm{K}$. The coupling capacitance C_κ was extracted numerically using FastCap. In general, the interdigital finger capacitors (blue filled circles) are suitable for the design of overcoupled ($g_\mathrm{c} > 1$) resonators, while undercoupled ($g_\mathrm{c} < 1$) resonators can be realized using gap capacitors (green circles). The solid red line visualizes Q_L calculated from Eqs. (2.29) and (2.31) while the dashed gray lines indicate the asymptotic behavior.

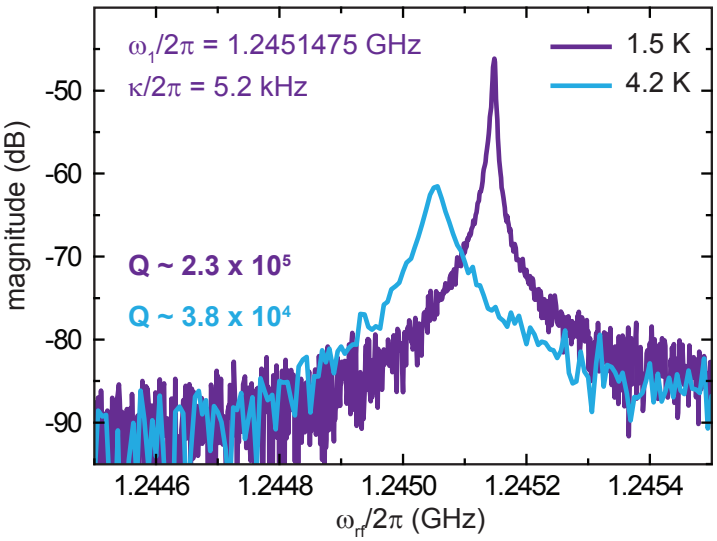

Figure 3.15: Transmission spectra of the $\lambda/2$-mode of an highly undercoupled resonator at $T = 4.2\,\mathrm{K}$ (light blue) and $T = 1.5\,\mathrm{K}$ (violet). The resonator with length $l = 48\,\mathrm{mm}$ and fundamental resonance frequency $\omega_1/2\pi = 1.245\,\mathrm{GHz}$ is coupled to the in- and output ports by gap capacitors (gap width $s_\mathrm{g} = 4\,\mu\mathrm{m}$). At $T = 1.5\,\mathrm{K}$ we extract a $Q_\mathrm{L} \approx Q_\mathrm{int}$ of $2.3 \cdot 10^5$. The strongly reduced transmission is a characteristic of undercoupled resonators.

and the measured quality factors $Q_\mathrm{L} \approx Q_\mathrm{int}$ of the fundamental $\lambda/2$-mode of an undercoupled CPW resonator. We observe a shift of ω_1 towards higher frequencies for decreasing temperature owing to the temperature dependence of the kinetic inductance L_kin. At $T = 1.5\,\mathrm{K}$ we measured a quality factor of $Q_\mathrm{int} \sim 2.3 \cdot 10^5$. We note, that this measurement was conducted at an input power corresponding to many thousands of photons on average. Therefore, dissipative two-level systems in the dielectric substrate (cf. section 2.3.4) are

saturated. A more detailed study on the power and temperature dependence of high-Q CPW resonators can be found in Refs. [147, 175].

Chapter 4

Characterization of flux qubits via dc-SQUID readout

Detecting the quantum state of a superconducting qubit can be achieved by several readout methods [60, 61, 102, 177–181]. In this chapter, we use a very common readout technique [64–67, 132], where the qubit state is determined by measuring the switching current of a nearby dc-SQUID. Simultaneous excitation of the qubit by microwave irradiation allows a reconstruction of the qubit transition frequency ω_q. In contrast to circuit QED experiments, no sophisticated microwave equipment is needed and therefore this measurement technique allows a relatively simple implementation and a large throughput.
The measurement technique relies on the fact, that the dc-SQUID's switching current depends in a oscillatory manner on the total flux Φ_{sq} threading its loop (see Fig. 2.4 in section 2.2.1). Here, Φ_{sq} is the sum of an externally applied flux bias and a small contribution from the qubit due to its finite inductance and the persistent current $\pm I_p$. Although the additional qubit-related flux contribution typically is very small ($\sim 10^{-3}\,\Phi_0$), it can be detected with a dc-SQUID inductively coupled to the flux qubit. Close to one of the qubit degeneracy points where the qubit's relative flux bias $\delta\Phi_x = \Phi_x - (n + 1/2)\Phi_0$ changes sign, I_p reverses direction. Consequently, sweeping the external flux close to $\delta\Phi_x \approx 0$ leads to a step-like structure – the so-called *qubit step* – superposed on the dc-SQUID signal.
Recording a qubit step under continuous microwave irradiation with fixed frequency ideally reveals a peak and a dip-like structure symmetrically located around $\delta\Phi_x = 0$. The peaks and dips result from microwave-induced transitions between the qubit ground $|g\rangle$ and first excited state $|e\rangle$ which have persistent currents with opposite sign. They occur at flux values for which $E_{ge} = \hbar\omega_s$, where E_{ge} reflects the energy difference between $|g\rangle$ and $|e\rangle$ and ω_s denotes the spectroscopy frequency. Measuring several qubit steps at different frequencies allows a reconstruction of the flux dependence of the qubit transition frequency $\omega_q(\delta\Phi_x)$. However, this spectroscopy technique is not suitable close to the qubit degeneracy point as $I_q = I_p\langle\hat{\sigma}_z\rangle \to 0$ for $\delta\Phi_x \to 0$ (see Fig. 2.8 b).
In the following, we describe the characterization procedure for flux qubits using an inductive dc-SQUID readout. Two cryogenic systems were available for measurements of Josephson junction devices. We will shortly address each cryostat's assets and drawbacks, a more detailed description can be found in Ref. [173, 182].

4.1 Switching current detection

A simplified measurement setup is shown in Fig. 4.1 a. For a fixed externally applied flux, the dc-SQUID is biased by a current source with a linearly increasing current I_{sq} while monitoring the amplified voltage across the SQUID. The principle of switching current detection is sketched in Figure 4.1 b. Since the switching to the voltage state is a statistical process based on quantum tunneling, 50-1000 switching events are typically recorded. The middle panel of Fig. 4.1 b illustrates the detection of a single switching event. Within a defined pulse sequence, I_{sq} is linearly increased with typically $0.1 - 0.2\,\mu A/ms$. When $I_{sq} \approx I_{sw}(\Phi_{sq})$, the SQUID switches to the voltage state. The voltage drop is detected by a threshold detector and a sample-and-hold circuit which allows to record the current value at which the switching occurred. After the switching event, the bias current is decreased to zero and the protocol can be repeated. Effectively, this yields a switching current histogram (see Fig. 2.5) with mean value I_{sw} for each flux value.
For a reliable readout, it is necessary to ensure that the SQUID is initialized in the zero-voltage state after a switching event was detected. For an unshunted SQUID this can be achieved by decreasing the bias current to zero. However, a highly underdamped SQUID (see Fig. 2.4 c) might remain in the voltage state even for zero bias current. Therefore, a short negative bias current should be applied after each current ramp to initialize the SQUID for the next measurement (see Fig. 4.1 b, middle panel). It is worthwhile men-

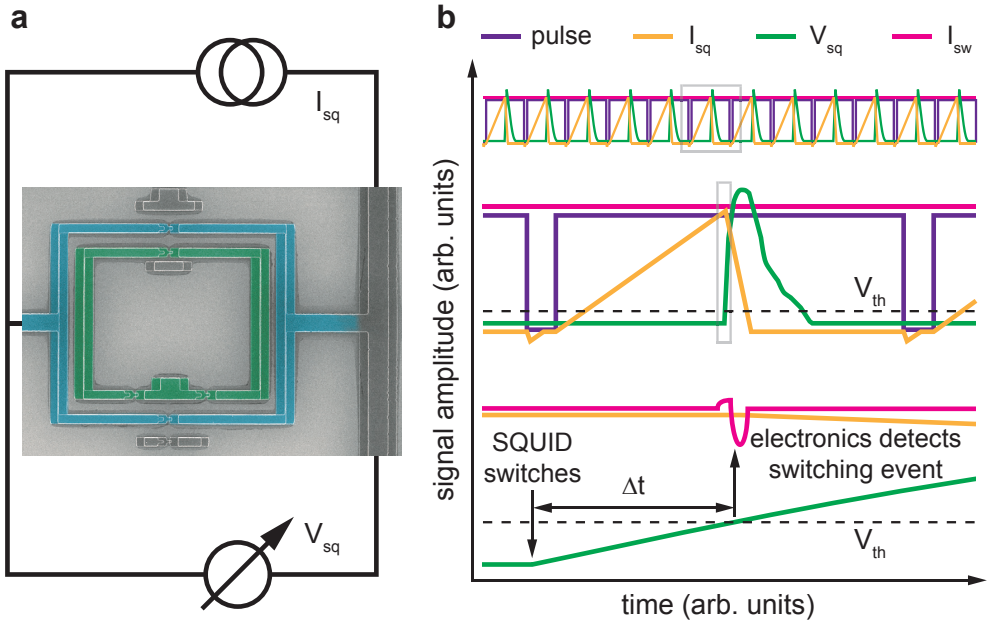

Figure 4.1: Experimental setup and measurement protocol. (a) Schematic of a simplified measurement setup for switching current detection. The voltage drop V_{sq} across the SQUID is monitored while biasing it with a dc current I_{sq}. (b) Principle of switching current detection. The signal amplitude is plotted as a function of time for three distinct time intervals. The gray boxes mark the areas magnified in subsequent panels. Top panel: schematic showing many consecutive detection cycles. Middle panel: single detection sequence. I_{sq} is linearly increased until the SQUID switches to the voltage state. The current value at which the voltage drop across the SQUID exceeds a threshold voltage V_{th} is detected as I_{sw}. Bottom panel: in order to avoid false negative detection events, V_{th} has to be adjusted accordingly while simultaneously minimizing the unavoidable time delay Δt.

tioning that the time difference Δt between the actual switching of the SQUID and the detection of this switching event (see Fig. 4.1 b, bottom panel) can be adjusted by varying the threshold voltage V_{th} of our electronics. In our experiments we adjust V_{th} to be large enough avoiding false negative detection events due to amplifier noise and small enough to not substantially distort I_{sw}. Typically Δt is of the order of $10 - 100\,\mu\mathrm{s}$ which leads to an increase of the measured I_{sw} of $1 - 10\,\mathrm{nA}$.

4.2 Initial characterization: ^{3}He refrigerator

The fridge used in the experiments presented in this section is based on evaporative cooling of condensed ^{3}He. It allows a fast cooldown within a few hours, however, the base temperature is limited to roughly 500 mK and microwave spectroscopy can not be performed due to space limitations and the consequential lack of a microwave coaxial line. Primarily, this cryostat was used to characterize the dc-SQUID and to detect the qubit step.
An image of the sample holder with four specimens is shown in Fig. 4.2 a. It consists of a printed circuit board (PCB) with copper contact pads and is screwed onto a copper block. 16 measurement lines are soldered to these contact pads which allows a characterization of up to four samples, each in a four-point configuration. After dicing, the individual specimen are glued onto the PCB using GE varnish and contacted by aluminum wire bonds[1]. The sample holder is then screwed to a copper rod and a magnet coil is fastened roughly 0.5 mm above the samples (see Fig. 4.2 b). After enclosing the sample holder with a cryoperm shield providing local magnetic shielding, the dip-stick is inserted into the ^{3}He insert

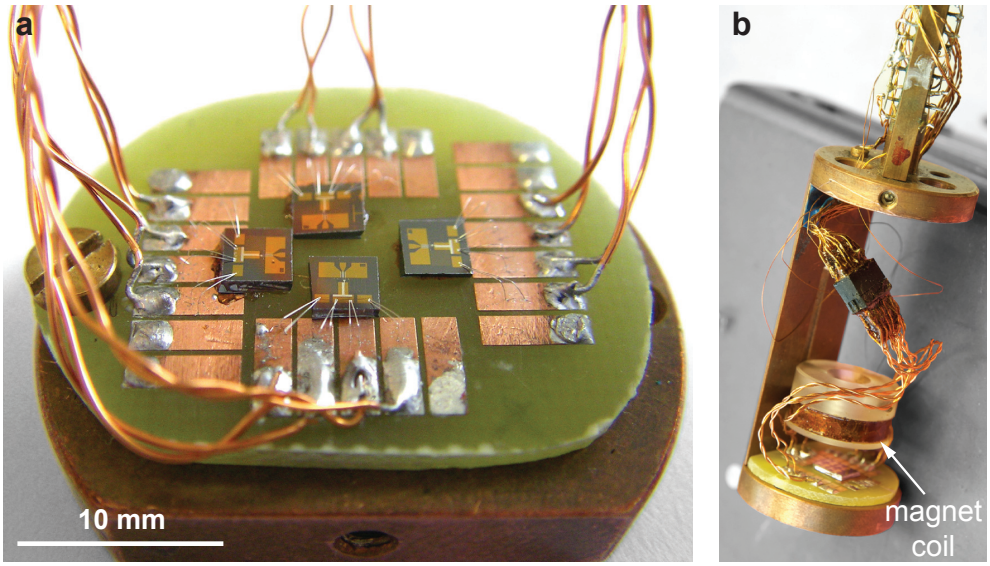

Figure 4.2: Sample mounting for low temperature measurements in a ^{3}He refrigerator. (a) After dicing, the individual samples are glued onto a printed circuit board and contacted via aluminum wire bonds. Each sample is measured in a four-point configuration. (b) After screwing the sample holder to the copper rod and fasten a small superconducting magnet coil, a cryoperm shield (not shown in the picture) enclosing the sample holder is attached.

[1]For that purpose, we use a manual thin-wire wedge bonder (F&K Delvotec). During the bonding procedure, all measurement lines and the person performing the bonding procedure should be grounded. Furthermore, it is advisable to clean the potentially oxidized copper contact pads mechanically using a glass fibre pencil prior to gluing the specimen.

which resides in a glass fibre reinforced cryostat with additional μ-metal shields. While the cryoperm and μ-metal shields provide sufficient[2] protection from static or slowly varying electromagnetic fields, they are ineffective at radio frequencies. For that purpose, the whole setup is located in a radio frequency shielded cabinet.

4.2.1 Current-voltage characteristic & switching current measurements

In order to get a first estimate of the Josephson junction properties, we measure the current-voltage characteristic (IVC) of the dc-SQUID. The IVC is recorded by biasing the readout SQUID with a dc current and sampling the time-averaged voltage drop across the SQUID. In the following, we will discuss a typical IVC of an unshunted SQUID at $\Phi_{\mathrm{sq}} = 0$ as shown in Fig. 4.3 b. Such a measurement allows determining important parameters like the normal resistance $R_{\mathrm{N}} = 139\,\Omega$ and the critical current $I_{\mathrm{c}} = 1.24\,\mu\mathrm{A}$. The critical current density $j_{\mathrm{c}} \sim 1.4\,\mathrm{kA/cm^2}$ can be calculated using the average area determined by SEM investigation of SQUID Josephson junctions similar in design and fabricated in the same run. From these values and with a specific capacitance of $c_{\mathrm{s}} \sim 100\,\mathrm{fF}/\mu\mathrm{m}^2$ we can estimate $E_{\mathrm{J}}/h \sim 310\,\mathrm{GHz}$ and $E_{\mathrm{C}}/h \sim 5\,\mathrm{GHz}$. This yields an $E_{\mathrm{J}}/E_{\mathrm{C}}$ ratio of roughly[3] 60 for a Josephson junction with area $A_{\mathrm{JJ}} \sim 0.04\,\mu\mathrm{m}^2$. The qubit's $E_{\mathrm{J}}/E_{\mathrm{C}}$ ratio has to be scaled accordingly by a factor β^2, if the area of one of the two regular Josephson junctions embedded in the qubit loop is βA_{JJ}. For the particular sample shown in Fig. 4.3 a, the scaling factor $\beta \sim 1$.

Furthermore, the gap voltage V_{gap} can be directly determined from the IVC. Here, $V_{\mathrm{gap}} \simeq 360\,\mu\mathrm{V}$ is close to the BCS value $V_{\mathrm{BCS}} = 2\Delta_{\mathrm{s}}/e = 3.52 k_{\mathrm{B}} T_{\mathrm{c}}/e = 364\,\mu\mathrm{V}$ which indicates a good quality of our aluminum thin films. For the calculation of V_{BCS} we used $T_{\mathrm{c}} = 1.2\,\mathrm{K}$ for the critical temperature of aluminum. The shape of the hysteresis strongly depends on the capacitance of the SQUID's Josephson junctions. In the case of an unshunted SQUID as shown in Fig. 4.3 a, the switching to the zero-voltage state occurs at a non-zero bias current. The IVC of a dc-SQUID with large area shunting capacitors (see Fig. 3.9) is discussed in the next section. Moreover, for decreasing currents below I_{c}, the SQUID shows a non-linear characteristic with additional structures. The subgap structure in Fig. 4.3 b most likely originates from a non-linear quasiparticle tunneling characteristic and non-equilibrium phenomena.

The flux dependence of the SQUID's switching current is shown in Fig. 4.3 c. The measured curve is close to the ideal $|\cos(\pi\Phi_{\mathrm{sq}}/\Phi_0)|$ dependence expected for a dc-SQUID for which the Josephson inductance dominates the geometric loop inductance (see Fig. 2.4 d). However, small step-like structures are visible (see Fig. 4.3 c, gray box) which originate from the additional flux contribution due to the presence of the qubit. The position of the qubit steps within the SQUID's cosine-shaped $I_{\mathrm{sw}}(\Phi_{\mathrm{sq}})$-pattern depends on the area ratio $A_{\mathrm{sq}}/A_{\mathrm{q}}$ of the two Josephson devices. Here, A_{sq} and A_{q} are the areas enclosed by SQUID and qubit loop, respectively. The flux-sensitivity of the SQUID is particulary low close to a maximum of I_{sw}. For this reason, we select an area ratio such that the qubit step is located at a position where $|\partial I_{\mathrm{sw}}/\partial\Phi_{\mathrm{sq}}|$ is large. A measurement with higher flux resolution in this region is shown in Fig. 4.3 d. The measurement clearly reveals the qubit

[2] Cryoperm and μ-metal are nickel-iron alloys. The magnetic permeability of cryoperm at cryogenic temperatures is comparable to that of μ-metal at room temperature ($\mu_{\mathrm{r}} \sim 10^4 - 10^5$).

[3] We note, that this estimation gives a lower bound of the $E_{\mathrm{J}}/E_{\mathrm{C}}$ ratio since the measured I_{c} depends on the temperature and on the effective filtering.

step superposed on the dc-SQUID signal which is in good approximation linear. The qubit degeneracy point $\delta\Phi_x = \Phi_x - 0.5\Phi_0 = 0$ is located at $\Phi_{sq} \approx 0.685\,\Phi_0$ which yields an experimentally determined area ratio of $A_{sq}/A_q \sim 1.37$, in very good agreement with the design value of 1.36 .

We note, that the presence of a qubit step in I_{sw} is not necessarily an indicator for a quantum two-level system suitable for further investigation by microwave spectroscopy. Figure 4.4 a and b show switching current histograms around $\delta\Phi_x = 0$ for two qubits with a substantially different E_J/E_C ratio. While Fig. 4.4 a reflects the gradual change of sign of $I_q = I_p\langle\hat{\sigma}_z\rangle$, the data plotted in Fig. 4.4 b lacks evidence for a superposition state at $I_q = 0$. Here, the tunnel barrier between the minima in the qubits double well potential is

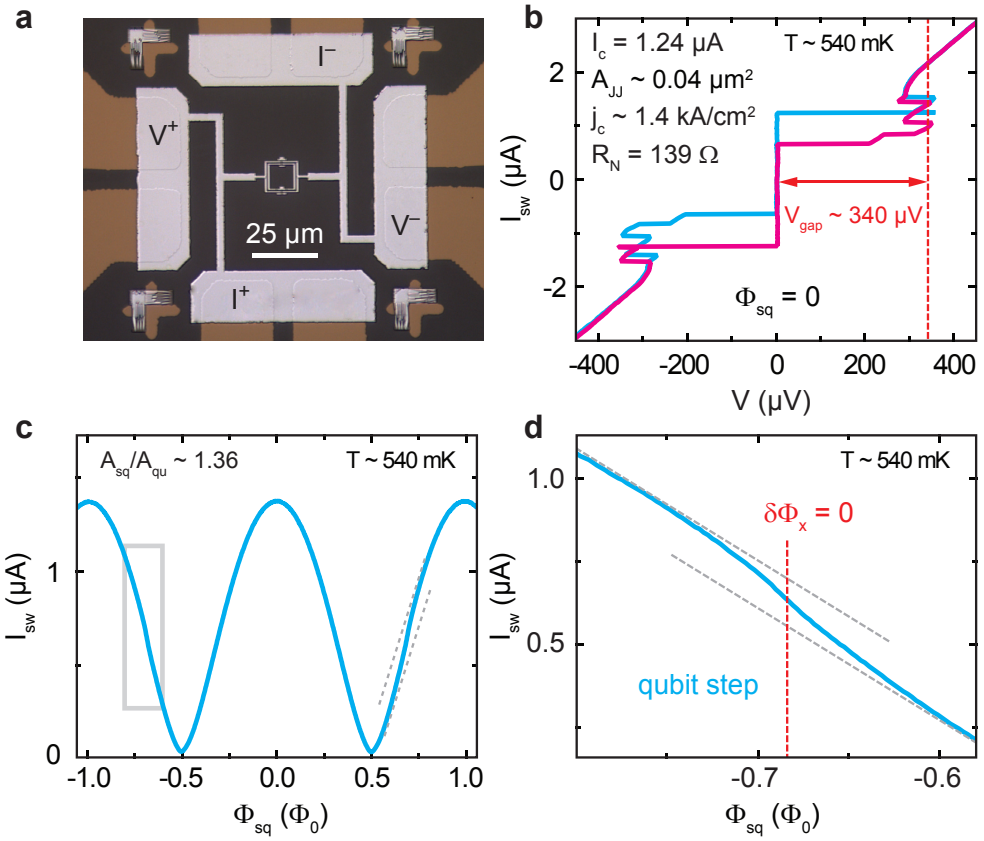

Figure 4.3: Initial characterization of an unshunted readout SQUID with an inductively coupled flux qubit. (a) Microscope image of the device. The measurement is performed in a four-point configuration. (b) Typical current-voltage characteristic (IVC) of an unshunted SQUID with slightly overdamped Josephson junctions. Following Fig. 2.4 c, increasing (decreasing) current is depicted light blue (magenta). For $\Phi_{sq} = 0$, the switching current $I_{sw} \approx I_c$. The normal resistance R_N is given by the inverse of the slope in the ohmic region. The gap voltage V_{gap} can be directly determined from the voltage drop across the SQUID. (c) dc-SQUID's $I_{sw}(\Phi_{sq})$ curve. The gray box marks the area where the first qubit step appears. The position of the qubit step in the $I_{sw}(\Phi_{sq})$-pattern can be estimated from the designed area ratio A_{sq}/A_q. The gray dashed lines are a guide to the eye highlighting the qubit step for positive Φ_{sq}. (d) Magnified view of the area marked by the gray box in (c). The qubit step is clearly visible (gray broken lines: guide to the eye). At the qubit degeneracy point $\delta\Phi_x = 0$ (dashed red line), the qubit's ground and excited state are symmetric and antisymmetric superpositions of persistent current states with opposite sign, yielding zero net current. From the position of the center of the qubit step, we calculate $A_{sq}/A_q \sim 1.37$ in good agreement with the design value.

too high and broad, leading to a vanishing tunnel matrix element. This can be caused by a unfortunate E_J/E_C ratio, either due to a large critical current density j_c and/or large areas of the qubit's Josephson junctions. In the picture of a phase particle in the qubit's double well this corresponds to a large mass and therefore a low tunneling matrix element. However, both data sets would yield a smooth qubit step (see Fig. 4.4 c) when computing I_{sw} as the mean value for each histogram.

According to Eq. (2.15), the qubit's energy level splitting between the ground and the first excited state E_{ge} is a function of $\epsilon \equiv \epsilon(\Phi_x) = 2I_p\delta\Phi_x$ and Δ. The latter denotes the qubit's level splitting at $\delta\Phi_x = 0$. In principle, Δ and ϵ could be reconstructed from the shape and the slope of the qubit step itself [183]. For a reasonable fit, the qubit step has to be recorded for several temperatures and in particular for temperatures $T \ll \Delta/k_B \approx 50 - 300\,\mathrm{mK}$. However, in the following sections we will determine Δ and ϵ by spectroscopy. Although the measurement principle is straightforward, the experiments can be very time consuming. The need for lower temperatures requires a more complicated cryogenic setup. Compared to the ^{3}He cryostat, roughly 30 hours have to be invested until the fridge reaches a stable base temperature of approximately 30 mK. Thus, only pre-characterized and promising samples (in terms of proper E_J/E_C ratios) should be investigated spectroscopically.

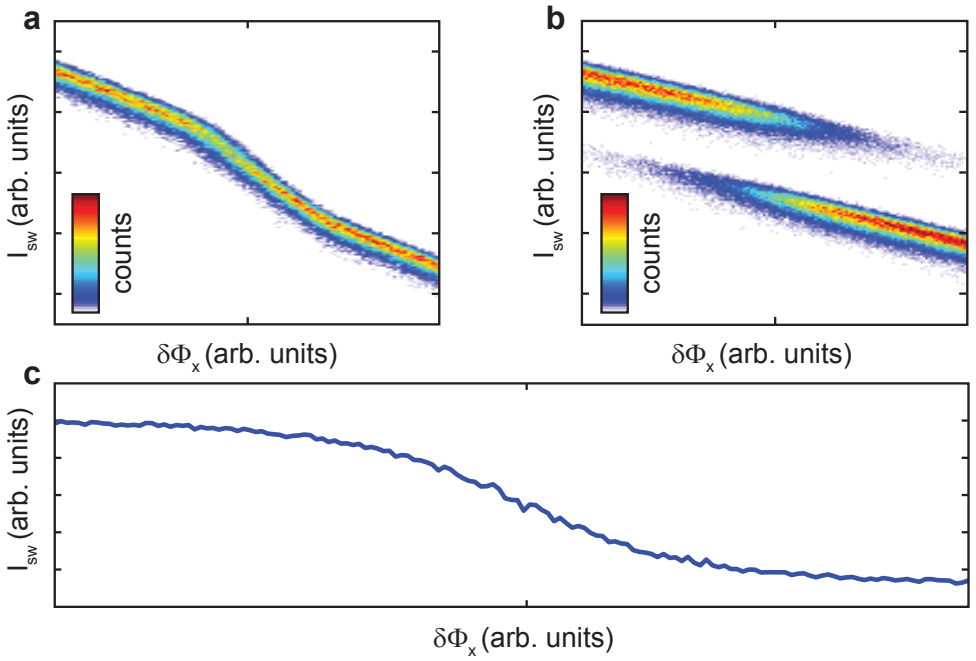

Figure 4.4: Color-coded switching current histograms for qubits with distinct E_J/E_C ratios. (a) Smooth qubit step showing evidence for superposition states at $\delta\Phi_x = 0$ where $I_q = I_p\langle\hat{\sigma}_z\rangle = 0$. (b) Switching current histograms for a qubit with $E_J/E_C > 200$. In the picture of the qubit's double-well potential, the tunneling barrier is too high and broad. Therefore, the wavefunctions corresponding to the persistent current states $|\pm I_p\rangle$ do not overlap sufficiently. (c) I_{sw} computed from the data set shown in (b). The linear SQUID contribution was subtracted.

4.3 Spectroscopy fridge: ^{3}He/^{4}He dilution refrigerator

The experiments presented in the remainder of this chapter were performed in the ^{3}He/^{4}He dilution refrigerator shown in Fig. 4.5 a. This homemade fridge was designed for the microwave spectroscopy of aluminum and niobium-based Josephson junction devices. During this thesis, the complete sample stage, the sample holder (see Fig. 4.5 b), the microwave coaxial cable and the cryogenic filtering were renewed. Especially the modification of sample holder and stage resulted in a much simpler mounting procedure compared to the previous setup. However, the fridge is not suited for time-domain characterization of Josephson junction devices owing to the limited space available. Such experiments require large bandwidth measurement lines and ideally a separate microwave line for every single sample. The compact sized dilution unit used here is optimized for large throughput. In our setup, up to four specimen can be irradiated by microwaves which are applied by the dismantled end of an superconducting coaxial line (see Fig. 4.5 c). This antenna – located approximately 2 mm above the sample plane – is thermally anchored at several temperature stages. The low bandwidth bias and readout lines are severely filtered against

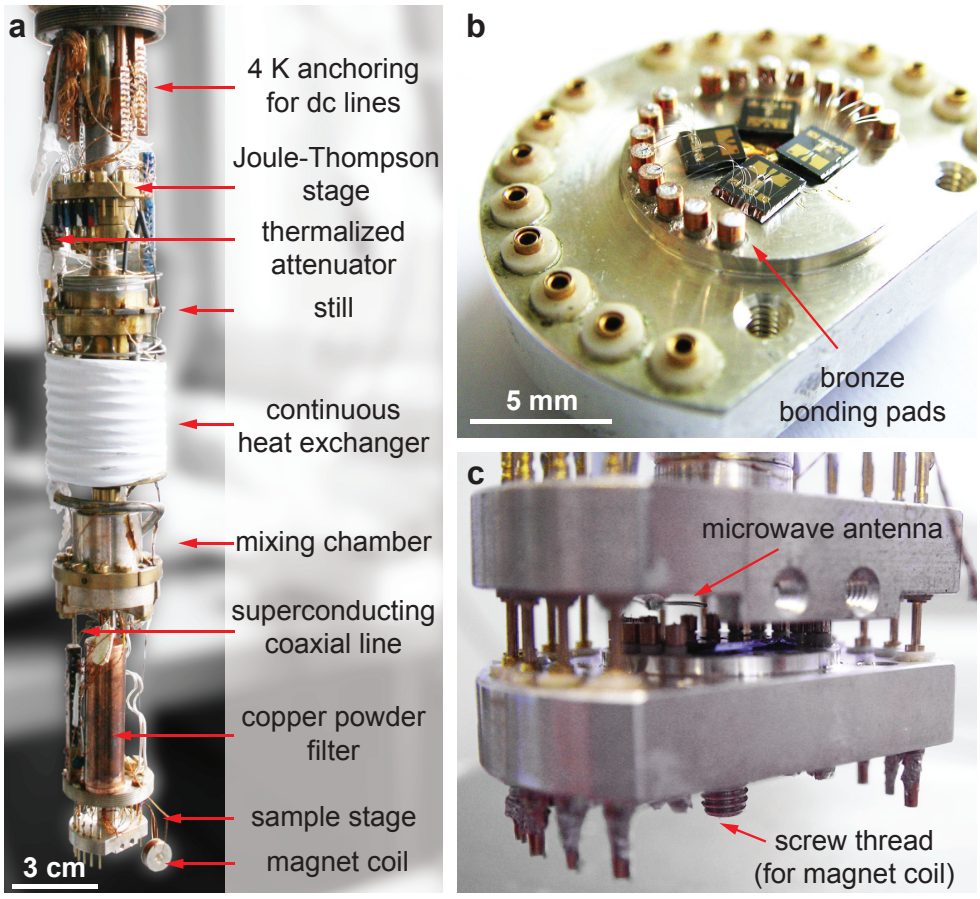

Figure 4.5: ^{3}He/^{4}He-fridge and sample mounting. (a) Image of the ^{3}He/^{4}He dilution unit used for qubit microwave spectroscopy. Important components of the setup are indicated. A more detailed description of the cryogenic hardware is found in Ref. [182]. (b) Renewed 'plug & play' sample holder with four bonded specimens. The bonding wires are additionally covered with silver glue for mechanical stability at the bronze pads. (c) Mounted sample holder. The dismantled end of the superconducting coaxial cable roughly 2 mm above the samples serves as microwave antenna.

high-frequency noise by stainless steel powder filters (cut-off frequency $\omega_c/2\pi \approx 2\,\mathrm{GHz}$). Details on the properties and the fabrication details of these particular filters can be found in Ref. [171]. Additional LCR-filters ($\omega_c/2\pi \approx 100\,\mathrm{kHz}$) and commercially available filters (Mini-Circuits, BLP 1.9 MHz+, $\omega_c/2\pi \approx 1.9\,\mathrm{MHz}$) complete the filtering at room temperature.
For the magnet coil we used a 100 µm thick single filament Nb-Ti-wire in a Cu-matrix. The coil body was fabricated of silver and can be fastened by a screw in a recess below the sample holder (see Fig. 4.5 c). The coil wire was soldered to the 4 K anchoring and thermalized at various temperature stages and in particular along the full length of the spiral continuous heat exchanger.

4.3.1 Preliminary measurements

Prior to spectroscopy measurements an IVC and - more importantly - the $I_{sw}(\Phi_{sq})$-curve have to be recorded. Figure 4.6 a and b show the IVC for a unshunted and a shunted (underdamped) SQUID, respectively. The latter has a more pronounced hysteresis owing to the additional shunt capacitors in parallel to the SQUID junctions. Since the dilution fridge provides a superior filtering and a lower base temperature compared to the ^{3}He refrigerator, the measured I_c at $\Phi_{sq} = 0$ is typically $20 - 40\,\%$ higher than at 540 mK. Analog to the initial characterization in the ^{3}He fridge, the qubit step has to be located within the oscillatory SQUID signal (see Fig. 4.6 c). Therefore, the area ratio between SQUID and qubit has to be known. The conversion factor between magnet coil current and a single flux quantum can be inferred from the Φ_0-periodicity of the SQUID.

4.4 Qubit microwave spectroscopy

In this section, we determine the qubit transition frequency $\omega_q \equiv \omega_q(\delta\Phi_x) = E_{ge}/\hbar$ by continuous-wave (cw) microwave spectroscopy [66,138]. To this end, the qubit is irradiated with a spectroscopy tone of fixed frequency ω_s while recording the qubit step in a region of roughly $\pm 15\,\mathrm{m}\Phi_0$ around $\delta\Phi_x = 0$. For flux values where the resonance condition $\omega_s \approx \omega_q$ is fulfilled, population of the excited state leads to a change in $I_q = I_p\langle\hat{\sigma}_z\rangle$ (see Fig. 2.8). Therefore, a peak and a dip appear symmetrically around $\delta\Phi_x = 0$ in the $I_{sw}(\delta\Phi_x)$ curve. Repeating such a measurement for various spectroscopy frequencies ω_s allows a reconstruction of ω_q. The experimental results of this protocol are summarized in Figure 4.7 for two different specimen. In both cases, the readout SQUID was highly underdamped ($C_{sh} \sim 10\,\mathrm{pF}$) and each qubit step is recorded with a flux resolution of roughly $0.05\,\mathrm{m}\Phi_0$. The qubit steps shown in Fig. 4.7 a and b were recorded with different power levels ranging from $-25\,\mathrm{dBm}$ up to $-13\,\mathrm{dBm}$ referred to the output of our microwave source. In general, the visibility of the peaks and dips within each qubit step depends in a complex manner on the applied power, the SQUID-qubit interaction and of course on the spectroscopy frequency ω_s. Figure 4.7 c and d show the frequency-dependent peak/dip positions extracted from the measurements in Fig. 4.7 a and b, respectively. A numerical fit to Eq.(2.15) yields the qubit parameters Δ and $\epsilon(\delta\Phi_x) = 2I_p\delta\Phi_x$, thus allowing the reconstruction of the hyperbolic $\delta\Phi_x$-dependence of the qubit transition frequency. Please note, that in the expression for ϵ in Fig. 4.7 c and d, $\delta\Phi_x$ is given in units of $\mathrm{m}\Phi_0$.
The significant deviation of the peak/dip positions from the asymptotic limit (see gray

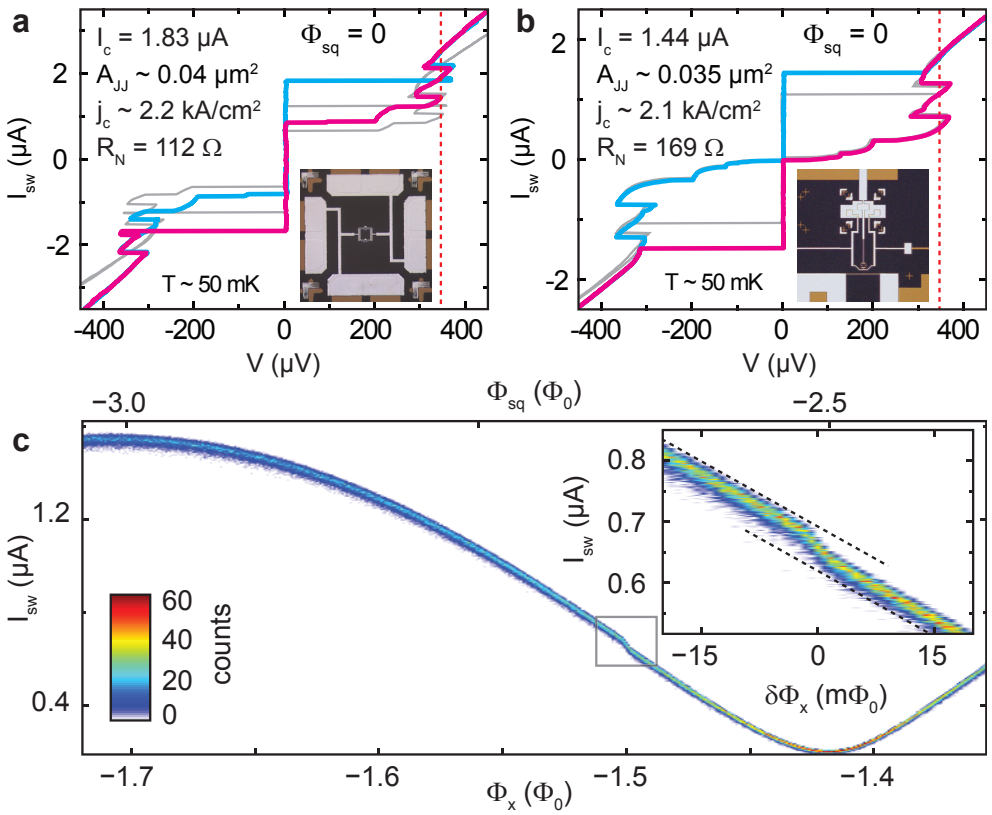

Figure 4.6: Preliminary characterization steps at 50 mK. (a) IVC for an unshunted SQUID at $\Phi_{sq} = 0$. The IVC for increasing (decreasing) bias current is plotted light blue (magenta). The gray line depicts the measurement at roughly 540 mK (see also Fig. 4.3 b). Due to the lower temperature and the improved filtering, a larger critical current is measured. The gap voltage ($V_{gap} \approx 340\,\mu V$) is indicated by the red dashed line. An optical microscope image is shown in the inset. (b) Same as in (a) but for a dc-SQUID shunted by additional capacitors (area $\sim 25 \times 25\,\mu m^2$, capacitance $C \approx 10$ pF). (c) Color-coded switching current histograms as a function of the external flux Φ_x threading the qubit loop. The data shows the qubit step at $\Phi_x = -1.5\,\Phi_0$ and roughly half an oscillation period of the SQUID. The top axis labels the flux Φ_{sq} in the SQUID loop. For this particular sample $A_{sq}/A_q \sim 1.76$. Inset: area marked by the gray box. The graph shows I_{sw} as a function of the qubit's relative flux bias $\delta\Phi_x$. The dashed black lines are guides to the eye.

lines in Fig. 4.7 c and d) near $\delta\Phi_x = 0$ is a direct consequence of the repulsion of the qubit's two lowest energy levels. From I_p and Eq.(2.14), a lower bound for the scaling factor α of the small Josephson junction in the qubit loop can be calculated analytically[4]. In contrast to the adiabatic-shift pulse method [85,87,140], our measurement scheme does not allow to determine Δ directly as the expectation value for the persistent current – for both, ground and excited state – is zero at $\delta\Phi_x = 0$. Moreover, the visibility of the peaks and dips in our measurements is virtually zero in a region $\pm 2\,m\Phi_0$ around the qubit degeneracy point, i.e. for spectroscopy frequencies close to Δ/h. Even for $\omega_s/2\pi \approx 2\Delta/h$, the peaks and dips are hard to identify (see lowest trace in Fig. 4.7 b) in comparison to higher spectroscopy frequencies.

[4]For the calculation of α, the critical current of a qubit junction has to be known. I_c cannot be determined directly, however, it can be estimated from the dc-SQUID's current-voltage characteristic.

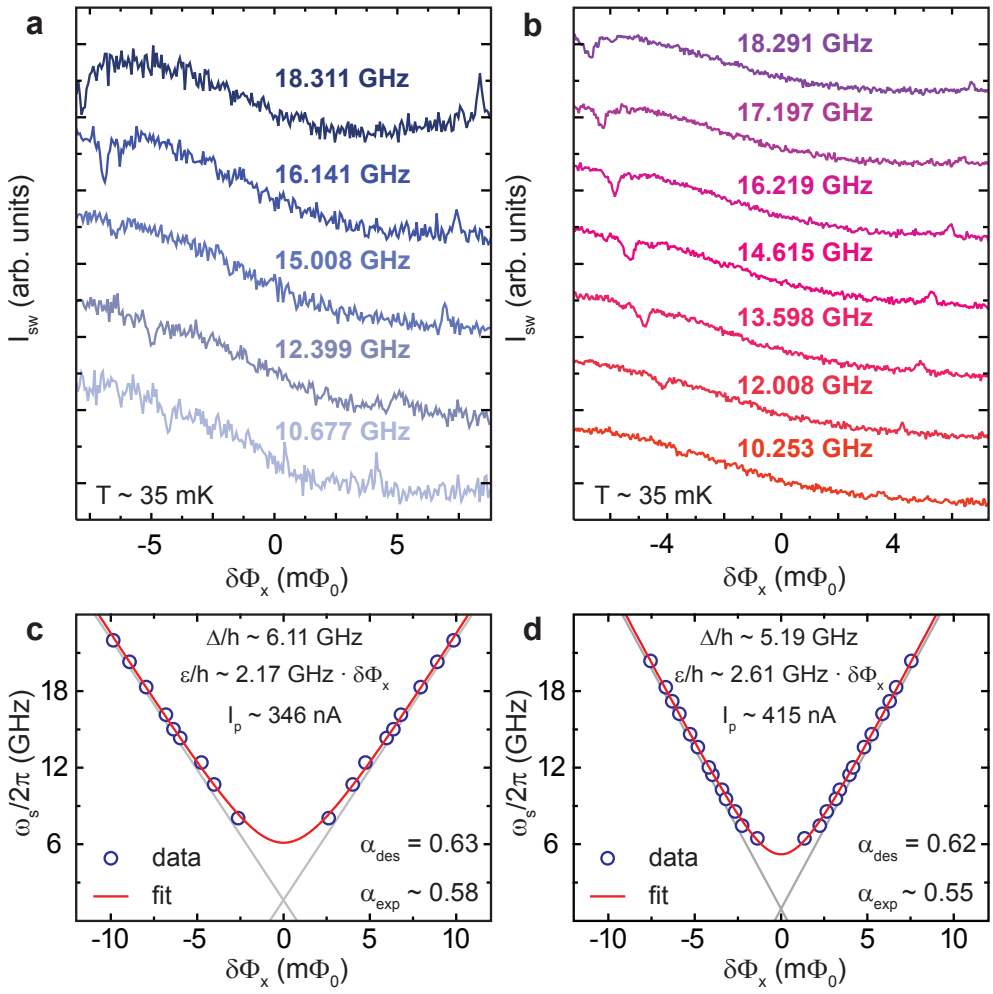

Figure 4.7: Qubit microwave spectroscopy and reconstruction of the qubit transition frequency ω_q. (a) and (b) Qubit step under continuous microwave irradiation for different spectroscopy frequencies $\omega_s/2\pi$. Symmetrically around $\delta\Phi_x = 0$ a peak and a dip appear. The background SQUID signal is subtracted and the traces are offset by arbitrary values for clarity. (c) and (d) Measured peak and dip positions (blue circles) as a function of $\delta\Phi_x$. The red line is a numerical fit to Eq.(2.15) and the gray lines denote the asymptotic limit $\epsilon(\delta\Phi_x) \gg \Delta$. The calculated α_{exp} is in reasonable agreement with the CAD design value α_{des}.

4.4.1 Multi-photon transitions

An atom exposed to a sufficiently intense radiation field can absorb several incident photons if the energy difference between the states is equal to the sum of the involved photon frequencies [184]. Multi-photon transitions appear in a large number of atomic and molecular systems and on different energy scales. In systems of artificial atoms at microwave frequencies, multi-photon resonances have been observed in a wide range of experiments [58,142,185–189]. In this section we will shortly address multi-photon resonances in a coupled qubit-SQUID system. This topic will be discussed more thoroughly in section 5.5.2 for a circuit QED system operating in the strong coupling limit.

The device discussed here was the first one where our spectroscopic data (see Fig. 4.8) suggested a substantial qubit energy gap $\Delta \gg k_B T \approx h \cdot 1\,\mathrm{GHz}$ at $T \sim 50\,\mathrm{mK}$. The SQUID's IVC and $I_{sw}(\Phi_{sq})$-dependence for $T \sim 540\,\mathrm{mK}$ as well as an optical image of our sample are shown in Fig. 4.3. It consists of a qubit with a loop area of $10\,\mathrm{x}\,10\,\mu\mathrm{m}^2$ coupled to

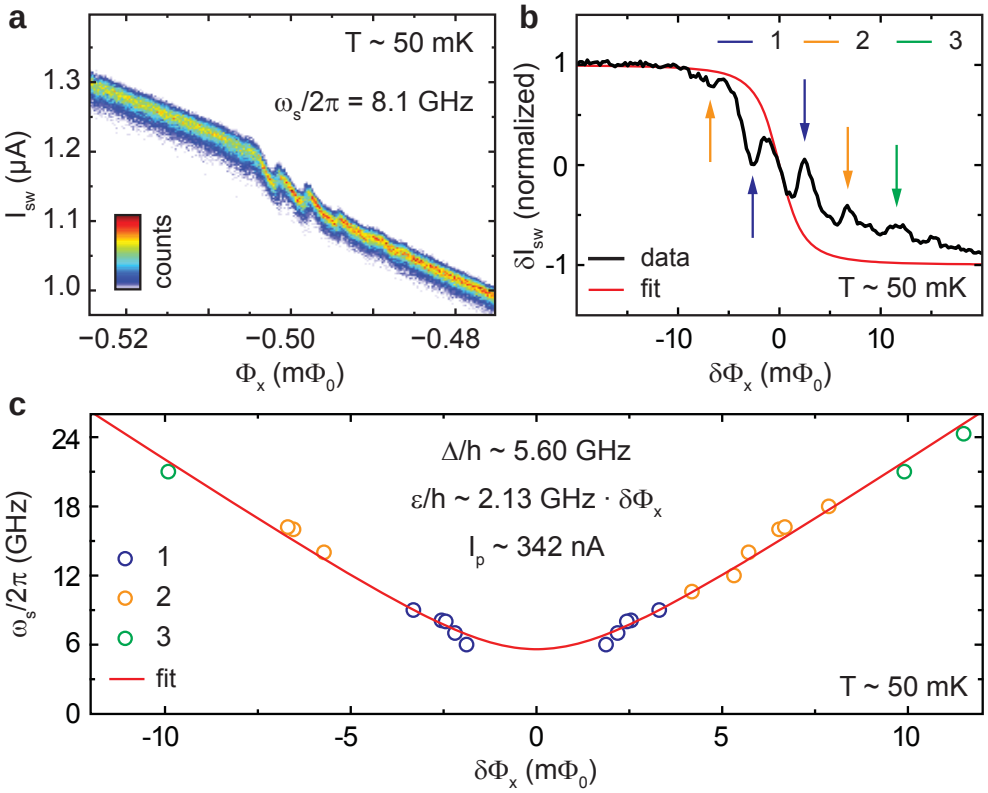

Figure 4.8: Qubit spectroscopy data. (a) dc-SQUID switching current histograms as a function of the flux Φ_x threading the qubit loop. The data is recorded close to the qubit degeneracy point $\Phi_x = -0.5\,\Phi_0$ and under continuous microwave irradiation with frequency $\omega_s/2\pi = 8.1\,\mathrm{GHz}$. (b) Normalized qubit contribution to the SQUID's I_{sw} as a function of the qubits relative flux bias $\delta\Phi_x$. The peaks and dips highlighted by colored arrows reflect n-photon transitions (blue: $n = 1$, orange: $n = 2$, green: $n = 3$) which occur when $\omega_q \approx n \cdot \omega_s$. The red line shows the theoretically expected curve for δI_{sw} [183] without microwave irradiation and with the parameters extracted from the data in (c). (c) Qubit spectroscopy data including data points from multi-photon resonances. A numerical fit (red solid line) to Eq.(2.15) yields $\Delta/h = 5.60\,\mathrm{GHz} \gg k_B T/h$.

an unshunted dc-SQUID. For a large amplitude microwave drive we observed additional peak/dip structures in our spectroscopic data for certain frequencies (see Fig. 4.8 a and b). These resonances could be attributed to multi-photon transitions which occur at flux positions where the flux-dependent qubit transition frequency ω_q equals an integer multiple of ω_s. Figure 4.8 b shows the normalized qubit contribution to the dc-SQUID switching current δI_{sw} as a function of the relative flux bias $\delta\Phi_x$. We observed resonant peaks and dips of up to three-photon processes for $\omega_s/2\pi = 7\,\mathrm{GHz}$. Owing to the large amplitude spectroscopy tone, the qubit is saturated and the probability of finding it in the ground or excited state is close to 1/2. Hence, the peak and dip associated with a single-photon excitation of the qubit approaches $\delta I_{sw} = 0$.

Compared to the measurements shown in Fig. 4.7 a and b, the peaks and dips might be significantly power broadened. However, due to the moderate quality of our data, possible power broadening could not be resolved. In general, the widths of the multi-photon absorption peaks and dips should scale as Bessel functions with arguments given by the ratio of the driving field strength to the frequency of the photons [185]. A detailed analysis would allow to estimate the relaxation $T_{r,n}$ and dephasing $T_{\varphi,n}$ times of the nth photon

absorption process. Figure 4.8 c shows the one-, two- and three-photon spectroscopy data. For the qubit we find a transition frequency of $\Delta/h \sim 5.60\,\mathrm{GHz}$ at $\delta\Phi_\mathrm{x} = 0$. We note that a more conservative fit including exclusively the one-photon data yields a substantially lower $\Delta/h = 4.08\,\mathrm{GHz}$ and $I_\mathrm{p} = 412\,\mathrm{nA}$.

4.4.2 Sideband transitions

In radio transmission, frequency modulation (FM) and amplitude modulation (AM) are used to encode audio frequency information on a much higher frequency electromagnetic wave, usually referred to as the carrier wave. Either form of modulation produces frequencies – the so-called *sidebands* – which are the sum and difference of the carrier and the modulation frequency. In this section we will spectroscopically investigate an inductively coupled qubit-oscillator system. For sufficiently large driving amplitudes, we resolve additional resonances that correspond to sidebands of the modulated qubit transition frequency.

The electromagnetic environment of the qubit consists of the readout dc-SQUID and a lumped element LC-circuit. An optical microscope image and the equivalent circuit diagram are shown in Fig. 4.9 a and b, respectively. Figure 4.9 c shows the Norton equivalent of the voltage-driven circuit displayed in Fig. 4.9 b. It consists of an ideal current source in parallel to the impedance Z_{LC} of the LC-resonator and the inductance of the dc-SQUID L_sq. The latter is dominated by the inductance of the Josephson junctions embedded in the SQUID loop. An equivalent circuit of Z_{LC} is depicted in Fig. 4.9 d. We now turn to the spectroscopic response of our coupled qubit-oscillator system. Figure 4.10 a shows the

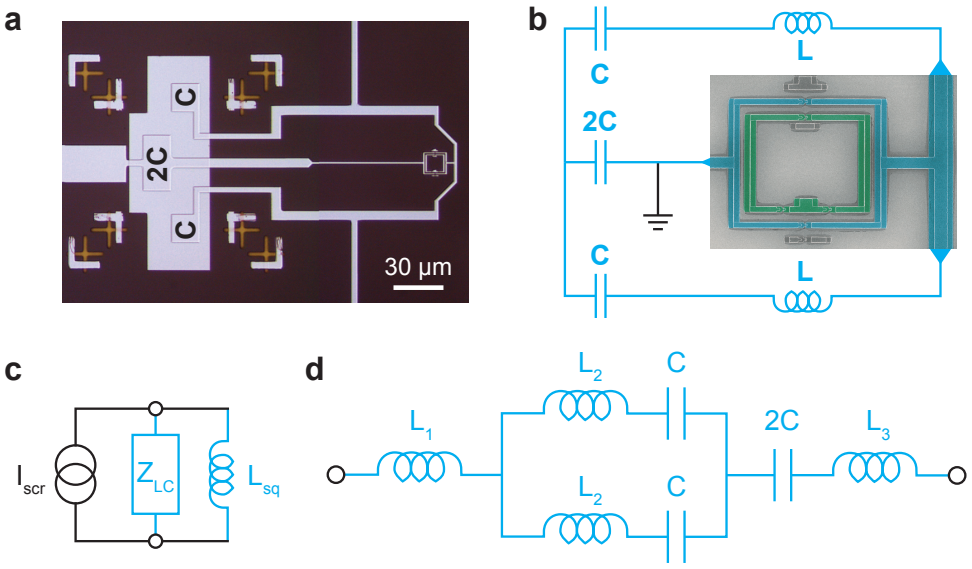

Figure 4.9: Electromagnetic environment of the flux qubit. (a) Optical microscope image of the relevant circuitry. The flux qubit is surrounded by the dc-SQUID which in turn is coupled to a lumped element LC-resonator. (b) Equivalent circuit with scanning electron microscope image of the qubit and the readout SQUID. The three shunting capacitors and the self-inductance of the aluminum leads form a resonant circuit with resonant frequency $\omega_\mathrm{r} = 1/\sqrt{LC}$. (c) Norton equivalent of the circuit shown in (b). The total impedance is given by the parallel combination of the impedance Z_{LC} and the total SQUID inductance L_sq. (d) Equivalent circuit of Z_{LC}.

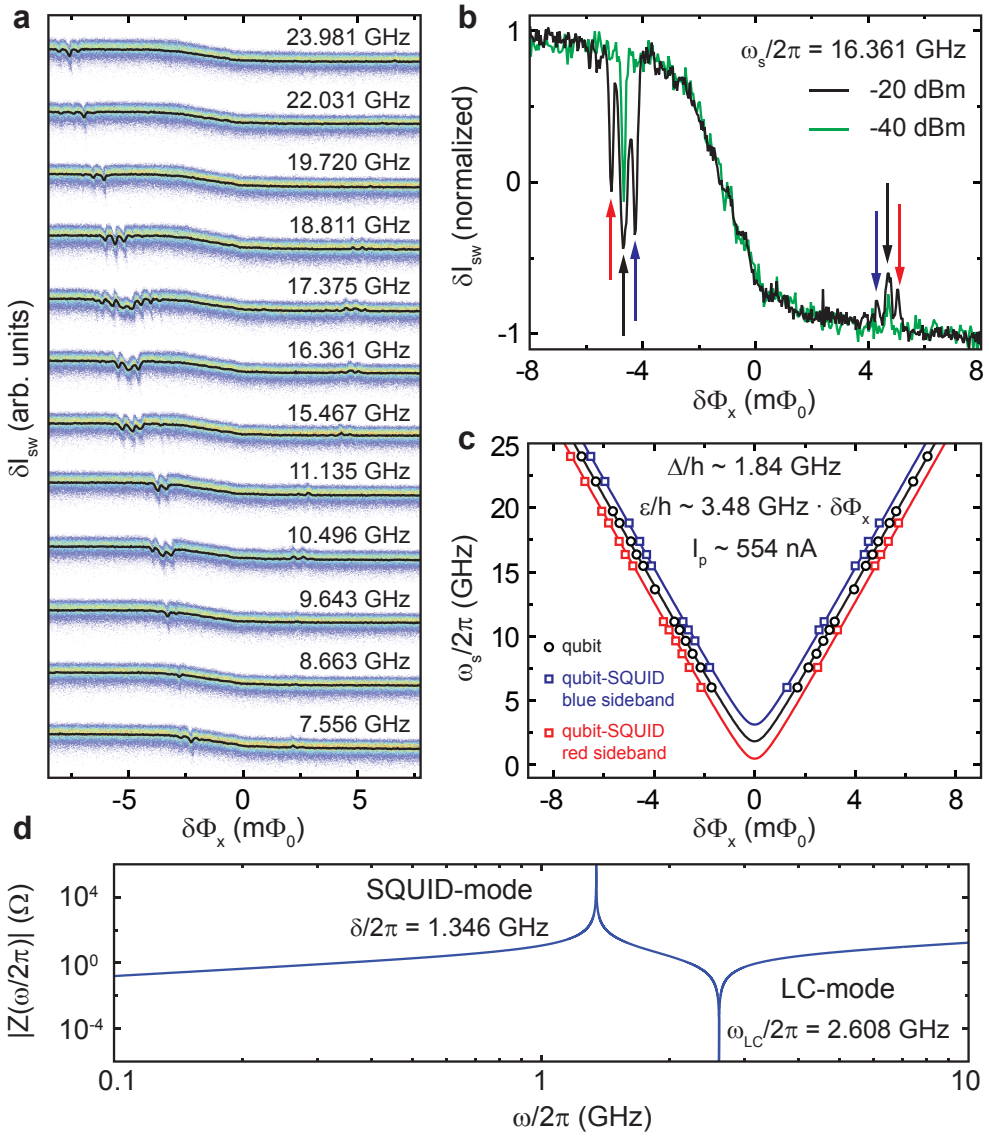

Figure 4.10: Spectroscopic response and resonant modes of the qubit environment. (a) Qubit contribution δI_{sw} after subtraction of the SQUID background under continuous microwave irradiation for various ω_{s}. (b) Normalized δI_{sw}-curve for $\omega_{\mathrm{s}}/2\pi = 16.361\,\mathrm{GHz}$. At large microwave powers (black) a multiplet of resonances are visible. The additional peaks/dips which were absent in the low power measurement (green) are resonantly driven sidebands of the coupled qubit-oscillator system (black arrow: bare qubit, ω_{q}; blue arrow: blue sideband, $\omega_{\mathrm{q}} + \delta$; red arrow: red sideband, $\omega_{\mathrm{q}} - \delta$) (c) Qubit spectroscopy data including the first blue and red sideband transitions (colored squares) as well as the bare qubit data (black circles). The latter was extracted from the low power measurement. (d) Absolute value of the total impedance for the calculated inductances of our circuit. The sidebands observed in (a)-(c) are attributed to the SQUID-mode at $\delta/2\pi = 1.346\,\mathrm{GHz}$.

qubit contribution δI_{sw} to the SQUID's switching current as a function of $\delta\Phi_{\mathrm{x}}$ and for various spectroscopy frequencies $\omega_{\mathrm{s}}/2\pi$. The data was recorded with a microwave power of $-20\,\mathrm{dBm}$ at the output of the generator. For specific frequencies, multiplets consisting of $3-7$ equidistant dips/peaks can be identified. In Fig. 4.10 b the normalized $\delta I_{\mathrm{sw}}(\delta\Phi_{\mathrm{x}})$ trace for $\omega_{\mathrm{s}}/2\pi = 16.361\,\mathrm{GHz}$ is shown for two different power levels. From the low power measurement, the central peak/dip of the high-power multiplets can be associated with the bare qubit transition frequency $\omega_{\mathrm{q}}/2\pi$. However, the resonances to the left and right

of the central peak/dip correspond to resonant transitions of the combined qubit-oscillator system. They occur at flux values for which the spectroscopy tone is resonant with

$$\omega_{\mathrm{bsb}} = \omega_{\mathrm{q}} + \delta_{\mathrm{bsb}} \quad \text{and} \quad \omega_{\mathrm{rsb}} = \omega_{\mathrm{q}} - \delta_{\mathrm{rsb}} \,. \tag{4.1}$$

Here, ω_{bsb} and ω_{rsb} denote the blue and red sideband transition frequencies, respectively,. We determine the frequency shifts δ_{bsb} and δ_{rsb} by first fitting the bare qubit spectroscopy data obtained from low power measurements to Eq.(2.15) which yields $\Delta/h = 1.84\,\mathrm{GHz}$ and $\epsilon/h = 3.48\,\mathrm{GHz} \cdot \delta\Phi_{\mathrm{x}}$ (see Fig. 4.10 d). From a separate fit to Eq.(4.1) we then extract $\delta_{\mathrm{bsb}}/2\pi = 1.279\,\mathrm{GHz}$ and $\delta_{\mathrm{rsb}}/2\pi = 1.411\,\mathrm{GHz}$. These values are in good agreement with the peak/dip distances that were observed in multiplets with a larger number of resonances (e.g. δI_{sw} trace for $\omega_{\mathrm{s}}/2\pi = 17.375\,\mathrm{GHz}$). In the following we assume $\delta_{\mathrm{bsb}} \approx \delta_{\mathrm{rsb}}$ in agreement with the experimental error and relate the frequency shift $\delta = (\delta_{\mathrm{bsb}} + \delta_{\mathrm{rsb}})/2 = 2\pi \cdot 1.345\,\mathrm{GHz}$ to a single resonant mode present in our system.
In general, the resonant modes of the circuit shown in Fig. 4.9 c are determined by the minima and maxima of the total impedance

$$Z(\omega) = \left(\frac{1}{Z_{LC}(\omega)} + \frac{1}{i\omega L_{\mathrm{sq}}} \right)^{-1} \quad . \tag{4.2}$$

Figure 4.10 d shows the absolute value of $Z(\omega)$ for $L_1 \approx 8\,\mathrm{pH}$, $L_2 \approx 200\,\mathrm{pH}$ and $L_3 \approx 115\,\mathrm{pH}$. These values were estimated using *FastHenry*. Furthermore, we used $L_{\mathrm{sq}} \approx 615\,\mathrm{pH}$ which we estimated from the dc-SQUID's IVC and $I_{\mathrm{sw}}(\Phi_{\mathrm{sq}})$-pattern [138]. Since the value of the SQUID's shunt capacitor represent the quantity with the largest uncertainty, we used C as free parameter. In the relevant frequency range and for $C = 16.7\,\mathrm{pF}$, the spectrum in Fig. 4.10 d shows two prominent resonances[5]. While the LC-circuit supports a single resonant mode with frequency $\omega_{\mathrm{LC}}/2\pi = 1/2\pi\sqrt{LC} = 2.608\,\mathrm{GHz}$ a second mode – which we will call SQUID-mode – is present at a frequency $\delta/2\pi = 1.346\,\mathrm{GHz}$.
The qubit transition frequency is shifted by $\pm\delta$ (see Fig. 4.10 c), resulting in the blue and red sidebands which we observe in our spectroscopy data. We believe that the bare qubit transition frequency ω_{q} is modulated by the SQUID-mode rather than the LC-mode due to the following reasons: first, our circuit only supports two modes which are well separated in frequency for reasonable values of inductances and capacitances. Thus, the small discrepancy between δ_{bsb} and δ_{rsb} is not related to different modes but is rather based on measurement uncertainties. Second, if the sidebands were related to the LC-mode only, we would have to assume an error of a factor of two in both, L and C. However, the numerically extracted inductances are in good agreement with values reported for very similar designs[6]. Furthermore, with an area of $25\,\mathrm{x}\,25\,\mu\mathrm{m}^2$, the fitted value for the shunt capacitor C yields an effective specific capacitance of $c_{\mathrm{s}} \approx 26\,\mathrm{fF}/\mu\mathrm{m}^2$. This value is in reasonable agreement with specific capacitances as realized with the oxidation protocol at the WMI Nano-Facilities [176]. Finally, by measuring the $I_{\mathrm{sw}}(\omega)$-dependence of the dc-SQUID for different flux biases, the resonance frequency of the LC-circuit can be inferred. Unfortunately, such a measurement was not carried out for the specific sample under discussion. However, for a different specimen with a very similar LC-circuit design we extracted a resonance frequency of $\omega_{\mathrm{LC}} \approx 2.091\,\mathrm{GHz}$ (data not shown).

[5] We note that by including the resistive bias leads into the expression for the total impedance, the frequency of the resonant modes is not changed. Therefore, resistive contributions were neglected in Eq.(4.2) which yields a purely imaginary $Z(\omega)$.

[6] Please note that we adapted the LC-circuit design as it was originally presented in Refs. [87, 132, 140]

Chapter 5

Circuit Quantum Electrodynamics

In the preceding chapters, two building blocks necessary for circuit QED experiments – a resonant cavity and the superconducting flux qubit – were introduced and characterized individually. This chapter is entirely devoted to the physics of strongly coupled qubit-cavity systems. After a theoretical description of the light-matter coupling within the Jaynes-Cummings model, the experimental techniques allowing the characterization of our artificial atom inside the cavity are introduced. In the resonant case, cavity transmission measurements allow to determine the atom-photon coupling strength while the dispersive regime is favorable for qubit spectroscopy. A central topic of this chapter is the engineering potential of circuit QED setups. In this context we will show how the atom-photon interaction can be strongly enhanced by introducing different coupling schemes. In turn, this enables experiments demonstrating multi-photon physics and controlled symmetry breaking in circuit QED systems. Finally, we will discuss a prototype of a circuit QED architecture pushing the light-matter interaction into the ultrastrong-coupling limit. Here, the atom-photon coupling rate g becomes comparable to the transition frequencies of both, qubit and cavity. With normalized coupling ratios g/ω_r of up to 12%, our cavity transmission data reveals unambiguous features that cannot be explained within the framework of the renowned Jaynes-Cummings model.

5.1 Jaynes-Cummings model

The coherent interaction between a two-level system and a quantized radiation mode is described by the Jaynes-Cummings Hamiltonian [3]

$$\hat{H} = \hbar\omega_\mathrm{r}\left(\hat{a}^\dagger\hat{a} + \frac{1}{2}\right) + \frac{\hbar}{2}\omega_\mathrm{q}\hat{\sigma}_\mathrm{z} + \hbar g\left(\hat{a}^\dagger\hat{\sigma}_- + \hat{a}\hat{\sigma}_+\right) \quad . \tag{5.1}$$

The first term describes a single electromagnetic mode with resonance frequency ω_r. In the resonator, $\hat{a}^\dagger$ and $\hat{a}$ are the bosonic creation and annihilation operators of the photon field, respectively. The second term represents a single two-level system with a transition frequency ω_q and $\hat{\sigma}_\mathrm{z}$ is a Pauli spin operator. Finally, the last term describes the interaction between atom and cavity field: the atom can absorb ($\hat{a}\hat{\sigma}_+$) or emit ($\hat{a}^\dagger\hat{\sigma}_-$) a photon from or into the cavity mode at a rate g. The interaction term in the Jaynes-Cummings Hamiltonian is an approximation of the more general dipole interaction Hamiltonian

$$\hat{H}_\mathrm{int} = \hbar g(\hat{a}^\dagger + \hat{a})(\hat{\sigma}_+ + \hat{\sigma}_-) \quad . \tag{5.2}$$

In this expression, $(\hat{\sigma}_+ + \hat{\sigma}_-) \propto \hat{\sigma}_\mathrm{x}$ describes the 'matter field' with $\hat{\sigma}_+$ and $\hat{\sigma}_-$ representing the atom's raising and lowering operators, respectively. Within the framework of the Jaynes-Cummings model, the terms proportional to $\hat{a}^\dagger\hat{\sigma}_+$ and $\hat{a}\hat{\sigma}_-$ in Eq.(5.2) are neglected by a rotating wave approximation. This approximation is valid when $\omega_\mathrm{r}+\omega_\mathrm{q} \gg g, |\omega_\mathrm{r}-\omega_\mathrm{q}|$. Almost all systems consisting of a harmonic oscillator and a two-level system can be described by a Jaynes-Cummings Hamiltonian although operating at different energy scales, e.g. superconducting circuits [6, 7], quantum dots [98, 99], nanomechanical systems [190] and hybrid systems [191, 192].
Owing to the off-diagonal interaction term in Eq.(5.1), the eigenstates of the uncoupled system (i.e. the tensor product of the cavity's photon number state $|n\rangle$ and the atoms ground $|\mathrm{g}\rangle$ and first excited state $|\mathrm{e}\rangle$, respectively) are no longer eigenstates of the Jaynes-Cummings Hamiltonian. However, the operator representing the total number of excitations, $M = \hat{a}^\dagger\hat{a} + \hat{\sigma}_+\hat{\sigma}_-$, commutes with the Hamiltonian in Eq.(5.1) and is a constant of motion [38]. Therefore, Eq.(5.1) only connects subspaces with an equal number of excitations and the new eigenstates can be calculated analytically (see e.g. Ref. [151]). The dipole coupled states are given by

$$|-, n\rangle = \cos\Theta|g, n\rangle - \sin\Theta|e, n-1\rangle \quad , \tag{5.3}$$

$$|+, n\rangle = \sin\Theta|g, n\rangle + \cos\Theta|e, n-1\rangle \quad , \tag{5.4}$$

where $2\Theta = \arctan(2g\sqrt{n}/\delta)$ is the photon number-dependent mixing angle and $\delta = \omega_\mathrm{q}-\omega_\mathrm{r}$ the atom-cavity detuning. $|q, n\rangle = |q\rangle \otimes |n\rangle$ denotes an eigenstate of the uncoupled system ($g = 0$) with photon occupation $n \in \mathbb{N}$ and $q = \{g, e\}$ representing the qubit ground or excited state, respectively. The entangled states given in Eq.(5.3) and Eq.(5.4) are the so-called *dressed states* of the joint qubit-cavity system.

5.1.1 Strong-coupling regime

The strong coupling regime is reached when the single-atom single-photon interaction rate is larger than any dissipation rate [34, 38]. This condition is fulfilled when $g > \kappa, \gamma$, where κ is the cavity's photon loss rate and γ the rate at which the atom decays into dissipative modes other than the cavity mode (see section 1.3). A different definition of strong coupling often used in cavity QED is given by $C = g^2/2\kappa\gamma > 1$, where C is the so-called cooperativity [95]. In the following we will discuss two important limits of the Jaynes-Cummings model in the strong coupling regime.

Resonant limit, $\delta = 0$

The form of the eigenstates of the Jaynes-Cummings Hamiltonian in Eq.(5.3) and Eq.(5.4) implies that the atom acquires a photonic component and vice versa. The interaction between atomic and photonic states becomes most prominent when the atom's transition frequency ω_q matches the cavity frequency ω_r and the two systems can exchange energy. Here, $\delta = 0$ and consequently $\sin\Theta = \cos\Theta = 1/\sqrt{2}$. In this special case, the eigenstates $|\pm, n\rangle$ of the joint system are symmetric and antisymmetric superpositions of the uncoupled basis states

$$|\pm, n\rangle = \frac{|g, n\rangle \pm |e, n-1\rangle}{\sqrt{2}} \quad . \tag{5.5}$$

Figure 5.1 a shows the energy level diagram of Eq.(5.1) in the resonant limit. The degener-

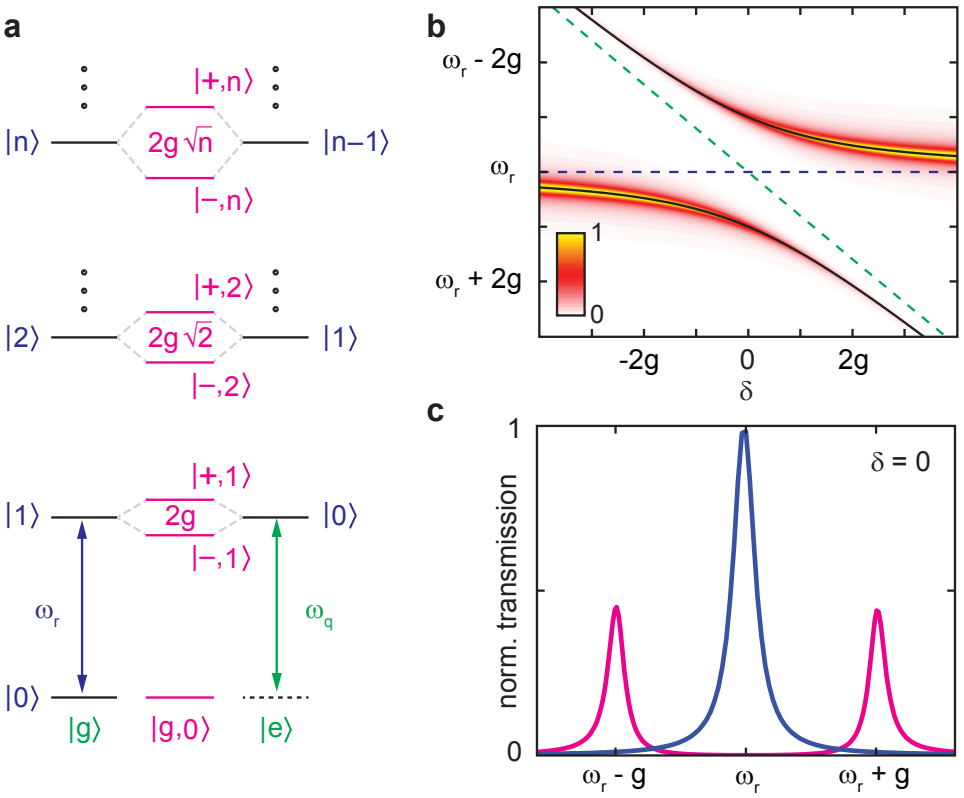

Figure 5.1: Resonant limit, $\delta = 0$. (a) Energy level diagram of the Jaynes-Cummings Hamiltonian. The uncoupled basis states are given by the solid black lines. On resonance ($\omega_r = \omega_q$), the eigenstates of the joint system (magenta) are separated in frequency by $2g\sqrt{n}$. (b) Simulated normalized cavity transmission (color coded; linear scale) in the anticrossing region as a function of the detuning δ. The dashed green and blue line correspond to the uncoupled qubit and cavity transition frequencies, respectively. In circuit QED with flux qubits, δ can be adjusted by an external flux bias. (c) Cavity transmission along $\delta = 0$ in (b). In the strong coupling regime, the linewidths associated with $|\pm, n\rangle$ are smaller than their separation in frequency which allows to resolve the corresponding eigenfrequencies $\omega_r \pm g$ (magenta Lorentzians). The blue line shows the expected cavity transmission for $g = 0$.

acy between the uncoupled basis states $|g, n\rangle$ and $|e, n-1\rangle$ is lifted due to the qubit-cavity coupling. The new eigenstates are separated by an energy gap $2\hbar g\sqrt{n}$ which depends on the number of excitations present in the system. Figure 5.1 b shows the resulting *avoided crossing* (or *anticrossing*) in a simulated transmission spectrum.

The underlying physics can be easily understood considering the case $n = 1$. Here, a quantum of energy coherently oscillates with the vacuum Rabi frequency $\Omega = 2g$ between an atomic excitation ($|e, 0\rangle$) and a cavity photon ($|g, 1\rangle$). Quantum mechanically, atom and cavity are maximally entangled and thus, lose their individual character. They form a kind of 'light-matter molecule' with new eigenenergies $E_\pm = \hbar(\omega_r \pm g)$. Moreover, if the system is in the strong coupling regime, it can undergo several Rabi cycles before the excitation is finally lost and $E_\pm$ can be resolved spectroscopically (see Fig. 5.1 c).

Dispersive limit, $|\delta| \gg g$

The dispersive (or non-resonant) limit is characterized by a substantial detuning $|\delta| \gg g$ between atom and cavity. However, both systems are still coupled and the interaction

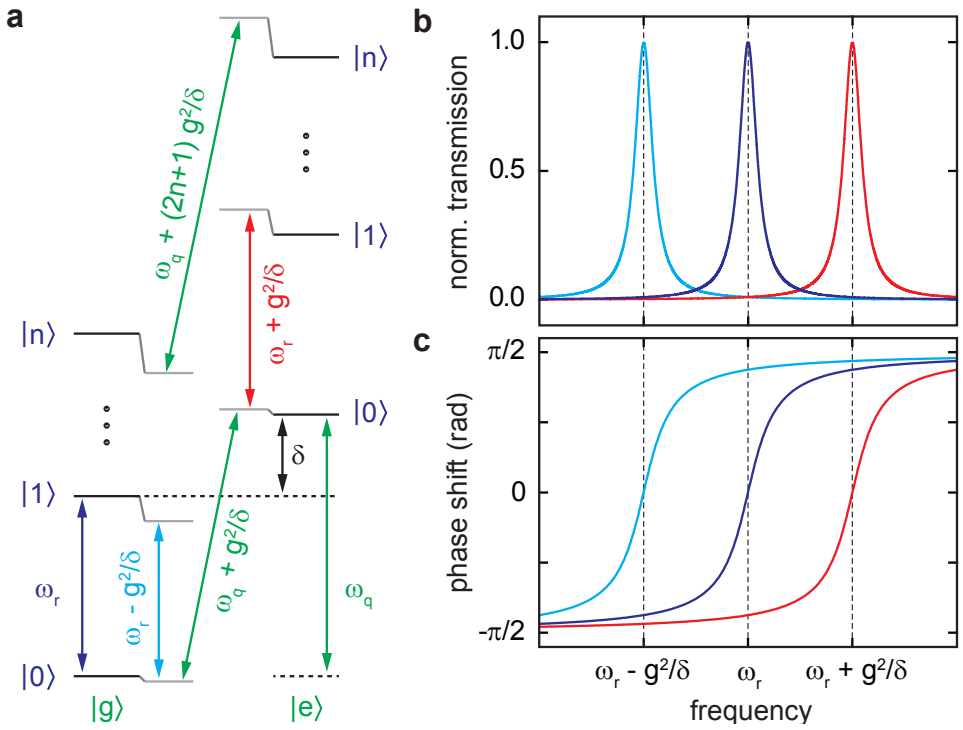

Figure 5.2: Dispersive limit, $|\delta| \gg g$. (a) Energy level diagram of Eq.(5.1) in the dispersive limit (gray solid lines) for $\delta = \omega_q - \omega_r > 0$. The uncoupled basis states are given by the solid black lines. Depending on the qubit state, the cavity frequency is shifted by an amount $\pm g^2/\delta$ (light blue and red arrows). The dressed atom frequency $\tilde{\omega}_q = \omega_q + (2n+1)g^2/\delta$ depends on the intracavity photon number n (green arrows). (b) Normalized transmission amplitude (top panel) and phase (bottom panel) in the dispersive limit. With the atom in the ground state, maximum transmission through the cavity occurs at $\omega_r - g^2/\delta$ (light blue), if the atom is in the excited state at $\omega_r + g^2/\delta$ (red). The unperturbed cavity resonance ($g = 0$) is indicated (dark blue). The state-dependent shift of the cavity resonance can be utilized in e.g. spectroscopy experiments.

is mediated by virtual photons. This leads to dispersive level shifts of both atom and cavity which are shown schematically in Fig. 5.2 a. In the dispersive limit, the Jaynes-Cummings Hamiltonian in Eq.(5.1) can be approximated using the unitary transformation $\hat{U} = \exp\left[\frac{g}{\delta}\left(\hat{a}\hat{\sigma}_+ - \hat{a}^\dagger\hat{\sigma}_-\right)\right]$ [6]. Expanding $\hat{U}\hat{H}\hat{U}^\dagger$ up to second order in g yields

$$\hat{H}_{\text{eff}} = \hat{U}\hat{H}\hat{U}^\dagger \approx \hbar\left(\omega_r + \frac{g^2}{\delta}\hat{\sigma}_z\right)\left(\hat{a}^\dagger\hat{a} + \frac{1}{2}\right) + \frac{\hbar}{2}\omega_q\hat{\sigma}_z \quad . \tag{5.6}$$

The first term describes a harmonic oscillator with an effective resonance frequency $\tilde{\omega}_r = \omega_r \pm g^2/\delta$ depending on the state of the atom (see Fig. 5.2 b and c). In other words, the qubit state is mapped onto the phase and amplitude of cavity photons. We will see in section 5.4.2 how the qubit state-dependent shift of the resonance frequency can be utilized for spectroscopy measurements [102, 181]. In order to highlight the effect of the dispersive interactions on the atom, Eq.(5.6) can be rearranged as

$$\hat{H}_{\text{eff}} \approx \hbar\omega_r\left(\hat{a}^\dagger\hat{a} + \frac{1}{2}\right) + \frac{\hbar}{2}\tilde{\omega}_q\hat{\sigma}_z \quad , \tag{5.7}$$

where

$$\tilde{\omega}_q = \omega_q + \frac{2g^2}{\delta}\hat{a}^\dagger\hat{a} + \frac{g^2}{\delta} \tag{5.8}$$

represents the dressed qubit transition frequency. Thus, the bare atomic transition frequency ω_q is shifted by the photon number-dependent ac-Zeeman term $2g^2\hat{a}^\dagger\hat{a}/\delta$ and the constant Lamb shift g^2/δ due to vacuum fluctuations. The ac-Zeeman shift is the magnetic analogue to the ac-Stark shift in atomic physics and was observed in e.g. cavity QED setups [193] or in circuit QED experiments with charge qubits [102]. In general, the dispersive regime allows for quantum non-demolition measurements of the intracavity photon number $n = \langle\hat{a}^\dagger\hat{a}\rangle$ and the atom state [91, 194–197]. In section 5.4.4 we will use the qubit's ac-Zeeman shift for a calibration of n.
Furthermore, the large coupling rates realizable in circuit QED architectures allow entering the strong dispersive regime which is not yet accessible in cavity QED setups. In this regime, $2g^2/\delta > \kappa, \gamma$ and the qubit transition spectrum decomposes into a separate spectral line for each photon number state of the microwave field [103, 104, 198, 199].

5.1.2 Multi-mode Jaynes-Cummings Hamiltonian and effective coupling

This thesis investigates flux qubits coupled to a distributed $\lambda/2$-transmission line resonator. The latter supports n resonant modes with resonance frequencies ω_n. In the case of a homogeneous transmission line geometry, $\omega_n = n \cdot \omega_1$ ($n \in \mathbb{N}$), where $\omega_1 = \omega_{\lambda/2}$ is the resonance frequency of the fundamental $\lambda/2$-mode. Furthermore, the expressions given in Eq.(5.1) and Eq.(5.6) are only valid at the qubit degeneracy point. Away from this point, flux-dependent terms have to be taken into account which arise from transforming the qubit Hamiltonian $\hat{H}_\mathrm{q}$ in Eq.(2.11) into the qubit energy eigenbasis, i.e. the eigenbasis of $\hat{H}_\mathrm{q}$. This results in an effective coupling $\tilde{g}_n = g_n \sin\theta$ where the flux dependence is encoded in the mixing angle

$$\theta \equiv \theta(\Phi_\mathrm{x}) = \arctan\left(\frac{\Delta}{\epsilon(\Phi_\mathrm{x})}\right) \quad . \tag{5.9}$$

In our notation, g_n represents the maximum coupling of the qubit to the nth resonator mode at the qubit degeneracy point where $\sin\theta = \Delta/\hbar\omega_\mathrm{q} = 1$. Thus, the multi-mode Jaynes-Cummings Hamiltonian can be expressed as

$$\hat{H} = \frac{\hbar}{2}\omega_\mathrm{q}\hat{\sigma}_\mathrm{z} + \sum_n \left[\hbar\omega_n\left(\hat{a}_n^\dagger\hat{a}_n + \frac{1}{2}\right) + \hbar\tilde{g}_n\left(\hat{a}_n^\dagger\hat{\sigma}_- + \hat{a}_n\hat{\sigma}_+\right) - \hbar g_n\cos\theta\left(\hat{a}_n^\dagger + \hat{a}_n\right)\hat{\sigma}_\mathrm{z}\right] \quad , \tag{5.10}$$

where we introduced $\hat{a}_n^\dagger$ and $\hat{a}_n$ as the photon creation and annihilation operators of the nth resonator mode, respectively.

5.2 Measurement setup for circuit QED experiments

In this section, the ^{3}He/^{4}He dilution unit used for the circuit QED experiments presented in this thesis is briefly introduced. Some of our measurements are conducted at a level of a single microwave photon present in our circuit. This translates to the feeble power of roughly 10^{-18} W and therefore, sophisticated microwave equipment is needed both inside the fridge and at room temperature.

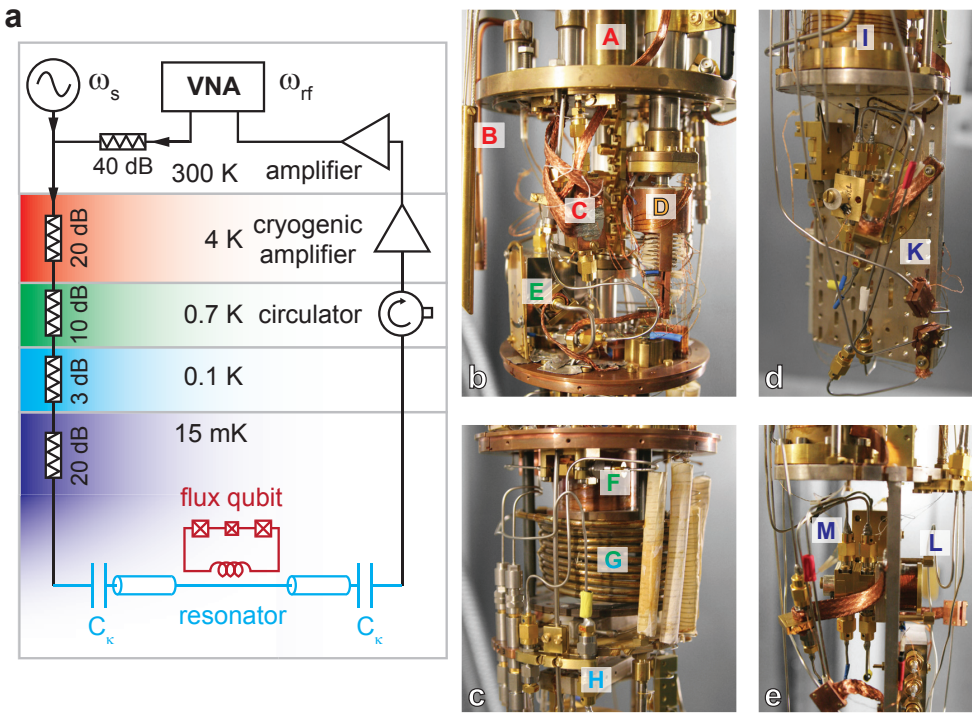

Figure 5.3: Experimental setup. (a) Schematic measurement circuit. The input signal ω_{rf} generated by the vector network analyzer (VNA) and the spectroscopy source ω_{s} is strongly attenuated at various temperature stages (colored regions) and coupled into the resonator (light blue) through the capacitor C_κ. Here, we schematically depict the case of a flux qubit (dark red; crossed boxes represent Josephson junctions) coupled by its geometric loop inductance to the cavity. (b) - (d) Photographs of parts of of the dilution unit. The most important elements are marked by capital letters (color indicates the approximate temperature, see (a)). (A) 4 K flange. (B) persistent switch for magnet coil. (C) cryogenic HEMT-amplifier. (D) 1 K-pot. (E) circulator. (F) still. (G) continuous heat exchanger. (H) step exchanger. (I) mixing chamber. (K) silver sample rod. (e) side view of (d) showing the magnet coil (L) and two gold-platted copper boxes (M), each containing a qubit-cavity system.

5.2.1 ^{3}He/^{4}He dilution refrigerator & instrument rack

Our homemade fridge is able to reach a base temperature of ~ 15 mK. It provides sufficient space for the necessary microwave components at low T and allows the characterization of two different samples during a single cooldown since it is equipped with two amplifier chains. A schematic measurement setup and photographs of the dilution unit are shown in Fig. 5.3. In our experiments, we probe the transmission through the coupled qubit-cavity system at ω_{rf} using a *R&S ZVA 24* vector network analyzer (VNA) (see Fig. 5.3 a). For qubit spectroscopy, an additional microwave signal at ω_{s} can be applied to the device under test using a *R&S SMF 100A* microwave signal generator. The two input signals are combined using a passive microwave splitter (*Mini-Circuits*, *ZFRSC 183-S+*). Fixed attenuators inside the fridge damp the microwave input signal and thermalize the coaxial cables' inner conductor. After passing our superconducting quantum circuit and a circulator[1] which prevents noise from entering our quantum system, the output signal is amplified at 4 K using a custom-made cryogenic low-noise amplifier (noise temperature

[1] The circulator is terminated at one port with a 50 Ω load and effectively acts as an isolator, suppressing any signal coming from higher temperature stages by ~ 20 dB.

$T_N \sim 6 \pm 1\,\mathrm{K}$, gain $\sim 27\,\mathrm{dB}$, bandwith $\sim 2 - 8\,\mathrm{GHz}$ [200]). An additional water-cooled amplifier (*MITEQ*, *JS2-293*) installed at room temperature (gain $\sim 26 - 28\,\mathrm{dB}$) completed the amplification chain. As depicted in Fig. 5.3 a, the probe tone signal (ω_{rf}) is attenuated by 40 dB more than the spectroscopy tone (ω_{s}). The difference in attenuation is necessary as ω_{s} is applied off-resonant to the cavity mode. Including all attenuators, the splitter and the loss of the coaxial lines, we measured a total attenuation of $\sim 106\,\mathrm{dB}$ at $\omega_{\mathrm{rf}} = 5.24\,\mathrm{GHz}$ of the input line[2]. Photographs of important elements of our dilution unit are shown in Fig. 5.3 b-e. For a more detailed description of the cryostat's interior we refer to Ref. [200]. For applying an external flux bias to our quantum circuit, a superconducting magnet coil is located on the backside of the sample rod (see Fig. 5.3 e). The coil consists of a thin single filament Nb-Ti-wire embedded in a Cu-matrix and has an inductance of $\sim 1\,\mathrm{mH}$ [201]. Moreover, the coil is equipped with a persistent switch (see Fig. 5.3 b), which allows to trap a dissipationless current in the solenoid for fixed flux bias measurements. Figure 5.4 shows our instrument rack. Besides the VNA and the SMF, it contains a dc-current source and a *Picowatt* resistance bridge and temperature controller. The current source provides two output ports, each controllable via an external $\pm 10\,\mathrm{V}$ signal from a *National Instruments PCI-6052E* 16-bit acquisition card[3]. Although the inductance of the magnet coil is quite large and current noise is suppressed quite effectively, additional low-pass filters (cut-off frequencies of 1.9 MHz and $\sim 100\,\mathrm{Hz}$, respectively) were installed at room temperature.

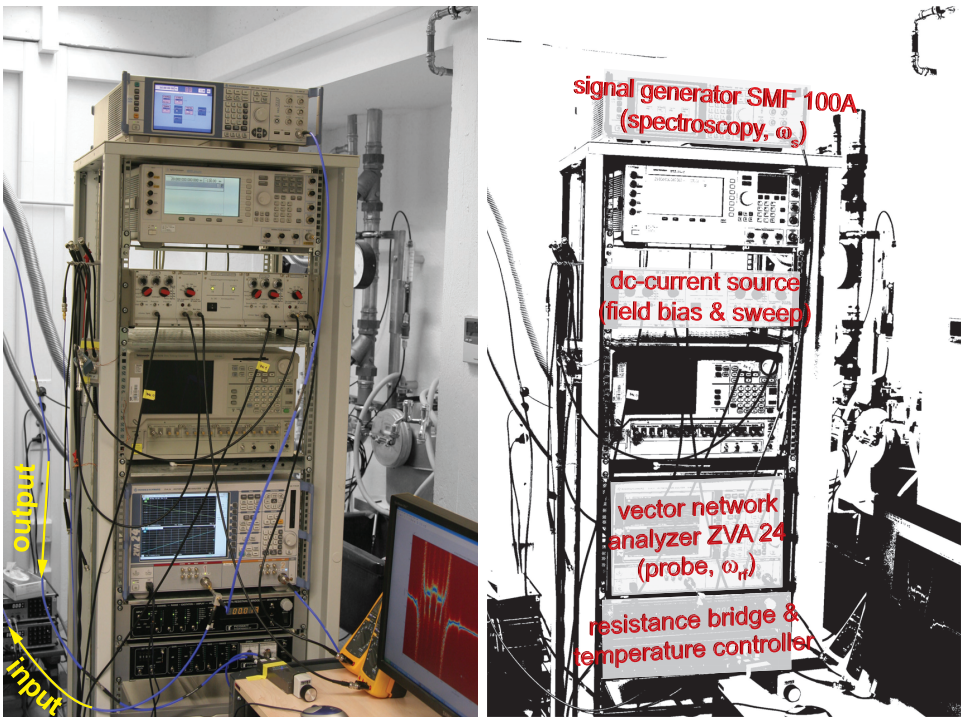

Figure 5.4: Instrument rack used for circuit QED experiments (left panel). For clarity, the important instruments are labeled in the black & white image on the right hand side.

[2]The second input line had a slightly different configuration of fixed attenuators (6 dB at 4 K and 10 dB at the 1 K-pot).

[3]Using our 16-bit PCI card, the minimum current resolution is $\sim 0.3\,\mathrm{nA}$.

5.3 Engineering coupling strengths in circuit QED

Before we start with the main results of this thesis, a short categorization of the experiments discussed in the following with respect to the different coupling schemes is presented. As mentioned already in the introduction, circuit QED setups have many advantages compared to cavity QED experiments based on natural atoms. One particular advantage is the design flexibility and the engineering potential inherent to superconducting artificial atoms.

Figure 5.5 shows scanning electron microscope images of the qubit-cavity systems that will be discussed in the subsequent sections. In order to compare the different coupling schemes it is convenient to express the coupling strength as

$$hg = M\, I_\mathrm{p}\, I_{\mathrm{r},n} \quad . \tag{5.11}$$

Here, M denotes the mutual inductance between qubit and cavity and I_p the qubit's persistent current. The quantity

$$I_{\mathrm{r},n} = \sqrt{\frac{\hbar\omega_n}{L_\mathrm{r}}} \tag{5.12}$$

is the vacuum current of the nth cavity mode which can be calculated if the total inductance L_r of the coplanar waveguide (CPW) resonator and the nth resonance frequency ω_n are known. We note that for coplanar waveguide resonators with a position-independent inductance and capacitance per unit length, ω_n is in good approximation an integer multiple of the fundamental mode frequency $\omega_{\lambda/2} = \omega_1$. According to Eq.(5.11), an easy way to engineer – and thereby increase – the coupling is to modify M.

In Fig. 5.5 a for example, the mutual inductance is of purely geometric origin ($M \sim 5\,\mathrm{pH}$ for the $8\,\mathrm{x}\,30\,\mu\mathrm{m}^2$ loop shown) and scales linearly with the edge length of the qubit. Thus, by using relatively large qubits, the strong-coupling limit of circuit QED can be reached.

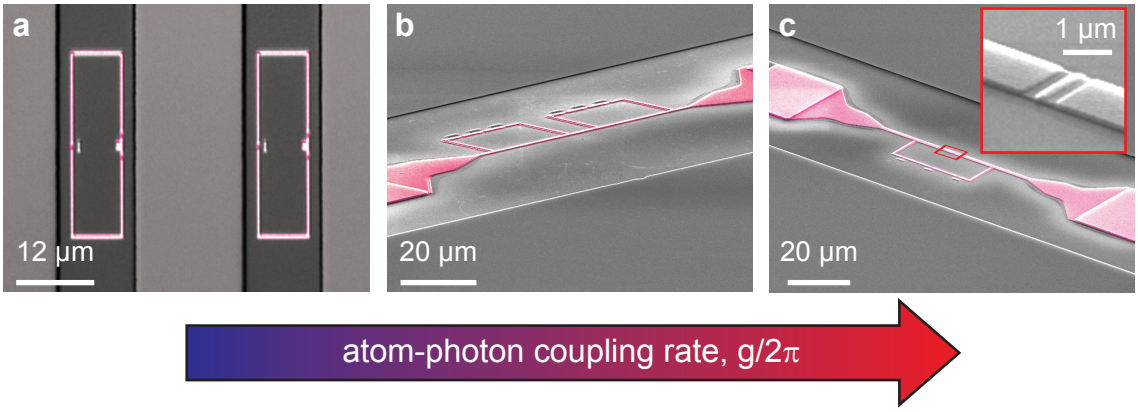

Figure 5.5: False-color scanning electron microscope images of qubit-cavity systems. The coupling rate $g/2\pi$ increases from (a)-(c) by more than an order of magnitude. This is achieved by design modifications and thus highlights the engineering potential in circuit QED. (a) Two flux qubits (magenta) fabricated in the gap of a coplanar waveguide (CPW) resonator. The mutual inductance between qubit and cavity is determined purely by geometry. (b) Two flux qubits coupled *galvanically* to the CPW center conductor by a narrow aluminum strip. In addition to the geometric inductance, the large kinetic inductance of the aluminum constriction has to be considered. (c) Circuit QED prototype for the exploration of ultrastrong-coupling physics. With its Josephson inductance L_J, the additional junction embedded in the aluminum strip (red box and inset) effectively acts as a local and very large inductance.

The system depicted in Fig. 5.5 a will be discussed in section 5.4. In Fig. 5.5 b, qubit and cavity are *galvanically* connected by a narrow strip (width $\sim 500\,\mathrm{nm}$) of aluminum. The kinetic inductance L_{kin} (see section 2.3.3) of this strip thus constitutes an additional large contribution to M. In such a setup, L_{kin} and thus g can be further enhanced by simply reducing the width and/or increasing the length of the shared edge. In turn, an enhanced coupling allows to observe and study e.g. multi-photon transitions and the controlled symmetry breaking in the strong-coupling limit of circuit QED as discussed in more detail in section 5.5.2. A different and more sophisticated approach for a further enhancement of the qubit-cavity coupling rate is depicted in Fig. 5.5 c. Here, an additional Josephson junction embedded in the narrow constriction of a galvanically coupled qubit-cavity system acts as a (non-linear) local inductance. We have seen in section 4.2.1 that typical current densities of our Josephson junctions are of the order of $1\,\mathrm{kA/cm^2}$. Considering a relatively large junction area of $0.3\,\mu\mathrm{m}^2$, this would yield $L_{\mathrm{J}} \approx 110\,\mathrm{pH}$. This value is roughly one order of magnitude larger than for a pure galvanic coupling without the additional coupling junction. Moreover, since $L_{\mathrm{J}} \propto 1/I_{\mathrm{c}} \propto 1/A_{\mathrm{JJ}}$, smaller and/or series configurations of Josephson junctions can increase the coupling dramatically. In section 5.6, a qubit-cavity system similar to the one shown in Fig. 5.5 c allowed for the first time the exploration of ultrastrong-coupling physics in a circuit QED architecture.

The ultrastrong-coupling regime will not be accessible in cavity QED setups dealing with natural atoms in the near future, if ever. Although the strong-coupling regime ($g \gg \kappa, \gamma$ and $C \sim 10^2 - 10^5$) is reached easily nowadays by minimizing cavity and atomic decay rates, g is still very small compared to the atomic and the cavity transition frequencies. In analogy to the definition of the cooperativity parameter $C = g^2/2\kappa\gamma$ we introduce a dimensionless parameter $C_{\mathrm{usc}} = g^2/2\omega_{\mathrm{q}}\omega_{\mathrm{r}}$ describing systems at the edge of ultrastrong-coupling physics. For typical cavity QED setups [33, 34, 91] we estimate $C_{\mathrm{usc}} \sim 10^{-12}$. In cavity QED, both the atom's dipole moment and the cavity mode volume are limiting factors for achieving large atom-photon coupling rates.
On the other hand, circuit QED architectures are pursuing to reach the strong-coupling regime by enhancing g due to their engineering potential. The enormous coupling rates g achieved in these systems benefit from the huge dipole moments of artificial atoms, the small cavity mode volumes and versatile capacitive and inductive coupling schemes. For strongly coupled circuit QED devices cooperativity parameters of up to $C \sim 10^5$ and $C_{\mathrm{usc}} \sim 10^{-4}$ were reported [116] while the ultrastrong-coupling prototype discussed in section 5.6 reaches $C \sim 10^3$ and remarkable $C_{\mathrm{usc}} \approx 1.7\,\%$.

5.4 Strong-coupling of superconducting qubit-cavity systems

The experiments discussed in this section are based on flux qubits coupled to the center strip of an overcoupled CPW resonator via a purely geometric mutual inductance. A schematic of the measurement setup and images of the flux qubits and the CPW resonator are shown in Fig. 5.6 a and b, respectively. Owing to the limited bandwidth of our cryogenic amplifier, we are able to observe the first three modes of our CPW resonator. The resonance frequencies are determined at a flux position where the qubit-cavity detuning $|\delta| \gg \omega_n, \omega_q, g$. The flux qubits have an area of $30\,\mathrm{x}\,8\,\mu\mathrm{m}^2$ and are fabricated in the gap of the CPW at an antinode of the λ-mode ($\omega_2/2\pi = 5.244\,\mathrm{GHz}$). In the following, we will introduce the experimental techniques necessary to characterize such a circuit QED system.

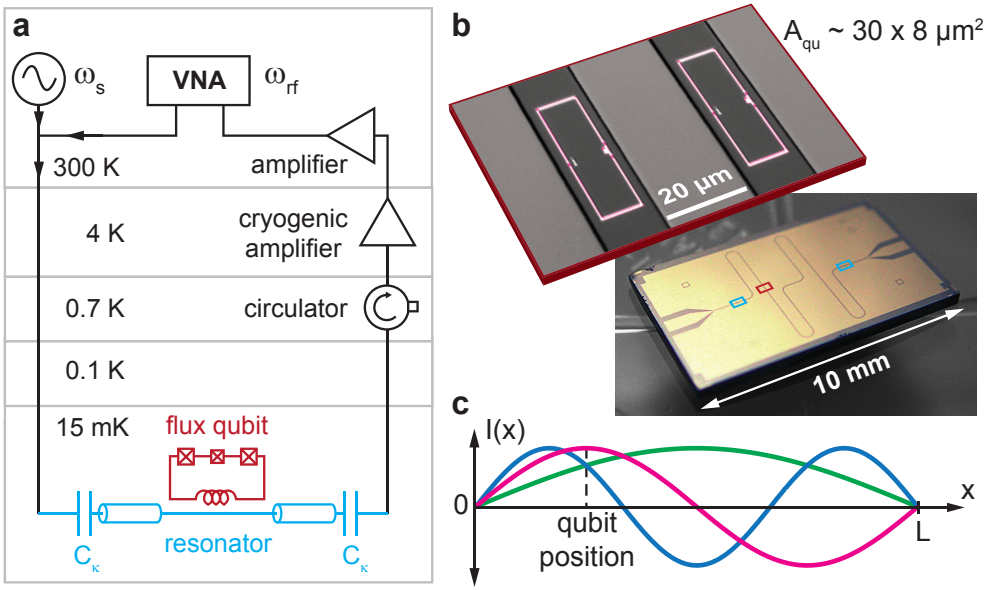

Figure 5.6: Measurement setup, images of the quantum circuit and sketch of the resonator's current distribution. (a) The amplified cavity transmission at ω_{rf} is probed using a vector network analyzer. For spectroscopy, a second tone ω_{s} can be applied to the cavity (light blue). For clarity, only one of the two qubits (dark red; crossed boxes represent Josephson junctions) is sketched. The microwave components are explained in the caption of Fig. 5.3. (b) Optical and false-color scanning electron images of the quantum circuit. The position of the flux qubits (magenta) is indicated by the red box and the light blue boxes mark the position of the coupling capacitors. (c) Sketch of the current distribution $I(x)$ of the first three resonator modes. Their resonance frequencies are: $\omega_1/2\pi = 2.624\,\mathrm{GHz}$ ($\lambda/2$-mode, green), $\omega_2/2\pi = 5.244\,\mathrm{GHz}$ (λ-mode, magenta) and $\omega_3/2\pi = 7.860\,\mathrm{GHz}$ ($3\lambda/2$-mode, blue). The cavity has a length $L = 23\,\mathrm{mm}$ and with $C_\kappa \sim 6\,\mathrm{fF}$, all quality factors $Q_n > 15 \cdot 10^3$.

5.4.1 Cavity transmission

Owing to the dispersive and/or resonant interactions, the cavity's mode frequencies are modified in presence of one or more qubits inside the resonator. With the qubit in the ground state, each cavity mode frequency is shifted by $\tilde{g}_n^2/\delta_n$, where $\delta_n = \tilde{\omega}_q(\Phi_x) - \omega_n$. Since δ_n is a flux-dependent quantity and periodic in Φ_0, the qubit's flux-periodicity is directly mapped to the cavity's mode frequencies.

Before we turn to the spectrum of the specimen shown in Fig. 5.6 b, it is instructive to

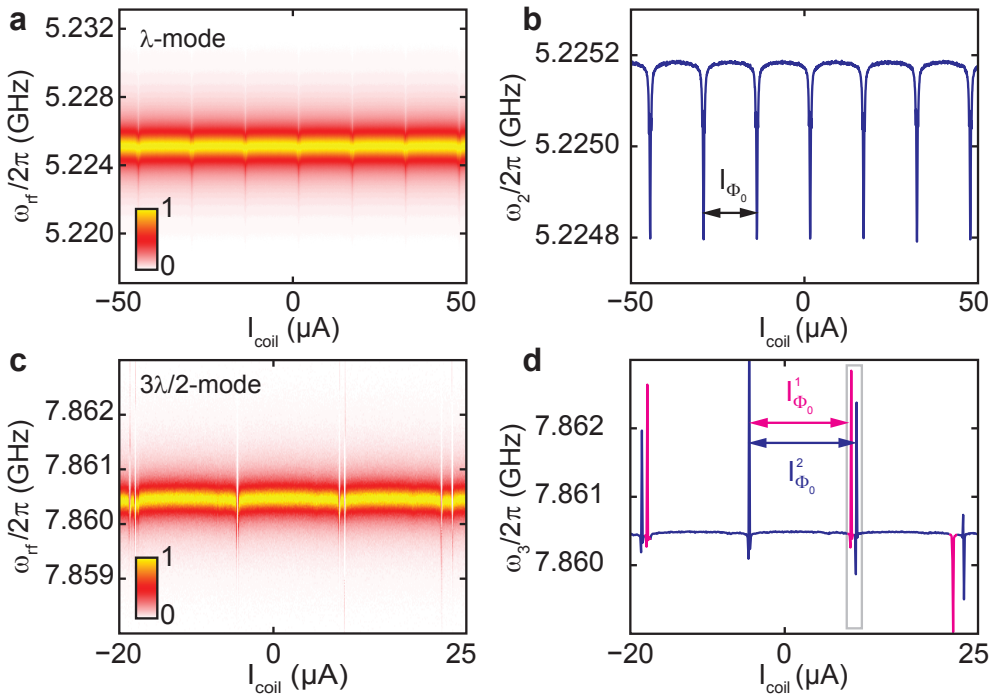

Figure 5.7: Resonator response. (a) Color-coded cavity transmission (λ-mode, linear scale, arbitrary units) as a function of the probe frequency $\omega_{\mathrm{rf}}/2\pi$ and the magnet coil current I_{coil} for a single qubit embedded in the resonator (yellow indicates high and white low transmission). The flux periodicity of the qubit is encoded in the spectrum. (b) Resonance frequency $\omega_2/2\pi$ as a function of I_{coil}. Furthermore, we observe an offset by almost $\Phi_0/2$ due to flux trapping during the cooldown procedure. (c) Same as in (a) but for two qubits and the $3\lambda/2$-mode. When qubit and resonator are on resonance, the transmission is strongly suppressed (white vertical regions). (d) An intended qubit area difference results in a different flux quantum periodicity ($I^1_{\Phi_0} \neq I^2_{\Phi_0}$) which is highlighted by different colors. At $I_{\mathrm{coil}} \sim -5\,\mu\mathrm{A}$, the degeneracy points of the qubits almost coincide and can not be distinguished within the measurement resolution. The area of the gray box is shown in Fig. 5.8.

look at a simpler system with only one qubit coupled to the resonator. Figure 5.7 a shows the cavity transmission spectrum of the λ-mode as a function of the applied magnet coil current I_{coil}. We observe periodic shifts of the resonance frequency ω_2 towards lower frequencies (see Fig. 5.7 b) which indicates that $\tilde{\omega}_{\mathrm{q}} > \omega_2$. In order to extract ω_2, a Lorentzian is fitted to each transmission spectrum $\omega_{\mathrm{rf}}(I_{\mathrm{coil}})$ in Fig. 5.7 a. Furthermore, the $\Phi_0 - I_{\mathrm{coil}}$ conversion factor is obtained from the spectrum. At the qubit degeneracy points, the dispersive cavity shift is maximum.

We now turn to the cavity spectrum for the case of two flux qubits present in our cavity. Figure 5.7 c and d show the cavity transmission spectrum of the $3\lambda/2$-mode and the resonance frequency ω_3 as function of I_{coil}, respectively. Here, the periodic features in the spectrum indicate qubit-cavity anticrossings due to resonant interaction. When $\omega_{\mathrm{q}} = \omega_3$ the cavity transmission is reduced substantially (white vertical regions in Fig. 5.7 c) which complicates the fitting procedure and leads to irregular shifts in ω_3 (see Fig. 5.7 d). A slightly different exposure dose ($\sim$ 13 % difference) results in an area difference of the qubits of $\sim$ 5 %. Figure 5.8 shows the flux-dependent transmission spectra for all observable cavity modes in the region indicated by the gray box in Fig. 5.7 d. The spectrum of the $3\lambda/2$-mode clearly reveals avoided crossings for current values where the flux-dependent

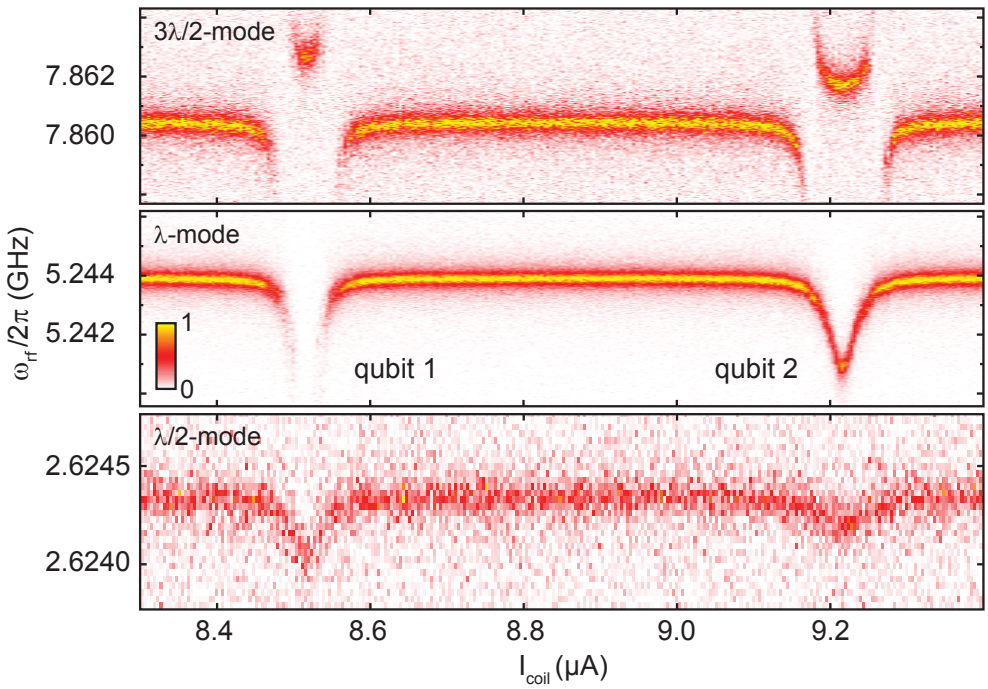

Figure 5.8: Cavity transmission (linear scale, arbitrary units) around 9 µA (see gray box in Fig. 5.7 d). In the spectrum of the $3\lambda/2$-mode (top panel) we observe two avoided crossings for each qubit. The other two modes (bottom panels) reveal dispersive frequency shifts which are maximum at the respective qubit degeneracy point.

qubit transition frequency ω_q is resonant with ω_3. At these points, the eigenstate of the qubit-cavity system is a superposition of qubit- and cavity-like excitations. Observing such a clear anticrossing is already a strong indication for coherent qubit-cavity interaction. The lower two panels of Fig. 5.8 show the flux-dependent transmission spectra of the λ- and $\lambda/2$-mode, respectively. If $\tilde{\omega}_q(\Phi_x)$ is known and if the dispersive cavity spectrum is recorded at a sufficiently low input power, the qubit-cavity coupling rate g_n can be extracted from the flux dependence of the resonance frequencies (see section 5.4.3).

5.4.2 Qubit microwave spectroscopy

In the dispersive limit ($\delta_n \gg g_n$), the qubit state can be inferred from the shift of the cavity's resonance frequency [6,7]. In the following we describe the measurement protocol for an experimental technique referred to as two-tone spectroscopy [102,181,202].
For fixed $\delta\Phi_x$, we monitor phase and amplitude at the probe tone frequency ω_{rf} where maximum cavity transmission occurs. A second microwave signal with frequency ω_s and power P_s is applied to the system (see Fig. 5.3 a). Since this so-called spectroscopy tone is off-resonant with respect to ω_{rf} and owing to the filtering effect of the cavity, P_s is typically $10^4 - 10^6$ times larger than the probe tone power P_{rf} of the readout mode. When $\omega_s = \tilde{\omega}_q$ and for sufficiently large amplitude of the continuous spectroscopy tone, the qubit is excited and saturated, yielding an equal population of ground and excited state, respectively. As illustrated in Fig. 5.9 a and b, this leads to a frequency shift of $\tilde{g}_n^2/\delta_n$ which is reflected in a phase shift (δ_P) and a decrease in magnitude (δ_M) at ω_{rf}. Repeating this protocol for different $\delta\Phi_x$ allows to map out the dressed qubit transition frequency $\tilde{\omega}_q$. In order to avoid frequency shifts due to the photon number dependence of $\tilde{\omega}_q$, the measurement

must be performed with a negligible photon population of the cavity mode ($P_{\mathrm{rf}} \to 0$) used for readout. The photon number calibration will be discussed in section 5.4.4. The upper panels in Fig. 5.9 c and d summarize the spectroscopic response of the two qubits with respect to the relative phase and magnitude shift at ω_{rf}, respectively. The cavity transmission data in Fig. 5.8 suggests to utilize the $\lambda/2$- and the λ-mode as readout tone for qubit 1 and qubit 2, respectively. In both data sets, the hyperbolic flux-dependence of $\tilde{\omega}_{\mathrm{q}}$ is visible. However, the spectroscopic response of qubit 2 shows a substantially better signal-to-noise ratio (SNR) since δ_2 is ~ 5 times smaller than δ_1 and in the small phase shift limit [151] the SNR is proportional to $(\tilde{g}_n/\delta_n)^2$. The lower panels in Fig. 5.9 c and d

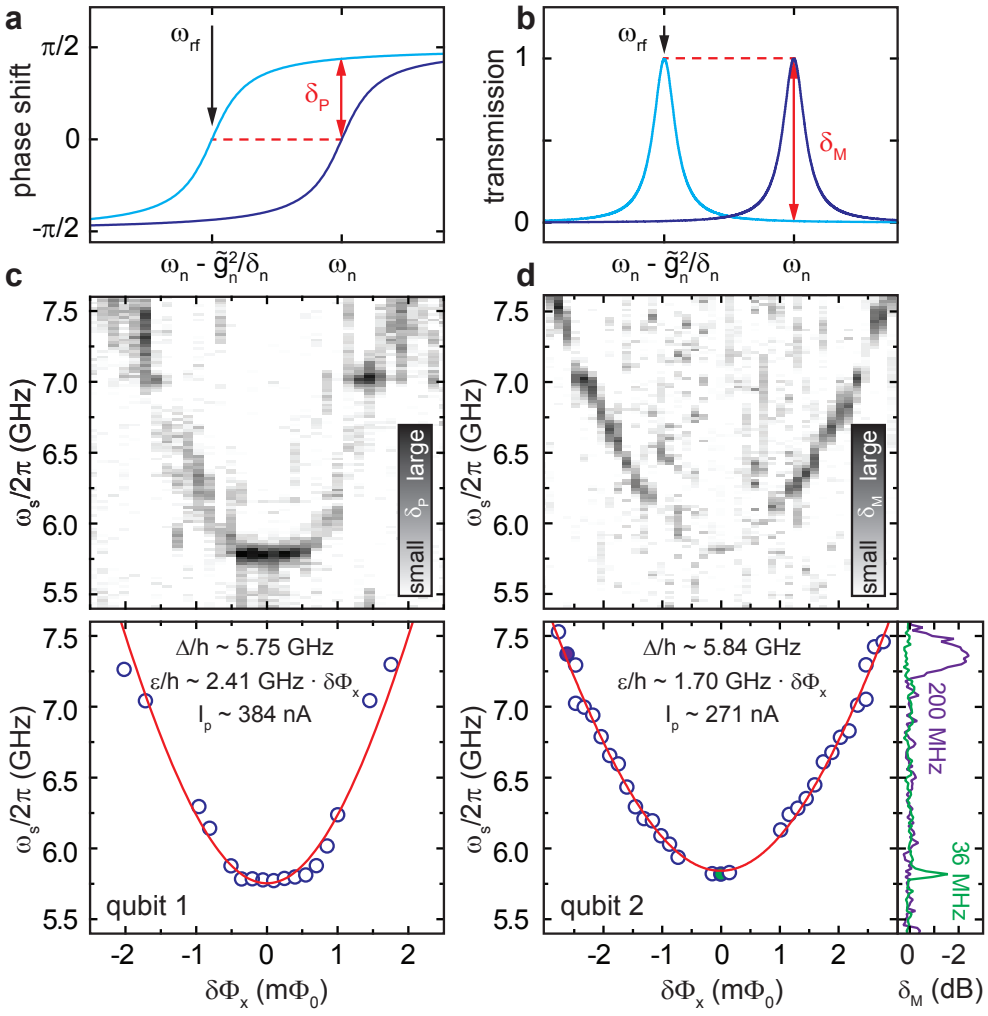

Figure 5.9: Two-tone qubit microwave spectroscopy. (a) Schematic of the dispersive qubit readout defining the (a) relative phase shift δ_{P} and (b) relative magnitude shift δ_{M}. (c) Top panel: δ_{P} of the readout tone (gray-scale) as a function of $\delta\Phi_{\mathrm{x}}$ for qubit 1 (see Fig. 5.8). Bottom panel: fitted center frequencies of the qubit signal (blue circles). The red solid line represents a numerical fit to Eq.(2.15) yielding the qubit parameters Δ and ϵ. (d) Same as in (a) but for qubit 2 and with respect to δ_{M}. The panel on the right hand side visualizes typical transmission spectra away from (violet) and close to (green) the qubit degeneracy point. The numbers give the FWHM of the qubit signal, which is slightly power broadened for the spectra shown. For qubit 2 we extract a FWHM $\sim 17\,\mathrm{MHz}$ at $\delta\Phi_{\mathrm{x}} = 0$ and in the low power limit ($P_{\mathrm{s}} \to 0$, data not shown). Around $\omega_{\mathrm{s}}/2\pi \sim 7.2\,\mathrm{GHz}$ the spectroscopic response is reduced significantly due to the presence of a spurious fluctuator coupled to the qubit.

depict the fitted center frequency of the qubit signal as a function of the relative flux bias $\delta\Phi_x$. Using Eq.(2.15) we find $\Delta/h \sim 5.75\,\mathrm{GHz}$ and $\Delta/h \sim 5.84\,\mathrm{GHz}$ for qubit 1 and 2, respectively. Furthermore, Fig. 5.9 d depicts two cuts along $\delta\Phi_x \approx 0$ and $\delta\Phi_x \approx -2.5\,\mathrm{m}\Phi_0$ for qubit 2. In the low power limit ($P_s \to 0$), the FWHM of the qubit signal is $\propto 1/T_2$, where T_2 is the dephasing time. Close to the qubit degeneracy point,

$$\frac{\partial E_{ge}}{\partial \Phi_x} = \frac{\partial \epsilon}{\partial \Phi_x}\cos\theta \tag{5.13}$$

is small which in turn yields optimum qubit coherence properties. This fact is qualitatively reflected by our spectroscopic data, however, we did not study the dephasing and energy relaxation of our qubits in detail within this thesis. Due to the lower SNR, the spectrum for qubit 1 shown in Fig. 5.9 c could not be recorded in the low power limit and the qubit signal is substantially power broadened. In section 5.4.5, the spectroscopic response of qubit 1 at $\delta\Phi_x = 0$ will be discussed for varying P_{rf} and P_s. Finally we note, that in contrast to a conventional dc-SQUID readout the dispersive circuit QED readout allows to determine $\tilde{\omega}_q$ spectroscopically at $\delta\Phi_x = 0$ since the qubit state is mapped onto the cavity's resonance frequency.

5.4.3 Determination of coupling strengths

Now that $\tilde{\omega}_q(\delta\Phi_x)$ is known, the coupling strengths between qubit and the respective cavity mode can be determined. In principle, there are several ways to determine g_n which all require a negligible photon population of the cavity modes.
The most straightforward way to investigate the coupling is to record the vacuum Rabi splitting, however, due to a low SNR we were not able to record the vacuum Rabi splitting with our setup. At the end of this section we will address this topic more thoroughly. Another possibility is to determine the coupling strengths by a two-tone qubit spectroscopy measurement. By sweeping the spectroscopy tone over a wide frequency range including the resonator modes, the spectrum could be fitted to the energy levels given by Eq.(5.10). However, when the spectroscopy tone is close to the frequency of the qubit-cavity anti-crossings, the large spectroscopy drive ($P_s \gg P_{rf}$) will populate the cavity mode which induces shifts and leads to a non-linear splitting of the (vacuum) Rabi resonance [116]. In the following, we determine the coupling strengths from the low-power cavity transmission spectrum shown in Fig. 5.10 a. The spectrum was recorded prior to the qubit spectroscopy

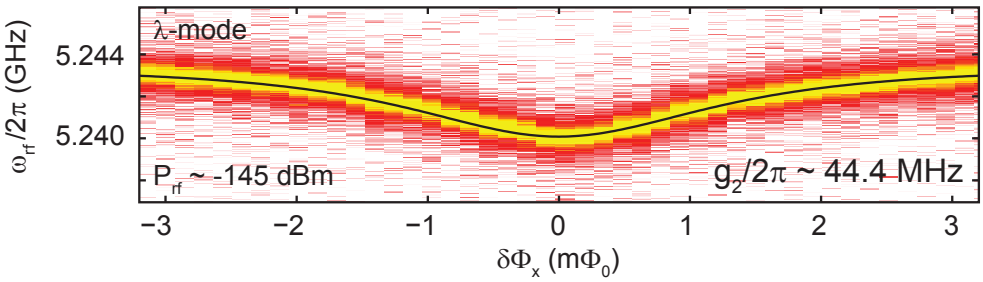

Figure 5.10: Determination of qubit-cavity coupling strength $g_2/2\pi$. (a) Cavity transmission (λ-mode, linear scale, arbitrary units) as a function of $\delta\Phi_x$ and probe frequency $\omega_{rf}/2\pi$. The spectrum is recorded at a power level of $P_{rf} \sim -145\,\mathrm{dBm}$ which corresponds to 0.67 photons on average (see section 5.4.4). The black solid line is a numerical fit to Eq.(5.14) yielding $g_2/2\pi = 44.4\,\mathrm{MHz}$.

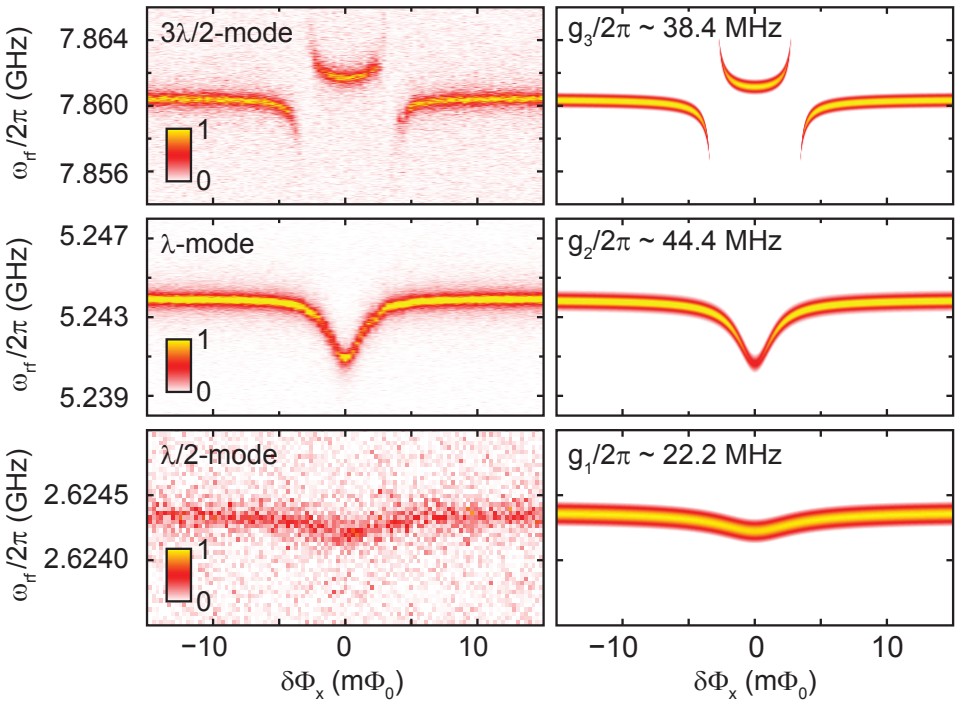

Figure 5.11: Measured and calculated spectra of all three resonator modes. The panels on the left hand side show the cavity transmission spectra of qubit 2 as a function of $\delta\Phi_x$ and probe frequency $\omega_{rf}/2\pi$. The spectra were recorded with the same input power $P_{rf} \sim -137\,\mathrm{dBm}$ but with different frequency resolution. On the right hand side, the simulated cavity transmission spectra are shown as obtained by solving Eq.(5.16). The spectra were simulated using the experimentally determined $\gamma/2\pi = 16.8\,\mathrm{MHz}$, $\kappa_1/2\pi = 113\,\mathrm{kHz}$, $\kappa_2/2\pi = 340\,\mathrm{kHz}$ and $\kappa_3/2\pi = 484\,\mathrm{kHz}$.

data in Fig. 5.9. With the qubit in the ground state, the flux dependence of the nth cavity mode is given by Eq.(5.6) and can be written as

$$\tilde{\omega}_n = \omega_n - \frac{\tilde{g}_n}{\delta_n} = g_n^2 \frac{\sin^2\theta}{\omega_q - \omega_n} \quad , \tag{5.14}$$

where ω_q and θ are given by Eq.(2.15) and Eq.(5.9), respectively. Fitting the spectrum of the λ-mode to Eq.(5.14) with $n = 2$ yields $g_2/2\pi = 44.4\,\mathrm{MHz}$. With $\gamma/2\pi = 1/T_2$ and $\kappa/2\pi < 1\,\mathrm{MHz}$, the system is in the strong-coupling limit. We note, that the evaluation of the coupling strength by Eq.(5.14) is only valid for moderate g_n. In the ultrastrong-coupling regime, the cavity transmission spectra are fitted to the energy-level spectrum of the full Hamiltonian as discussed in section 5.6. For moderate g_n and in the case of a homogeneous transmission line resonator[4], the coupling constants g_1 and g_3 can be determined from g_2 by

$$g_i = g_2 \sqrt{\frac{\omega_i}{\omega_2}}\,\eta_i \qquad \text{with} \qquad i = 1, 3 \quad . \tag{5.15}$$

According to Eq.(5.11) and Eq.(5.12), the square root term accounts for the decrease or increase of the vacuum current and η_i is a factor arising from the geometry of our quantum

[4]The coplanar waveguide cavities discussed so far (see section 2.3 and section 3.2) are homogeneous transmission line resonators. They are distinguished by a position-independent inductance and capacitance per unit length.

circuit as depicted in Fig. 5.6 c. Since the qubit is fabricated at an antinode of the λ-mode, the amplitudes of the standing current waves for the other observable modes are reduced by a factor $\eta_1 = \eta_3 = 1/\sqrt{2}$ (see Fig. 5.6 c). Using Eq.(5.15) we calculate $g_1 = 22.2\,\mathrm{MHz}$ and $g_3 = 38.4\,\mathrm{MHz}$ for the coupling strengths to the $\lambda/2$- and $3\lambda/2$-mode, respectively.
In order to verify our results, we simulate the transmission spectra numerically solving the master equation

$$\frac{d\hat{\rho}}{dt} = -i\left[\hat{H}, \hat{\rho}\right] + \kappa\mathcal{D}[\hat{a}]\hat{\rho} + \gamma\mathcal{D}[\hat{\sigma}_-]\hat{\rho} \tag{5.16}$$

where the superoperators $\mathcal{D}[\hat{L}]$ have the standard Lindblad form

$$\mathcal{D}[\hat{L}]\hat{\rho} = \left(2\hat{L}\hat{\rho}\hat{L}^\dagger - \hat{L}^\dagger\hat{L}\hat{\rho} - \hat{\rho}\hat{L}^\dagger\hat{L}\right)/2 \tag{5.17}$$

and describe the effect of damping. The calculations were carried out using *Matlab* and the *Quantum Tool Box*, an easy to use computational tool for quantum and atomic physics systems [203]. The Hamiltonian in Eq.(5.16) is given by the Jaynes-Cummings Hamiltonian in Eq.(5.1) plus an additional external driving term

$$\mathcal{E}\left(e^{-i\omega_\mathrm{d}t}\hat{a}^\dagger + e^{\omega_\mathrm{d}t}\hat{a}\right) \quad , \tag{5.18}$$

where $\mathcal{E}$ and ω_d are the amplitude and angular frequency of the drive, respectively. Figure 5.11 shows the simulated spectra side by side with the experimental results (cf. Fig. 5.8). The excellent agreement between experiment and theory confirms the fitted and calculated g_n. We note that Eq.(5.16) was solved for each cavity mode separately which is valid[5] for $g_n/\omega_n \ll 1$. From our results and using Eq.(5.11) we estimate a mutual inductance between qubit and resonator of $\sim 5.8\,\mathrm{pH}$. This result is also in good agreement with the extracted coupling rates of qubit 1.

Rabi mode splitting

Recording a low-power cavity transmission spectrum at a flux position of an avoided crossing ($\delta_n = \omega_\mathrm{q} - \omega_n = 0$) reveals two peaks separated by $2\tilde{g}_\mathrm{n}/2\pi$ (vacuum Rabi mode splitting, see Fig. 5.1 c). With $\tilde{g}_\mathrm{n} = g_n \sin\theta$ and $\sin\theta = \Delta/\hbar\omega_\mathrm{q}(\delta\Phi_\mathrm{x})$ the maximum coupling strength can be calculated. Observing the vacuum Rabi splitting is experimentally challenging but has been demonstrated with different kinds of qubits [7, 107, 109, 204, 205]. Typically, the amplitude of the two peaks corresponding to the entangled qubit-cavity states is significantly reduced compared to the bare cavity mode [7, 151] because on resonance, the two systems can exchange energy and a decay of the qubit into non-radiative channels eliminates the shared excitation of the joint system. Such processes thus lead to a significant reduction of the transmitted microwave photons which in turn requires more averaging time. Furthermore, the Rabi peaks become inhomogeneously broadened with increasing power. On the one hand, this indicates that the Rabi splitting is not simply the avoided crossing of two harmonic oscillators but has indeed the character of a harmonic mode coupled to a highly non-linear system. On the other hand, the average photon population has to be negligible small ($n \sim 0.01$) in order to avoid obscuring the spectrum. Unfortunately, we were not able to record a spectrum at such low input powers in a reasonable amount of time owing to our measurement setup and the relative large qubit decay rate into channels not captured by the cavity. Figure 5.12 shows the resonator transmission

[5] In the ultrastrong-coupling regime, $g_n \sim \omega_n$, and $\hat{H}$ in Eq.(5.16) had to be replaced with a multi-mode Jaynes-Cummings Hamiltonian (see Eq.(5.10)) and Lindblad operators for each cavity mode.

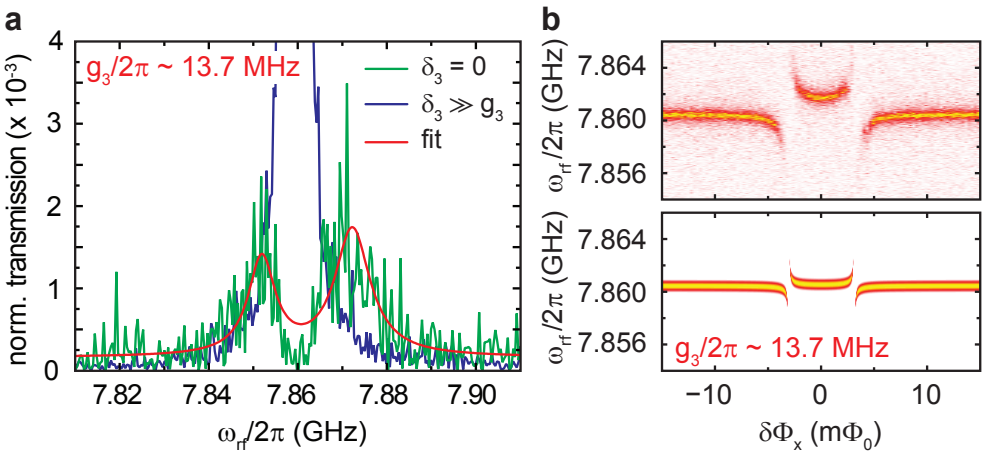

Figure 5.12: Cavity transmission spectra. (a) Resonator response for different $\delta\Phi_x$ where $\delta_3 = 0$ (green) and $\delta_3 \gg g_3$ (blue). The spectra are normalized with respect to the latter and the red curve represents a fit to two Lorentzians for $\delta_3 = 0$. Note that the maximum transmission for $\delta_3 = 0$ is reduced by a factor of $\sim 5 \cdot 10^2$ compared to $\delta_3 \gg g_3$. The fitted FWHM is in reasonable agreement with the expected width of $(\gamma + \kappa_3)/2$ [6]. Due to the strongly reduced transmission on resonance, the spectra were recorded with an input power of $P_{\mathrm{rf}} \sim -130\,\mathrm{dBm}$. Therefore, the photon population $n_3 \sim 9.8$ of the mode is too large and the Rabi peaks become inhomogeneously broadened and frequency shifted [151]. (b) A comparison between the measured (top panel) and simulated (bottom panel) cavity transmission spectra contradicts the qubit-cavity coupling $g_3/2\pi \sim 13.7\,\mathrm{MHz}$ extracted from the Rabi splitting.

of the $3\lambda/2$-mode for flux values where $\delta_3 \gg g_3$ and $\delta_3 = 0$. The spectra were recorded with an input power corresponding to an average photon number of $n_3 \sim 9.8$. Although we observe the split peak situation, the extracted coupling strength $g_3/2\pi = 13.7\,\mathrm{MHz}$ is strongly reduced compared to our result obtained from fitting the flux-dependent cavity frequency shift. The discrepancy between the coupling strength extracted from the mode splitting and our experimental results is visualized in Fig. 5.12 b.

5.4.4 ac-Zeeman shift & photon number calibration

Although we presented in the previous sections spectra recorded at specific average photon numbers, the relation between the vector network analyzer's output power and the mean number of intracavity photons n can only be calibrated when the coupling rates g_n are known. In this section we explain how the photon number dependence of the dispersive ac-Zeeman shift can be utilized for a calibration of P_{rf} on the basis of qubit 2.

The qubit's ac-Zeeman shift is measured spectroscopically at $\delta\Phi_x = 0$ for a fixed spectroscopy power $P_s \sim -25\,\mathrm{dBm}$ referred to the output of the SMF microwave source. The qubit state is inferred from the frequency shift of the cavity's λ-mode when $\tilde{\omega}_q = \omega_s$. For increasing P_{rf}, the qubit transition frequency is shifted towards higher frequencies as shown in Fig. 5.13 a. Since our readout tone represents a coherent signal, the photon distribution inside the cavity is Poissonian with photon number fluctuations of the order $\sqrt{n}$. It can be shown that the spectrum of the qubit is given by a sum of Lorentzians centered around $\tilde{\omega}_q$ but with different widths and weights [103]. If the average photon number n is small, only a few terms contribute and the qubit spectrum has a Lorentzian line shape slightly broadened due to measurement-induced dephasing. On the other hand, for large n, the qubit spectrum is given by the sum of many Lorentzians, effectively resulting in a

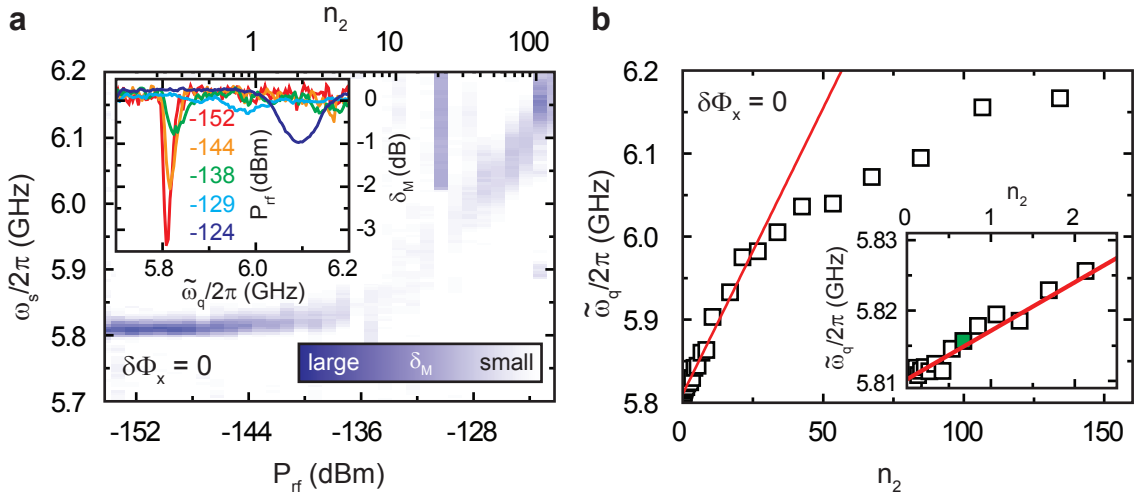

Figure 5.13: Qubit ac-Zeeman shift. (a) Relative shift in transmission magnitude δ_M (color coded; blue: large; white: small) as a function of P_{rf} and the spectroscopy frequency $\omega_s/2\pi$ at $\delta\Phi_x = 0$. For increasing P_{rf}, the effective qubit transition frequency is shifted due to the photon number dependence of $\tilde{\omega}_q$. The top axis refers to the average photon number n_2 in the readout mode (λ-mode) as extracted from the data in (b). Inset: typical qubit spectra for different input powers P_{rf}. The transition from a Lorentzian to a Gaussian line shape is clearly visible. (b) Fitted center frequencies (black squares) of $\tilde{\omega}_q/2\pi$ as a function of n_2. The red line represents a fit to the linear region and has a slope of $2g_2^2/\delta_2 \approx 6.9\,\mathrm{MHz}$. Around $n_{crit,2} \approx 41$, the ac-Zeeman shift per photon becomes power-dependent and decreases with increasing n_2. Inset: magnified view of $\tilde{\omega}_q$ in the low-n_2 region. The green filled data point represents the average photon number at which the qubit spectroscopy data in Fig. 5.9 d was recorded.

Gaussian line shape. The transition between these two limits is visualized by the spectra shown in the inset of Fig. 5.13 a.

Since the coupling constant g_2 and $\delta_2 = \omega_q - \omega_2$ are known, the shift per cavity photon $2g_2^2/\delta_2 \approx 6.9\,\mathrm{MHz}$ can be calculated. In order to obtain this shift, we have to assume a total attenuation of 110 dB which is in good agreement with the estimated attenuations in our measurement setup (see section 5.2.1). In Fig. 5.13 b, the fitted center frequencies of the qubit signal are plotted for increasing n_2, where we used the relation $P_{rf} = n_2\hbar\omega_2\kappa_2$. We note, that the linear relation between P_{rf} and n_2 is valid only for low photon numbers and tends to break down [6, 151] in a region close to the critical photon number $n_{crit,2} = \delta_2^2/4g_2^2 \sim 41$ in good agreement with our experimental results. For $n > n_{crit}$, the lowest-order dispersive approximation breaks down and $\chi_n = 2g_n^2/\delta_n$ becomes a power-dependent quantity.

Measuring the qubit ac-Zeeman shift thus allows a calibration of the average photon number (e.g. $n_2 \sim 0.67$ in our spectroscopy experiment, see Fig. 5.9 d). When the shift per cavity photon is larger than the qubit linewidth, this measurement allows to spectroscopically resolve the photon number states inside the cavity [104], which is not the case in our situation.

5.4.5 Sidebands & multi-photon spectroscopy

In section 4.4.2, we spectroscopically resolved sideband transitions of a coupled SQUID-qubit system for sufficiently large drive amplitudes of the spectroscopy tone. Such an

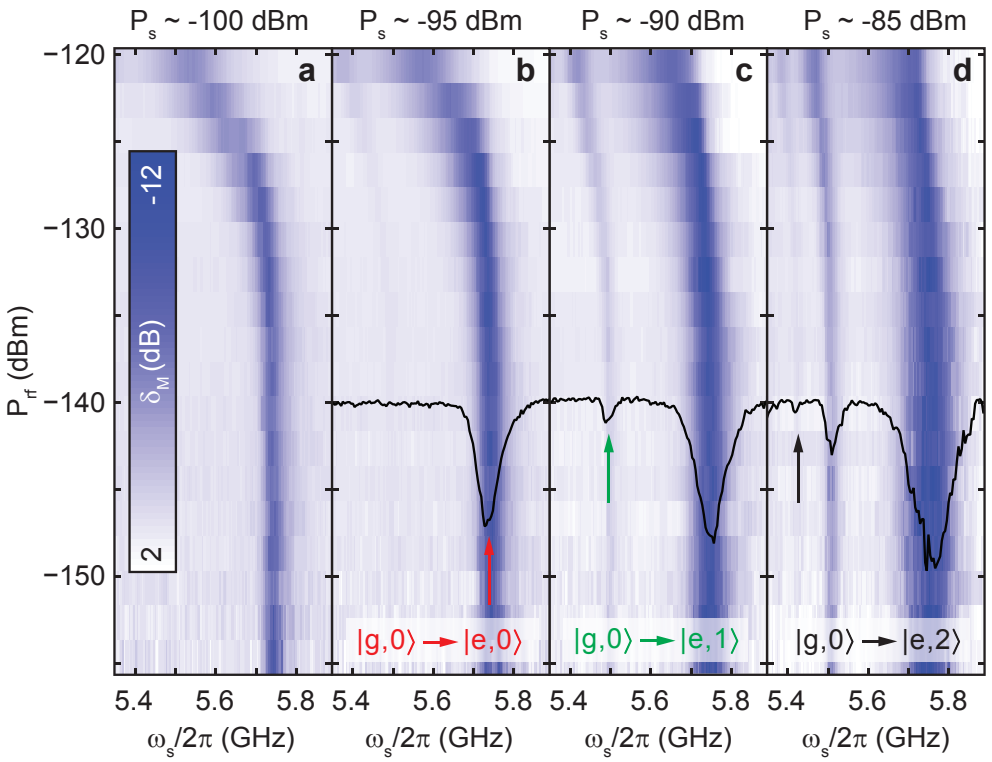

Figure 5.14: Two-tone spectroscopy of qubit 1 at $\delta\Phi_x = 0$. (a) The relative magnitude shift δ_M at ω_{rf} (color-coded) is plotted as a function of $\omega_s/2\pi$ and the probe tone power P_{rf}. In this measurement, $P_s \sim -100\,\mathrm{dBm}$ and the $3\lambda/2$-mode ($\omega_3/2\pi = 7.860\,\mathrm{GHz}$) was used as readout cavity mode. Since $\omega_3 > \tilde{\omega}_q$, the qubit transition frequency $\tilde{\omega}_q$ is shifted towards lower frequencies for increasing P_{rf}. (b) $P_s \sim -95\,\mathrm{dBm}$. At small P_{rf} only the $|g,0\rangle \rightarrow |e,0\rangle$ transition (red arrow) is visible. The black solid line in (b) - (d) represents the spectrum at $P_{rf} \sim -140\,\mathrm{dBm}$. (c) $P_s \sim -90\,\mathrm{dBm}$. The two-photon induced transition $|g,0\rangle \rightarrow |e,1\rangle$ (green arrow) becomes more prominent. (d) $P_s \sim -85\,\mathrm{dBm}$. A third spectroscopic feature corresponding to the three-photon induced transition $|g,0\rangle \rightarrow |e,2\rangle$ is unveiled.

experiment can be conducted in a circuit QED architecture, too. Figure 5.14 shows two-tone spectroscopy measurements[6] of qubit 1 at its degeneracy point $\delta\Phi_x = 0$. For small spectroscopy powers P_s (see Fig. 5.14 a), we observe the expected ac-Zeeman shift of $\tilde{\omega}_q$ for increasing probe tone powers P_{rf}. The most prominent feature in our data corresponds to the transition from the qubit ground to its first excited state. Since we are well in the dispersive limit ($\delta_3 = 7.860\,\mathrm{GHz} - 5.753\,\mathrm{GHz} \gg g_n$), this transition corresponds to $|g,0\rangle \rightarrow |e,0\rangle$, where we followed the notation introduced in section 5.1. Furthermore, we only take into account the λ-mode ($\omega_2/2\pi = 5.243\,\mathrm{GHz}$) as the other cavity modes are far detuned and, in addition, $g_2 = 62.8\,\mathrm{MHz} > g_1, g_3$. For increasing P_s, a second spectroscopic feature becomes visible. This feature appears only for large P_{rf} but with increasing P_s, already at moderate probe tone powers (see Fig. 5.14 c and d) and could be identified as the two-photon driven transition $|g,0\rangle \rightarrow |e,1\rangle$. In other words, this transition can be driven when $2\omega_s = \tilde{\omega}_q + \omega_2$ and constitutes a second order process. Therefore, the transition probability is significantly reduced compared to single-photon processes which is

[6]The full data set for each panel in Fig. 5.14 comprises 18 probe powers P_{rf}. The spectroscopy tone was swept between 5.35 GHz and 6.25 GHz with an increment of 4 MHz. We operated the VNA in cw-mode and averaged 20 times over 2 points with an intermediate frequency (IF) bandwidth of 10 Hz. Thus, the measurement time for each spectroscopy power P_s was approximately 225 min.

reflected by a strongly reduced amplitude in our spectroscopy data[7]. By further increasing the spectroscopy amplitude, a third line becomes visible (see Fig. 5.14 d). We identify this spectroscopic signature as the three-photon induced transition $|\mathrm{g},0\rangle \rightarrow |\mathrm{e},2\rangle$ which can be driven when $3\omega_\mathrm{s} = \tilde{\omega}_\mathrm{q} + 2\omega_2$. At such large spectroscopic drives, the linewidths of the one- and two-photon transition are substantially power broadened.
In this section we introduced techniques for characterizing coupled qubit-cavity systems by means of spectroscopy and cavity transmission experiments. Furthermore, our experiments show that the fabrication process of our flux qubits - initially optimized for SQUID-qubit systems - could be successfully expanded into circuit QED architectures. Moreover, even for qubits coupled via a purely geometric inductance, the strong-coupling limit could be reached. In the following section we will exploit the engineering potential of our quantum devices to further increase the qubit-cavity coupling rates g_n.

[7]We note that two-photon driving of the qubit alone is not possible at $\delta\Phi_\mathrm{x} = 0$ owing to symmetry considerations (see section 5.5.2).

5.5 Selection rules in a strongly coupled qubit-cavity system

One of the key features of circuit QED setups is their design flexibility and the ability to tune their properties *in situ* by an external control parameter. This triggered experimental studies of multi-photon driven artificial atoms, including population inversion [206], Mach-Zehnder interferometry [186], Landau-Zener interference [188], qubits coupled to microscopic defects [207], amplitude spectroscopy [208], multi-photon spectroscopy of hybrid quantum systems [209] and sideband transitions [202]. Recently, an experimental investigation of a two-photon driven flux qubit coupled to a lumped-element LC resonator shed light on the controllability of fundamental symmetry properties of circuit QED systems [142]. However, in that particular work, the effect of microscopic defects and a weak-coupling scenario caused by the high loss rate of the lumped element LC-resonator complicated the analysis of the data.
In this section, we present one- and two-photon spectroscopy data of a qubit-resonator system in the strong coupling limit. Our results provide clear experimental evidence for the controlled transition from an operating point governed by dipolar selection rules [210] to a regime where one- and two-photon excitations of the artificial atom coexist. In addition, we find that the vacuum coupling between qubit and resonator can be straightforwardly extracted from the two-photon spectra because the detuned two-photon drive does not populate the relevant resonator mode significantly. The results presented in this section

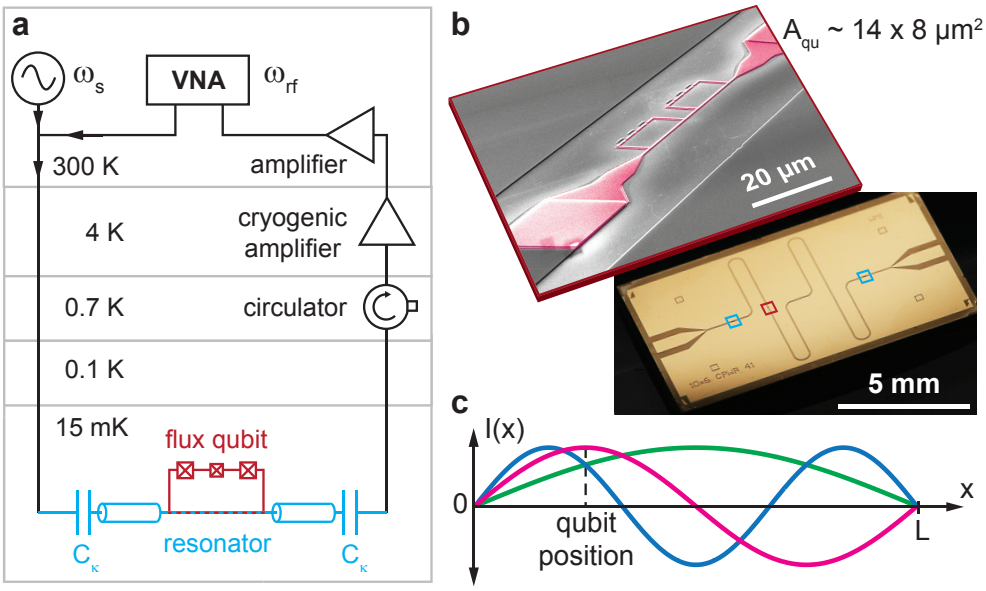

Figure 5.15: Measurement setup, images of our quantum circuit and sketch of the current distribution. (a) The experimental setup is identical to the one depicted in Fig. 5.6, however, the qubits are coupled galvanically to the resonator which is indicated by the dashed red-blue line. (b) Optical and false-color scanning electron images of the galvanically coupled quantum circuit. The position of the flux qubits (magenta) is indicated by the red box and the light blue boxes mark the position of the coupling capacitors. (c) Sketch of the current distribution $I(x)$ of the first three resonator modes. Their resonance frequencies are: $\omega_1/2\pi = 2.745\,\mathrm{GHz}$ ($\lambda/2$-mode, green), $\omega_2/2\pi = 5.324\,\mathrm{GHz}$ (λ-mode, magenta) and $\omega_3/2\pi = 7.775\,\mathrm{GHz}$ ($3\lambda/2$-mode, blue). The center conductor has a length $L = 23\,\mathrm{mm}$ and is terminated at both ends with interdigital finger capacitors ($C_\kappa \sim 10\,\mathrm{fF}$). The quality factors $Q_n > 6.3 \cdot 10^3$ and the resonance frequencies were determined at maximum qubit-cavity detuning.

are summarized in Ref. [211]. Figure 5.15 a and b show a schematic of the measurement setup and images of our quantum circuit, respectively. The setup is identical to the one used in the previous section, however, the two qubits are now coupled galvanically to the resonator [181]. At a current antinode of the λ-mode, a 80 µm section of the resonator's center conductor is replaced by a narrow ($\sim$ 500 nm) aluminum strip with two galvanically connected flux qubits (see Figure 5.15 b). This modification of the transmission line geometry gives rise to a position-dependent inductance $L(x)$ and capacitance $C(x)$ per unit length. In turn, this leads to an asymmetric[8] distribution [212] of the higher mode frequencies, $\omega_n \neq n \cdot \omega_1$ with $n \in \mathbb{N}$. More importantly, the kinetic inductance L_{kin} of the narrow strip constitutes an additional large contribution to the overall mutual inductance M, thereby enhancing the qubit-cavity coupling. In the following, we extract the coupling rates g_n from qubit spectroscopy and cavity transmission measurements employing the experimental techniques presented in the last section. Although two qubits are present in our system, our analysis will focus on one qubit only.

5.5.1 Transmission spectra and one-photon qubit spectroscopy

Figure 5.16 summarizes the initial characterization measurements. The spectroscopic response of the coupled qubit-cavity system is shown in Fig. 5.16 a and reflects the hyperbolic flux dependence of $\tilde{\omega}_{\mathrm{q}}$. For this measurement, we used the λ-mode as probe tone and performed two-tone spectroscopy. Fitting the center frequencies of the qubit's spectroscopic response to Eq.(2.15) yields the qubit parameters $\Delta/h = 6.88\,\mathrm{GHz}$ and $\epsilon/h = 1.66\,\mathrm{GHz} \cdot \delta\Phi_{\mathrm{x}}[\mathrm{m}\Phi_0]$ (see Fig. 5.16 b). Additional features can be identified in our spectroscopy data: first, around $\omega_{\mathrm{s}}/2\pi \sim 7.00\,\mathrm{GHz}$, a flux-independent signature is faintly visible and can be attributed to a spurious fluctuator present in our system. Such fluctuators can be either resonant modes or microscopic two-level systems and can significantly degrade the coherence properties of solid-state based artificial atoms [78]. We extract a relatively large splitting of $\sim 81\,\mathrm{MHz}$ at the flux positions of the qubit-fluctuator avoided crossing ($\delta\Phi_{\mathrm{x}} \sim \pm 1\,\mathrm{m}\Phi_0$). Recently, a time-domain characterization of the qubit-fluctuator dynamics [213] and multi-photon spectroscopy [207] were performed in systems exhibiting similar large qubit-fluctuator couplings. Furthermore, it was shown that the presence of two-level fluctuators can lead to symmetry breaking [142], however, this was not the case in our experiment and for the remainder of this section we will therefore neglect the presence of the fluctuator level. Second, in the region $\omega_{\mathrm{s}}/2\pi \approx 7.4 - 7.6\,\mathrm{GHz}$ our data reveals a flux-dependent spectroscopic signature which is consistent with a two-photon driven blue-sideband transition of the qubit and the $3\lambda/2$-mode (resonance condition: $2\omega_{\mathrm{s}} = \tilde{\omega}_{\mathrm{q}} + \omega_3$) [142, 202, 214]. Figure 5.16 c and d show the cavity transmission spectra of the λ- and $3\lambda/2$-mode, respectively. We extract the couplings g_n by fitting the energy level spectrum of the multi-mode Jaynes-Cummings Hamiltonian given in Eq.(5.10) to the measured spectra. For the fit procedure we use the qubit parameters from Fig. 5.16 b and from two-tone spectroscopy performed on the second qubit ($\Delta/h = 2.12\,\mathrm{GHz}, \epsilon/h = 1.69\,\mathrm{GHz} \cdot \delta\Phi_{\mathrm{x}}[\mathrm{m}\Phi_0]$; data not shown). We find qubit-cavity coupling rates of $g_1/2\pi = 56.7\,\mathrm{MHz}$, $g_2/2\pi = 106.5\,\mathrm{MHz}$ and $g_3/2\pi = 90.7\,\mathrm{MHz}$ in excellent

[8] For our CPW, the resonance frequencies scale as $1 : 1.93 : 2.83$.

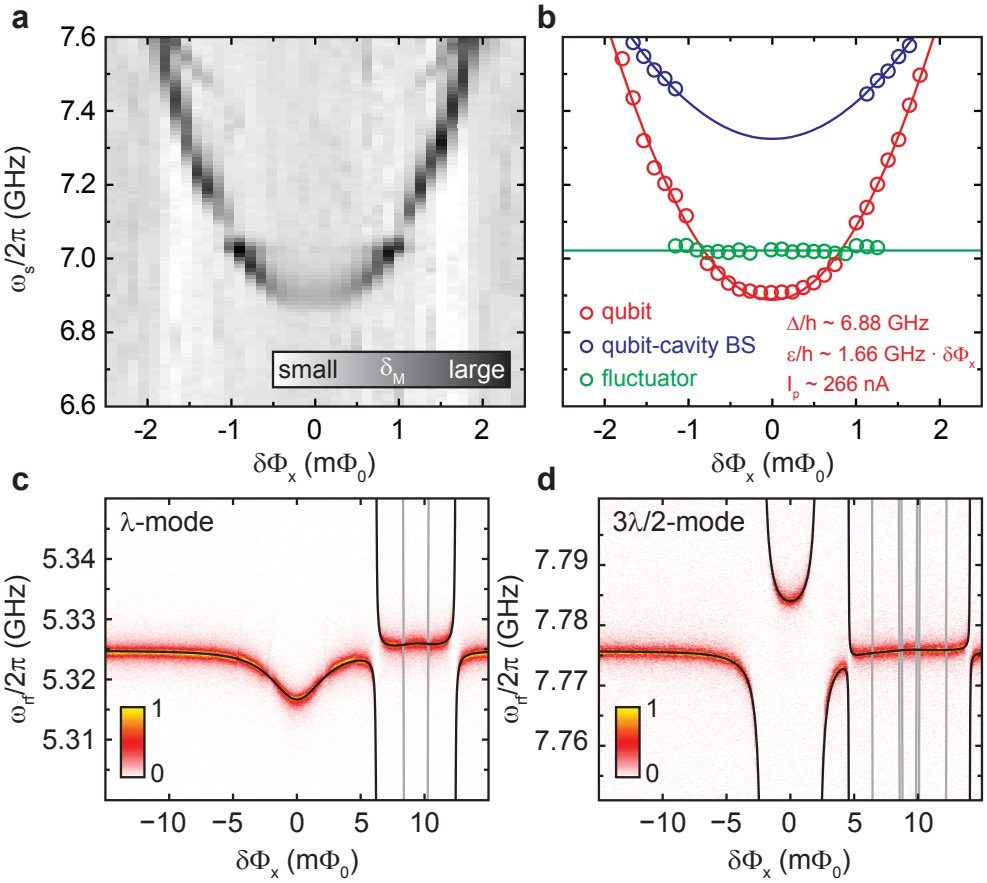

Figure 5.16: Microwave spectroscopy and cavity transmission measurements. (a) Relative shift in transmission magnitude δ_{M} (gray-scale) of the readout tone as a function of $\delta\Phi_{\mathrm{x}}$ and $\omega_{\mathrm{s}}/2\pi$. (b) Fitted center frequencies of the spectroscopic response (colored circles) shown in (a). The solid red line is a fit to Eq.(2.15) while the green line represents a fit to the fluctuator data points. The solid blue curve corresponding to the qubit-cavity blue sideband (BS) is evaluated using the fit parameters from the qubit data and the experimentally determined frequency ω_3. (c) Cavity transmission spectrum of the λ-mode (linear scale, arb. units) as a function of $\delta\Phi_{\mathrm{x}}$ and probe frequency $\omega_{\mathrm{rf}}/2\pi$. The solid lines represent a numerical fit of the spectrum according to Eq.(5.10) to the data. In contrast to the black lines, the gray lines represent energy levels of states with more than one excitation. (d) Same as in (c) but for the $3\lambda/2$-mode.

agreement with the data shown in Fig. 5.16 c[9] and d. Moreover, we find a FWHM of the qubit spectroscopy signal of $\gamma/2\pi \approx 43\,\mathrm{MHz}$ (see section 5.5.3) and since $\kappa_n < 1.4\,\mathrm{MHz}$ for all cavity modes, our quantum circuit is in the strong-coupling limit. Using Eq.(5.11), g_2, I_{p} and $I_{\mathrm{r},2} = 19.0\,\mathrm{nA}$ we find $M \approx 14\,\mathrm{pH}$. The value for M can be further enhanced by reducing the width of the narrow aluminum strip connecting qubit and resonator [212]. Finally, a measurement of the power-dependence of the qubit's ac-Zeeman shift yields a calibration for P_{rf} and thus for the average photon number ($n < 0.94$ for all measurements shown in Fig. 5.16).

[9] We note, that a fit to the cavity's ac-Zeeman shift of the λ-mode according to Eq.(5.14) yields a slightly larger $g_2/2\pi = 110\,\mathrm{MHz}$. The discrepancy is attributed to the presence of the additional strongly coupled cavity modes which is not captured by Eq.(5.14).

5.5.2 Two-photon spectroscopy: selection rules and controlled symmetry breaking

We now investigate the spectroscopic response of the qubit-cavity system under direct two-photon driving. Again we use the flux-dependent transmission maximum of the λ-mode (see Fig. 5.16 c) as probe frequency. However, to induce two-photon transitions, the spectroscopy drive is applied in a frequency range where $2\omega_\mathrm{s} \approx \tilde{\omega}_\mathrm{q}$. The gray-scale data and the fitted center frequencies of the spectroscopy signal are shown in Fig. 5.17 a and b, respectively. We observe a feature with a hyperbolic flux dependence and two anticrossings located symmetrically around $\delta\Phi_\mathrm{x} = 0$. These signatures are the two-photon spectroscopic response of the qubit strongly coupled to the $3\lambda/2$-mode. Furthermore, a one-photon driven red sideband transition (resonance condition $\omega_\mathrm{s} = \tilde{\omega}_\mathrm{q} - \omega_2$) can be identified. This transition corresponds to an exchange of an excitation between the qubit and the λ-mode ($|g,1\rangle \leftrightarrow |e,0\rangle$). A fit of the qubit-like spectroscopic response to Eq. (2.15) yields the two-photon qubit parameters $\Delta^{2\mathrm{p}}/h = 3.48\,\mathrm{GHz}$ and $\epsilon^{2\mathrm{p}}/h = 0.926\,\mathrm{GHz}\cdot\delta\Phi_\mathrm{x}[\mathrm{m}\Phi_0]$ which are in good agreement with the expected values $\Delta^{2\mathrm{p}} = \Delta/2$ and $\epsilon^{2\mathrm{p}} = \epsilon/2$. We attribute the deviations in the two-photon response to a higher intracavity photon number ($n_2 \sim 2.2$) inducing an ac-Zeeman shift in $\tilde{\omega}_\mathrm{q}$ towards higher frequencies.

In the following, we analyze the gradual disappearance of the qubit spectroscopy signal (see Fig. 5.17 a) for $\delta\Phi_\mathrm{x} \to 0$. Depending on the value of the external control parameter $\delta\Phi_\mathrm{x}$, the symmetry of the Jaynes-Cummings Hamiltonian will imply selection rules on the allowed transitions. Formally, selection rules are intimately connected to the quantum mechanical concept of parity. The parity operator[10] $\hat{\Pi}$ divides the set of all states into

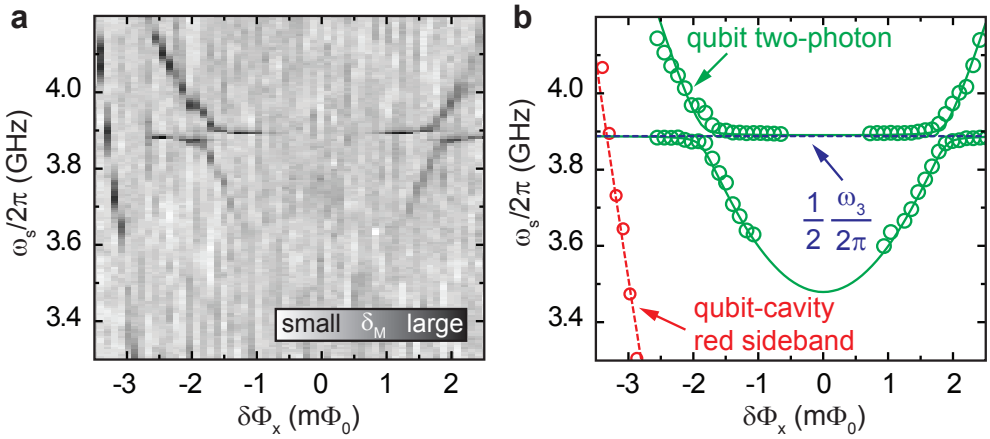

Figure 5.17: Microwave spectroscopy under two-photon driving. (a) Relative shift in the transmission magnitude δ_M (gray-scale) at the probe tone frequency ω_rf as a function of $\delta\Phi_\mathrm{x}$ and the spectroscopy frequency $\omega_\mathrm{s}/2\pi$. The two avoided crossings correspond to the qubit-cavity anticrossings visible in the cavity transmission spectrum of the $3\lambda/2$-mode (see Fig. 5.16 d). On the left hand side, a one-photon driven red sideband transition is visible. (b) Fitted center frequencies of the two-photon spectroscopy signal (green circles) as a function of $\delta\Phi_\mathrm{x}$. The solid green line represents the numerically evaluated energy level spectrum of Hamiltonian (5.10) with $\omega_n \to \omega_n/2$, $\omega_\mathrm{q} \to \omega_\mathrm{q}/2$ and $g_n \to g_n/2$. Dotted blue line: $1/2\cdot\omega_3/2\pi$. Dashed red line: calculated flux dependence of the red sideband transition using Δ and ϵ extracted from the one-photon spectroscopy data.

[10] A very good pedagogical introduction to the parity operator can be found in Ref. [215].

three groups: even states $|\psi_+\rangle$, odd states $|\psi_-\rangle$ and states without well-defined parity. The former two are eigenstates of $\hat{\Pi}$ with eigenvalues $+1$ and -1, respectively. In a similar fashion, it is possible to divide the set of all operators into the same classes. While an even operator $\hat{A}_+$ commutes with $\hat{\Pi}$, an odd operator $\hat{A}_-$ anticommutes with $\hat{\Pi}$. It can be shown [141], that the matrix elements of an even operator are zero between states of different parity

$$\langle\psi_+|\hat{A}_+|\psi_-\rangle = \langle\psi_-|\hat{A}_+|\psi_+\rangle = 0 \quad , \tag{5.19}$$

while the matrix elements of an odd operator are zero between states of equal parity

$$\langle\psi_+|\hat{A}_-|\psi_+\rangle = \langle\psi_-|\hat{A}_-|\psi_-\rangle = 0 \quad . \tag{5.20}$$

At $\delta\Phi_\mathrm{x} = 0$, the two lowest qubit energy eigenstates $|\mathrm{g}\rangle$ and $|\mathrm{e}\rangle$ represent symmetric and antisymmetric superpositions of the persistent current states $|\pm I_\mathrm{p}\rangle$. Transitions between $|\mathrm{g}\rangle$ and $|\mathrm{e}\rangle$ are induced by an external drive $\propto (\hat{a}^\dagger + \hat{a})$ with respect to a frame rotating at the drive frequency (see Eq. (5.18)). It is easy to verify that the drive $(\hat{a}^\dagger + \hat{a})$ is an odd parity operator [215]. Since $|\mathrm{g}\rangle$ and $|\mathrm{e}\rangle$ correspond to states with different parities, one-photon transitions are allowed at the qubit degeneracy point. On the other hand, a two-photon (n-photon) transition is equivalent to the application of two (n) subsequent drives with frequency $\tilde{\omega}_\mathrm{q}/2$ ($\tilde{\omega}_\mathrm{q}/n$). With

$$(\hat{\Pi}\hat{A}_-\hat{\Pi})^n = (-1)^n \hat{A}_-^n \quad , \tag{5.21}$$

the two-photon drive acts as an even parity operator and two-photon transitions between $|\mathrm{g}\rangle$ and $|\mathrm{e}\rangle$ are strictly forbidden.

Away from the qubit degeneracy point ($\delta\Phi_\mathrm{x} \neq 0$), the parity of the Hamiltonian (5.10) is not well-defined owing to the asymmetry of the qubit's double well potential (see Fig. 2.8 b). Mathematically, the operator representing the total number of excitations, $M = \hat{a}^\dagger\hat{a} + \hat{\sigma}_+\hat{\sigma}_-$ (see section 5.1) does not commute with the Hamiltonian due to the presence of terms $\propto g_n \cos\theta(\hat{a}_n^\dagger + \hat{a}_n)\hat{\sigma}_\mathrm{z}$.

In the dispersive limit, the effective Hamiltonian can be derived by means of a Schrieffer-Wolff transformation yielding finite transition matrix elements [132, 142, 149]

$$D^{(1)} = \frac{\Omega}{4}\sin\theta \quad , \tag{5.22}$$

$$D^{(2)} = \frac{\Omega^2}{4\Delta}\sin^2\theta\cos\theta \tag{5.23}$$

for one- and two-photon transitions, respectively. In the above expressions, Ω refers to the driving strength. The $\cos\theta$-dependence of the two-photon spectroscopy signal is qualitatively reproduced by our data (see Fig. 5.17 a) and explains the gradual disappearance of the qubit signature ($\cos\theta \to 0$ for $\delta\Phi_\mathrm{x} \to 0$). The selection rules for one- and two-photon driven red and blue sideband transitions can be derived [214] in a similar fashion. The two-photon blue sideband illustrated in Fig. 5.16 corresponds to the transition $|g, 0\rangle \to |e, 1\rangle$. These states have the same parity and since the two-photon drive has even parity, the transition is in principle possible for arbitrary $\delta\Phi_\mathrm{x}$. However, as a second-order transition, its amplitude is small and the spectroscopic signature can not be resolved within our measurement resolution and for low spectroscopy powers P_s. Finally we note, that for

the harmonic resonator potential multi-photon transitions are forbidden in general [142], which is illustrated by the absence of a flux-independent spectroscopic feature at $\omega_s = \omega_3/2$ except for the anticrossing regions. Here, a flux-independent resonator-like signature is visible owing to the large qubit-like component in the eigenstates of the Jaynes-Cummings Hamiltonian (see Eqs. (5.3) and (5.4)).

5.5.3 Anticrossing under two-photon driving

The anticrossings in the spectrum shown in Fig. 5.17 a represent the spectroscopically resolved Rabi mode splitting between the qubit and the $3\lambda/2$-mode using a two-photon drive. Figure 5.18 a shows the relative shift in magnitude δ_M at the probe tone frequency as a function of $\delta\Phi_x$ and $\omega_s/2\pi$ for the anticrossing at positive $\delta\Phi_x$. The fact that we observe a resonator-like (i.e. flux-independent) two-photon response indicates that the corresponding eigenstate is considerably 'dressed' by the qubit. However, at flux values where qubit and cavity mode are detuned, the different linewidths allow to clearly distinguish qubit and cavity. On resonance, the eigenstates $|\pm, 1\rangle$ of the coupled system are symmetric and antisymmetric superpositions of $|g, 1\rangle$ and $|e, 0\rangle$. Here, the linewidths become equal and are given by $(\gamma + \kappa_3)/2 \approx 22\,\mathrm{MHz}$. From the fitted center frequencies of the spectroscopy signal we extract a minimum separation of $1/2 \cdot 2\tilde{g}_3/2\pi = \tilde{g}_3/2\pi = 77.4\,\mathrm{MHz}$. Taking into account that $\sin\theta = 0.89$ at that particular flux position, we obtain $g_3/2\pi \approx 87.0\,\mathrm{MHz}$. The experimentally determined qubit-cavity coupling rate is in very good agreement with $g_3/2\pi = 90.7\,\mathrm{MHz}$ determined from fits to the low-power cavity transmission spectra and one-photon qubit spectroscopy (see Fig. 5.16). Thus, a dispersive readout of the qubit-cavity anticrossings constitutes an alternative experimental technique to determine the vacuum Rabi splitting. In contrast to a resonant readout (see section 5.4.3), the drive tones ω_{rf} and ω_s do not populate the relevant cavity mode since they are applied both off-resonant.

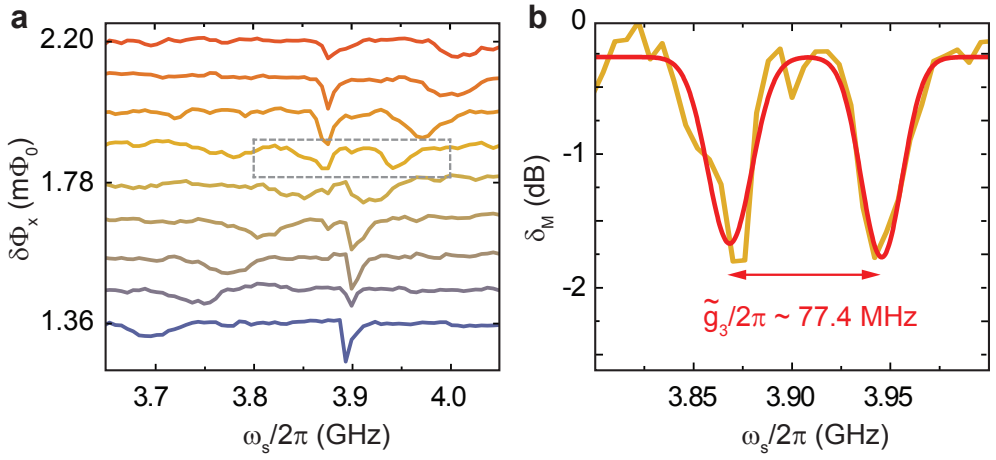

Figure 5.18: Vacuum Rabi splitting. (a) Qubit-cavity anticrossing under two-photon driving for positive $\delta\Phi_x$. The plot shows the shift in magnitude δ_M at ω_{rf} as a function of $\delta\Phi_x$ and $\omega_s/2\pi$. The strongly flux-dependent and broad spectroscopic feature corresponds to a qubit-like response while the flux-independent signature has cavity-like character. (b) On resonance, the separation between the two dips is $g_3 \sin\theta = 77.4\,\mathrm{MHz}$. The red solid line represents a fit to Lorentzian line shapes. From the FWHM, $\gamma/2\pi \approx 43\,\mathrm{MHz}$ can be estimated. This value is in agreement with the linewidth obtained from low-power one-photon spectroscopy.

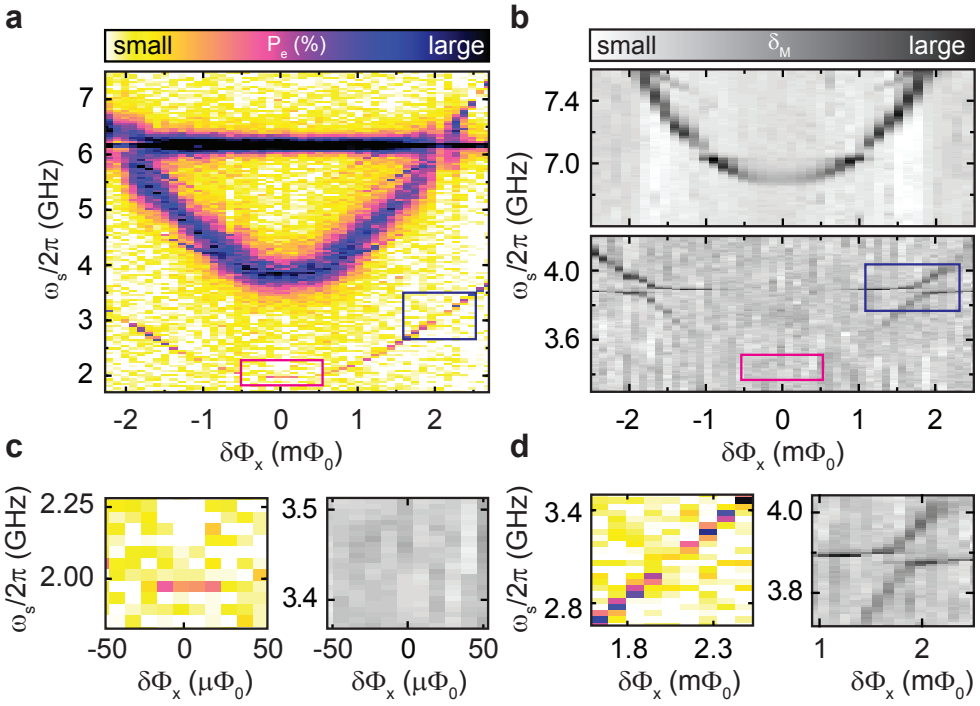

Figure 5.19: One- and two-photon spectroscopy of superconducting flux qubits. (a) Measured probability P_e (color-coded) of finding the qubit in the excited state as a function of $\delta\Phi_\mathrm{x}$ and the spectroscopy frequency $\omega_\mathrm{s}/2\pi$ for a weakly coupled oscillator-qubit system. Around 6 GHz, the flux-independent resonator level is directly driven. The data is taken from Ref. [142]. The color boxes in (a) and (b) mark the areas which are compared to our results in (c) and (d), respectively. (b) One- and two photon spectroscopy of the circuit QED setup discussed in this section. The plot shows the relative shift in the transmission magnitude δ_M (gray-scale) as a function of $\delta\Phi_\mathrm{x}$ and the spectroscopy frequency $\omega_\mathrm{s}/2\pi$. (c) Comparison of the two-photon spectroscopy data at $\delta\Phi_\mathrm{x} = 0$. While the presence of a fluctuator level breaks the symmetry (left panel) thus allowing two-photon transitions, the signal amplitude vanishes in our setup owing to dipolar selection rules (right panel). (d) Two-photon avoided crossing. The vacuum Rabi splitting can not be resolved due to the large resonator loss rate κ (weak-coupling limit, see left panel). In our setup (right panel), the avoided crossing can be clearly resolved since the strong coupling condition $g_n > \kappa_n, \gamma$ is fulfilled.

Finally, we compare our results to an experimental investigation of a two-photon driven flux qubit published recently [142]. Here, the state of the qubit was detected using a dc-SQUID coupled to a lumped-element LC resonator. The setup is almost identical to the SQUID-qubit system discussed in section 4.4.2. Microwave spectroscopy was performed using the adiabatic shift pulse method [85, 87], yielding the one- and two-photon spectroscopy data depicted in Fig. 5.19 a. The extracted qubit-resonator coupling rate $g/2\pi = 115\,\mathrm{MHz}$ is similar to the coupling strength realized in our circuit QED setup. While the one-photon branch has a very broad linewidth owing to a large resonator decay rate of $\kappa/2\pi \sim 210\,\mathrm{MHz}$, the linewidth of the two-photon branch is considerably smaller. This constitutes direct evidence that a two-photon drive is not populating the resonator but selectively drives the qubit.

In contrast to our results which are summarized in Fig. 5.19 b, a non-vanishing two-photon signal is visible at $\delta\Phi_\mathrm{x} = 0$. This is attributed to a flux-independent two-level fluctuator around $\omega_\mathrm{f} = 3.94\,\mathrm{GHz}$. The presence of this fluctuator breaks the symmetry of the total system, leading to a not well-defined parity. Thus, the strict selection rules discussed

above do not apply and only a reduction in signal amplitude is observed, while in our measurements the two-photon signal vanishes at $\delta\Phi_x = 0$ (see Fig. 5.19 c). Furthermore, κ is larger than g near the two-photon qubit-resonator anticrossing (weak coupling limit) and compared to our measurement, the vacuum Rabi splitting can not be resolved experimentally (see Fig. 5.19 d). The excitation energy is rapidly lost to the environment via the low-quality factor ($Q \sim 100$) lumped element LC resonator.

Our data presented in this section provides clear experimental evidence for the existence of selection rules in a strongly coupled circuit QED setup. Moreover, a two-photon readout of the qubit-resonator avoided crossing allows to determine the vacuum Rabi frequency using a dispersive readout scheme.

5.6 Circuit QED in the ultrastrong-coupling regime

In this section we present one of the central results of this thesis. We report on the first experimental realization of a circuit QED system operating in the ultrastrong-coupling regime [212, 216–218]. In this regime, the qubit-cavity coupling rates g_n reach a considerable fraction of the cavity transition frequencies ω_n and consequently, the rotating wave approximation (RWA) inherent to the Jaynes-Cummings model is not applicable. In our system we realized remarkable normalized coupling strengths g_n/ω_n of up to 12% by enhancing the inductive coupling [212] of a flux qubit to a transmission line resonator. To this end, we use the large non-linear inductance of a Josephson junction shared between qubit and cavity.

The observation of ultrastrong-coupling was recently reported in a solid-state semiconductor system [219, 220] consisting of *multiple* quantum wells embedded in a microcavity with resonance frequency ω_r. The presented data only showed quantitative deviations from the Jaynes-Cummings model and although $g_N/\omega_r \approx 0.24$ could be realized in a system consisting of $N = 25$ quantum wells [221], the experiment effectively probed the collective N-atom interaction strength given by $g_N = g\sqrt{N}$. This $\sqrt{N}$-scaling – theoretically analyzed by the Tavis-Cummings model [222] – has been observed in many different experimental setups operating in various energy regimes (see Ref. [115] and references therein).

In our setup, however, ultrastrong-coupling is realized between a *single* atom and a cavity

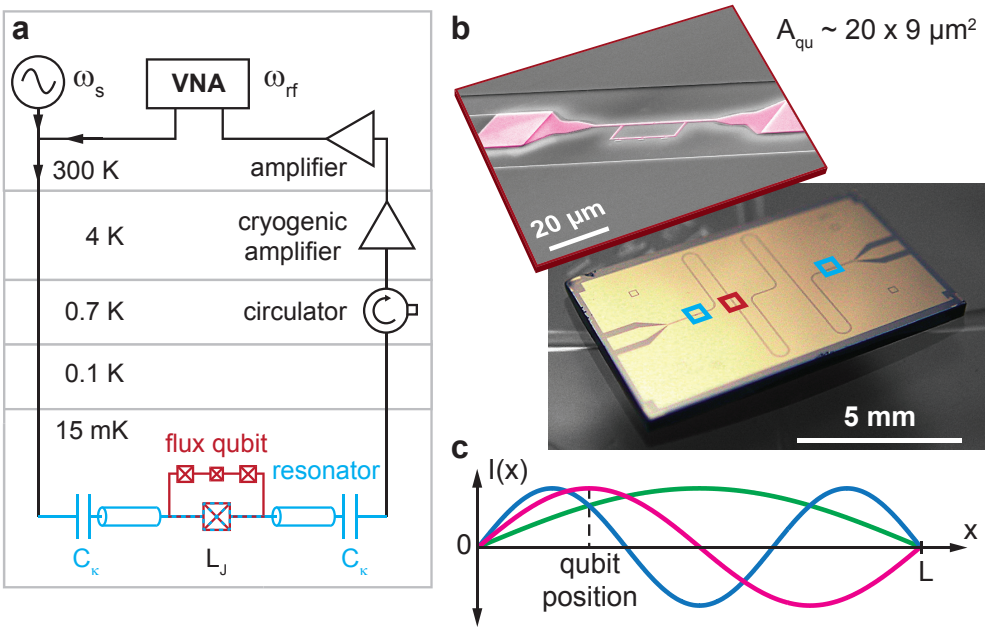

Figure 5.20: Measurement setup, images of our quantum circuit and sketch of the current distribution. (a) The experimental setup is identical to the one depicted in Fig. 5.15. In addition to a galvanic coupling (dashed red-blue line), qubit and resonator share a large-area Josephson junction (dashed red-blue crossed box). The large Josephson inductance L_J of this junction mediates the ultrastrong coupling. (b) Optical and false-color scanning electron images of the quantum circuit. The position of the flux qubit (magenta) is indicated by the red box and the light blue boxes mark the position of the interdigital finger capacitors ($C_\kappa \sim 10\,\mathrm{fF}$). (c) Sketch of the current distribution $I(x)$ of the first three resonator modes. Their resonance frequencies are: $\omega_1/2\pi = 2.782\,\mathrm{GHz}$ ($\lambda/2$-mode, green), $\omega_2/2\pi = 5.357\,\mathrm{GHz}$ (λ-mode, magenta) and $\omega_3/2\pi = 7.777\,\mathrm{GHz}$ ($3\lambda/2$-mode, blue).

mode ($N = 1$). Furthermore, the transmission spectra of our qubit-cavity system reveal anticrossings that cannot be explained within the Jaynes-Cummings model. These anticrossings result from counterrotating terms in the qubit-cavity interaction Hamiltonian and become prominent only in the ultrastrong-coupling regime with large normalized coupling strengths g_n/ω_n. The most important results of this section are summarized in Ref. [8].

5.6.1 Experimental setup & circuit design

Figure 5.20 a and b show a schematic of the measurement setup and images of our quantum circuit, respectively. The qubit-cavity system can be characterized by cavity transmission and two-tone spectroscopy measurements [102, 181] as explained in sections 5.4 and 5.5. The qubit is fabricated at a maximum of the current distribution for the λ-mode (see Fig. 5.20 c). The galvanic connection to the resonator's center conductor is realized by a narrow ($\sim 1\,\mu$m) aluminum strip as shown in Fig. 5.21 a. For the bottom and top aluminum layer we evaporate a 50 nm and 80 nm thick aluminum film, respectively. In order to ensure a smooth galvanic coating (see Fig. 5.21 b and c), we used a niobium film thickness of 100 nm for our CPW resonator. The crucial building block of our quantum circuit is a large-area Josephson junction interrupting the narrow constriction (see Fig. 5.21 d). This junction shared between qubit and cavity represents a large inductance L_J and mediates the ultrastrong-coupling. According to Eq. (5.11), the qubit-cavity coupling is determined by the mutual inductance $M = L_\mathrm{J} + L$. Here, L represents the inductance of the shared edge between center conductor and the qubit including kinetic and geometric contributions. Although $L_\mathrm{J} > L$ dominates M, it has negligible influence

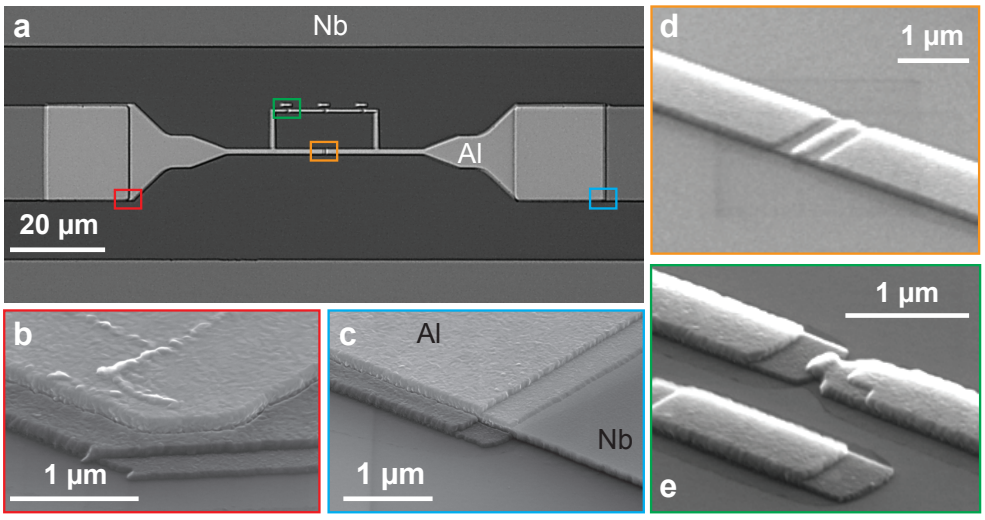

Figure 5.21: Optical microscope and SEM images of our flux quantum circuit. (a) Optical microscope image of the 80 µm gap interrupting the CPW's center conductor and the galvanically connected flux qubit (loop area: $20\,\mathrm{x}\,9\,\mu\mathrm{m}^2$). The Nb-Al interface in the overlap regions is formed by native Nb oxides and is not specially cleaned prior to the aluminum deposition. The color boxes mark the areas magnified in (b)-(e). (b) and (c) SEM images of the edges in the overlap regions. (d) SEM image of the large Josephson junction. The area of the coupling junction is approximately $7\,A_\mathrm{JJ}$. Here, $A_\mathrm{JJ} \approx 250\,\mathrm{x}\,140\,\mathrm{nm}^2$ represents the area of a regular Josephson junction embedded in the qubit loop as shown in (e). From SEM images of test samples fabricated in the same run we determined the scaling factor for the small qubit junction $\alpha \sim 0.7$.

on the vacuum current $I_{\mathrm{r},n} \approx \sqrt{\hbar\omega_n/L_\mathrm{r}}$ in the resonator because the total resonator inductance $L_\mathrm{r} \gg L_\mathrm{J}, L$. For typical critical current densities $j_\mathrm{c} \sim 1-2\,\mathrm{kA/cm^2}$ a coupling junction area of $500\,\mathrm{x}\,500\,\mathrm{nm}^2$ results in a Josephson inductance $L_\mathrm{J} \sim 65-130\,\mathrm{pH}$. This inductance – and thus the qubit-cavity coupling rates g_n – can be further increased by reducing the area of the coupling junction as long as $L_\mathrm{J} \propto 1/I_\mathrm{c}$ is small compared to the total inductance of the qubit which is typically $L_\mathrm{tot} \approx 2-3\,\mathrm{nH}$.
In the qubit eigenbasis, the combined system can be described by the Hamiltonian

$$\hat{H} = \hat{H}_\mathrm{q} + \sum_n \left[\hat{H}_\mathrm{n} + \hbar g_n \left(\hat{a}_n^\dagger + \hat{a}_n\right)\left(\cos\theta\,\hat{\sigma}_\mathrm{z} - \sin\theta\,\hat{\sigma}_\mathrm{x}\right)\right] \quad . \tag{5.24}$$

Here, $\hat{H}_\mathrm{q} = \hbar\omega_\mathrm{q}\hat{\sigma}_\mathrm{z}/2$ is the qubit Hamiltonian and $\hat{H}_n = \hbar\omega_n(\hat{a}_n^\dagger\hat{a}_n + 1/2)$ represents the Hamiltonian of the nth cavity mode. The Pauli operator $\hat{\sigma}_\mathrm{x}$ can be expressed as sum of the qubit raising ($\hat{\sigma}_+$) and lowering ($\hat{\sigma}_-$) operator. Thus, the Hamiltonian in Eq. (5.24) explicitly contains counterrotating terms of the form $\hat{a}_n^\dagger\hat{\sigma}_+$ and $\hat{a}_n\hat{\sigma}_-$. Using a RWA, Eq. (5.24) reduces to the well-known multi-mode Jaynes-Cummings model given by Eq. (5.10).

5.6.2 Microwave spectroscopy & power calibration

The qubit-cavity system is characterized by two-tone spectroscopy techniques as described in the previous sections. Figure 5.22 a shows the dressed qubit transition frequency with the expected hyperbolic flux dependence and a minimum at $\delta\Phi_\mathrm{x} = 0$. Furthermore, the two lowest resonator modes (ω_1 and ω_2) are visible. Our measurement resolution does not allow us to reliably determine the undressed qubit energy gap Δ and the coupling constants

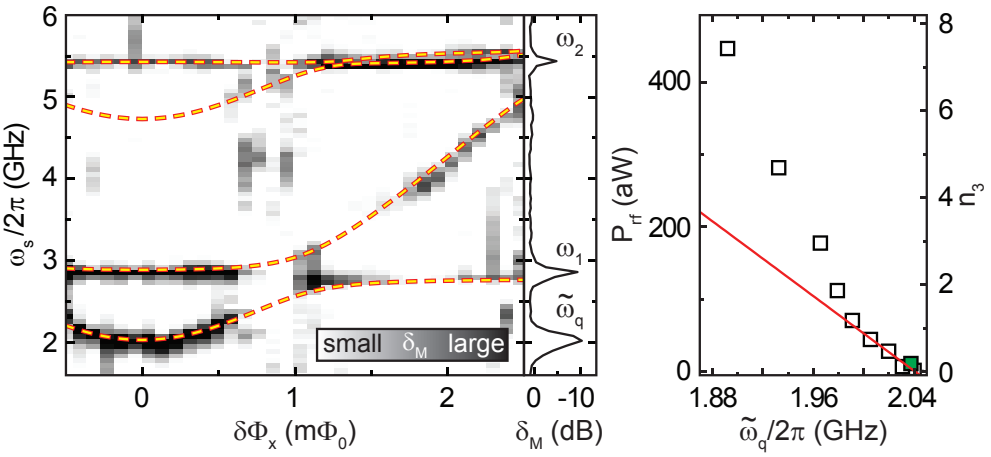

Figure 5.22: Two-tone spectroscopy and ac-Zeeman shift. (a) Microwave spectroscopy of the qubit using the $3\lambda/2$-mode ($\omega_3/2\pi = 7.777\,\mathrm{GHz}$) for readout. The shift in magnitude δ_M (gray-scale) is measured as a function of $\delta\Phi_\mathrm{x}$ and $\omega_\mathrm{s}/2\pi$. The spectrum was recorded at P_rf corresponding to $n_3 \sim 0.5$. Near the anticrossing regions with the two lowest cavity modes, the transmitted signal through the readout mode ω_3 disappears in the noise floor. The yellow-red dashed line indicates the dressed energy level spectrum of the Hamiltonian in Eq. (5.24) obtained with the fit parameters from the cavity transmission data in Fig. 5.23. (b) Center frequency of the qubit spectroscopy signal at $\delta\Phi_\mathrm{x} = 0$ as a function of the probe power P_rf. In the low-power limit ($P_\mathrm{rf}, P_\mathrm{s} \to 0$), the FWHM of the qubit signal is approximately 80 MHz. The red line is a fit to the linear region using Eq. (5.25). The green filled dot indicates the power level at which the cavity transmission spectrum in Fig. 5.23 a was recorded.

g_n in this situation. Instead, we extract them from a cavity transmission spectrum with negligible photon population. For that purpose, we first measure the power-dependent ac-Zeeman shift of the qubit transition frequency at $\delta\Phi_\mathrm{x} = 0$ as shown in Fig. 5.22 b. The average photon number n_3 can be estimated using the relation $P_\mathrm{rf} = n_3\hbar\omega_3\kappa_3$, where $\kappa_3 = 3.7\,\mathrm{MHz}$ is the FWHM of the cavity resonance.
In the dispersive limit of the Jaynes-Cummings model, the qubit's ac-Zeeman shift per cavity photon is given by $\chi_n = 2g_n^2/\delta_n$. In the ultrastrong-coupling limit, counterrotating terms have to be taken into account. An expression for χ_n in the dispersive limit can be found by an analytical treatment beyond the RWA [223] and is given by

$$2g_n^2\left(\frac{1}{\omega_\mathrm{q}-\omega_n}+\frac{1}{\omega_\mathrm{q}+\omega_n}\right) \quad . \tag{5.25}$$

The analytical theory shows good quantitative agreement with numerical results up to $g_n/\omega_n = 0.1$. In general, the dispersive frequency shifts are overestimated (underestimated) for $\delta_n < 0$ ($\delta_n > 0$) within the RWA.

5.6.3 Low-power cavity transmission spectra

Figure 5.23 a and b show the color-coded low-power cavity transmission spectra for the $3\lambda/2$- and λ-mode, respectively. In contrast to the spectra presented in the previous sections (see Fig. 5.8 and Fig. 5.16 c and d), we observe a rich structure with additional anticrossings. The origin of these anticrossings will be discussed later in more detail. To extract the individual coupling constants g_n and the qubit parameters Δ and ϵ, we compute the lowest nine transition frequencies of the Hamiltonian given in Eq. (5.24) incorporating the first three resonator modes. Fitting the results to the spectrum of the $3\lambda/2$-mode shows excellent agreement with the measured data as shown in Fig. 5.23 c. We note that the spectrum for the λ-mode shown in Fig. 5.23 d can be well described *without* additional fitting using the parameters extracted from the $3\lambda/2$-mode. For the qubit, we obtain $\epsilon/h = 1.97\,\mathrm{GHz}\cdot\delta\Phi_\mathrm{x}[\mathrm{m}\Phi_0]$ and $\Delta/h = 2.25\,\mathrm{GHz}$. The latter deviates significantly from the dressed qubit transition frequency $\tilde{\omega}_\mathrm{q} = 2.04\,\mathrm{GHz}$ at $\delta\Phi_\mathrm{x} = 0$ (see Fig. 5.22) due to the strong qubit-cavity interaction. Most importantly, we find coupling rates of $g_1/2\pi = 314\,\mathrm{MHz}$, $g_2/2\pi = 636\,\mathrm{MHz}$, and $g_3/2\pi = 568\,\mathrm{MHz}$ corresponding to normalized coupling rates g_n/ω_n of remarkable 11.2 %, 11.8 %, and 7.3 %, respectively. These values are up to one order of magnitude larger than the highest values reported so far in a circuit QED architecture [116, 224].
The significant deviation of 210 MHz between Δ and $\tilde{\omega}_\mathrm{q}$ at $\delta\Phi_\mathrm{x} = 0$ (see Fig. 5.22) can be attributed to vacuum induced Lamb shifts. Taking into account that the quantum mechanical zero-point energy is present in all three cavity modes, we calculate a total Lamb shift of $\delta_\mathrm{L,tot} \approx 203\,\mathrm{MHz}$ in good agreement with our data. Since the detuning between ω_1 and Δ/h is smallest, the $\lambda/2$-mode contributes 112 MHz to the total Lamb shift. Even with only the vacuum present, the qubit is extensively 'dressed' due to the enormous qubit-cavity interaction. While in typical cavity QED setups the Lamb shift constitutes $10^{-7} - 10^{-6}$ of the corresponding atomic transition frequency [38, 193], the enormous coupling rates in our system give rise to $\delta_\mathrm{L,tot}/\Delta \approx 0.09$. Furthermore, this ratio is almost 7 times larger than the value of 0.014 reported recently in a strongly coupled circuit QED setup [198]. According to Eq. (5.11) we can calculate the total mutual inductance $M \approx 70\,\mathrm{pH}$, where we used $g_2/2\pi = 636\,\mathrm{MHz}$, $I_\mathrm{r,2} = 18.8\,\mathrm{nA}$ and $I_\mathrm{p} = 315\,\mathrm{nA}$. With $L \approx 10\,\mathrm{pH}$ combing

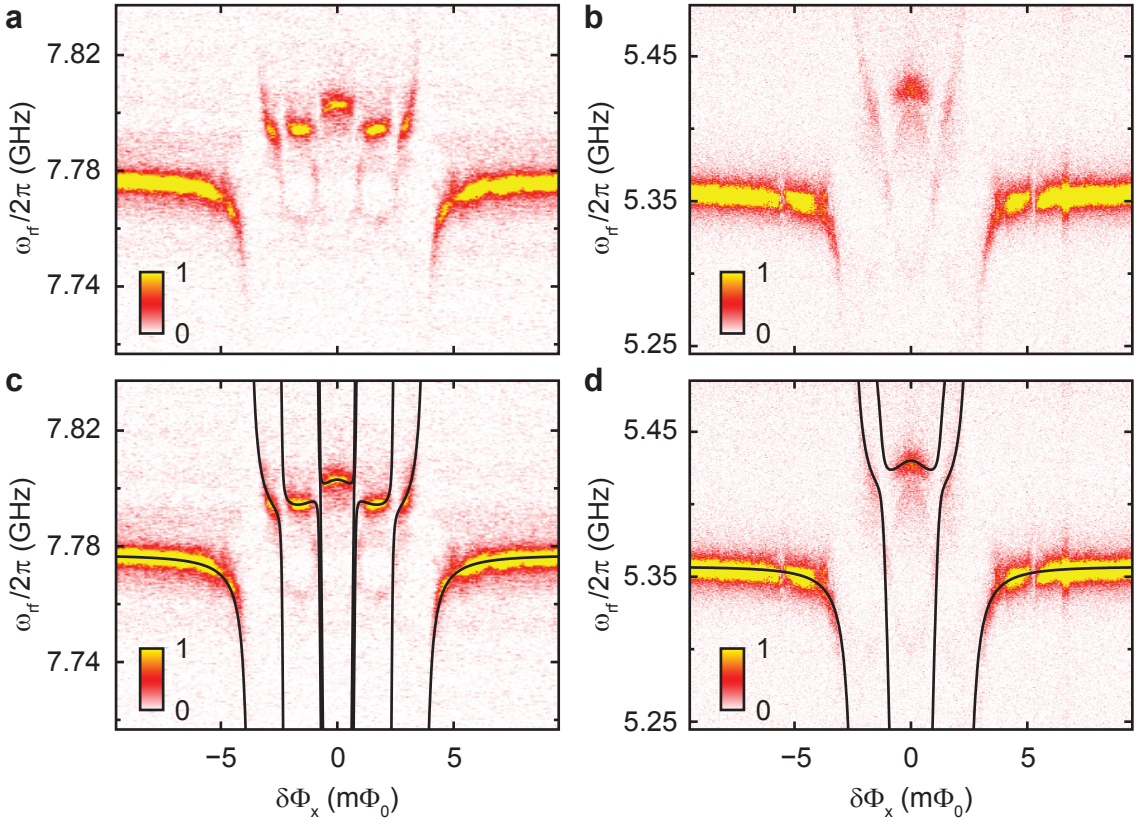

Figure 5.23: Cavity transmission spectra in the ultrastrong-coupling regime and determination of coupling rates g_n. (a) Spectrum of the $3\lambda/2$-mode (linear scale, arb. units) as a function of $\delta\Phi_x$ and probe frequency $\omega_{rf}/2\pi$. The data is recorded at an input power $P_{rf} \approx -140\,\mathrm{dBm}$ (green data point in Fig. 5.22 b) corresponding to $n_3 \approx 0.18$. (b) Same as in (a) but for the λ-mode. Owing to a higher insertion loss of this cavity mode, the spectrum is recorded at P_{rf} corresponding to $n_2 \approx 0.9$. (c) Same spectrum as in (a). The black lines represent a numerical fit of the spectrum of the Hamiltonian given by Eq. (5.24) to the data. (d) Same spectrum as in (b). Here, the black lines represent the numerically evaluated energy level spectrum without additional fitting using the parameters extracted from (c).

geometrical and kinetic contributions to M, we estimate a Josephson inductance of the coupling junction of $L_J \approx 60\,\mathrm{pH}$ in agreement with our junction parameters.

5.6.4 Beyond the Jaynes-Cummings model

The large coupling rates realized in our setup allow us to enter the ultrastrong coupling regime and, as we will show below, lead to significant deviations from the Jaynes-Cummings physics. In this section, we analyze the features in our data which constitute unambiguous evidence for the breakdown of the RWA inherent to the Jaynes-Cummings model.
In the following, we use the notation $\varphi = |q, N_1, N_2, N_3\rangle = |q\rangle \otimes |N_1\rangle \otimes |N_2\rangle \otimes |N_3\rangle$, where $q = \{g, e\}$ denote the qubit ground or excited state, respectively, and $|N_n\rangle = \{|0\rangle, |1\rangle, |2\rangle, \dots\}$ represents the Fock-state with photon occupation N in the nth resonator mode. The origin of the additional anticrossings in the cavity transmission spectra can be intuitively understood by first considering the energy level diagram of the Hamiltonian in Eq. (5.24) for $g_n = 0$. Figure 5.24 a and b show the lowest transition frequencies and parts

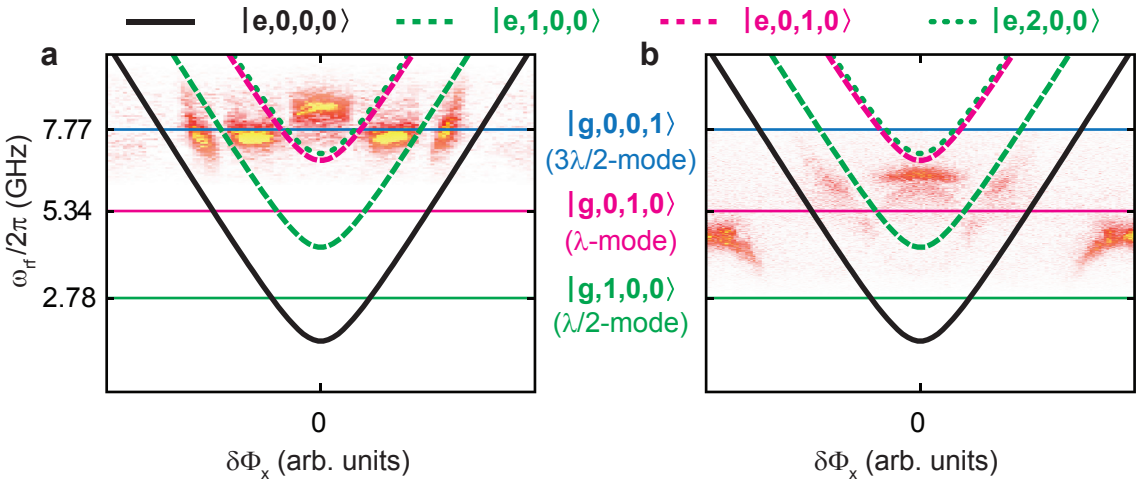

Figure 5.24: Lowest transition frequencies given by Eq. (5.24) for $g_n = 0$. (a) The color-coded plot represents a part of the spectrum of the $3\lambda/2$-mode (see Fig. 5.23). The flux-independent levels represent the first three cavity modes. The lines with the hyperbolic flux-dependence represent the bare qubit transition ($|e,0,0,0\rangle$) and transitions consisting of combined qubit and cavity excitations ($|e,1,0,0\rangle$, $|e,0,1,0\rangle$ and $|e,2,0,0\rangle$). We note that the states $|e,0,1,0\rangle$ and $|e,2,0,0\rangle$ have slightly different energies since $2\omega_1 \neq \omega_2$ due to the inhomogeneous transmission line geometry. (b) Same as (a) but with parts of the spectrum of the λ-mode.

of the cavity transmission spectrum for the $3\lambda/2$- ($|g,0,0,1\rangle$) and λ-mode ($|g,0,1,0\rangle$), respectively. In addition to the expected crossings where a cavity mode is resonant with the qubit ($|e,0,0,0\rangle$), further level crossings exist, where a higher cavity mode is degenerate with a level combining a qubit excitation and excitations in a lower cavity mode.
For a quantitative analysis, we compute the energy level spectrum of the Hamiltonian in Eq. (5.24) as shown in Fig. 5.25. The largest six contributions to the eigenstate of the cou-

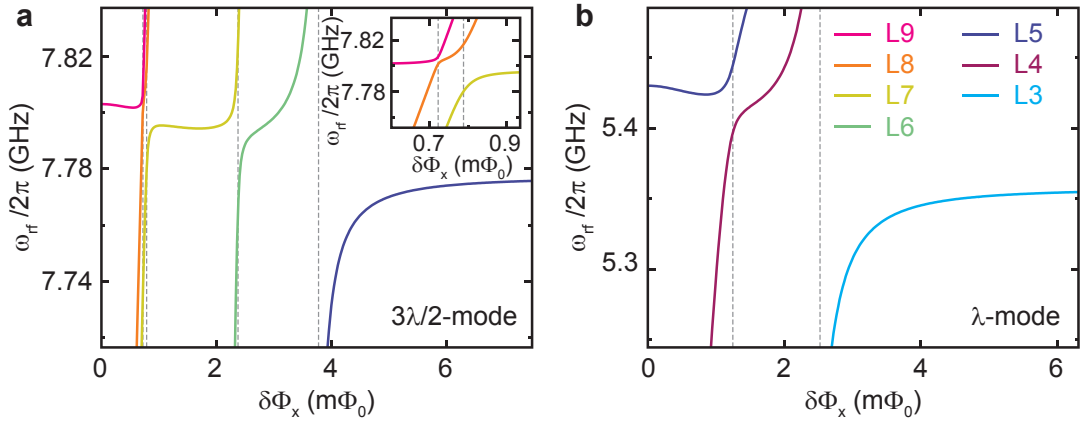

Figure 5.25: Energy level spectrum. (a) Numerically evaluated frequency spectrum obtained from Eq. (5.24) in close vicinity of the $3\lambda/2$-mode (see Fig. 5.23 c and d). The dashed gray lines indicate the flux values of anticrossings between adjacent levels. The inset shows a magnified view of the area close to the innermost anticrossings. (b) Same as in (a) but for the λ-mode. The energy levels are color-coded, Lx denotes the xth energy level of the Hamiltonian in Eq. (5.24).

pled system

$$|\psi_{\pm}\rangle = \sum_m c_m \varphi_m \quad . \tag{5.26}$$

at the positions of the respective anticrossings are summarized in Table 5.1. At the outermost anticrossing of the $3\lambda/2$-mode ($\delta\Phi_x = 3.780\,\mathrm{m}\Phi_0$; see Fig. 5.25 a), where $\omega_3 \approx \tilde{\omega}_q$, the eigenstates $|\psi_{\pm}\rangle$ of the coupled system are in good approximation symmetric and antisymmetric superpositions of $|e,0,0,0\rangle$ and $|g,0,0,1\rangle$ (see L6 and L5 in Tab. 5.1). This exchange of a single excitation between qubit and resonator is a characteristic of the Jaynes-Cummings model.
On the contrary, the origin of the anticrossing at $\delta\Phi_x = 2.378\,\mathrm{m}\Phi_0$ is of different nature: here, the dominant contributions to the eigenstates $|\psi_{\pm}\rangle$ are superpositions of the degenerate states $\varphi_1 = |g,0,0,1\rangle$, $\varphi_2 = |e,1,0,0\rangle$ and $\varphi_3 = |g,1,1,0\rangle$ (see L7 and L6 in Tab. 5.1). A transition from φ_1 to φ_2 can be understood as the creation of two excitations, one in the $\lambda/2$-mode *and* one in the qubit, while, simultaneously, annihilating only one excitation

$\delta\Phi_x(\mathrm{m}\Phi_0)$		**$3\lambda/2$-mode**						
0.723	L9	$\lvert c_m\rvert^2$	0.477	0.191	0.148	0.106	0.023	0.007
		φ_m	$\lvert g,0,0,1\rangle$	$\lvert e,2,0,0\rangle$	$\lvert g,3,0,0\rangle$	$\lvert e,0,1,0\rangle$	$\lvert g,1,1,0\rangle$	$\lvert e,0,0,0\rangle$
	L8	$\lvert c_m\rvert^2$	0.417	0.301	0.230	0.010	0.005	0.004
		φ_m	$\lvert g,0,0,1\rangle$	$\lvert e,2,0,0\rangle$	$\lvert g,3,0,0\rangle$	$\lvert g,2,1,0\rangle$	$\lvert g,2,0,0\rangle$	$\lvert e,0,0,0\rangle$
0.788	L8	$\lvert c_m\rvert^2$	0.477	0.245	0.126	0.052	0.042	0.016
		φ_m	$\lvert g,0,0,1\rangle$	$\lvert e,0,1,0\rangle$	$\lvert g,1,1,0\rangle$	$\lvert e,2,0,0\rangle$	$\lvert g,3,0,0\rangle$	$\lvert g,0,2,0\rangle$
	L7	$\lvert c_m\rvert^2$	0.483	0.299	0.117	0.025	0.019	0.018
		φ_m	$\lvert g,0,0,1\rangle$	$\lvert e,0,1,0\rangle$	$\lvert g,1,1,0\rangle$	$\lvert e,2,0,0\rangle$	$\lvert g,0,2,0\rangle$	$\lvert g,3,0,0\rangle$
2.378	L7	$\lvert c_m\rvert^2$	0.464	0.290	0.185	0.018	0.007	0.006
		φ_m	$\lvert g,0,0,1\rangle$	$\lvert e,1,0,0\rangle$	$\lvert g,1,1,0\rangle$	$\lvert e,0,0,0\rangle$	$\lvert e,2,0,0\rangle$	$\lvert g,0,1,1\rangle$
	L6	$\lvert c_m\rvert^2$	0.490	0.303	0.153	0.014	0.006	0.005
		φ_m	$\lvert g,0,0,1\rangle$	$\lvert e,1,0,0\rangle$	$\lvert g,1,1,0\rangle$	$\lvert g,1,0,1\rangle$	$\lvert e,2,0,0\rangle$	$\lvert g,0,1,1\rangle$
3.780	L6	$\lvert c_m\rvert^2$	0.475	0.434	0.047	0.009	0.007	0.007
		φ_m	$\lvert e,0,0,0\rangle$	$\lvert g,0,0,1\rangle$	$\lvert g,1,1,0\rangle$	$\lvert e,1,0,0\rangle$	$\lvert e,0,1,0\rangle$	$\lvert g,0,1,1\rangle$
	L5	$\lvert c_m\rvert^2$	0.518	0.442	0.007	0.006	0.005	0.005
		φ_m	$\lvert g,0,0,1\rangle$	$\lvert e,0,0,0\rangle$	$\lvert g,1,1,0\rangle$	$\lvert e,0,1,0\rangle$	$\lvert g,0,1,1\rangle$	$\lvert e,1,0,0\rangle$
$\delta\Phi_x(\mathrm{m}\Phi_0)$		**λ-mode**						
1.245	L5	$\lvert c_m\rvert^2$	0.459	0.401	0.070	0.028	0.008	0.008
		φ_m	$\lvert g,2,0,0\rangle$	$\lvert g,0,1,0\rangle$	$\lvert e,1,0,0\rangle$	$\lvert e,0,0,0\rangle$	$\lvert g,3,0,0\rangle$	$\lvert g,1,0,0\rangle$
	L4	$\lvert c_m\rvert^2$	0.517	0.331	0.090	0.012	0.011	0.009
		φ_m	$\lvert g,0,1,0\rangle$	$\lvert g,2,0,0\rangle$	$\lvert e,1,0,0\rangle$	$\lvert g,1,1,0\rangle$	$\lvert e,0,0,0\rangle$	$\lvert g,0,2,0\rangle$
2.523	L4	$\lvert c_m\rvert^2$	0.867	0.037	0.028	0.023	0.019	0.011
		φ_m	$\lvert g,2,0,0\rangle$	$\lvert g,0,1,0\rangle$	$\lvert g,3,0,0\rangle$	$\lvert e,0,0,0\rangle$	$\lvert g,1,0,0\rangle$	$\lvert g,2,1,0\rangle$
	L3	$\lvert c_m\rvert^2$	0.573	0.384	0.012	0.007	0.004	0.004
		φ_m	$\lvert g,0,1,0\rangle$	$\lvert e,0,0,0\rangle$	$\lvert g,0,2,0\rangle$	$\lvert g,0,0,0\rangle$	$\lvert e,0,1,0\rangle$	$\lvert e,1,0,0\rangle$

Table 5.1: Calculated contributions to the eigenstate $|\psi_{\pm}\rangle$. The contributions are evaluated at $\delta\Phi_x[\mathrm{m}\Phi_0]$ of the anticrossings of adjacent levels Lx and $L(x-1)$ (see Fig. 5.25). Only the outermost anticrossing of the $3\lambda/2$-mode ($\delta\Phi_x = 3.780$) can be understood within the Jaynes-Cummings model. All other anticrossings are caused by non-negligible contribution from counterrotating terms in the qubit-cavity Hamiltonian.

in the $3\lambda/2$-mode. Such a process[11] can only result from counterrotating terms as they are present in the Hamiltonian given in Eq. (5.24), but not within the Jaynes-Cummings approximation. At the innermost anticrossings of the $3\lambda/2$-mode ($\delta\Phi_x = 0.723\,\mathrm{m}\Phi_0$ and $0.788\,\mathrm{m}\Phi_0$; see Fig. 5.25 a, inset), the structure of $|\psi_\pm\rangle$ has a more complicated character. Here, the eigenstates $|\psi_\pm\rangle$ are composed of $|g,0,0,1\rangle$ and non-negligible contributions from states with up to three excitations, e.g. $|e,2,0,0\rangle$ and $|g,3,0,0\rangle$ (see L9, L8 and L7 in

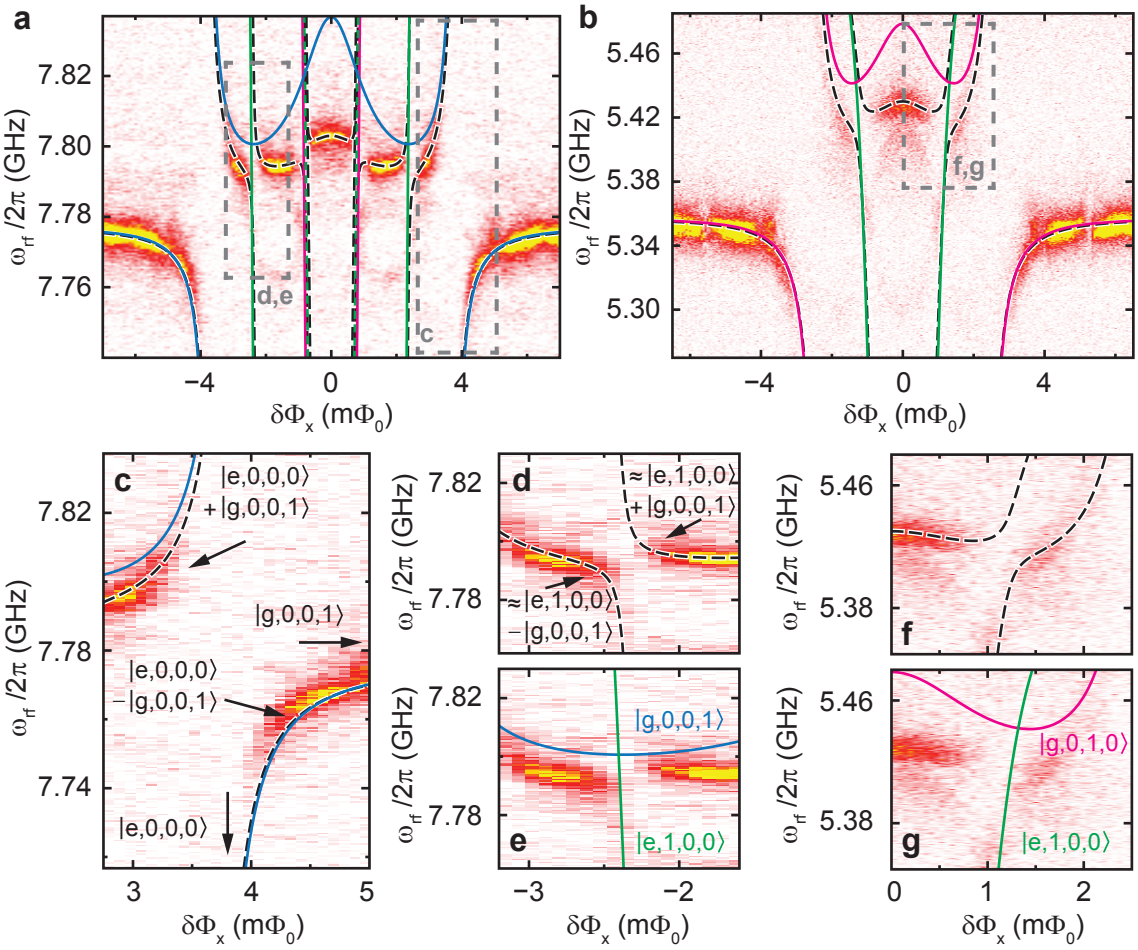

Figure 5.26: Breakdown of the Jaynes-Cummings-model. (a) Cavity transmission ($3\lambda/2$-mode, linear scale, arb. units) as a function of $\delta\Phi_x$ and probe frequency $\omega_{rf}/2\pi$. Dashed black lines in all plots: energy level spectrum obtained from the Hamiltonian given in Eq. (5.24). Colored lines in all plots: energy level spectrum obtained from the Jaynes-Cummings model (blue: $|g,0,0,1\rangle$, except for anticrossing region shown in (c); solid green: $|e,1,0,0\rangle$; dashed green: $|e,2,0,0\rangle$; magenta: $|e,0,1,0\rangle$. The latter two are indistinguishable within the resolution of this plot. The area marked by the gray broken boxes is magnified in (c) - (e). (b) Same as in (a) but for the λ-mode. With the exception of the single excitation anticrossing region, the magenta line represents $|g,0,1,0\rangle$. (c) Single excitation anticrossing for the $3\lambda/2$-mode. (d) Avoided crossing due to a coupling between the degenerate states $|g,0,0,1\rangle$ and $|e,1,0,0\rangle$. The contribution from $|g,1,1,0\rangle$ in the expression for the eigenstate is omitted in this plot for clarity. (e) Same as (d), but for the Jaynes-Cummings model. Within numerical accuracy, no anticrossing is predicted, clearly contradicting the data. (f) The dominant contributions to the superposition states of the innermost anticrossings are $|g,0,1,0\rangle$, $|g,2,0,0\rangle$ and $|e,1,0,0\rangle$. (g) Same as (f), but for the Jaynes-Cummings model.

[11] The transitions $|g,0,0,1\rangle \leftrightarrow |e,1,0,0\rangle$ correspond to terms of the form $\hat{a}_1\hat{\sigma}_-\hat{a}_3^\dagger$ and $\hat{a}_1^\dagger\hat{\sigma}_+\hat{a}_3$ in the Hamiltonian.

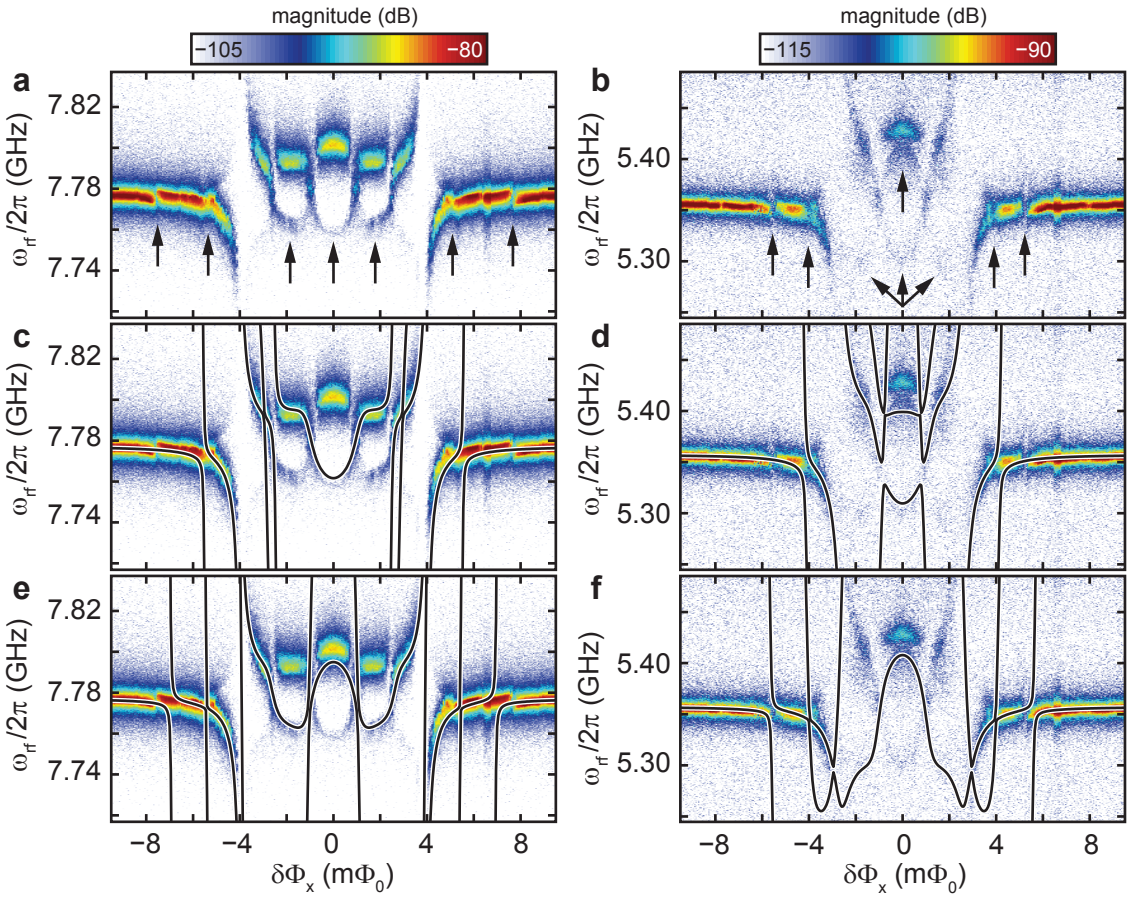

Figure 5.27: Higher-order transitions. (a) Color-coded cavity transmission ($3\lambda/2$-mode, logarithmic scale) as a function of $\omega_{\mathrm{rf}}/2\pi$ and $\delta\Phi_{\mathrm{x}}$. The data is recorded at an input power $P_{\mathrm{rf}} \approx -124\,\mathrm{dBm}$ corresponding to $n_3 \approx 6.1$. The black arrows mark additional spectroscopic features that cannot be explained by excitations from the ground state to a higher energy level. (b) Same as in (a) but for the λ-mode and $n_2 \approx 0.9$. (c) and (d) Same as in (a) and (b). The solid black lines in both plots represent the energy difference between the eigenenergies of the Hamiltonian given in Eq. (5.24) with respect to the 2^{nd} lowest eigenenergy. (e) and (f) Same as in (c) and (d) but for the 3^{rd} lowest eigenenergy.

Tab. 5.1). Similar arguments apply to the anticrossings visible in the spectrum of the λ-mode ($\delta\Phi_{\mathrm{x}} = 1.245\,\mathrm{m}\Phi_0$ and $2.523\,\mathrm{m}\Phi_0$; see Fig. 5.25 b), however, both anticrossings have non-Jaynes-Cummings character. Although one expects a single excitation anticrossing between L3 and L4 at $\delta\Phi_{\mathrm{x}} = 2.523\,\mathrm{m}\Phi_0$, the eigenstate of the coupled system attains a large (86.7 % for L4) contribution from the $|g,2,0,0\rangle$ state (two excitations in the $\lambda/2$-mode). The size of the contribution can be understood by taking into account that even though the cavity modes are non-harmonically spaced, $2\omega_1 - \omega_2 = 2\pi\,207\,\mathrm{MHz} \ll g_2$.
Finally, we compare the energy level spectrum of the Hamiltonian in Eq. (5.24) to that of a three-mode Jaynes-Cummings model on the basis of our fit parameters. Depending on $\delta\Phi_{\mathrm{x}}$, there are regions where our data can be well described by the Jaynes-Cummings model, and regions where there are significant deviations (see Fig. 5.26 a and b). Figure 5.26 c shows a magnified view of one of the outermost anticrossings of the $3\lambda/2$-mode which is in good agreement with predictions based on the Jaynes-Cummings model. The quantitative deviations from Eq. (5.24) can be attributed to the small admixture of the state $|g,1,1,0\rangle$ (see Tab. 5.1). Although counterrotating terms in principle exist in any real circuit QED

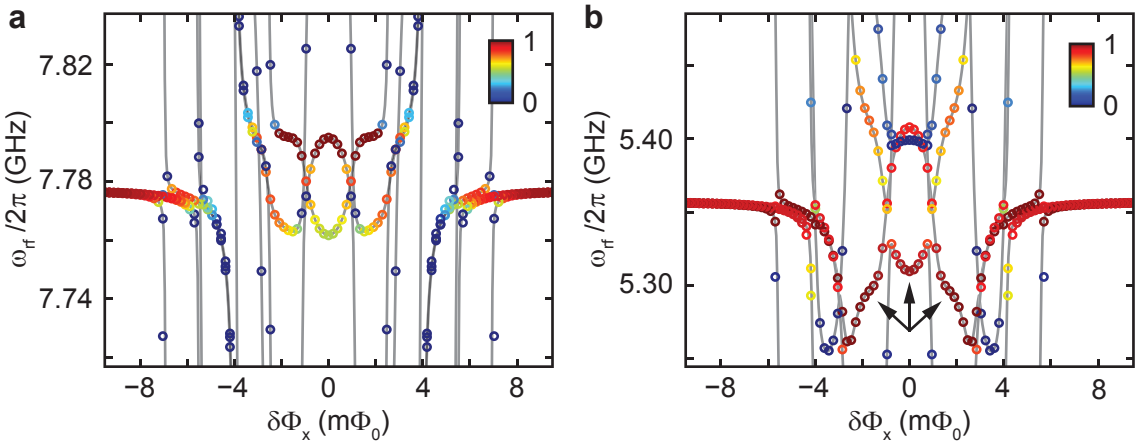

Figure 5.28: Numerically evaluated transition matrix elements. (a) Color-coded plot (normalized) of $|M_{i,f}|^2$ according to Eq. (5.27). The different intensity of the innermost spectroscopic features in Fig.5.27 a (black arrows at $\delta\Phi_x = 0\,\mathrm{m}\Phi_0$ and $\delta\Phi_x = \pm 2\,\mathrm{m}\Phi_0$) is reproduced quantitatively for the $3\lambda/2$-mode. (b) Same as in (a) but for the λ-mode. The spectroscopic features indicated by the black arrows (cf. Fig. 5.27 b) are much less pronounced in our spectroscopic data than predicted by theory.

system, their effects become prominent only in the ultrastrong coupling limit with large normalized couplings g_n/ω_n as realized in our system. The observed anticrossing shown in Fig. 5.26 d and f are a direct experimental manifestation of physics beyond the rotating wave approximation in the Jaynes-Cummings model. As shown in Fig. 5.26 e and g, the latter would imply a crossing of the involved energy levels, which is not observed.
Additional less pronounced structures and anticrossings are visible in the low-power transmission spectra (see Fig. 5.23). To elucidate their origin, we measure the cavity transmission of the $3\lambda/2$-mode at a higher intracavity photon number, where these patterns become more distinct. The data in Fig. 5.27 a and b shows the color-coded cavity transmission on a logarithmic scale for the $3\lambda/2$- and λ-mode, respectively. Most of the additional features in our spectra can be explained by computing the lowest 16 energy levels of the Hamiltonian given in Eq. (5.24) and calculating the energy differences with respect to the 2^{nd} (see Fig.5.27 c and d) and 3^{rd} lowest eigenenergy (see Fig.5.27 e and f), respectively. For both spectra, the observed features are in good agreement with the numerically evaluated transitions given by Eq. (5.24). Only the outer anticrossings in the spectrum of the $3\lambda/2$-mode (i.e. the anticrossings at $\delta\Phi_x \approx \pm 8\,\mathrm{m}\Phi_0$) lack quantitative agreement. We attribute the deviations to the presence of higher cavity modes[12] which cannot be captured numerically due to computational limitations. Furthermore, the larger intracavity photon number leads to an ac-Zeeman shift of $\tilde{\omega}_q$ which is not explicitly included in our theoretical model. The observed intensity of the involved transitions can be qualitatively understood by calculating the corresponding matrix elements

$$|M_{i,f}|^2 = |\langle\psi_f|\hat{H}_{\mathrm{d},n}|\psi_i\rangle|^2 \quad \text{with } i = 2,3 \quad . \tag{5.27}$$

Here,

$$\hat{H}_{\mathrm{d},n} = \mathcal{E}\left(\hat{a}_n^\dagger + \hat{a}_n\right) \tag{5.28}$$

[12] While the qubit-cavity coupling of the 2λ-mode should be negligible due to a current node at the qubit position, the presence of the $5\lambda/2$-mode may not be neglected.

is the drive Hamiltonian of the nth cavity mode inducing transitions between the initial ψ_i and final ψ_f eigenstate of the full Hamiltonian given in Eq. (5.24). The calculated matrix elements are shown in Fig. 5.28 a and b for the $3\lambda/2$- and λ-mode, respectively. Except for the spectroscopic features indicated by the black arrows in Fig. 5.28 b, the relative intensity of the observed transitions are in good agreement with the spectrum of the respective mode. Even at large intracavity photon numbers, similar higher-order transitions were not observed in circuit QED systems which can described within the Jaynes-Cummings model. The fact, that some of these transitions can be spectroscopically resolved even at low intracavity photon numbers emphasizes the importance of the counterrotating terms for the physics of our system.

Chapter 6

Summary and outlook

The rapidly developing and prospering field of circuit QED studies the fundamental interaction between light and matter using superconducting circuits. Circuit QED systems are promising candidates for conceptual building blocks in quantum information processing (QIP). Basic gate operations and quantum computing algorithms have successfully been demonstrated [118, 225–227]. Compared to cavity QED with natural atoms, circuit QED architectures have numerous advantages.
First, the design flexibility inherent to superconducting circuits make them one of the most versatile architectures for quantum engineering, i.e. the tailoring of quantum systems. The non-linearities and tuning capabilities provided by SQUIDs and qubits allow for the development of parametric amplifiers for quantum limited amplification and the generation of squeezed light [228–235]. In addition, *in situ* rapidly tunable resonators [236] have been suggested for a parametric generation of photons and the observation of quantum vacuum radiation [237–240].
Furthermore, the large effective dipole moments of superconducting qubits and the small mode volumes realized in quasi-1-dimensional transmission line resonators allow reaching the strong-coupling regime far more easily. In this regime, the atom-photon interaction is coherent which permits e.g. the transfer of quantum information [108, 109] and synthesizing arbitrary quantum states [112].
While major breakthroughs [7, 104, 106, 108–110, 112–114, 118, 121, 122] in the field of circuit QED were achieved using charge, phase and transmon-type qubits, the potential of flux qubits for circuit QED applications has not yet been explored thoroughly. This is caused by the fact that in general the fabrication of flux qubits is more demanding since high critical current densities in combination with submicron Josephson junction areas are needed. However, flux qubits are particularly promising for experiments situated in the regime of ultrastrong light-matter interaction due to the possibility of enhancing the qubit-resonator coupling drastically by implementing additional Josephson elements. Up to now, no architectures based on other superconducting qubit types capable of going beyond Jaynes-Cummings physics have been envisioned.

In the scope of this thesis, the main building blocks for circuit QED applications – artificial atoms and resonant cavities – were successfully developed, fabricated and characterized [149]. Different qubit-resonator coupling schemes were explored with the main focus

on enhancing the qubit-cavity coupling rate g. Utilizing the non-linear inductance of a Josephson junction, we were able to enter the ultrastrong-coupling regime in a circuit QED architecture for the first time.

The fabrication process for superconducting flux quantum bits was implemented in the new evaporation facility of the WMI, thus enabling experiments on 'homemade' flux qubits for the first time. At first, the qubits were characterized using an inductive dc-SQUID readout technique. The microwave excitation of the qubits leads to characteristic peaks and dips in the flux dependence of the SQUID's switching current histograms. From the position of these peaks and dips and by measuring at different excitation frequencies, the transition frequency of the qubit can be reconstructed. Our measurement data provide evidence that we are able to fabricate flux qubits with energy gaps $\Delta \gg k_\mathrm{B}T \approx h \cdot 0.5\,\mathrm{GHz}$ at $T = 25\,\mathrm{mK}$. Moreover, on-chip circuit elements like shunt capacitors and microwave antennas were successfully implemented in our designs and improved the readout significantly. This allowed observing sideband transitions in a system consisting of a flux qubit, a dc-SQUID and a lumped element LC-resonator. Simultaneously, high-quality superconducting transmission line resonators tailored for the needs of circuit QED experiments were designed, fabricated and characterized at cryogenic temperatures.

The large dipole moments of our flux qubits combined with small cavity mode volumes allow for coupling rates g exceeding the decay rates of our quantum circuits. With a coupling scheme based purely on the geometric component of the mutual inductance we were able to meet the criteria for strong-coupling: a cornerstone for studying coherent interactions between light and matter. Embedded in distributed coplanar waveguide resonators, the flux qubits were characterized by cavity transmission and dispersive two-tone spectroscopy experiments. Our spectra and the extracted coupling rates are in excellent agreement with the Jaynes-Cummings-model and to simulations based on the quantum Markovian master equation.

Using a galvanic coupling scheme, the coupling strengths could be increased further. Multiphoton spectroscopy in a strongly-coupled qubit-cavity system provided clear experimental evidence for the existence of selection rules similar to those of electric dipole transitions in atomic physics. At the degeneracy point of the qubit, two-photon transitions are strictly forbidden due to symmetry considerations. Away from the degeneracy point, the system has no well-defined parity and one- and two-photon excitations can coexist. Moreover, two-photon spectroscopy in the dispersive limit allows observing the vacuum Rabi splitting. While the feeble entanglement between light and matter states is difficult to observe in a transmission experiment with qubit and cavity on resonance, the dispersive readout technique does not populate the relevant resonator modes.

Most importantly, the engineering potential inherent to circuit QED allowed increasing the coupling rate g between a flux quantum bit and a transmission line resonator into a new regime: the ultrastrong-coupling regime [8]. This was achieved by utilizing the non-linear inductance of a Josephson junction shared between qubit and cavity. With $g/\omega_\mathrm{r} \approx 12\,\%$, the normalized coupling rates in our system exceed those of other circuit QED setups by one order of magnitude. Owing to the non-negligible contribution of counterrotating terms in the system Hamiltonian, the observed transmission spectra exhibit anticrossings which result from a coupling between eigenstates with a distinct number of excitations. Our spectra are in excellent agreement with theoretical predictions and for the first time provide clear evidence for physics beyond the renowned Jaynes-Cummings-model. In the

latter, only states with an equal number of excitations can be coupled.
Although the ultrastrong-coupling limit was investigated both theoretically and experimentally in semiconductor systems in recent years [216, 217, 219–221, 241], the extracted couplings in these studies refer to a collective N-atom interaction. Compared to our results, the normalized couplings of $g_N/\omega = 0.09$ and $g_N/\omega = 0.24$ reported in Refs. [219] and [221] for $N = 50$ and $N = 25$, respectively, would only correspond to ratios $g_n/\omega_n \approx 1.3\,\%$ and $g_n/\omega_n \approx 4.8\,\%$. This emphasizes once more the uniqueness of our prototype circuit, where the ultrastrong-coupling regime is reached with only a *single* artificial atom coupled to a resonant cavity mode.

Many exciting phenomena have been predicted to arise in systems realizing ultrastrong light-matter interaction [212,216,217,242–244]. When the coupling strength is large enough and the rotating wave approximation is non-applicable, these systems resemble solid-state implementations of the $E\otimes\beta$ Jahn-Teller model [212,243,245–248]. The quantum mechanical description of this model predicts an entangled ground state of the qubit-resonator entity. In this ground state, the oscillator is displaced by a qubit state-dependent quantity and contains a finite number of virtual 'bound' photons [212, 216, 243]. While these photons can not escape the cavity directly, their presence and distribution could be measured using a second qubit in a photon number splitting experiment [103, 104] or by switching off the qubit-resonator interaction [249] in a non-adiabatic way. Then, the system will relax towards the new ground state which corresponds to the standard vacuum [216] and the emitted photons can be measured. Furthermore, the average photon number and higher-order statistical correlations between the emitted photons could be inferred using a dual-path setup [250, 251].
As mentioned in section 5.6.1 the coupling strengths can be further increased either by reducing the size of the coupling junction or making use of the $\sqrt{N}$-scaling of g_N within the Tavis-Cummings model. Combining both approaches, it could be possible to observe the Dicke[1] superradiant phase transition [255, 256]. In the large N limit and above the critical coupling $g_n > (\omega_\mathrm{q}\omega_n/4)^{1/2}$, such systems are known to exhibit power-law scaling [257], quantum chaos [258] and critical entanglement [259, 260].
Another interesting quantum phenomenon is to be observed in the deep strong coupling regime [244] where $g_n/\omega_n \gtrsim 1$. Here, the system evolves along different parity chains depending on the initial state of the coupled qubit-resonator system. Interestingly, in a parity basis, the photon statistics of an initial single photon Fock state will spread independently, reach an energy barrier and bounce back repeatedly. Starting from a Fock state with higher photon number generates counter-propagating photon number wave packets in both directions and leads to interference effects.
Recently, a scheme for one-step N-qubit Greenberger-Horne-Zeilinger (GHZ) state generation was proposed [261]. This scheme is robust to operation errors and decoherence and it was shown, that the preparation time t of the GHZ state is minimum for $g_n/\omega_n = 1/4$.
Last but not least, qubit-cavity systems operating in the ultrastrong-coupling regime are promising candidates for studying strongly interacting polaritons in cavity arrays [262–264]

[1] In his publication, Dicke treated the electromagnetic field semiclassically [252]. Nevertheless, superradiant behavior – the collective, spontaneous emission of photons from N atoms – is often referred to as *Dicke model* although the fields are quantized. For a recent overview of the Dicke model we refer to Refs. [253, 254].

and causality effects in quantum field theory [265] using an open transmission line instead of a resonant cavity.
During this thesis work, tremendous progress has been made with solid-state based systems both in quantum information processing and in studying fundamental quantum physics phenomena. For a very thorough overview of the prospects of strongly coupled circuit QED setups in general, we refer the interested reader to Ref. [199]. The circuit QED architecture is and will continue to be an ideal test bed for future explorations of quantum mechanical systems owing to its numerous advantages: design and engineering flexibility, *in situ* variability and scalability. Although there are several technological challenges ahead, there is a considerable chance that the first 'meaningful' quantum computation and simulation will be carried out using a circuit QED setup.

Appendix A

Fabrication recipes & electron beam evaporator details

The following sections summarize the process steps for the fabrication of on-chip bias lines (see section 3.1.1), CPW resonators (see section 3.2) and Josephson junction devices (see section 3.1.2). As mentioned in the introductory paragraph of chapter 3, the parameters given in the following tables should serve as a good starting point but have to be adjusted eventually. Additional fabrication recipes for circuit QED devices - with emphasis on charge and transmon qubits - can be found in Refs. [151, 175, 199].

A.1 Wafer cleaning

Process step	Details	Comments
Wafer cleaning	Acetone bath (hotplate, 5 min, 70° C), ultrasonic cleaning (2 min, power 4)	Removes dicing protection resist or silver glue remnants. Keep wafer under constant acetone flow when switching to the next basin.
	Acetone bath, ultrasonic cleaning (2 min, power 2)	Keep wafer under constant acetone flow when switching to the next basin.
	Acetone bath, ultrasonic cleaning (2 min, power 2)	Rinse wafer with isopropanol before switching to the isopropanol basin.
	Isopropanol bath, ultrasonic cleaning (2 min, power 2)	Rinse wafer with fresh isopropanol.
	Dry wafer with N_2	Do not scratch with tweezers.
	Inspect wafer under optical microscope	Repeat cleaning procedure and/or initiate RIE O_2 plasma ashing for 60 s to remove stubborn dirt/resist remnants.

A.2 RIE O_2 plasma ashing

Process step	Details	Comments
Sample mounting	Vent the RIE process chamber, place wafer centrally on silicon coverplate and evacuate the recipient Parameters: O_2 flow: 50 sccm Ar flow: 0 sccm SF_6 flow: 0 sccm RF power: 100 W ICP power: 0 W He backing: 10 sccm Chamber pressure: 5 mTorr Strike pressure: 50 mTorr Ramp rate: 5 mTorr/s	

A.3 On-chip bias lines

The following table outlines the steps necessary for the fabrication of bias lines as shown in Fig. 3.2. The structures defined by the optical lithography process described below, exhibit a pronounced undercut which is needed for sputtering thin metal films.

Process step	Details	Comments
Wafer cleaning	Clean wafer according to App. A.1	
Resist spinning	Place wafer centrally on corresponding chuck of the resist spinner	
	Initiate vacuum and clean wafer with N_2	
	Program spinner (4000 rpm for 1 min)	
	Use fresh pipette and place at least $3-4$ droplets of AZ 5214E resist centrally on wafer	**The tip of the pipette must not contact anything else except the resist.** It is advisable to dry the tip of the pipette with N_2 before use, too.
	Closing the resist spinner lid initiates the program	Using AZ 5214E and 4000 rpm results in a resist thickness $\approx 1.4\,\mu$m.
Softbake	Bake wafer on hotplate (70 s, 110° C)	
Flood exposure	Turn on MJB3 Photomask Aligner according to instruction manual	The UV lamp should be turned on 20 min before the first exposure.
	Expose wafer to UV-light without any photomask ($0.1-0.2$ s, MJB3 Photomask Aligner)	

continued on next page

continued from previous page

Process step	Details	Comments
Reversal bake	Bake wafer on hotplate (120 s, 130° C)	The temperature should be kept constant within ±1° C.
Mask exposure	Adjust exposure time to obtain an energy density of 36 mJ/cm^2 using the 365 nm UV-metre	Typically the exposure time should be $4-5$ s.
	Clean chrome and glass side of optical mask rinsing with acetone and isopropanol; dry mask with N_2	Stubborn resist remnants can be removed using a wet cleanroom fabric. Do not use extensive pressure on the chromium side to avoid damaging the coating mechanically.
	Follow instruction manual for exposure processes	Use vacuum contact (**H**igh-**P**recision) mode and press *'Vakuum Kammer'* button.
Development	Microchemicals AZ 726 MIF developer ($\sim$ 15 min)	Move basin occasionally. The development time can vary by several minutes.
	Stop development by placing the wafer subsequently in two H_2O basins (each $\sim$ 1 min)	
	Dry extensively with N_2	
	Check structure under optical microscope	If the structure is not fully developed, repeat developing procedure for additional short time intervals using fresh developer and H_2O. After successful development, the chip is ready to be mounted in the table top sputtering chamber.
Sputtering	Place wafer in table top process chamber and follow instruction manual	
	sputter 5 nm Cr ($I_{sp} = 120$ mA, $t = 30$ s, $p_{Ar} = 5 \cdot 10^{-2}$ mbar)	The Cr layer is used as adhesive layer for the subsequent Au sputter process.
	sputter 25 nm Au ($I_{sp} = 15$ mA, $t = 135$ s, $p_{Ar} = 5 \cdot 10^{-2}$ mbar)	
Lift-off	Acetone bath (hotplate, 15 min, 70° C), ultrasonic cleaning (2 min, power 2)	Repeat process if gold film is not completely removed. Renew acetone bath if necessary but keep chip wet when switching basins.
	Isopropanol bath, ultrasonic cleaning (2 min, power 2)	
	Dry wafer carefully with N_2 and inspect under optical microscope	Damaged structures can be used for EBL dose series tests.

A.4 CPW resonators

The following table comprises the fabrication steps for Nb CPW resonators as discussed in section 3.2. For circuit QED applications with galvanically coupled flux qubits, we chose a Nb thickness of 100 nm.

Process step	Details	Comments
Wafer cleaning	Clean wafer according to App. A.1	After mounting up to six substrates ($10 \times 6\,\mathrm{mm}^2$), the sample holder can be moved to the niobium sputtering facility.
Sputtering	Transfer sample holder from loadlock to ultra-high vacuum sputtering chamber	The pressure before sputtering should be $1 - 3 \cdot 10^{-9}$ mbar.
	Position sample holder in front of Nb chimney (rot: 199°, long: 0°)	
	Follow sputtering manual and adjust process parameters	
	Process pressure: $2.73 \cdot 10^{-3}$ mbar	
	Ar flow: 10 sccm	
	Power: 200 W	
	Ramp: 5 s	
	Open manual shutter earliest after 60 s pre-sputtering; sputter rate: $\sim$ 40 nm/min	The sputter rate may vary over time and should be checked by reflectometry methods regularly. After sputtering the desired thickness, the wafer can be transferred to the clean room facilities for optical lithography and reactive ion etching.
Wafer cleaning	Clean wafer according to App. A.1	
Resist spinning	Place wafer centrally on corresponding chuck of the resist spinner	
	Initiate vacuum and clean wafer with N_2	
	Program spinner (8000 rpm for 1 min)	
	Use fresh pipette and place at least $3-4$ droplets of AZ 5214E resist centrally on wafer	**The tip of the pipette must not contact anything else except the resist.** Dry the tip of the pipette with N_2 before use, too.
	Closing the resist spinner lid initiates the program	Using AZ 5214E and 8000 rpm results in a resist thickness $< 1.14\,\mu$m.
Softbake	Bake wafer on hotplate (70 s, 110° C)	
Edge bead removal	Expose wafer to UV-light using specially designed edge-bead removal structure ($\sim$ 20 s, MJB3 Photomask Aligner)	This structure protects the resist from UV-light, except for a 150 µm-thick strip at the edges of the wafer.

continued on next page

continued from previous page

Process step	Details	Comments
Development	Microchemicals AZ 726 MIF developer (60 s)	Move basin occasionally.
	Stop development by placing the wafer subsequently in two H_2O basins ($\sim$ 1 min each)	
	Dry extensively with N_2	
Mask exposure	Adjust exposure time to obtain an energy density of 36 mJ/cm^2 using the 365 nm UV-metre	Typically the exposure time should be $4-5$ s.
	Clean chrome and glass side of optical mask rinsing with acetone and isopropanol; dry mask with N_2	Stubborn resist remnants can be removed using a wet cleanroom fabric. Do not use extensive pressure on the chromium side to avoid damaging the coating mechanically.
	Follow instruction manual for exposure processes	Use vacuum contact (**H**igh-**P**recision) mode and press *'Vakuum Kammer'* button.
Development	Microchemicals AZ 726 MIF developer (85 s)	Move basin occasionally.
	Stop development by placing the wafer subsequently in two H_2O basins ($\sim$ 1 min each)	
	Dry extensively with N_2	
	Check resonator under optical microscope intensively	It is of utmost importance, that the center strip, the lateral gaps, the coupling capacitors and the alignment marks for EBL are well defined. Any particles and/or resist remnants have to be removed by short ultrasonic pulses (H_2O, power 2) and/or subsequent developing intervals. After successful development, the chip is ready to be processed in the RIE.
RIE physical etching	Initiate etching procedure according to App. A.5 (2 min 50 s for 200 nm Nb)	
RIE O_2 plasma ashing	Initiate plasma ashing according to App. A.2 for 2 min	
Chip inspection	Check resonator under optical microscope intensively	If the niobium is not removed completely, repeat RIE etching process for shorter time intervals.

continued on next page

continued from previous page

Process step	Details	Comments
Resist stripping	Acetone bath (hotplate, 10 min, 70° C), ultrasonic cleaning (2 min, power 4)	Stubborn resist remnant can be removed using subsequent RIE O_2 plasma ashing for $15 - 30$ s.

A.5 RIE physical etching

Process step	Details	Comments
Sample mounting	Vent the RIE process chamber, place wafer centrally on silicon coverplate and evacuate the recipient Parameters: O_2 flow: 0 sccm Ar flow: 10 sccm SF_6 flow: 20 sccm RF power: 100 W ICP power: 50 W He backing: 10 sccm Chamber pressure: 15 mTorr Strike pressure: 30 mTorr Ramp rate: 5 mTorr/s	

A.6 Electron beam lithography

The fabrication of circuit QED devices with only one or a few qubits patterned in the gap of a CPW differs from processing an 1-inch wafer with 36 SQUID-qubit devices. With bias lines, shunt capacitors, microwave antenna and the actual flux quantum circuits, the latter comprises structures with distinct areas. The following table summarizes the fabrication steps for defining Josephson junction devices as presented in chapter 4. Special fabrication steps and parameters necessary for circuit QED devices (i.e. flux qubits coupled to CPW resonators) are emphasized by a gray color. In general, all Josephson junction devices discussed in this thesis were fabricated using a $120\,\mathrm{x}\,120\,\mu\mathrm{m}^2$ writefield and a magnification of 650.

Process step	**Details**	**Comments**
Wafer cleaning	Clean wafer according to App. A.1	Be careful not to not scratch the wafer with the tweezers.
Resist spinning	Place wafer centrally on corresponding chuck of the resist spinner	
	Initiate vacuum and clean wafer with N_2	
	Program spinner (2000 rpm for 2 min)	
	Use fresh pipette and place at least $6-7$ droplets of PMMA/MA 33 % resist centrally on 1-inch wafer ($2-3$ droplets for $6\,\mathrm{x}\,10\,\mathrm{mm}^2$ wafer)	**The tip of the pipette must not contact anything else except the resist.** Dry the tip of the pipette with N_2 before use.
	Closing the resist spinner lid initiates the program	Using PMMA/MA 33 % and 2000 rpm results in a resist thickness $\approx 680\,\mathrm{nm}$.
	Clean back side of $6\,\mathrm{x}\,10\,\mathrm{mm}^2$ wafer carefully using acetone	To ensure a good thermal contact between the wafer and the hotplate, resist remnants sticking to the backside of the wafer have to be removed.
Baking procedure	Bake wafer on hotplate ($10\,\mathrm{min}, 160^\circ$ C)	It is advisable to heat-up the hotplate already 30 min earlier and start a dummy bake procedure to ensure a good temperature stability during the actual process. The temperature should not vary more than $\pm 0.5^\circ$ C.
Resist spinning	Place wafer centrally on corresponding chuck of the resist spinner	
	Initiate vacuum and clean wafer with N_2	
	Program spinner (4000 rpm for 2 min)	
	Use fresh pipette and place at least $4-5$ droplets of PMMA 950k resist centrally on 1-inch wafer (2 droplets for $6\,\mathrm{x}\,10\,\mathrm{mm}^2$ wafer)	**Use fresh pipette. The tip of the pipette must not contact anything else except the resist.** Dry the tip of the pipette with N_2 before use, too.

continued on next page

continued from previous page

Process step	Details	Comments
	Closing the resist spinner lid initiates the program	Using PMMA 950k and 4000 rpm results in a resist thickness $\approx 70\,\text{nm}$.
	Clean back side of $6 \times 10\,\text{mm}^2$ wafer carefully using acetone	To ensure a good thermal contact between the wafer and the hotplate, resist remnants sticking to the backside of the wafer have to be removed.
Baking procedure	Bake wafer on hotplate ($10\,\text{min}, 160^\circ$ C)	The temperature should not vary more than $\pm 0.5^\circ$ C. The wafer is now ready for EBL.
Chip mounting	Place wafer centrally on specially designed 1-inch wafer holder and screw tight holding frame	If the wafer is not in the correct position, it may break when fasten the screws of the holding frame.
	Place $6 \times 10\,\text{mm}^2$ wafer on flat holder	The edges of the wafer should be parallel to the edges of the sample holder.
	Vent, slide sample holder on laser stage and evacuate EBL recipient	
Preliminary setup	Push *'HT'* button and set 30 kV gun voltage (spot size 1)	
	Reset all global and local 3-point adjustments	
	Execute *'Find Home Position'* routine	
	Set writefield ($120\,\mu\text{m}$, magnification 650)	
	Chose SE detector, use the Elphy Plus software to approach the respective Faraday cup (*'Faraday Cup (1" holder)'* or *'Faraday Cup (flat holder)'*) and save current position under *'Aktueller Faraday Cup'*	Coarse positions of the different Faraday cups (FC) are saved within the Elphy Plus software. The crosshair can be adjusted centrally either by using the joystick or by taking an image and adjusting the stage via the Elphy Plus software.
	Measure and write down beam current in EBL logbook ($\sim 27\,\text{pA}$ for 30 kV, spot 1)	The beam current is measured executing the *'Dwell Time Correction'* script.
3-point alignment	Go to *'Approach Point'* and use the joystick to find the first alignment mark	Depending on the gun voltage and spot size, contrast and brightness will differ strongly and have to be adjusted.
	Use the joystick to find the lower left corner of the $6 \times 10\,\text{mm}^2$ using a small magnification; carefully approach the first alignment mark and increase magnification	Critical chip regions (e.g. center strip and lateral gaps) should not be exposed during alignment.

continued on next page

continued from previous page

Process step	Details	Comments
	Go to maximum magnification and burn a **circular** contamination dot (diameter $20-30$ nm) close to the gold alignment mark; monitor beam current	A working distance of $6.6-6.8$ mm is a good starting point when using the 1-inch holder. When in focus, the beam current will drop by 2 % in less than 10 s. **To obtain a circular dot, the focus and stigmatism have to be adjusted iteratively by burning several dots in vicinity to the alignment mark.**
	Go to maximum magnification and burn a **circular** contamination dot (diameter $20-30$ nm) close on the silicon alignment mark; monitor beam current	A working distance of $6.0-6.3$ mm is a good starting point when using the flat holder. When in focus, the beam current will drop by 2 % in less than 10 s. **To obtain a circular dot, the focus and stigmatism have to be adjusted iteratively by burning several dots in vicinity to the alignment mark.**
	Set writefield (120 µm, magnification 650) and	
	Read and adjust working distance (WD); save center of alignment mark as first U- and V-coordinate according to mask design	The focus correction in the *'Adjust UVW (Global)'* window should be on.
	Repeat contamination dot procedure at two additional distant alignment marks	The WD is only adjusted at the first alignment mark. The software internally saves the WD at the other marks and interpolates linearly between them. Adjusting the stigmatism is one of the most important steps during EBL. Note, that in contrast to the WD (focus), the stigmatism is a global setting.
	Approach all alignment marks and refine 3-point alignment coordinates if necessary	Use Elphy Plus image scans for coordinate refinement.
	Approach all alignment marks and perform 10 µm line scans; execute 'Threshold algorithm'	If the algorithm (*'Align Write Field'* for sputtered and *'Niob'* for etched alignment marks) is not able to detect the center of a mark, adjust contrast, brightness, threshold levels and/or width range.
Exposure	Prepare and check CAD file	It is of utmost importance to check the correct definition and order of the auto alignment marks (for each alignment mark: first U-direction scan, then V-direction scan). Also check the in-file dose factor and the order of the exposed polygons. Best results were obtained when exposing the Josephson junctions of the SQUID and qubit layer at the end. Furthermore, the working area edges should be integer multiples of the writefield size.

continued on next page

continued from previous page

Process step	Details	Comments
	Prepare and check position list (PL)	Double-check correct coordinates, sequence and dose factor (DF) of exposed layers. For large-area structures (e.g. microwave antenna) switch to spot size 3 within the position list and perform a dwell time correction.
	Execute an auto alignment scan (layer 61, DF 0.02) from the PL	Check if all alignment marks were detected correctly and save *'Zoom'*, *'Shift'* and *'Rotation'* values displayed in the *'Align Writefield'* window.
	Go to *'Aktueller Faraday Cup'* and perform dwell time correction	Check the area dwell time and the standard dose ($200\,\mu C/cm^2$) using the 'Calculator' in the 'Exposure' window.
	Exposure parameters:	
	Microwave antenna and T-structure: $300\,\mu C/cm^2$	These structures are written using a larger aperture (spot size 3).
	Shunt capacitor groundplane: $300\,\mu C/cm^2$	
	Shunt capacitor and aluminum bias lines: $360 - 460\,\mu C/cm^2$	
	SQUID and qubit: $500 - 560\,\mu C/cm^2$	
	Qubit: $660 - 760\,\mu C/cm^2$	The exposure doses are higher due to the missing proximity effect of the dc-SQUID.
	Step size: $5.5\,nm \leftrightarrow 3\,pixel$	The polygons in the CAD file have to be an integer multiple of the step size.
	Area mode: meander	In this mode, the *'Flyback factor'* is not used.
	Settling time: 0.1 ms	The settling time is the waiting period at the beginning of each element. An optimum settling time depends on the order and distance of different elements. If the settling time is too short, the beam blanker opens already although the deflection unit has not yet positioned the electron beam at the desired position.

continued on next page

continued from previous page

Process step	Details	Comments
Development	AllResist AR-P 600-56 developer (2 min 20 s)	
	Stop development by placing the wafer subsequently in two Isopropanol basins (45 s each)	
Chip inspection	Check wafer under optical microscope intensively	
Sample mount for electron beam evaporation	Mount wafer in 1-inch sample holder	The $6 \times 10\,\mathrm{mm}^2$ wafer is fastened by a small droplet of silver glue to a 1-inch copper plate. After 10 min the silver glue dried and the copper plate can be inserted in the 1-inch sample holder. In general, the wafer hast be aligned according to the tilt direction of the evaporation sample stage. The wafer is now ready for aluminum shadow evaporation.

A.7 Shadow evaporation

The following table comprises the details of the shadow evaporation procedure established during this thesis. Images of the relevant instruments and components can be found in Fig. A.1.

Process step	Details	Comments
Sample mounting	Close large gate valve to UHV process chamber	The magnetic transfer arm must be retreated completely in order to be able to close the gate valve (micro switch).
	Close gate valve of load lock (LL) turbomolecular pump (TMP)	
	Vent LL chamber (N_2), open fast entry air lock door and mount sample on magnetic transfer arm; close air lock door	
Pump down procedure	Use scroll pump and open corresponding valve by hand; wait until LL pressure reaches $\sim 5 \cdot 10^{-2}$ mbar	
	Close scroll valve and open gate valve of LL TMP; wait until LL pressure reaches $\sim 1 \cdot 10^{-7}$ mbar ($\sim$ 1 h)	If the load lock pressure is not dropping below $\sim 1 \cdot 10^{-6}$ mbar, close corresponding valves and vent the load lock chamber. Use a wet isopropanol fabric and/or N_2 to clean the rubber o-ring. Repeat the pump down procedure.

continued on next page

continued from previous page

Process step	Details	Comments
Sample transfer	Open gate valve to UHV chamber	
	Transfer sample to manipulator according to instruction manual	
	Retreat magnetic transfer arm and close gate vale of UHV chamber	The sample is now ready for evaporation of aluminum.
Preliminaries	Turn on high-pressure cooling water circulation and compressor	
	Turn on high-voltage power supply, evaporation controller, rate controller, voltage supply for manipulator and PC	
	Check distance of oscillating crystal used for aluminum processes	The second oscillating crystal is used to determine the film thickness when evaporating gold.
	Tilt manipulator ($\pm 4267 \approx \pm 16^\circ$) using *IP-CommV2* software	The sign of the tilt depends on the wafer alignment on the sample holder. In general, the finger-like structure of the Josephson junctions (see Fig. 3.5) is evaporated as top-layer.
	Use process 4 and enter desired final thickness of bottom layer using LabView (*'Set_Process&FinalThickness.vi'*)	The aggregated total thickness of the previous user can be reset by pressing *'Reset'* and *'F1'* on the rate controller.
	Bottom layer thickness:	
	40 nm = 0.4 kÅ	Suitable for SQUID-qubit devices with 30 nm-thick gold bias lines and for non-galvanically coupled flux qubits.
	50 nm = 0.5 kÅ	Suitable for galvanically coupled flux qubits.
	Double-check crucial evaporation parameters: density, Z-ratio, final thickness and evaporation rate (12 Å/s)	
	Chose sufficiently filled aluminum liner	The liners that have been filled recently and can be used for evaporation are listed in the logbook.
	Turn on scroll pump, wait until ready and use scroll as backing pump of the UHV's chamber TMP	
	Check and equilibrate the capacitive pressure gauge	Use the *Maxi Gauge* for electronic (channel 6) or the respective screw driver for manual equilibration. The measured pressure should vary between $\pm 1 \cdot 10^{-5}$mbar.

continued on next page

continued from previous page

Process step	Details	Comments
	Set VAT adaptive pressure controller *'Setpoint 3'*	
	Check settings of mass flow controller (*'SP1'*, 3 sccm)	
	Equilibrate VAT controller (press *'Zero'* for 5 s)	
Evaporation	Start and execute LabView script (*'V 2.4.0.vi'*, measuring mode: *'Inficon'*)	
	Write down all parameters in evaporation log	
	Turn on high-voltage using the evaporation controller (8 kV)	All interlocks (e.g. cooling water, vacuum, liner) have to be enabled in order to be able to turn on the high-voltage.
	Press *'Start Process'* in the LabView front panel; monitor emission current on evaporation controller ($\sim$ 430 − 480 mA during actual evaporation)	The shutter opens automatically when the desired rate is stabilized within $\pm$20% for more than 5 s. After the desired final thickness is reached, the shutter closes and the emission current is reduced automatically.
	Press *'Stop'* in LabView panel and turn of high-voltage on evaporation controller	
Oxidation	Bring manipulator in horizontal position (*IP-CommV2* software, 0)	
	Switch to measuring mode: *'Oxidation'*	
	enter desired L-product (0.275 mbar s)	The L-product is defined as: $L = p_{O_2} \cdot t$, where p_{O_2} is the partial O_2 pressure and t the oxidation time.
	Execute LabView script and enter filename	
	Press *'On'* on mass flow controller and *'Position Mode'* on VAT pressure controller simultaneously; start stop-watch for additional time reference	The gate valve in front of the large TMP is in a half-open position. With the constant O_2 flow of 3 sccm, an constant oxidation pressure of $2 \cdot 10^{-4}$ mbar is established. The status of the oxidation process is visualized by LabView. Typically, $L = 0.275$ mbar s corresponds to an oxidation time of $t \approx 23$ min.

continued on next page

continued from previous page

Process step	Details	Comments
	Stop oxidation by pressing *'Off'* on mass flow controller and *'Open'* on VAT pressure controller	Within a few seconds, the pressure in the UHV chamber (*Maxi Gauge*, channel 2) drops below $5 \cdot 10^{-7}$ mbar.
Evaporation	Tilt manipulator (bottom layer: $\pm 4267 \rightarrow$ top layer: ∓ 4267) using *IP-CommV2* software	
	Use process 4 and enter desired final thickness of top layer using LabView (*'Set_Process&FinalThickness.vi'*)	The aggregated total thickness of the previous evaporation is reset by *'F1'* on the rate controller.
	Top layer thickness:	
	50 nm = 0.5 kÅ	Suitable for SQUID-qubit devices with 30 nm-thick gold bias lines and for non-galvanically coupled flux qubits.
	80 nm = 0.8 kÅ	Suitable for galvanically coupled flux qubits.
	Execute LabView script (*'V 2.4.0.vi'*, measuring mode: *'Inficon'*)	
	Turn on high-voltage using the evaporation controller (8 kV)	
	Press *'Start Process'* in the LabView front panel; monitor emission current on evaporation controller ($\sim 430 - 480$ mA during actual evaporation)	After the desired final thickness is reached, the shutter closes and the emission current is reduced automatically.
	Retreat sample from manipulator according to instruction manual	To close the gate vale to the UHV chamber, the magnetic transfer arm has to be retreated completely (micro switch).
	Switch back to diaphragm pump as backing pump of the UHV's chamber TMP	The scroll pump is used for evacuating the LL after the sample is retreated.
	Close gate valve of load lock LL TMP	
	Vent LL chamber (N_2), open fast entry air lock door and retreat sample; close air lock door and use scroll to evacuate LL chamber ($\sim 5 \cdot 10^{-2}$ mbar)	
	Close scroll valve and open gate valve of LL TMP; shutdown scroll pump	
	After 15 min, turn off compressor and high-pressure cooling water circulation except for large TMP	

continued on next page

continued from previous page

Process step	**Details**	**Comments**
Logbook	Write down aggregated thickness of both evaporation processes using the LabView log files	The aluminum liner should be switched after evaporation of a total thickness of 20 kÅ. The sample is further processed in the cleanroom.
Resist stripping	Acetone bath (hotplate, 30 − 45 min, 70° C), ultrasonic cleaning (4 min, power 2) Isopropanol bath (hotplate, 5 min, 70° C), ultrasonic cleaning (2 min, power 2)	Repeat process if aluminum film is not completely removed. After the aluminum is removed **completely**, switch to a clean acetone basin (hotplate, 10 min, 70° C). Keep the wafer constantly wet when switching basins.
Dicing	1-inch wafer can be diced using the manual wafer scratcher and the dicing tool	

A.8 Wafer specifications

Device	Details
SQUID-qubit devices	Manufacturer: *CrysTec* 1-inch wafer with flat Orientation: (100) Thickness: 525 µm Specific resistance: $1 - 20\,\Omega$cm Dopant: Bor (p-type) Oxide: 50 nm (thermally oxidized)
Circuit QED devices & CPW resonators	Manufacturer: *CrysTec* 4-inch wafer diced into $6 \times 10\,\text{mm}^2$ wafer Orientation: (100) Thickness: 525 µm Specific resistance: $> 3000\,\Omega$cm Dopant: none (n-type) Oxide: 50 nm (thermally oxidized)

A.9 Electron beam evaporator

Figure A.1 shows images of the electron beam evaporation (EVAP) facility and its components. This thin film deposition system (see Fig. A.1 a) installed by T. Brenniger [169] was used for the production of all Josephson junction devices presented in this thesis. It consists of a large process UHV chamber (A) evacuated by a turbomolecular pump (TMP) with a pumping speed of 1000 l/s (D; see also Fig. A.1 d). The process chamber is equipped with a 5 kW electron beam evaporator (B) from the company *MBE-Komponenten*. In contrast to the old evaporation facility [169], the distance between the evaporation source and substrate was increased by 100 % to 65 cm. Therefore, backside cooling of the sample to avoid a collapse of the sensitive resist bridges owing to a high thermal load can be omitted. A pneumatically activated gate valve separates the process chamber from the load lock (C). The load lock is equipped with a TMP (pumping speed 260 l/s; not shown in this picture) and can be evacuated to a pressure of $1 \cdot 10^{-7}$ mbar within 1 h. A magnetic transfer arm (E) with a specially designed sample holder (see Fig. A.1 b) allows an easy transfer of the sample from the load lock to the tiltable manipulator (see Fig. A.1 c) installed in the process chamber.
Both TMP's use diaphragm pumps as backing pumps (F and G; see Fig. A.1 d). During the oxidation of the Josephson tunnel junctions, the oil-free scroll pump (H) is used as backing pump of the process chamber's TMP. Using a bypass, the scroll pump is also used to evacuate the load lock chamber to a sufficiently low pressure for the load lock's TMP. A capacitive pressure gauge (I) in front of the adaptive gate valve (K) is used for measuring the O_2 pressure during the formation of the Josephson tunnel barriers. Figure A.1 e shows a part of the pressure control rack. The adaptive gate valve is connected to a *VAT* pressure controller (L). In combination with a mass flow controller (M), the oxygen pressure in the

process chamber can be controlled very precisely in a range $1 \cdot 10^{-4}$ mbar $- 5 \cdot 10^{-2}$ mbar. All pressure gauges are connected to a *Pfeiffer Maxi Gauge* vacuum measurement and control unit (O). The evaporation unit is controlled by an *FerroTec* evaporation controller (P) and an *Inficon* IC5 thin film deposition controller (Q) shown in Fig. A.1 f. A high-voltage power supply (R) and a filament power supply (not shown) complete the evaporation unit. The manipulator stepping motors and the IC5 are controlled via a LabView interface (T). The electron beam is created by heating a tungsten filament coil. For our fabrication process, we use an acceleration voltage of 8 kV. A permanent magnet forces the electrons on a 270° circle while four magnet coils are used for focusing the electron beam in the crucible. For the fabrication of Josephson junction devices, high purity (5N) aluminum is used. A typical process diagram is shown in Fig. A.2 a. First, the emission current I_e is ramped to 30 % of its maximum value ($I_{e,max} = 500$ mA) and kept constant for 30 s in order to heat up the aluminum. Then, I_e is further increased to $\approx 85\,\% - 90\,\%$ of $I_{e,max}$. When the rate is stabilized around 12 Å/s by the *Inficons* IC5 PID controller, the shutter opens. The evaporation rate and aggregated film thickness is determined by measuring the mass-dependent resonance frequency (~ 6 MHz) of a quartz crystal. After the desired

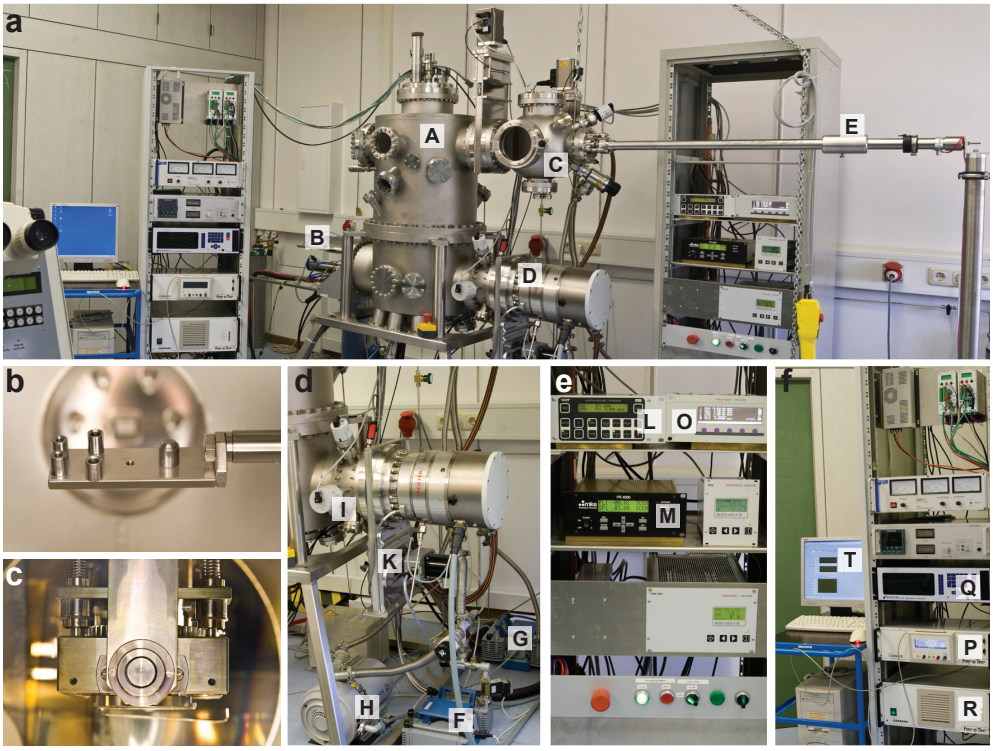

Figure A.1: Images of the aluminum evaporation system. (a) Overview image. The most important elements are marked by capital letters: (A) UHV process chamber. (B) Evaporation unit. (C) Load lock with fast entry air lock door. (D) Process chamber's TMP. (E) Magnetic transfer arm system. (b) Image of the magnetic transfer arm's sample holder. (c) Image of the revolvable and tiltable manipulator inside the UHV process chamber (maximum rotation angle: ±180°; maximum tilt angle: ±90°). (d) Magnified view of the pumping system. (F) and (G) Diaphragm backing pumps. (H) Scroll pump. (I) Capacitive pressure gauge used during oxidation processes. (K) Adaptive gate valve. (e) Part of the pressure control rack. (L) Pressure controller (controls the adaptive gate valve). (O) Maxi Gauge vacuum measurement and control unit. (M) Mass flow controller. (f) Image of the evaporation control rack. (P) Evaporation controller. (R) High-voltage supply. (Q) Rate controller. (T) LabView interface.

thickness is evaporated, the shutter closes automatically and I_e is reduced in two steps to zero.

The oxidation process (see Fig. A.2 b) is initiated promptly after evaporation of the Josephson junction's bottom layer. A precise equilibration of the VAT pressure controller and the capacitive pressure gauge via the *Maxi Gauge* (see Fig. A.1 d and e) has to be accomplished prior to evaporation of the first aluminum layer. While the oxidation is started and stopped manually, the oxidation progress is monitored using a LabView interface. In order to obtain Josephson junctions with a high critical current density $j_c \sim 1.0 - 2.5\,\mathrm{kA/cm^2}$, we oxidize the bottom aluminum layer $22 - 23\,\mathrm{min}$ at $p_{O_2} \approx 2 \cdot 10^{-4}\,\mathrm{mbar}$ which corresponds to a L-product of $0.264 - 0.276\,\mathrm{mbar \cdot s}$.

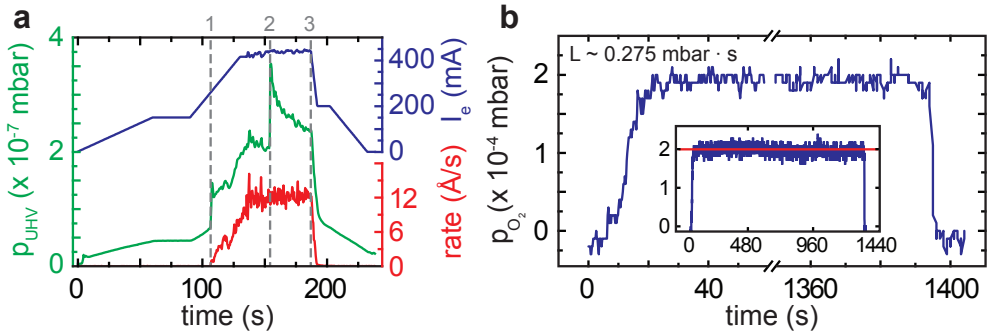

Figure A.2: Evaporation and oxidation process diagrams. (a) Evaporation diagram showing typical evaporation parameters for pressure (p_{UHV}, green), emission current (I_e, blue) and evaporation rate (red) as a function of time. The dashed gray lines indicate: (1) melting point of aluminum; $I_e \approx 260 - 280\,\mathrm{mA}$. (2) shutter opens. (3) shutter closes. (b) Oxidation pressure p_{O_2} as a function of time. The oxidation can be stopped within a few seconds by fully opening the adaptive gate valve (K, see Fig. A.1 d) in front of the process chamber's TMP. Inset: complete process diagram. The red solid line is a a fit to the data yielding $p_{O_2} = 1.96 \cdot 10^{-4}\,\mathrm{mbar}$.

A.10 Reproducibility of critical current densities

One of the main goals during this thesis was to establish a reliable fabrication processes for Josephson junction devices in the new evaporation system. In contrast to other types of qubits, large critical current densities and small Josephson junction areas are a prerequisite for flux qubits with energy gaps $\Delta \gg k_B T \approx 1\,\mathrm{GHz}$ at $T = 50\,\mathrm{mK}$ (see section 2.2.2). While the areas of Josephson junctions can be reliably fabricated by EBL within $6\,\% - 8\,\%$ margins, the oxide layer thickness is more difficult to control. Figure A.3 a shows the measured critical current densities of our dc-SQUIDs as a function of $L = p_{O_2} \cdot t$. During this thesis, various designs of Josephson junction devices were realized. In the beginning of junction optimization $t \approx 18\,\mathrm{min}$ was sufficient to form Josephson junctions with $j_c \approx 1 - 2\,\mathrm{kA/cm^2}$. Very abruptly, the oxidation time had to be increased by more than 4 min to obtain similar values for j_c. Unfortunately, we can give no final conclusion concerning the circumstances which led to this sudden, large variation in L. The expected power-law dependence of $j_c(L)$ can not be inferred from Fig. A.3 a. Based on a good estimate for L from the 'old' evaporation facility, the pressure-time-product had to be varied only slightly. Figure A.3 shows the linear relation between $1/R_n$ and the measured switching current of

our dc-SQUIDs. A numerical fit to the Ambegaokar-Baratoff relation given in Eq. (2.7) yields $V_g = (352 \pm 11)\,\mu V$ in agreement with the expected value of $V_{BCS} = 2\Delta_s/e = 3.52 k_B T_c/e = 364\,\mu V$. Although an increase of V_g and T_c was observed for $5-30\,nm$ thick aluminum films [172, 266], we observe a gap voltage close to the bulk value for our 90 nm thick aluminum junctions indicating high-quality thin films.
The data depicted in Fig. A.3 indicates a good control of crucial fabrication parameters for realizing Josephson junction devices. At present, the yield of flux qubits with an intended $\Delta > 2\,GHz$ embedded in CPW resonators – all in all 16 devices – is 100%.

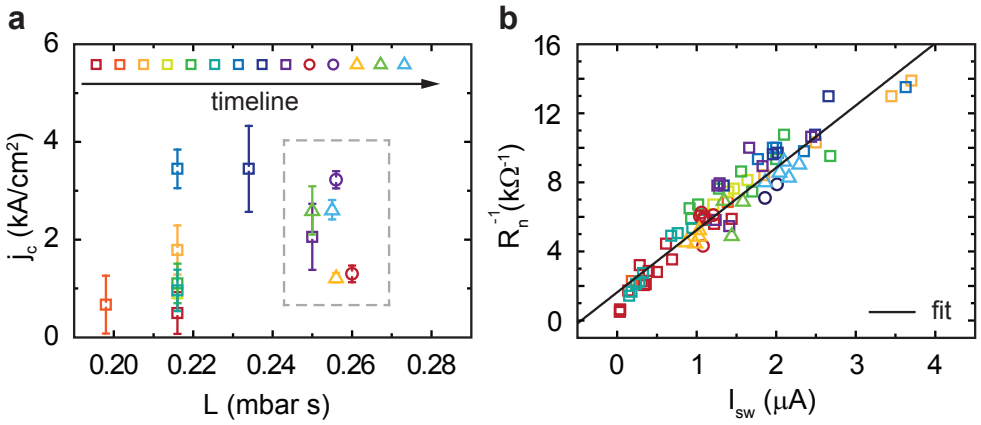

Figure A.3: Comprehensive overview of junction properties. (a) Experimentally determined critical current densities j_c of our dc-SQUIDs as a function of the pressure-time product L (error bars: standard deviation). The symbols represent different layouts (squares: no shunt capacitors, see Fig. 3.2 a for layout and Fig. 4.3 a for sample image; circles: modified layout (not shown) with additional shunt capacitors; triangles: shunt capacitors and microwave antenna, see Fig. 3.2 a for layout and Fig. 3.9 d for sample image). The color of the symbols indicates different fabrication runs and the dashed gray box encloses the fabrication runs including flux qubits with $\Delta > 2\,GHz$. (b) Measured inverse normal resistance R_n^{-1} as a function of the maximum switching current I_{sw} for various dc-SQUIDs. The red solid line is a numerical fit yielding $V_g = (352 \pm 11)\,\mu V$. The color and symbol code is the same as in (a).

Bibliography

[1] Josephson, B. D. Possible new effects in superconductive tunnelling. *Phys. Lett.* **1**, 251–253 (1962).

[2] Anderson, P. & Rowell, J. Probable Observation of the Josephson Superconducting Tunneling Effect. *Phys. Rev. Lett.* **10**, 230–232 (1963).

[3] Jaynes, E. T. & Cummings, F. W. Comparison of quantum and semiclassical radiation theories with application to the beam maser. *Proc. IEEE* **51**, 89 (1963).

[4] Eberly, J. H., Narozhny, N. B. & Sanchez-Mondragon, J. J. Periodic Spontaneous Collapse and Revival in a Simple Quantum Model. *Phys. Rev. Lett.* **44**, 1323–1326 (1980).

[5] Rempe, G., Walther, H. & Klein, N. Observation of quantum collapse and revival in a one-atom maser. *Phys. Rev. Lett.* **58**, 353–356 (1987).

[6] Blais, A., Huang, R.-S., Wallraff, A., Girvin, S. M. & Schoelkopf, R. J. Cavity quantum electrodynamics for superconducting electrical circuits: An architecture for quantum computation. *Phys. Rev. A* **69**, 062320 (2004).

[7] Wallraff, A. *et al.* Strong coupling of a single photon to a superconducting qubit using circuit quantum electrodynamics. *Nature* **431**, 162–167 (2004).

[8] Niemczyk, T. *et al.* Circuit quantum electrodynamics in the ultrastrong-coupling regime. *Nature Physics* **6**, 772–776 (2010).

[9] Feynman, R. P. Simulating physics with computers. *Int. J. Theo. Phys.* **21**, 467–488 (1982).

[10] Benioff, P. The computer as a physical system: A microscopic quantum mechanical Hamiltonian model of computers as represented by Turing machines. *J. Stat. Phys.* **22**, 563–591 (1980).

[11] Benioff, P. Quantum mechanical hamiltonian models of turing machines. *J. Stat. Phys.* **29**, 515–546 (1982).

[12] Albert, D. Z. On quantum-mechanical automata. *Phys. Lett. A* **98**, 249 – 252 (1983).

[13] Deutsch, D. Quantum Theory, the Church-Turing principle and the universal quantum computer. *Proc. R. Soc. London, Ser. A* **400**, 97 (1985).

[14] Deutsch, D. & Jozsa, R. Rapid Solution of Problems by Quantum Computation. *Proc. R. Soc. London A* **439**, 553–558 (1992).

[15] Shor, P. W. Algorithms for Quantum Computation: Discrete Logarithms and Factoring. In Goldwasser, S. (ed.) *Proceedings of the 35th Annual Symposium on the Foundations of Computer Science*, 124–134 (IEEE Computer Society, Los Alamitos, 1994).

[16] Grover, L. K. A fast quantum mechanical algorithm for database search. In *STOC '96: Proceedings of the twenty-eighth annual ACM symposium on Theory of computing*, 212–219 (ACM, New York, NY, USA, 1996).

[17] Grover, L. K. Quantum Mechanics Helps in Searching for a Needle in a Haystack. *Phys. Rev. Lett.* **79**, 325–328 (1997).

[18] Simon, D. R. On the Power of Quantum Computation. *SIAM J. Comp.* **26**, 1474–1483 (1997).

[19] Lloyd, S. Universal Quantum Simulators. *Science* **273**, 1073–1078 (1996).

[20] Bennett, C. & Brassard, G. Quantum cryptography: Public key distribution and coin tossing. In *Proceedings of IEEE International Conference on Computers, Systems, and Signal Processing*, 175–179 (1984).

[21] Ekert, A. K. Quantum cryptography based on Bell's theorem. *Phys. Rev. Lett.* **67**, 661–663 (1991).

[22] Chuang, I. L., Vandersypen, L. M. K., Zhou, X., Leung, D. W. & Lloyd, S. Experimental realization of a quantum algorithm. *Nature* **393**, 143–146 (1998).

[23] Vandersypen, L. M. K. *et al.* Experimental realization of Shor's quantum factoring algorithm using nuclear magnetic resonance. *Nature (London)* **414**, 883–887 (2001).

[24] Cirac, J. I. & Zoller, P. Quantum Computations with Cold Trapped Ions. *Phys. Rev. Lett.* **74**, 4091–4094 (1995).

[25] Cirac, J. I., Zoller, P., Kimble, H. J. & Mabuchi, H. Quantum State Transfer and Entanglement Distribution among Distant Nodes in a Quantum Network. *Phys. Rev. Lett.* **78**, 3221–3224 (1997).

[26] Sackett, C. A. *et al.* Experimental entanglement of four particles. *Nature* **404**, 256–259 (2000).

[27] Cirac, J. I. & Zoller, P. A scalable quantum computer with ions in an array of microtraps. *Nature* **404**, 579–581 (2000).

[28] Leibfried, D., Blatt, R., Monroe, C. & Wineland, D. Quantum dynamics of single trapped ions. *Rev. Mod. Phys.* **75**, 281–324 (2003).

[29] Bouwmeester, D. *et al.* Experimental quantum teleportation. *Nature* **390**, 575–579 (1997).

[30] Bouwmeester, D., Pan, J.-W., Daniell, M., Weinfurter, H. & Zeilinger, A. Observation of Three-Photon Greenberger-Horne-Zeilinger Entanglement. *Phys. Rev. Lett.* **82**, 1345–1349 (1999).

[31] Zeilinger, A. Experiment and the foundations of quantum physics. *Rev. Mod. Phys.* **71**, S288–S297 (1999).

[32] Walther, P. *et al.* Experimental one-way quantum computing. *Nature* **434**, 169–176 (2005).

[33] Hood, C. J., Lynn, T. W., Doherty, A. C., Parkins, A. S. & Kimble, H. J. The Atom-Cavity Microscope: Single Atoms Bound in Orbit by Single Photons. *Science* **287**, 1447–1453 (2000).

[34] Raimond, J. M., Brune, M. & Haroche, S. Manipulating quantum entanglement with atoms and photons in a cavity. *Rev. Mod. Phys.* **73**, 565–582 (2001).

[35] Monroe, C. Quantum information processing with atoms and photons. *Nature* **416**, 238–246 (2002).

[36] Mabuchi, H. & Doherty, A. C. Cavity Quantum Electrodynamics: Coherence in Context. *Science* **298**, 1372–1377 (2002).

[37] Walther, H., Varcoe, B. T. H., Englert, B.-G. & Becker, T. Cavity Quantum Electrodynamics. *Rep. Prog. Phys.* **69**, 1325–1382 (2006).

[38] Haroche, S. & Raimond, J.-M. *Exploring the Quantum* (Oxford University Press Inc., New York, 2006).

[39] DiVincenzo, D. P. The Physical Implementation of Quantum Computation. *Fortschr. Phys.* **48**, 771 (2000).

[40] Kane, B. E. A silicon-based nuclear spin quantum computer. *Nature* **393**, 133–137 (1998).

[41] Loss, D. & DiVincenzo, D. P. Quantum computation with quantum dots. *Phys. Rev. A* **57**, 120–126 (1998).

[42] Kroutvar, M. *et al.* Optically programmable electron spin memory using semiconductor quantum dots. *Nature* **432**, 81–84 (2004).

[43] Petta, J. R. *et al.* Coherent Manipulation of Coupled Electron Spins in Semiconductor Quantum Dots. *Science* **309**, 2180–2184 (2005).

[44] Hanson, R., Kouwenhoven, L. P., Petta, J. R., Tarucha, S. & Vandersypen, L. M. K. Spins in few-electron quantum dots. *Rev. Mod. Phys.* **79**, 1217–1265 (2007).

[45] Jelezko, F., Gaebel, T., Popa, I., Gruber, A. & Wrachtrup, J. Observation of Coherent Oscillations in a Single Electron Spin. *Phys. Rev. Lett.* **92**, 076401 (2004).

[46] Childress, L. *et al.* Coherent Dynamics of Coupled Electron and Nuclear Spin Qubits in Diamond. *Science* **314**, 281–285 (2006).

[47] Makhlin, Yu., Schön, G. & Shnirman, A. Quantum-state engineering with Josephson-junction devices. *Rev. Mod. Phys.* **73**, 357–400 (2001).

[48] Devoret, M. H., Wallraff, A. & Martinis, J. M. Superconducting qubits: A short review (2004). ArXiv:cond-mat/0411174v1.

[49] Clarke, J. & Wilhelm, F. K. Superconducting quantum bits. *Nature* **453**, 1031–1042 (2008).

[50] Ladd, T. D. *et al.* Quantum computers. *Nature* **464**, 45–53 (2010).

[51] Bennett, C. H. & DiVincenzo, D. P. Quantum information and computation. *Nature* **404**, 247–255 (2000).

[52] Likharev, K. K. *Dynamics of Josephson Junctions and Circuits* (Taylor & Francis Ltd., Gordon and Breah Publishers, 1986).

[53] Tinkham, M. *Introduction to Superconductivity* (McGraw-Hill, New York, 1996).

[54] Nakamura, Y., Chen, C. D. & Tsai, J. S. Spectroscopy of Energy-Level Splitting between Two Macroscopic Quantum States of Charge Coherently Superposed by Josephson Coupling. *Phys. Rev. Lett.* **79**, 2328–2331 (1997).

[55] Shnirman, A., Schön, G. & Hermon, Z. Quantum Manipulations of Small Josephson Junctions. *Phys. Rev. Lett.* **79**, 2371–2374 (1997).

[56] Bouchiat, V., Vion, D., Joyez, P., Esteve, D. & Devoret, M. H. Quantum coherence with a single Cooper pair. *Physica Scripta* **T 76**, 165–170 (1998).

[57] Nakamura, Y., Pashkin, Yu. A. & Tsai, J. S. Coherent control of macroscopic quantum states in a single-Cooper-pair box. *Nature* **398**, 786–788 (1999).

[58] Nakamura, Y., Pashkin, Y. A. & Tsai, J. S. Rabi Oscillations in a Josephson-Junction Charge Two-Level System. *Phys. Rev. Lett.* **87**, 246601 (2001).

[59] Vion, D. *et al.* Manipulating the Quantum State of an Electrical Circuit. *Science* **296**, 886–889 (2002).

[60] Siddiqi, I. *et al.* Dispersive measurements of superconducting qubit coherence with a fast latching readout. *Phys. Rev. B* **73**, 054510 (2006).

[61] Metcalfe, M. *et al.* Measuring the decoherence of a quantronium qubit with the cavity bifurcation amplifier. *Phys. Rev. B* **76**, 174516 (2007).

[62] Manucharyan, V. E., Koch, J., Glazman, L. I. & Devoret, M. H. Fluxonium: Single Cooper-Pair Circuit Free of Charge Offsets. *Science* **326**, 113–116 (2009).

[63] Orlando, T. P. *et al.* Superconducting persistent-current qubit. *Phys. Rev. B* **60**, 15398–15413 (1999).

[64] Mooij, J. E. *et al.* Josephson Persistent-Current Qubit. *Science* **285**, 1036–1039 (1999).

[65] Friedman, J. R., Patel, V., Chen, W., Tolpygo, S. K. & Lukens, J. E. Quantum superposition of distinct macroscopic states. *Nature (London)* **406**, 43–46 (2000).

[66] van der Wal, C. H. *et al.* Quantum Superposition of Macroscopic Persistent-Current States. *Science* **290**, 773–777 (2000).

[67] Chiorescu, I., Nakamura, Y., Harmans, C. J. P. M. & Mooij, J. E. Coherent Quantum Dynamics of a Superconducting Flux Qubit. *Science* **299**, 1869–1871 (2003).

[68] Koch, J. *et al.* Charge-insensitive qubit design derived from the Cooper pair box. *Phys. Rev. A* **76**, 042319 (2007).

[69] Schreier, J. A. *et al.* Suppressing charge noise decoherence in superconducting charge qubits. *Phys. Rev. B* **77**, 180502 (2008).

[70] Houck, A. A. *et al.* Controlling the Spontaneous Emission of a Superconducting Transmon Qubit. *Phys. Rev. Lett.* **101**, 080502 (2008).

[71] Martinis, J. M., Devoret, M. H. & Clarke, J. Energy-Level Quantization in the Zero-Voltage State of a Current-Biased Josephson Junction. *Phys. Rev. Lett.* **55**, 1543–1546 (1985).

[72] Clarke, J., Cleland, A. N., Devoret, M. H., Esteve, D. & Martinis, J. M. Quantum Mechanics of a Macroscopic Variable: The Phase Difference of a Josephson Junction. *Science* **239**, 992–997 (1988).

[73] Martinis, J. M., Nam, S., Aumentado, J. & Urbina, C. Rabi Oscillations in a Large Josephson-Junction Qubit. *Phys. Rev. Lett.* **89**, 117901 (2002).

[74] Yu, Y., Han, S., Chu, X., Chu, S.-I. & Wang, Z. Coherent Temporal Oscillations of Macroscopic Quantum States in a Josephson Junction. *Science* **296**, 889–892 (2002).

[75] Martinis, J. Superconducting phase qubits. *Quantum Information Processing* **8**, 81–103 (2009).

[76] Paladino, E., Faoro, L., Falci, G. & Fazio, R. Decoherence and $1/f$ Noise in Josephson Qubits. *Phys. Rev. Lett.* **88**, 228304 (2002).

[77] Martinis, J. M., Nam, S., Aumentado, J., Lang, K. M. & Urbina, C. Decoherence of a superconducting qubit due to bias noise. *Phys. Rev. B* **67**, 094510 (2003).

[78] Simmonds, R. W. *et al.* Decoherence in Josephson Phase Qubits from Junction Resonators. *Phys. Rev. Lett.* **93**, 077003 (2004).

[79] Astafiev, O., Pashkin, Y. A., Nakamura, Y., Yamamoto, T. & Tsai, J. S. Quantum Noise in the Josephson Charge Qubit. *Phys. Rev. Lett.* **93**, 267007 (2004).

[80] Van Harlingen, D. J. *et al.* Decoherence in Josephson-junction qubits due to critical-current fluctuations. *Phys. Rev. B* **70**, 064517 (2004).

[81] Ithier, G. *et al.* Decoherence in a superconducting quantum bit circuit. *Phys. Rev. B* **72**, 134519 (2005).

[82] Bertet, P. *et al.* Dephasing of a Superconducting Qubit Induced by Photon Noise. *Phys. Rev. Lett.* **95**, 257002 (2005).

[83] Martinis, J. M. *et al.* Decoherence in Josephson Qubits from Dielectric Loss. *Phys. Rev. Lett.* **95**, 210503 (2005).

[84] Yoshihara, F., Harrabi, K., Niskanen, A. O., Nakamura, Y. & Tsai, J. S. Decoherence of Flux Qubits due to $1/f$ Flux Noise. *Phys. Rev. Lett.* **97**, 167001 (2006).

[85] Kakuyanagi, K. *et al.* Dephasing of a Superconducting Flux Qubit. *Phys. Rev. Lett.* **98**, 047004 (2007).

[86] Koch, R. H., DiVincenzo, D. P. & Clarke, J. Model for $1/f$ Flux Noise in SQUIDs and Qubits. *Phys. Rev. Lett.* **98**, 267003 (2007).

[87] Deppe, F. *et al.* Phase coherent dynamics of a superconducting flux qubit with capacitive bias readout. *Phys. Rev. B* **76**, 214503 (2007).

[88] Ye, J., Vernooy, D. W. & Kimble, H. J. Trapping of Single Atoms in Cavity QED. *Phys. Rev. Lett.* **83**, 4987–4990 (1999).

[89] Vahala, K. J. Optical microcavities. *Nature* **424**, 839–846 (2003).

[90] Rauschenbeutel, A. *et al.* Step-by-Step Engineered Multiparticle Entanglement. *Science* **288**, 2024–2028 (2000).

[91] Gleyzes, S. *et al.* Quantum jumps of light recording the birth and death of a photon in a cavity. *Nature* **446**, 297–300 (2007).

[92] Painter, O. *et al.* Two-Dimensional Photonic Band-Gap Defect Mode Laser. *Science* **284**, 1819–1821 (1999).

[93] Akahane, Y., Asano, T., Song, B.-S. & Noda, S. Fine-tuned high-Q photonic-crystal nanocavity. *Opt. Express* **13**, 1202–1214 (2005).

[94] Nomura, M., Kumagai, N., Iwamoto, S., Ota, Y. & Arakawa, Y. Laser oscillation in a strongly coupled single-quantum-dot-nanocavity system. *Nature Physics* **6**, 279–283 (2010).

[95] Kimble, H. J. Strong interactions of single atoms and photons in cavity QED. *Physica Scripta* **T 76**, 127–137 (1998).

[96] Meschede, D., Walther, H. & Müller, G. One-Atom Maser. *Phys. Rev. Lett.* **54**, 551–554 (1985).

[97] Thompson, R. J., Rempe, G. & Kimble, H. J. Observation of normal-mode splitting for an atom in an optical cavity. *Phys. Rev. Lett.* **68**, 1132–1135 (1992).

[98] Reithmaier, J. P. *et al.* Strong coupling in a single quantum dot-semiconductor microcavity system. *Nature* **432**, 197–200 (2004).

[99] Yoshie, T. *et al.* Vacuum Rabi splitting with a single quantum dot in a photonic crystal nanocavity. *Nature* **432**, 200–2003 (2004).

[100] Chiorescu, I. *et al.* Coherent dynamics of a flux qubit coupled to a harmonic oscillator. *Nature* **431**, 159–162 (2004).

[101] Wallraff, A. *et al.* Approaching Unit Visibility for Control of a Superconducting Qubit with Dispersive Readout. *Phys. Rev. Lett.* **95**, 060501 (2005).

[102] Schuster, D. I. *et al.* ac Stark Shift and Dephasing of a Superconducting Qubit Strongly Coupled to a Cavity Field. *Phys. Rev. Lett.* **94**, 123602 (2005).

[103] Gambetta, J. *et al.* Qubit-photon interactions in a cavity: Measurement-induced dephasing and number splitting. *Phys. Rev. A* **74**, 042318 (2006).

[104] Schuster, D. I. *et al.* Resolving photon number states in a superconducting circuit. *Nature* **445**, 515–518 (2007).

[105] Steffen, M. *et al.* State Tomography of Capacitively Shunted Phase Qubits with High Fidelity. *Phys. Rev. Lett.* **97**, 050502 (2006).

[106] Steffen, M. *et al.* Measurement of the Entanglement of Two Superconducting Qubits via State Tomography. *Science* **313**, 1423–1425 (2006).

[107] Houck, A. A. *et al.* Generating single microwave photons in a circuit. *Nature* **449**, 328–331 (2007).

[108] Majer, J. *et al.* Coupling superconducting qubits via a cavity bus. *Nature* **449**, 443–447 (2007).

[109] Sillanpää, M. A., Park, J. I. & Simmonds, R. W. Coherent quantum state storage and transfer between two phase qubits via a resonant cavity. *Nature* **449**, 438–442 (2007).

[110] Hofheinz, M. *et al.* Generation of Fock states in a superconducting quantum circuit. *Nature* **454**, 310–314 (2008).

[111] Wang, H. *et al.* Measurement of the Decay of Fock States in a Superconducting Quantum Circuit. *Phys. Rev. Lett.* **101**, 240401 (2008).

[112] Hofheinz, M. *et al.* Synthesizing arbitrary quantum states in a superconducting resonator. *Nature* **459**, 546–549 (2009).

[113] Astafiev, O. *et al.* Single artificial-atom lasing. *Nature* **449**, 588–590 (2007).

[114] Fink, J. *et al.* Climbing the Jaynes-Cummings ladder and observing its $\sqrt{n}$ nonlinearity in a cavity QED system. *Nature* **454**, 315–318 (2008).

[115] Fink, J. M. *et al.* Dressed Collective Qubit States and the Tavis-Cummings Model in Circuit QED. *Phys. Rev. Lett.* **103**, 083601 (2009).

[116] Bishop, L. *et al.* Nonlinear response of the vacuum Rabi resonance. *Nature Physics* **5**, 105–109 (2008).

[117] Ansmann, M. *et al.* Violation of Bell's inequality in Josephson phase qubits. *Nature* **461**, 504–506 (2009).

[118] DiCarlo, L. *et al.* Demonstration of two-qubit algorithms with a superconducting quantum processor. *Nature* **460**, 240–244 (2009).

[119] Paik, H. *et al.* How coherent are Josephson junctions ? (2011). ArXiv:quant-ph/1105.4652v2.

[120] Altomare, F. *et al.* Tripartite interactions between two phase qubits and a resonant cavity. *Nature Physics* **6**, 777–781 (2010).

[121] Neeley, M. *et al.* Generation of three-qubit entangled states using superconducting phase qubits. *Nature* **467**, 570–573 (2010).

[122] DiCarlo, L. *et al.* Preparation and measurement of three-qubit entanglement in a superconducting circuit. *Nature* **467**, 574–578 (2010).

[123] Voss, R. F. & Webb, R. A. Macroscopic Quantum Tunneling in 1-μm Nb Josephson Junctions. *Phys. Rev. Lett.* **47**, 265–268 (1981).

[124] London, F. *Superfluids*, vol. 76 (John Wiley & Sons, Inc., New York, 1950).

[125] Little, W. A. & Parks, R. D. Observation of Quantum Periodicity in the Transition Temperature of a Superconducting Cylinder. *Phys. Rev. Lett.* **9**, 9 (1962).

[126] Orlando, T. P. & Delin, K. A. *Foundations of Applied Superconductivity* (Addison-Wesley Publishing Company, New York, 1991).

[127] Gross, R. & Marx, A. Applied Superconductivity: Josephson Effect and Superconducting Electronics (2005). Lecture notes.

[128] Ambegaokar, V. & Baratoff, A. Tunneling Between Superconductors. *Phys. Rev. Lett.* **10**, 486 (1963).

[129] McCumber, D. E. Effect of ac Impedance on dc Voltage-Current Characteristics of Superconductor Weak-Link Junctions. *J. Appl. Phys.* **39**, 3113–3118 (1968).

[130] Stewart, W. C. Current-Voltage characteristics of Josephson junctions. *App. Phys. Lett.* **12**, 277–280 (1968).

[131] Chen, Y. Macroscopic Quantum Tunneling in a dc SQUID. *J. Low Temp. Phys.* **65**, 133–147 (1986).

[132] Deppe, F. *Superconducting Flux Quantum Circuits: Characterization, Quantum Coherence, and Controlled Symmetry Breaking.* Ph.D. thesis, TU München (2009).

[133] Doll, R. & Näbauer, M. Experimental Proof of Magnetic Flux Quantization in a Superconducting Ring. *Phys. Rev. Lett.* **7**, 51–52 (1961).

[134] Deaver, B. S. & Fairbank, W. M. Experimental Evidence for Quantized Flux in Superconducting Cylinders. *Phys. Rev. Lett.* **7**, 43–46 (1961).

[135] Grabert, H. & Weiss, U. Crossover from Thermal Hopping to Quantum Tunneling. *Phys. Rev. Lett.* **53**, 1787–1790 (1984).

[136] Wallraff, A. *et al.* Switching current measurements of large area Josephson tunnel junctions. *Rev. Sci. Instrum.* **74**, 3740–3748 (2003).

[137] Lisenfeld, J., Lukashenko, A. & Ustinov, A. V. High-contrast readout of superconducting qubits beyond the single-shot resolution limit. *Appl. Phys. Lett.* **91**, 232502 (2007).

[138] van der Wal, C. H. *Quantum Superpositions of Persistent Josephson Currents*. Ph.D. thesis, TU Delft (2001).

[139] Robertson, T. L. *et al.* Superconducting quantum interference device with frequency-dependent damping: Readout of flux qubits. *Phys. Rev. B* **72**, 024513 (2005).

[140] Johansson, J. *et al.* Vacuum Rabi Oscillations in a Macroscopic Superconducting Qubit *LC* Oscillator System. *Phys. Rev. Lett.* **96**, 127006 (2006).

[141] Cohen-Tannoudji, C., Diu, B. & Laloë, F. *Quantum Mechanics* (Wiley-Interscience, New York, 2005).

[142] Deppe, F. *et al.* Two-photon probe of the Jaynes-Cummings model and controlled symmetry breaking in circuit QED. *Nature Physics* **4**, 686–691 (2008).

[143] Götz, M. *et al.* Preparation of self-aligned in-line tunnel junctions for applications in single-charge electronics. *J. Appl. Phys.* **78**, 5499–5502 (1995).

[144] Deppe, F., Saito, S., Tanaka, H. & Takayanagi, H. Determination of the capacitance of nm scale Josephson junctions. *J. App. Phys.* **95**, 2607–2613 (2004).

[145] Frunzio, L., Wallraff, A., Schuster, D., Majer, J. & Schoelkopf, R. Fabrication and characterization of superconducting circuit QED devices for quantum computation. *IEEE Trans. Appl. Supercond* **15**, 860–863 (2005).

[146] Barends, R. *et al.* Niobium and tantalum high Q resonators for photon detectors. *IEEE Trans. Appl. Supercond.* **17**, 263 – 266 (2007).

[147] O'Connell, A. D. *et al.* Microwave dielectric loss at single photon energies and millikelvin temperatures. *App. Phys. Lett.* **92**, 112903 (2008).

[148] Göppl, M. *et al.* Coplanar waveguide resonators for circuit quantum electrodynamics. *J. App. Phys.* **104**, 113904 (2008).

[149] Niemczyk, T. *et al.* Fabrication technology of and symmetry breaking in superconducting quantum circuits. *Supercond. Sci. Technol.* **22**, 034009 (2009).

[150] Pozar, D. M. *Microwave Engineering* (John Wiley & Sons, Inc., New York, 2005).

[151] Schuster, D. I. *Circuit Quantum Electrodynamics*. Ph.D. thesis, Yale University (2007).

[152] Simons, R. N. *Coplanar Waveguide Circuits, Components, and Systems* (Wiley-Interscience, New York, 2001).

[153] Watanabe, K., Yoshida, K., Aoki, T. & Kohjiro, S. Kinetic Inductance of Superconducting Coplanar Waveguides. *Jap. J. Appl. Phys.* **33**, 5708–5712 (1994).

[154] Yoshida, K., Watanabe, K., Kisu, T. & Enpuku, K. Evaluation of magnetic penetration depth and surface resistance of superconducting thin films using coplanar waveguides. *IEEE Trans. Appl. Supercond* **5**, 1979 – 1982 (1995).

[155] Rauch, W. *et al.* Microwave properties of $YBa_2Cu_3O_{7-x}$ thin films studied with coplanar transmission line resonators. *J. Appl. Phys.* **73**, 1866–1872 (1993).

[156] Bardeen, J., Cooper, L. N. & Schrieffer, J. R. Theory of Superconductivity. *Phys. Rev.* **108**, 1175–1204 (1957).

[157] Einzel, D. Interpolation of BCS response functions. *Journal of Low Temperature Physics* **130**, 493–508 (2003).

[158] Bardeen, J., Cooper, L. N. & Schrieffer, J. R. Microscopic Theory of Superconductivity. *Phys. Rev.* **106**, 162–164 (1957).

[159] Wang, H. *et al.* Improving the coherence time of superconducting coplanar resonators. *App. Phys. Lett.* **95**, 233508 (2009).

[160] Shnirman, A., Schön, G., Martin, I. & Makhlin, Y. Low- and High-Frequency Noise from Coherent Two-Level Systems. *Phys. Rev. Lett.* **94**, 127002 (2005).

[161] Gao, J., Zmuidzinas, J., Mazin, B. A., LeDuc, H. G. & Day, P. K. Noise properties of superconducting coplanar waveguide microwave resonators. *App. Phys. Lett.* **90**, 102507 (2007).

[162] Gao, J. *et al.* Experimental evidence for a surface distribution of two-level systems in superconducting lithographed microwave resonators. *App. Phys. Lett* **92**, 152505 (2008).

[163] Gao, J. *et al.* A semiempirical model for two-level system noise in superconducting microresonators. *App. Phys. Lett.* **92**, 212504 (2008).

[164] Macha, P. *et al.* Losses in coplanar waveguide resonators at millikelvin temperatures. *App. Phys. Lett.* **96**, 062503 (2010).

[165] Barends, R. *et al.* Minimal resonator loss for circuit quantum electrodynamics. *App. Phys. Lett.* **97**, 023508 (2010).

[166] Vayonakis, A. & Zmuidzinas, J. Radiative Losses from 2D Apertures (2002). Private notes.

[167] Mazin, B. A. *Microwave Kinetic Inductance Detectors.* Ph.D. thesis, California Institute of Technology (2004).

[168] Schwabl, F. *Quantenmechanik* (Springer Verlag, Berlin, 1998).

[169] Brenninger, T. A new thin film deposition system for the preparation of persistent current qubits (2007). Master Thesis.

[170] Dolan, G. J. Offset masks for lift-off photoprocessing. *Appl. Phys. Lett.* **31**, 337–339 (1977).

[171] Eggenstein, L. Optimierung und Charakterisierung von supraleitenden Quantenschaltkreisen auf der Basis von Fluss-Qubits (2009). Diploma thesis (TU München).

[172] Schuler, J. *Ferromagnetische Einzelladungs-Transistoren.* Ph.D. thesis, TU München (2005).

[173] Göppl, M. Quantenelektronik mit supraleitenden Bauelementen - Herstellung und Charakterisierung von Fluss-Qubits (2006). Diploma thesis (TU München).

[174] Niskanen, A. O. *et al.* Quantum Coherent Tunable Coupling of Superconducting Qubits. *Science* **316**, 723–726 (2007).

[175] Göppl, M. *Engineering Quantum Electronic Chips - Realization and Characterization of Circuit Quantum Electrodynamics Systems.* Ph.D. thesis, ETH Zürich (2009).

[176] Dandl, S. Herstellung und Charakterisierung einer definierten elektromagnetischen Umgebung für supraleitende Fluss-Qubits (2006). Diploma thesis (TU München).

[177] Lupaşcu, A., Verwijs, C. J. M., Schouten, R. N., Harmans, C. J. P. M. & Mooij, J. E. Nondestructive Readout for a Superconducting Flux Qubit. *Phys. Rev. Lett.* **93**, 177006 (2004).

[178] Siddiqi, I. *et al.* RF-Driven Josephson Bifurcation Amplifier for Quantum Measurement. *Phys. Rev. Lett.* **93**, 207002 (2004).

[179] Lupaşcu, A., Driessen, E. F. C., Roschier, L., Harmans, C. J. P. M. & Mooij, J. E. High-Contrast Dispersive Readout of a Superconducting Flux Qubit Using a Nonlinear Resonator. *Phys. Rev. Lett.* **96**, 127003 (2006).

[180] Lupaşcu, A. *et al.* Quantum non-demolition measurement of a superconducting two-level system. *Nature Physics* **3**, 119–125 (2007).

[181] Abdumalikov, A. A., Astafiev, O., Nakamura, Y., Pashkin, Y. A. & Tsai, J. Vacuum Rabi splitting due to strong coupling of a flux qubit and a coplanar-waveguide resonator. *Phys. Rev. B* **78**, 180502 (2008).

[182] Wild, G. Macroscopic quantum tunneling in Josephson junctions - a method to characterise a well-shielded low temperature setup (2004). Diploma thesis (TU München).

[183] Tanaka, H. *et al.* Single-Shot Readout of Macroscopic Quantum Superposition State in a Superconducting Flux Qubit (2004). ArXiv:cond-mat/0407299v1.

[184] Cohen-Tannoudji, C., Dupont-Roc, J. & Grynberg, G. *Atom-photon intractions* (Wiley-Interscience, New York, 1998).

[185] Saito, S. *et al.* Multiphoton Transitions in a Macroscopic Quantum Two-State System. *Phys. Rev. Lett.* **93**, 037001 (2004).

[186] Oliver, W. D. *et al.* Mach-Zehnder Interferometry in a Strongly Driven Superconducting Qubit. *Science* **310**, 1653–1657 (2005).

[187] Saito, S. *et al.* Parametric Control of a Superconducting Flux Qubit. *Phys. Rev. Lett.* **96**, 107001 (2006).

[188] Sillanpää, M., Lehtinen, T., Paila, A., Makhlin, Y. & Hakonen, P. Continuous-Time Monitoring of Landau-Zener Interference in a Cooper-Pair Box. *Phys. Rev. Lett.* **96**, 187002 (2006).

[189] Wilson, C. M. *et al.* Coherence Times of Dressed States of a Superconducting Qubit under Extreme Driving. *Phys. Rev. Lett.* **98**, 257003 (2007).

[190] Irish, E. K. & Schwab, K. Quantum measurement of a coupled nanomechanical resonator–Cooper-pair box system. *Phys. Rev. B* **68**, 155311 (2003).

[191] LaHaye, M. D., Suh, J., Echternach, P. M., Schwab, K. C. & Roukes, M. L. Nanomechanical measurements of a superconducting qubit. *Nature* **459**, 960–964 (2009).

[192] O'Connell, A. D. *et al.* Quantum ground state and single-phonon control of a mechanical resonator. *Nature* **464**, 697–703 (2010).

[193] Brune, M. *et al.* From Lamb shift to light shifts: Vacuum and subphoton cavity fields measured by atomic phase sensitive detection. *Phys. Rev. Lett.* **72**, 3339–3342 (1994).

[194] Grangier, P., Levenson, J. A. & Poizat, J.-P. Quantum non-demolition measurements in optics. *Nature* **396**, 537–542 (1998).

[195] Nogues, G. *et al.* Seeing a single photon without destroying it. *Nature* **400**, 239–242 (1999).

[196] Guerlin, C. *et al.* Progressive field-state collapse and quantum non-demolition photon counting. *Nature* **448**, 889–893 (2007).

[197] Johnson, B. R. *et al.* Quantum non-demolition detection of single microwave photons in a circuit. *Nature Physics* **6**, 663–667 (2010).

[198] Fragner, A. *et al.* Resolving Vacuum Fluctuations in an Electrical Circuit by Measuring the Lamb Shift. *Science* **322**, 1357–1360 (2008).

[199] Fink, J. M. *Quantum Nonlinearities in Strong Coupling Circuit QED.* Ph.D. thesis, ETH Zürich (2010).

[200] Caballero, M. A. A. A Setup for Quantum Signal Detection in a Circuit QED Architecture (2008). Diploma thesis (TU München).

[201] Menzel, E. P. Private communication.

[202] Wallraff, A. *et al.* Sideband Transitions and Two-Tone Spectroscopy of a Superconducting Qubit Strongly Coupled to an On-Chip Cavity. *Phys. Rev. Lett.* **99**, 050501 (2007).

[203] Tan, S. M. A computational toolbox for quantum and atomic optics. *J. Opt. B.* **1**, 424 (1999).

[204] Fedorov, A. *et al.* Strong Coupling of a Quantum Oscillator to a Flux Qubit at Its Symmetry Point. *Phys. Rev. Lett.* **105**, 060503 (2010).

[205] Steffen, M. *et al.* High-Coherence Hybrid Superconducting Qubit. *Phys. Rev. Lett.* **105**, 100502 (2010).

[206] Il'ichev, E. *et al.* Multiphoton excitations and inverse population in a system of two flux qubits. *Phys. Rev. B* **81**, 012506 (2010).

[207] Lupaşcu, A., Bertet, P., Driessen, E. F. C., Harmans, C. J. P. M. & Mooij, J. E. One- and two-photon spectroscopy of a flux qubit coupled to a microscopic defect. *Phys. Rev. B* **80**, 172506 (2009).

[208] Berns, D. M. *et al.* Amplitude spectroscopy of a solid-state artificial atom. *Nature* **455**, 51–57 (2008).

[209] Bushev, P. *et al.* Multiphoton spectroscopy of a hybrid quantum system. *Phys. Rev. B* **82**, 134530 (2010).

[210] Liu, Y.-x., You, J. Q., Wei, L. F., Sun, C. P. & Nori, F. Optical Selection Rules and Phase-Dependent Adiabatic State Control in a Superconducting Quantum Circuit. *Phys. Rev. Lett.* **95**, 087001 (2005).

[211] Niemczyk, T. *et al.* Selection rules in a strongly coupled qubit-resonator system (2011). *submitted to Phys. Rev. B.*

[212] Bourassa, J. *et al.* Ultrastrong coupling regime of cavity QED with phase-biased flux qubits. *Phys. Rev. A* **80**, 032109 (2009).

[213] Lisenfeld, J. *et al.* Rabi spectroscopy of a qubit-fluctuator system. *Phys. Rev. B* **81**, 100511 (2010).

[214] Blais, A. *et al.* Quantum-information processing with circuit quantum electrodynamics. *Phys. Rev. A* **75**, 032329 (2007).

[215] Bruskiewich, P. The parity operator for the quantum harmonic oscillator - A pedagogical introduction. *Can. Undergrad. Phys. J.* **VI**, 30–32 (2007).

[216] Ciuti, C., Bastard, G. & Carusotto, I. Quantum vacuum properties of the intersubband cavity polariton field. *Phys. Rev. B* **72**, 115303 (2005).

[217] Ciuti, C. & Carusotto, I. Input-output theory of cavities in the ultrastrong coupling regime: The case of time-independent cavity parameters. *Phys. Rev. A* **74**, 033811 (2006).

[218] Devoret, M., Girvin, S. & Schoelkopf, R. Circuit-QED: How strong can the coupling between a Josephson junction atom and a transmission line resonator be? *Ann. Phys.* **16**, 767–779 (2007).

[219] Günter, G. *et al.* Sub-cycle switch-on of ultrastrong light-matter interaction. *Nature* **458**, 178–181 (2009).

[220] Anappara, A. A. *et al.* Signatures of the ultrastrong light-matter coupling regime. *Phys. Rev. B* **79**, 201303 (2009).

[221] Todorov, Y. *et al.* Ultrastrong Light-Matter Coupling Regime with Polariton Dots. *Phys. Rev. Lett.* **105**, 196402 (2010).

[222] Tavis, M. & Cummings, F. W. Exact Solution for an N-Molecule—Radiation-Field Hamiltonian. *Phys. Rev.* **170**, 379–384 (1968).

[223] Zueco, D., Reuther, G. M., Kohler, S. & Hänggi, P. Qubit-oscillator dynamics in the dispersive regime: Analytical theory beyond the rotating-wave approximation. *Phys. Rev. A* **80**, 033846 (2009).

[224] Schoelkopf, R. J. & Girvin, S. M. Wiring up quantum systems. *Nature* **451**, 664–669 (2008).

[225] Yamamoto, T., Pashkin, Y. A., Astafiev, O., Nakamura, Y. & Tsai, J. S. Demonstration of conditional gate operation using superconducting charge qubits. *Nature* **425**, 941–944 (2003).

[226] Plantenberg, J. H., de Groot, P. C., Harmans, C. J. P. M. & Mooij, J. E. Demonstration of controlled-NOT quantum gates on a pair of superconducting quantum bits. *Nature* **447**, 836–839 (2007).

[227] Lucero, E. *et al.* High-Fidelity Gates in a Single Josephson Qubit. *Phys. Rev. Lett.* **100**, 247001 (2008).

[228] Walls, D. F. Squeezed states of light. *Nature* **306**, 141–146 (1983).

[229] Yurke, B. *et al.* Observation of 4.2-K equilibrium-noise squeezing via a Josephson-parametric amplifier. *Phys. Rev. Lett.* **60**, 764–767 (1988).

[230] Yurke, B. *et al.* Observation of parametric amplification and deamplification in a Josephson parametric amplifier. *Phys. Rev. A* **39**, 2519–2533 (1989).

[231] Movshovich, R. *et al.* Observation of zero-point noise squeezing via a Josephson-parametric amplifier. *Phys. Rev. Lett.* **65**, 1419–1422 (1990).

[232] Castellanos-Beltran, M. A. & Lehnert, K. W. Widely tunable parametric amplifier based on a superconducting quantum interference device array resonator. *Appl. Phys. Lett.* **91**, 083509 (2007).

[233] Yamamoto, T. *et al.* Flux-driven Josephson parametric amplifier. *Appl. Phys. Lett.* **93**, 042510 (2008).

[234] Teufel, J. D., Donner, T., Castellanos-Beltran, M. A., Harlow, J. W. & Lehnert, K. W. Nanomechanical motion measured with an imprecision below that at the standard quantum limit. *Nature Nanotech.* **4**, 820–823 (2009).

[235] Baust, A. Characterization of flux-driven josephson parametric amplifiers (2010). Diploma thesis (TU München).

[236] Sandberg, M. *et al.* Tuning the field in a microwave resonator faster than the photon lifetime. *Appl. Phys. Lett.* **92**, 203501 (2008).

[237] Johansson, J. R., Johansson, G., Wilson, C. M. & Nori, F. Dynamical Casimir Effect in a Superconducting Coplanar Waveguide. *Phys. Rev. Lett.* **103**, 147003 (2009).

[238] De Liberato, S., Gerace, D., Carusotto, I. & Ciuti, C. Extracavity quantum vacuum radiation from a single qubit. *Phys. Rev. A* **80**, 053810 (2009).

[239] Wilson, C. M. *et al.* Photon Generation in an Electromagnetic Cavity with a Time-Dependent Boundary. *Phys. Rev. Lett.* **105**, 233907 (2010).

[240] Johansson, J. R., Johansson, G., Wilson, C. M. & Nori, F. Dynamical Casimir effect in superconducting microwave circuits. *Phys. Rev. A* **82**, 052509 (2010).

[241] Hagenmüller, D., De Liberato, S. & Ciuti, C. Ultrastrong coupling between a cavity resonator and the cyclotron transition of a two-dimensional electron gas in the case of an integer filling factor. *Phys. Rev. B* **81**, 235303 (2010).

[242] Ashhab, S. & Nori, F. Qubit-oscillator systems in the ultrastrong-coupling regime and their potential for preparing nonclassical states. *Phys. Rev. A* **81**, 042311 (2010).

[243] Meaney, C. P., Duty, T., McKenzie, R. H. & Milburn, G. J. Jahn-Teller instability in dissipative quantum systems. *Phys. Rev. A* **81**, 043805 (2010).

[244] Casanova, J., Romero, G., Lizuain, I., García-Ripoll, J. J. & Solano, E. Deep Strong Coupling Regime of the Jaynes-Cummings Model. *Phys. Rev. Lett.* **105**, 263603 (2010).

[245] Jahn, H. A. & Teller, E. Stability of Polyatomic Molecules in Degenerate Electronic States. I. Orbital Degeneracy. *Proc. R. Soc. London, Ser. A* **161**, 220–235 (1937).

[246] Levine, G. & Muthukumar, V. N. Entanglement of a qubit with a single oscillator mode. *Phys. Rev. B* **69**, 113203 (2004).

[247] Hines, A. P., Dawson, C. M., McKenzie, R. H. & Milburn, G. J. Entanglement and bifurcations in Jahn-Teller models. *Phys. Rev. A* **70**, 022303 (2004).

[248] Larson, J. Jahn-Teller systems from a cavity QED perspective. *Phys. Rev. A* **78**, 033833 (2008).

[249] Peropadre, B., Forn-Díaz, P., Solano, E. & García-Ripoll, J. J. Switchable Ultrastrong Coupling in Circuit QED. *Phys. Rev. Lett.* **105**, 023601 (2010).

[250] Menzel, E. P. *et al.* Dual-Path State Reconstruction Scheme for Propagating Quantum Microwaves and Detector Noise Tomography. *Phys. Rev. Lett.* **105**, 100401 (2010).

[251] Bozyigit, D. *et al.* Antibunching of microwave-frequency photons observed in correlation measurements using linear detectors. *Nature Physics* **7**, 154–158 (2011).

[252] Dicke, R. H. Coherence in Spontaneous Radiation Processes. *Phys. Rev.* **93**, 99–110 (1954).

[253] Garraway, B. M. The Dicke model in quantum optics: Dicke model revisited. *Proc. R. Soc. London A* **369**, 1137–1155 (2010).

[254] Scully, M. O. & Svidzinsky, A. A. The Super of Superradiance. *Science* **325**, 1510–1511 (2009).

[255] Chen, G., Chen, Z. & Liang, J. Simulation of the superradiant quantum phase transition in the superconducting charge qubits inside a cavity. *Phys. Rev. A* **76**, 055803 (2007).

[256] Lambert, N., Chen, Y.-n., Johansson, R. & Nori, F. Quantum chaos and critical behavior on a chip. *Phys. Rev. B* **80**, 165308 (2009).

[257] Vidal, J. & Dusuel, S. Finite-size scaling exponents in the Dicke model. *Europhys. Lett.* **74**, 817–822 (2006).

[258] Emary, C. & Brandes, T. Chaos and the quantum phase transition in the Dicke model. *Phys. Rev. E* **67**, 066203 (2003).

[259] Lambert, N., Emary, C. & Brandes, T. Entanglement and the Phase Transition in Single-Mode Superradiance. *Phys. Rev. Lett.* **92**, 073602 (2004).

[260] Lambert, N., Emary, C. & Brandes, T. Entanglement and entropy in a spin-boson quantum phase transition. *Phys. Rev. A* **71**, 053804 (2005).

[261] Wang, Y.-D., Chesi, S., Loss, D. & Bruder, C. One-step multiqubit Greenberger-Horne-Zeilinger state generation in a circuit QED system. *Phys. Rev. B* **81**, 104524 (2010).

[262] Hartmann, M. J., Brandao, F. G. S. L. & Plenio, M. B. Strongly interacting polaritons in coupled arrays of cavities. *Nature Physics* **2**, 849–855 (2006).

[263] Hartmann, M. J. & Plenio, M. B. Strong Photon Nonlinearities and Photonic Mott Insulators. *Phys. Rev. Lett.* **99**, 103601 (2007).

[264] Leib, M. & Hartmann, M. J. Bose-Hubbard dynamics of polaritons in a chain of circuit quantum electrodynamics cavities. *New J. Phys.* **12**, 093031 (2010).

[265] Sabín, C., García-Ripoll, J. J., Solano, E. & León, J. Dynamics of entanglement via propagating microwave photons. *Phys. Rev. B* **81**, 184501 (2010).

[266] Court, N. A., Ferguson, A. J. & Clark, R. G. Energy gap measurement of nanostructured aluminium thin films for single Cooper-pair devices. *Supercond. Sci. Technol.* **21**, 015013 (2008).

List of publications

- T. Niemczyk, F. Deppe, M. Mariantoni, E.P. Menzel, E. Hoffmann, G. Wild, L. Eggenstein, A. Marx and R. Gross. Fabrication technology of and symmetry breaking in superconducting quantum circuits. *Supercond. Sci. Technol.* **22**, 034009 (2009)

- T. Niemczyk, F. Deppe, H. Huebl, E. P. Menzel, F. Hocke, M. J. Schwarz, J. J. Garcia-Ripoll, D. Zueco, T. Hümmer, E. Solano, A. Marx and R. Gross. Circuit quantum electrodynamics in the ultrastrong-coupling regime. *Nature Physics* **6**, 772-776 (2010)

- E. P. Menzel, F. Deppe, M. Mariantoni, M. Á. Araque Caballero, A. Baust, T. Niemczyk, E. Hoffmann, A. Marx, E. Solano and R. Gross. Dual-Path State Reconstruction Scheme for Propagating Quantum Microwaves and Detector Noise Tomography. *Phys. Rev. Lett.* **105**, 100401 (2010)

- M. Mariantoni, E. P. Menzel, F. Deppe, M. Á. Araque Caballero, A. Baust, T. Niemczyk, E. Hoffmann, E. Solano, A. Marx and R. Gross. Planck Spectroscopy and Quantum Noise of Microwave Beam Splitters. *Phys. Rev. Lett.* **105**, 133601 (2010)

- E. Hoffmann, F. Deppe, T. Niemczyk, T. Wirth, E. P. Menzel, G. Wild, H. Huebl, M. Mariantoni, T. Weißl, A. Lukashenko, A. P. Zhuravel, A. V. Ustinov, A. Marx and R. Gross. A superconducting 180° hybrid ring coupler for circuit quantum electrodynamics. *Appl. Phys. Lett.* **97**, 222508 (2010)

- T. Niemczyk, F. Deppe, E. P. Menzel, M. J. Schwarz, H. Huebl, M. Häberlein, F. Hocke, M. Danner, A. Baust, E. Hoffmann, J. J. Garcia-Ripoll, E. Solano, A. Marx and R. Gross. Selection rules in a strongly coupled qubit-resonator system. *in preparation for submission to Phys. Rev. B* (2011)

Acknowledgements

First of all, I want to thank my girlfriend Denise, my family and my friends for the constant support during the last years. When you start dreaming about fridges, the clean room facility and microwave equipment, these people remind you that the 'real' world is truly classic.
I want to thank Prof. Rudolf Gross for giving me the opportunity to participate in the WMI's qubit group. He gave me the freedom to explore the fascinating world of experimental quantum physics and confidence concerning my scientific work.
I am very grateful for the support by my supervisor Dr. Achim Marx whose door was and is open for me at any time. He always provided valuable input concerning smaller and bigger problems.
Many of the results presented in this thesis could not have been realized without Thomas Brenninger's engineering skills. He developed the new aluminum evaporation facility and thus provided the corner stone for a successful qubit fabrication. Give that man a prize!
From my current PhD colleagues I first want to thank Edwin Menzel and Dr. Frank Deppe. While I was responsible for device production, Edwin did impressive work on the setup of the K04 fridge in which the circuit QED measurements were performed. The discussions with Frank Deppe were of great help to me due to his huge experience concerning flux quantum bits, experimental techniques, theory and condensing a lot of physics within 1500 words.
No less important were the contributions from my other qubit group members: Georg Wild introduced me to the ^{3}He fridge in his own unique style and helped me maintaining the fridges. The discussions with Manuel Schwarz and the pleasant time in the clean room facilities were a constant source of inspiration. I want to thank Dr. Hans Hübl for the various helpful discussions and his input to the understanding of the circuit QED data. A special thank goes to my former diploma student and now PhD colleague Elisabeth Hoffmann, who is one of the most helpful people I ever met. Likewise, I thank Fredrik Hocke for valuable input concerning resonant cavities and vegan cuisine. In addition, I want to explicitly mention my appraisal for his adoring clothing style. I want to thank our new PhD students Alex Baust, Max Häberlein and Matthias Danner. All of them did tremendous work concerning the LabView infrastructure and the (re)construction of the K04 fridge. Additionally, Max and Matthias could answer many of my theoretical questions. Last but not least, I am very grateful to the work accomplished by my diploma students Lars Eggenstein and Susanne Hofmann and by my working students Stefan Nimmrichter, Friedrich Wulschner and Philip Matthies.

I am also very grateful for the fruitful collaboration with Prof. Juan Jose Garica-Ripoll, Prof. Enrique Solano, Dr. David Zueco and Thomas Hümmer. From the non-qubit staff, I want to thank my colleagues Stephan Geprägs and Andreas Brandlmaier for sharing so many laughs with me. Also, I want to thank my former PhD colleagues Tobias Heimbeck, Karl Madek and Wolfgang Prestel for sharing the same sense of humor and for their work-related input concerning EBL and advanced cryogenics. In particular, I want to mention Dr. Christian Probst who designed and fabricated the new sample holder of the dilution unit and helped me maintaining the fridge. Furthermore, I am grateful for the help of Dr. Kurt Uhlig, Dr. Karl Neumaier and Sepp Höß with the K04 fridge. I also wish to express my gratitude to our workshop staff Robert Müller, Helmut Thies, Christian Reichlmeier, Julius Klaus and Georg Nitschke. While these people milled, lathed and assembled several boxes, sample holders and even fridges, the people from the helium liquefaction - Harald Schwaiger, Jan Naundorf and Peter Binkert - prevented supply shortfalls of liquid gases. Finally, I want to thank all the motivated people at the WMI who helped me in one way or another during the last years: Dr. Werner Biberacher, Emel Dönertas, Dr. Andreas Erb, Joachim Geismann, Dr. Sebastian Gönnenwein, Ulrich Guggenberger, Dieter Guratzsch, Astrid Habel, Dr. Rudi Hackl, Karen Helm-Knapp, Namvar Jahanmehr, Dr. Mark Kartsovnik, Prof. Anton Lerf, Dr. Matthias Opel, Ludwig Ossiander, Tina Pinkert, Sybilla Plöderl, Brigitte Steinberg and Siegfried Wanninger. Special thanks go out to Dr. Dietrich Einzel for theory support, Prof. Bellur Sivaramiah Chandrasekhar for reading and improving my thesis and Dr. Robert Doll for being a role model of a true physicist.